Imperial College London

The Drivers and Timescales of Solar Wind-Magnetosphere-Ionosphere Coupling in Global MHD Simulations

Joseph W. B. Eggington

Space and Atmospheric Physics Group
Department of Physics
Imperial College London

Submitted in fulfilment of the requirements for the degree of
Doctor of Philosophy

29th June 2021

Declaration of Authorship

I declare that all work presented in this thesis is my own, unless explicitly stated and referenced.

Joseph Eggington - June 2021

The work presented in this thesis has contributed to two published journal articles, the latter of which was peer-reviewed:

- **Chapter 2** - J. W. B. Eggington et al. "Forging links in Earth's plasma environment". In: *Astronomy & Geophysics* 59.6. DOI: 10.1093/astrogeo/aty275
- **Chapter 3** - J. W. B. Eggington et al. "Dipole Tilt Effect on Magnetopause Reconnection and the Steady-State Magnetosphere-Ionosphere System: Global MHD Simulations". In: *Journal of Geophysical Research: Space Physics* 125.7. DOI: 10.1029/2019JA027510

Abstract

The interaction between the solar wind and the terrestrial magnetosphere-ionosphere system is highly dynamic and non-linear, strongly influencing conditions in near-Earth space. Understanding the coupling between each component of the system is crucial to mitigating societal effects, known as space weather. Global magnetohydrodynamic (MHD) simulations are an invaluable tool in studying this interaction. This thesis entails the use of the Gorgon MHD code for simulating the Earth's magnetosphere. An updated version of the code is presented, including a newly developed ionosphere module which is tested and benchmarked to validate its proper coupling to the magnetosphere.

The model is applied to study the effect of the geomagnetic dipole tilt angle on magnetopause reconnection and ionospheric current systems. The location of the reconnection line is identified for tilt angles up to 90°, with reconnection found to be weaker and more unsteady at large tilt angles. The tilt introduces a North-South asymmetry driving more FAC in the sunward-facing hemisphere, highlighting the sensitivity to onset time in the potential impact of a severe space weather event.

An idealised example of such an event is then simulated by impacting the magnetosphere with an interplanetary shock. The location and intensity of dayside reconnection is found to be highly time-dependent following impact, with reconnection enhanced in the vicinity of the shock. These results suggest that steady models of reconnection may not be reliable immediately after onset.

Finally, an extended version of the code is implemented to simulate a real geomagnetic storm. The key response timescales of the magnetosphere-ionosphere system to the varying solar wind are investigated, and found to be consistent with those of global convection, being sensitive to the particular mode of driving. It is shown that Gorgon is a capable space weather modelling tool, forming a crucial step towards future operational forecasting purposes.

Acknowledgements

Firstly, I would like to thank my supervisor Jonathan for his constant guidance, insight and encouragement throughout these three and a half years. I owe a great deal to Lars, for patiently passing on his expertise and providing the foundation for this work, and to Ravi, for his generous advice and many valuable discussions. I look forward to working more on Gorgon in the coming months, and seeing everyone's efforts continue to bear fruit.

My PhD experience was made so much more enjoyable thanks to the people I shared it with. I was fortunate to start at the same time as my office mates - Ned, Maks, Emma and Arthur - which has led to many great memories, be it a conference trip, a spontaneous pub visit or just general procrastination. A pandemic may have robbed us of our last year as students, but I'm sure we'll make up for it up soon. The same is true of so many other people in SPAT who have come and gone; a special mention to Alex, the one constant of my university education and who joined the group a whole year earlier just to warm my office chair.

I owe the most to my family, without whose support I would never have had the opportunity or belief to get this far. To my housemates, for sharing these years together in London, especially when we were locked away at home. And to Jo, for keeping me sane and smiling even in these hermitic last few months. This thesis would have been much harder to write without you.

Contents

List of Figures

List of Tables

Nomenclature

Abbreviations

MHD	Magnetohydrodynamics
IMF	Interplanetary magnetic field
CME	Coronal mass ejection
CIR	Corotating interaction region
FTE	Flux transfer event
OCB	Open-closed (field line) boundary
FAC	Field-aligned current
TFAC	Total field-aligned current
CPCP	Cross-polar cap potential
EUV	Extreme ultraviolet (radiation)
GIC	Geomagnetically-induced current
MMS	Magnetospheric Multiscale (mission)
THEMIS	Time History of Events and Macroscale Interactions during Substorms (mission)
AMPERE	Active Magnetosphere and Planetary Electrodynamics Response Experiment
ACE	Advanced Composition Explorer (spacecraft)
L1	First Lagrange point
GSE	Geocentric Solar Ecliptic (coordinates)
GSM	Geocentric Solar Magnetic (coordinates)
SM	Solar Magnetic (coordinates)
GMHD	Global magnetohydrodynamic (code)
CCMC	Community-Coordinated Modeling Center

Physical Constants

c	Speed of light, 3.00×10^{8} m·s^{-1}
m_p	Proton mass, 1.67×10^{-27} kg
m_e	Electron mass, 9.11×10^{-31} kg
e	Elementary charge, 1.60×10^{-19} C
μ_0	Permeability of free-space, 1.26×10^{-6} m·kg·s^{-2}A^{-2}
ϵ_0	Permittivity of free-space, 8.85×10^{-12}m^{-3}kg^{-1}s^{4}A^{2}
k_B	Boltzmann constant, 1.38×10^{-23} m^{2}kg·s^{-2}K^{-1}
R_E	Earth radius, 6.37×10^{6} m
AU	Astronomical unit, 1.50×10^{11} m

Symbols

t	Time
ρ	Plasma mass density
n	Plasma number density
$T_{i,p,e}$	Plasma ion/proton/electron temperature
P	Plasma thermal pressure
γ	Adiabatic index
c_s	Sound speed

c_{ms}	Magnetosonic speed
ω	Angular frequency
$\mathbf{k}$	Wavevector
$\mathbf{v}$	Plasma flow velocity
$\mathbf{p}$	Plasma momentum density
$\mathbf{J}$	Electric current density
$\mathbf{E}$	Electric field
$\mathbf{B}$	Magnetic field
$\mathbf{A}$	Magnetic vector potential
η	Electrical resistivity
ψ	Electric potential
$j_{\|\|}$	Field-aligned current density
$\Phi_{D,N}$	Dayside/nightside reconnection voltage
F_{PC}	Polar cap flux content
$\Sigma_{P,H}$	Pedersen/Hall conductance
μ	Dipole tilt angle
θ_{IFM}	IMF clock angle

Chapter 1

Introduction

Over the last half a century, our understanding of the near-Earth space environment has evolved dramatically. Whilst it has been known since the early space age that the region surrounding the planet is populated with charged particles originating from the Sun, the means by which these interact with the terrestrial magnetic field, penetrate into the atmosphere and generate bright auroral displays has only been understood after decades of space missions and ground-based observations. The solar wind - a supersonic stream of plasma emanating from the solar atmosphere - bombards the planetary field which acts as a barrier protecting the Earth's atmosphere from ionising particles. The region bounded by this shield is known as the magnetosphere, and is a highly complex, dynamical physical system host to a broad spectrum of plasma phenomena.

Magnetospheres have been identified through remote observations and in-situ measurements at all the magnetised planets in the solar system (as well as Jupiter's moon Ganymede), with that of Earth being the most closely-studied (Vasyliunas, 2009). On more distant scales, radio observations of magnetospheric features around exoplanets (Nichols and Milan, 2016) demonstrate the relevance of these structures as fundamental in the broader astrophysical context. Whilst all the magnetospheres in the solar system are driven by the solar wind in some way, interior processes (such as planetary rotation) can be extremely important, particularly at the gas giants Jupiter and Saturn which harbour significant internal plasma sources in the form of their natural satellites.

The terrestrial magnetosphere is, conversely, largely controlled by its interaction with the solar wind, resulting in a system strongly sensitive to changing conditions in the interplanetary medium and thus solar activity. The magnetosphere is further connected to the ionosphere through large-scale current systems, forming a coupled dynamical system from the solar wind down to the Earth's surface (Ganushkina et al., 2018). Studying the mechanisms responsible for this coupling is therefore not only relevant to planetary science in general, but is of central importance in understanding what controls the near-Earth space environment, on which modern society is increasingly dependent.

The processes by which geospace phenomena can impact society are described under the blanket term 'space weather', and manifest not only out in space but also on the ground (Eastwood et al., 2017). For instance, satellites can be damaged via irradiation by high-energy particles, and those in a low-Earth orbit are vulnerable to atmospheric drag resulting from heating of the thermosphere by ionospheric currents. These same

current systems are responsible for geomagnetic perturbations, which drive geoelectric fields and geomagnetically-induced currents (GICs) within the conducting Earth.

Whilst our understanding of these processes is greatly improved through observations and empirical/physical modelling, the non-linear nature of the magnetosphere makes accurate predictions significantly challenging. Furthermore, its enormous spatial size is such that in-situ measurements can provide only a limited perspective of the global dynamics. Over the last few decades, advancements in computational capabilities and plasma simulations have allowed for the rapid development of global simulations of the coupled solar wind-magnetosphere-ionosphere system (Raeder, 2003). These models are capable of increasingly complex studies which have shed much light on the fundamental physics at play, and have begun to provide operational-scale forecasts of space weather at Earth. This thesis entails the use of one such model - the Gorgon MHD code - to study the key drivers of magnetospheric dynamics, and the timescales over which these evolve and generate signatures in the Earth's ionosphere.

1.1 Space Plasmas

Plasma, the fourth state of matter, is composed of electrically-charged electrons and ions which freely flow in equal quantity, and is produced when a neutral gas is sufficiently ionised. Due to the equal population of positive and negative charges, plasmas are quasi-neutral and hence obey the laws of thermodynamics like any neutral gas. However, the motion of individual charged particles generates electromagnetic fields throughout the plasma. The particles are then influenced by these fields, which act over long ranges and cause the plasma to exhibit 'collective behaviour', a key trait which distinguishes plasmas from a neutral gas.

A number of well-defined criteria exist based on these properties which determine whether a collection of such particles exists within the parameter regime of a plasma. The first relates to the quasi-neutrality condition, which initially requires equal ion and electron number densities: n_i and n_e, respectively. This can be disturbed by thermodynamic motions of individual particles creating a local charge imbalance which must be restored. Quasi-neutrality is then only achieved above a characteristic spatial scale given by the Debye length (Kivelson and Russell, 1995),

$$\lambda_D = \sqrt{\frac{\epsilon_0 k_B T_e}{n_e e^2}}. \tag{1.1}$$

Here ϵ_0 is the permittivity of free space, k_B is the Boltzmann constant, T_e is the electron temperature, n_e is the electron number density and e is the electron charge. Over a scale $L \gg \lambda_D$, the electrostatic potential arising from the charge imbalance is effectively shielded by the neighbouring particles. For this shielding to be possible within the plasma there must thus be a sufficient number of particles within a sphere of radius a Debye length, i.e. a Debye sphere. This is measured by the plasma parameter Λ, which is defined as

$$\Lambda = n_e \lambda_D^3, \tag{1.2}$$

and so we require that $\Lambda \gg 1$. Quasi-neutrality can also be disturbed if the plasma is displaced by some external force. Since electrons have a much smaller mass than ions, they are more mobile and hence are displaced further than the ions; an electric field is thus set up due to charge separation, providing a restoring force that results in simple harmonic motion. These plasma oscillations, known as Langmuir waves, have a characteristic plasma frequency which for a plasma of protons and electrons is

$$\omega_{pe} = \sqrt{\frac{n_e e^2}{m_e \epsilon_0}}. \tag{1.3}$$

Since a gas does not have to be fully ionised to transition into a plasma, there may be some effect on the plasma dynamics due to collisions between neutrals and charged particles. If the timescale τ_n for electron-neutral collisions to occur is sufficiently short, then they can dominate over the plasma oscillations and force the plasma to behave more like a gas where the electrons and neutrals are in equilibrium. The plasma frequency must thus be much greater than the electron-neutral collision frequency within the parameter regime of a plasma, i.e. $\omega_{pe}\tau_n \gg 1$. This condition, in combination with those described above, must be met for the plasma approximation to be valid.

Any ensemble of particles which meet these criteria can be treated as a plasma, which can occur over an extremely broad parameter space. Astrophysical plasmas are found throughout the universe, ranging from extremely dense and energetic plasma environments like the interiors of stars (Tayler and Morgan, 1981) and black hole accretion discs (Abramowicz and Fragile, 2013), to the most tenuous plasmas propagating through interplanetary and interstellar space (Richardson et al., 2019). Man-made laboratory plasmas provide a stark contrast to these, where the small spatial scales of interest yield very different phenomena which are a focus of much research, e.g. using tokamaks to create viable nuclear fusion reactors (Menard et al., 2016).

Developing a theoretical framework to describe the dynamics of a plasma requires understanding the full interaction between the particles and the fields. The fields are defined by the fundamental Maxwell's equations for electrodynamics, which are as follows:

$$\nabla \cdot \boldsymbol{E} = \frac{\rho_c}{\epsilon_0}, \tag{1.4}$$

$$\nabla \times \boldsymbol{E} = -\frac{\partial \boldsymbol{B}}{dt}, \tag{1.5}$$

$$\nabla \cdot \boldsymbol{B} = 0, \tag{1.6}$$

$$\nabla \times \boldsymbol{B} = \mu_0 \boldsymbol{J} + \mu_0 \epsilon_0 \frac{\partial \boldsymbol{E}}{\partial t}. \tag{1.7}$$

Here **E** and **B** are the electric and magnetic field, respectively, ρ_c is the charge density, **J** is the electric current density and μ_0 is the permeability of free space. Changes in the

plasma thus result in changes in ρ_c and $\mathbf{J}$, altering the fields which in turn dictate the particle motion according to the Lorentz force,

$$m\frac{d\mathbf{v}}{dt} = q(\mathbf{E} + \mathbf{v} \times \mathbf{B}), \tag{1.8}$$

for a particle with charge q, mass m and velocity $\mathbf{v}$. Collisions between particles also provide an exchange of momentum which can be included via an additional term in this equation. However, since the motion of every individual particle in the system is responsible for changes in the fields, solving the dynamics of the plasma requires accounting for the entire particle population which is neither practical theoretically nor feasible computationally. Simplifications are thus required to develop a suitable framework for modelling the plasma.

1.1.1 Single Particle Motion and Collisions

By neglecting the effects of particles on the fields and just considering the motion of single particles in the presence of the fields, we can gain some basic insight into the plasma dynamics. A particle which is drifting in the presence of a uniform magnetic field of strength B and zero electric field will experience a Lorentz force perpendicular to the magnetic field, resulting in gyratory motion about a given field line with perpendicular velocity $v_\perp$. The gyroradius r_g and gyrofrequency ω_g, also known as the Larmor radius and cyclotron frequency, respectively, are given by:

$$r_g = \frac{mv_\perp}{qB}, \tag{1.9}$$

$$\omega_g = \frac{qB}{m}. \tag{1.10}$$

It follows that ions gyrate more slowly and over a larger radius than the much less massive electrons. In the presence of an additional force, e.g. due to a non-zero electric field or some external influence like gravity, the particles also undergo additional drifts (such as the ExB-drift), which arise due to changes in the gyroradius/gyrofrequency in the direction of said force. Similarly, a non-uniform magnetic field results in gradient and curvature drifts due to varying strength and/or direction of the field along the particle trajectory.

Since some of these drifts depend on the particle masses and charges, they are species-dependent and thus result in an electric current due to differential flow of ions and electrons, where the current density is given by

$$\mathbf{J} = en(\mathbf{v}_i - \mathbf{v}_e). \tag{1.11}$$

for plasma density n, assuming the ions and electrons all have charge e and velocity $\mathbf{v}_i$ and $\mathbf{v}_e$, respectively. Currents are also associated with particle collisions: as mentioned earlier, equation (1.8) is modified where momentum is exchanged between particles. For

generic collisions of frequency ν_c, the resulting force on a particle of mass m travelling with velocity $\mathbf{v}$ is given by $-m\nu_c(\mathbf{v}-\mathbf{v}')$, where $\mathbf{v}'$ is the velocity of the collision partners (Baumjohann and Treumann, 1997).

In a fully ionised plasma these collisions occur only between ions and electrons. Any collisions will be anisotropic in the presence of a magnetic field, since the direction of the Lorentz force depends on the field orientation. Provided however that the rate of collisions is very small, this anisotropy can be neglected, and by solving by solving equation (1.8) for a steady-state plasma ($d\mathbf{v}/dt = 0$) in the rest frame of the collision partners we obtain the generalised Ohm's law,

$$\mathbf{J} = \sigma_0(\mathbf{E} + \mathbf{v} \times \mathbf{B}), \tag{1.12}$$

where the conductivity σ_0 is a scalar and is given by

$$\sigma_0 = \frac{n_e e^2}{m_e \nu_c}. \tag{1.13}$$

This approximation is valid for most space plasmas, which are fully ionised and highly rarefied such that ν_c is negligibly small and hence σ_0 is extremely large. In a fully collisionless scenario where $\sigma_0 \to \infty$, it follows that $\mathbf{E} = -\mathbf{v} \times \mathbf{B}$. In a partially ionised plasma, however, these collisions also occur between charged particles and neutrals, and may occur much more frequently if there is sufficient particle density. The field orientation must then be accounted for, and the conductivity can no longer be treated as scalar. A more general solution is thus obtained whereby

$$\mathbf{J} = \boldsymbol{\sigma} \cdot \mathbf{E}, \tag{1.14}$$

where the conductivity tensor $\boldsymbol{\sigma}$ contains different components of the conductivity relative to the magnetic field orientation, as follows:

$$\boldsymbol{\sigma} = \begin{pmatrix} \sigma_P & \sigma_H & 0 \\ -\sigma_H & \sigma_P & 0 \\ 0 & 0 & \sigma_{||} \end{pmatrix}. \tag{1.15}$$

Here σ_P is the Pedersen conductivity, σ_H is the Hall conductivity, and $\sigma_{||}$ is the parallel conductivity. The Pedersen conductivity determines the 'Pedersen current' in the $\mathbf{E}_\perp$ direction, i.e. the electric field perpendicular to the magnetic field; the Hall conductivity acts in the direction of $\mathbf{E} \times \mathbf{B}$ to produce the 'Hall current'; and the parallel conductivity governs the current in the direction of $\mathbf{B}$, termed the 'field-aligned current'. Expressions for these depend on the relative contribution of collisions between different particle species; for example, we may need to account separately for electron and ion collisions with neutrals, such as for the plasma in the Earth's ionosphere (Cowley, 2000). This is discussed in more detail in section 1.3.3.

We have seen that the motion of individual particles results in the flow of current and the redistribution of charge throughout a plasma. Whilst the resulting effect on the total electric and magnetic fields is small for individual particles, this becomes important across the entire particle population and is only negligible in the presence of strong background fields. Hence, whilst single particle motion helps to reveal these important effects, a fully self-consistent treatment is required to accurately capture any influence on the overall plasma dynamics.

1.1.2 Kinetic Theory

The most general approach to modelling a plasma is to apply kinetic theory, which describes the motion of mutually-interacting particles in a six-dimensional velocity phase space. Rather than treating particle motion on an individual basis, ensemble averages are taken to obtain particle distribution functions of the form $f(\mathbf{x}, \boldsymbol{v}, t)$, for a given position $\mathbf{x}$ and velocity $\boldsymbol{v}$ in phase space at a given time t. The evolution of the distribution function in the presence of averaged electromagnetic fields $\mathbf{E}$ and $\mathbf{B}$ is given in the collisionless case by the Vlasov equation (Gurnett and Bhattacharjee, 2005):

$$\frac{\partial f}{\partial t} + \boldsymbol{v} \cdot \nabla_{\mathbf{x}} f + \frac{q}{m} \left(\mathbf{E} + \boldsymbol{v} \times \mathbf{B} \right) \cdot \nabla_{v} f = 0. \tag{1.16}$$

The addition of a collisional term yields the more general Boltzmann equation, though the Vlasov equation is typically applicable to space plasmas where collective forces dominate over collisional forces. These are both highly non-linear, and hence finding a solution can be extremely challenging, though this can be simplified by making certain approximations. Even then, solving such an equation computationally is highly intensive, precluding its use for simulating the global magnetosphere with present capabilities, and limiting kinetic models to only smaller-scale plasma simulations (Markidis et al., 2020).

One alternative approach is to solve the Vlasov/Boltzmann equation for one particle species, e.g. ions, treating the electrons as a fluid since kinetic electron effects correspond to smaller scales than with ions. These 'hybrid' models reduce the computational cost sufficiently to allow 2-D global simulations of the magnetosphere (von Alfthan et al., 2014), with 3-D global simulations recently becoming a possibility (Pfau-Kempf et al., 2020). However, this is still a computationally expensive approach and so is not yet appropriate for the purposes of studying space weather. A simplified treatment of the plasma is thus needed, in which we neglect kinetic scale phenomena entirely.

1.2 Magnetohydrodynamics

Magnetohydrodynamics (MHD), in its most basic form, treats the plasma as a single conducting fluid with behaviour governed by both fluid dynamics and electrodynamics. This involves the combination of the Navier-Stokes equations for fluids with Maxwell's equations (1.4-1.7), requiring various assumptions that are generally only applicable on large spatial and temporal scales. However, the benefit of MHD is in its ability to capture

plasma dynamics on such scales without the need for complex mathematical treatment, making it highly efficient when applied computationally, for example in simulating the magnetosphere.

1.2.1 The MHD Equations

Taking a fluid approach to modelling plasma requires a loss of generality versus the use of the distribution functions $f(\mathbf{x}, \boldsymbol{\nu}, t)$. However, in cases where we are only interested in macroscopic quantities it is sufficient to eliminate the velocity dependence in the distribution function, achieved by multiplying it by the velocity raised to some power and then integrating over the velocity space. These are known as the moments of the distribution function, the zeroth-order and first-order of which yield the number density n and bulk velocity $\mathbf{v}$ for a given species, respectively:

$$n = \int f(\boldsymbol{\nu}) d^3\nu, \tag{1.17}$$

$$\mathbf{v} = \frac{1}{n} \int \boldsymbol{\nu} f(\boldsymbol{\nu}) d^3\nu. \tag{1.18}$$

Going to second-order provides the pressure tensor $\mathbf{P}$, and third-order the heat flux $\mathbf{q}$, but moments beyond this lose clear physical meaning. From these definitions and by integrating the Vlasov equation (1.16) (multiplied by powers of velocity), we can thus obtain fluid equations for each particle species which depend only on macroscopic quantities. However, even when combined with Maxwell's equations the closure of these fluid equations is not possible without making key assumptions about the plasma.

The MHD equations are a result of these assumptions, obtained by summing the fluid equations across each species to obtain a model for a single conducting fluid with mass density ρ and temperature T. Namely, these assumptions include that the timescales of variation of the plasma are slow (thus neglecting displacement currents), that the plasma is quasi-neutral, that the velocities of interest are non-relativistic and that the electron mass is negligible compared to the ion mass. Provided also that the particles are in thermal equilibrium, their velocity distribution will be Maxwellian and the pressure tensor becomes a scalar pressure P, which is isotropic and allows for a well-defined equation of state via the ideal gas law ($P = nk_BT$). This finally closes the set of resistive MHD equations, which are as follows (Gurnett and Bhattacharjee, 2005):

$$\frac{\partial \rho}{\partial t} + \nabla \cdot (\rho \mathbf{v}) = 0, \tag{1.19}$$

$$\frac{\partial}{\partial t}(\rho \mathbf{v}) + (\mathbf{v} \cdot \nabla)\rho \mathbf{v} = -\nabla P + \mathbf{J} \times \mathbf{B}, \tag{1.20}$$

$$\frac{d}{dt}\left(\frac{P}{\rho^\gamma}\right) = 0, \tag{1.21}$$

$$\eta \mathbf{J} = \mathbf{E} + \mathbf{v} \times \mathbf{B}. \tag{1.22}$$

In full, the equations are: the continuity equation (1.19), the momentum equation (1.20), the equation of state (1.21) and the resistive Ohm's law (1.22). The choice of γ allows for various scenarios, e.g. $\gamma = 5/3$ in the adiabatic case (treating the plasma as a monatomic gas), or $\gamma = 1$ if the plasma is isothermal. These equations are applicable on length scales much larger than the Debye length and the ion/electron gyroradius, and time scales much longer than ion/electron gyroperiod.

The role of collisions here is essentially in determining the value of the electrical resistivity $\eta = 1/\sigma$ in the resistive Ohm's law, which is equivalent to the form in equation (1.12) for a more general conductance σ. In the collisionless case, referred to as 'ideal MHD', $\eta \to 0$ and we have $\mathbf{E} = -\mathbf{v} \times \mathbf{B}$. This scenario is generally applicable in the magnetosphere; however, the use of a scalar pressure requires sufficient collisions to maintain a thermal equilibrium, and hence neglecting these entirely would imply the equation of state above is invalid. Instead, the isotropic pressure is maintained via wave-particle interactions, which act akin to collisions in establishing a Maxwellian distribution.

Inspecting the $\mathbf{J} \times \mathbf{B}$ force in equation (1.20) in more detail reveals some valuable insight into the magnetic forces exerted on the plasma. Substituting for $\mathbf{J}$ via Ampère's law (1.7) to express this just in terms of the magnetic field, we can write:

$$\mathbf{J} \times \mathbf{B} = \frac{1}{\mu_0} \nabla \cdot (\mathbf{B}\mathbf{B}) - \nabla \left(\frac{B^2}{2\mu_0} \right). \tag{1.23}$$

The first term on the right-hand side represents the magnetic tension, given by the divergence of the magnetic stress tensor. Analogous to mechanical tension in a string, it describes the tendency of the field to restore itself under stress and exert tension and torsion in the plasma. The second term represents the effect of magnetic pressure; like thermal pressure in a fluid, magnetic fields produce an opposing force when they are compressed. One could thus rewrite the right-hand side of equation (1.20) and group the pressure terms as $\nabla(P - \frac{B^2}{2\mu_0})$. This idea of total pressure gives rise to an important parameter in MHD, the 'plasma beta', given by:

$$\beta = \frac{P}{P_B} = \frac{n k_B T}{B^2/2\mu_0}. \tag{1.24}$$

As the ratio between the thermal pressure and magnetic pressure P_B, the value of β can be used to determine which of these most influence the dynamics of a given plasma. Within the magnetosphere β is typically less than 1, decreasing closer to the Earth as the magnetic field strength increases, implying that the field generally dominates the plasma. Conversely, within the solar wind and especially in the magnetosheath where the plasma is decelerated and heated, β is often greater than 1 and the thermal pressure dominates (Baumjohann and Treumann, 1997).

1.2.2 The Frozen-in Flux Theorem

The evolution of the magnetic field in a plasma is determined by two key processes: the advection of the field due to the flow of the plasma, and the diffusion of the field through

the plasma itself. The competing effect of each of these is described by the magnetic induction equation, obtained by combining Ampère's law (1.7) and Faraday's law (1.5) with the resistive Ohm's law (1.22):

$$\frac{\partial \mathbf{B}}{\partial t} = \nabla \times (\mathbf{v} \times \mathbf{B}) + \eta \nabla^2 \mathbf{B}. \tag{1.25}$$

Taking the ratio between the two terms on the right-hand yields another useful parameter: the magnetic Reynolds' number, R_m. If we apply dimensional analysis over a length scale L and a velocity scale U, then we can approximate $R_m \sim \frac{UL}{\eta}$. In the ideal (collisionless) MHD case $R \to \infty$, whereas in the diffusive limit $R_m \to 0$. Since space plasmas are generally collisionless, the magnetic Reynolds number tends to be extremely large and the evolution of the field can be described solely by the convection of the plasma.

This is the basis for an important concept in ideal MHD: the frozen-in condition, or Alfvén's theorem. In the frame co-moving with the plasma the electric field disappears entirely, and hence the magnetic flux threading an open surface fixed in this frame must be constant over time. This can be understood by considering a closed loop (a 2-D cut of the open surface) which is translated and distorted by the flow of the plasma; regardless of how it evolves over time, this loop must always enclose the same amount of flux. It follows that entire cylindrical volume elements of plasma (or 'flux tubes') centred around a given field line always remain associated with the same field line, so that the field and plasma evolve together. Elements of plasma situated far apart but attached to the same field line are therefore topologically connected until the frozen-in condition eventually breaks down.

1.2.3 Magnetic Reconnection

The approximations of ideal MHD (and thus Alfven's theorem) become invalid where diffusion of the field occurs. This must be mediated by non-ideal electric fields appearing in Ohm's law (1.26), which if arising from collisions results in a resistive electric field. However, extensions to the MHD equations as listed earlier are possible, and reveal further contributions to the total electric field that are neglected through other approximations, such as the time and length scales of interest. For example, the generalised Ohm's law can take the form:

$$\mathbf{E} + \mathbf{v} \times \mathbf{B} = \eta \mathbf{J} + \frac{1}{ne}\mathbf{J} \times \mathbf{B} - \frac{1}{ne}\nabla \cdot \mathbf{P}_e + \frac{m_e}{ne^2}\frac{\partial \mathbf{J}}{\partial t}. \tag{1.26}$$

The new terms on the right-hand side after the resistive term $\eta \mathbf{J}$ are, in order: the Hall term, the anisotropic electron pressure term, and the electron inertia term. These can be important on length scales close to the ion gyroradius, and the latter two terms are only negligible in the presence of weak electron pressure gradients and slowly-varying currents. However, the Hall term remains relevant in such a case, and away from the centre of strong current layers (where η is maximal) it can even dominate over the resistive

term (Treumann and Baumjohann, 1997). Where this is true the electrons and ions decouple and behave as separate fluids, and the ideal MHD case is only recovered where the current is predominantly parallel to the magnetic field. Extensions to MHD thus require further complications to achieve closure, e.g. separate ion and electron energy equations. However, these effects can generally be neglected within the Earth's magnetosphere, provided one is sufficiently far from any strong currents such as those at the subsolar magnetopause.

Nonetheless, where the electric field becomes non-ideal the condition that the field is rigidly tied-in to the plasma relaxes. At current sheets dividing regions of oppositely-directed field, diffusion then allows for reconfiguration of the magnetic field topology as shown in Figure 1.1. This process is called magnetic reconnection, and is ubiquitous throughout astrophysical and laboratory plasmas. Reconnection also results in heating and acceleration of the plasma, providing a source of energy conversion from stored magnetic energy into kinetic and thermal energy. The classical view of reconnection is as a 2-dimensional picture, whereby two regions of inflowing plasma meet at a current sheet. These fields mix within a central diffusion region, generating reconnection outflows perpendicular to the inflows thus forming an X-type geometry.

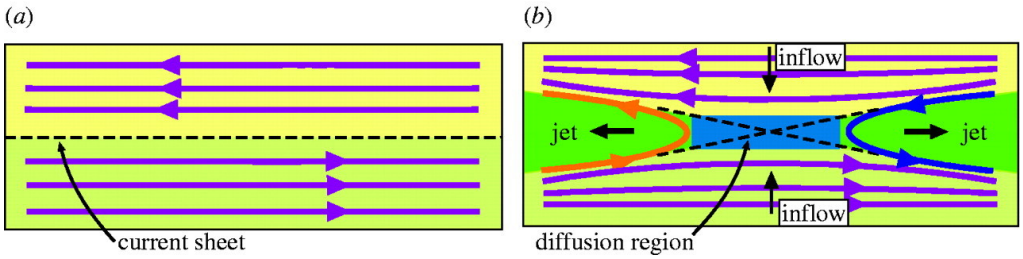

Figure 1.1 – A cartoon showing (a) an unperturbed current sheet dividing regions of oppositely directed field, which is then (b) broken down by the inflowing plasma within a diffusion region, leading to reordering of the field topology and reconnection jets (from Eastwood, 2008).

Here the newly-reconnected field lines experience a strong tension due to the bend in the field topology, exerting a $\mathbf{J} \times \mathbf{B}$ force on the local plasma. Microscopically, the reconnection process is determined by non-linear interactions between the particles and fields, which can occur even in a collisionless regime. In MHD, the (collisional) resistivity must provide a proxy for these, which may not seem applicable for a rarefied space plasma. However, these non-linear interactions can result in anomalous collisions within the diffusion region, providing a source for a non-zero resistivity (Treumann and Baumjohann, 1997). MHD can therefore still be used to describe reconnection at the magnetopause provided we are not interested in the small scale mechanisms at play, e.g. the exact contributions to the electric field local to the X-line.

The 2-D description of reconnection is in fact only a local perspective; extending into 3-D, reconnection occurs over a finite extent along an 'X-line'. Topologically, the superposition of two equal and anti-parallel fields results in magnetic null points where $\mathbf{B}$ is identically zero (Parnell et al., 1996). These are associated with field lines which

enter or exit the null point in a divergence-free manner to divide different magnetic domains, forming 2-D 'separatrix' surfaces. Where multiple nulls exist and the resulting separatrices are transverse to one-another, their intersection forms a null-null line called a 'separator', as shown in Figure 1.2.

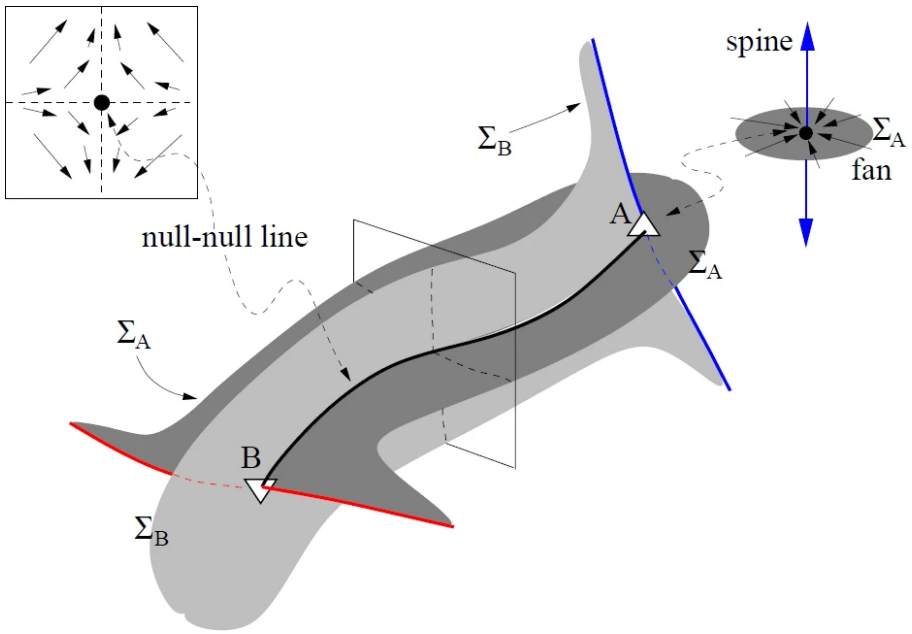

Figure 1.2 – Schematic showing the formation of a magnetic separator by the intersection of two separatrices Σ_A and Σ_B ('fan' surfaces bounded by 'spines') associated with null points A and B. The local field direction in a plane normal to the separator is indicated (from Longcope, 2005).

Hence 3-dimensionally the separator represents a topological merging line along which reconnection can occur in the presence of non-ideal electric fields. In the local 2-D picture, the rate of reconnection is given by the electric field perpendicular to the plane of reconnection; in 3-D this becomes the electric field parallel to the separator. This provides a means to quantify the rate at which the plasma is topologically reconfigured on large scales - for which MHD is applicable - and this 3-D reconnection description is studied widely in astrophysical plasmas such as the solar corona (e.g. Hesse et al., 2005).

1.2.4 Waves, Shocks and Discontinuities

Waves are a prime example of collective behaviour in a plasma, and act as a fundamental mechanism in the propagation of information through the system. As in a neutral gas, these can be propagated due to changes in pressure like sound waves; however, the existence of a magnetic field, and hence the $\mathbf{J} \times \mathbf{B}$ force, creates an additional and anisotropic propagation mechanism. In MHD, this results in two separate types of waves. These can be obtained by linearising the MHD equations in the presence of perturbations to the plasma quantities, and are therefore general over any spatial or temporal scale for which MHD is valid.

The most simple of these is the Alfvén wave, which propagates in the direction of the magnetic field. Analogous to a wave on a taut string, it occurs in response to a

local perturbation perpendicular to the field; the tension force opposes any curvature, exerting a force on the plasma, which due to its inertia results in oscillatory motion about equilibrium. The Alfvén wave propagates with phase velocity v_A, known as the Alfvén speed, given by

$$v_A = \frac{B}{\sqrt{\mu_0 \rho}}. \tag{1.27}$$

This has a form similar to the hydrodynamic sound speed $c_s = \gamma P/\rho$, with the magnetic pressure replacing the role of the thermal pressure. The result is that the Alfvén wave propagates information most rapidly in regions of rarefied, highly magnetised plasma. It has the simple dispersion relation

$$\omega_A = \pm v_A k_{||} \tag{1.28}$$

for frequency ω_A and wavevector $\mathbf{k} = (k_{\parallel}, k_{\perp})$, such that the Alfvén wave is non-dispersive and its energy flows along the unperturbed field direction. However, more generally MHD waves can propagate in any direction (i.e. also perpendicular to the magnetic field), and are affected by gradients in the thermal pressure. The result is the magnetosonic wave, with the following more complex dispersion relation:

$$\omega_{ms}^2 = \frac{k^2}{2}\left[c_{ms}^2 \pm \left((v_A^2 - c_s^2) + 4v_A^2 c_s^2 \frac{k_\perp^2}{k^2}\right)^{\frac{1}{2}}\right]. \tag{1.29}$$

The two solutions to this relation yield a pair of separate, dispersive wave modes: the slow and fast magnetosonic modes. The terms in the square brackets correspond to the phase velocity of each wave mode, clearly dependent on the angle between the wave vector and the magnetic field, i.e. $\theta_k = \sin^{-1}(k_\perp/k)$. The result is that the fast mode propagates most quickly in the direction perpendicular to the field, i.e. where $k = k_\perp$ and $\theta_k = 90°$, for which it has phase velocity equal to the magnetosonic speed $c_{ms} = \sqrt{c_s^2 + v_A^2}$. In this case the slow mode has zero phase velocity and hence cannot propagate; since the Alfvén wave only propagates parallel to the field, the fast mode is the sole perpendicular MHD wave mode. If the wave vector is instead parallel to the field ($\theta_k = 0°$) then the phase velocity of each mode depends on which of c_s and v_A is largest; as per the nomenclature, the fast mode takes the fastest of these and the slow mode the slowest. Hence whilst magnetosonic waves propagate in all directions - like an ordinary sound wave - the anisotropy due to the magnetic field significantly complicates how information is transmitted throughout the plasma.

This complication further applies to the regime where the plasma flow exceeds the local magnetosonic speed, i.e. the plasma becomes supersonic with a magnetosonic mach number $M_{ms} = v/c_{ms} > 1$. Similar to the hydrodynamic case, this results in the formation of a shock, where plasma properties sharply transition upstream and downstream; as with the magnetosonic wave modes, there exist both fast and slow shocks. In the region local to a shock, complex dissipation mechanisms cause the plasma to be heated

irreversibly and decelerated to subsonic speeds. Within MHD these mechanisms are not captured since they occur only on small scales. However, on larger scales away from the immediate shock vicinity the problem can be reduced to a series of conservation laws. In MHD these are given by the Rankine-Hugoniot jump conditions, describing the change between upstream and downstream parameters. These treat the shock as planar, within its own rest frame, and are defined in terms of components tangential and normal to the plane of the shock denoted by subscript t and n, respectively. The full set of conditions is as follows, where square brackets represent taking the difference between upstream and downstream parameters (Burgess and Scholer, 2015):

$$[\rho v_n] = 0, \tag{1.30}$$

$$[B_n] = 0, \tag{1.31}$$

$$\left[\rho v_n^2 + p^2 + \frac{B_t^2}{2\mu_0}\right] = 0, \tag{1.32}$$

$$\left[\rho v_n \mathbf{v_t} - \frac{\mathbf{B_t} B_n}{\mu_0}\right] = 0, \tag{1.33}$$

$$\left[\left(\frac{\gamma}{\gamma - 1}\frac{p}{\rho} + \frac{v^2}{2}\right)\rho v_n + \frac{v_n B_t^2}{\mu_0} - \frac{B_n \mathbf{B_t}\cdot\mathbf{v_t}}{m u_0}\right] = 0, \tag{1.34}$$

$$[(\mathbf{v}\times\mathbf{B})_t] = 0. \tag{1.35}$$

In turn, these equations correspond to the conservation of: (1.30) momentum, (1.31) divergence of $\mathbf{B}$, (1.32) total pressure, (1.33) total shear, (1.34) total energy, and (1.35) electric field (where we assume ideal MHD). It is clear upon inspecting these equations that they are highly non-linear, with a strong distinction between magnetic field components normal and tangential to the plane of the shock, again due to the anisotropy in the Lorentz force. This gives rise to two unique classes of shock where the conserved properties vary significantly: parallel ($B = B_n$) and perpendicular ($B = B_t$) shocks. In these cases the Rankine-Hugoniot conditions simplify from those above and it becomes more trivial to solve for the upstream and downstream parameters. In the parallel case the field is continuous through the shock and plays no role in decelerating or heating the plasma; in the perpendicular case both the density and the magnitude of the field are increased, with the heating and acceleration of the plasma dependent on the change in magnetic energy.

In general however, the field can take any orientation with respect to the shock normal, and in reality shocks will usually be found under the category of 'oblique' shocks. In this case the Rankine-Hugoniot conditions are more difficult to solve and a wide variety of transitions are possible. One condition which remains is that the tangential field $\mathbf{B}_t$ must be parallel on either side of the shock front despite any change in B_t, known as the coplanarity theorem. Since B_n must remain constant either side, this allows for rotations of the magnetic field through the shock. Fast shocks correspond to an increase in the magnetic pressure P_B through the shock, and thus a rotation of the field towards the shock front; slow shocks are conversely a rotation in the direction away from the

shock and thus a decrease in P_B, whilst the thermal pressure P increases in both cases (see Figure 1.3).

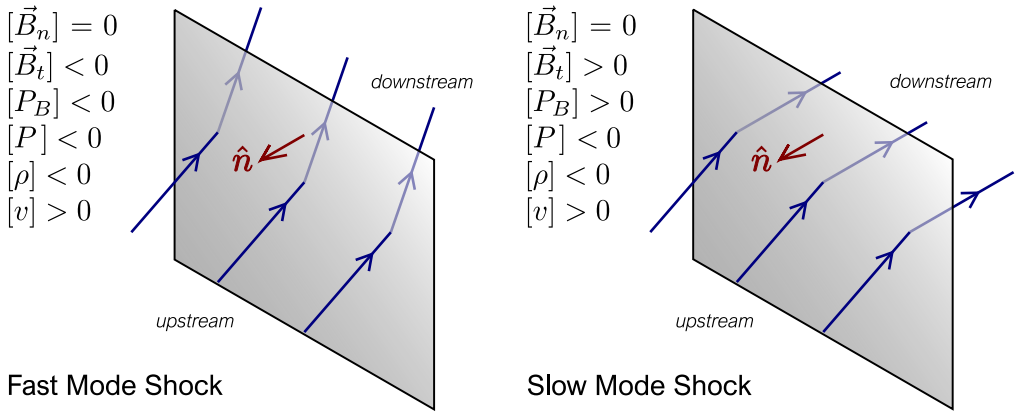

Figure 1.3 – A schematic showing the change in MHD parameters (upstream minus downstream) for both fast and slow mode shocks. The rotation of magnetic field through the shock plane is shown by the blue lines, and the shock normal $\hat{\mathbf{n}}$ is shown by the red arrow.

Such sharp transitions in the field are not unique to shocks, however. In fact, shocks are simply a class of MHD discontinuities unique to a supersonic medium, whereby there is always a non-zero momentum normal to the plane of the discontinuity. In a subsonic regime there are a variety of discontinuities that exist as a result of naturally-forming fluid boundaries, dividing two distinct regions of plasma. In the case of zero flow normal to the boundary, we have 'contact' ($B_n \neq 0$) and 'tangential' ($B_n = 0$) discontinuities. If $v_n \neq 0$ then instead we have a 'rotational' discontinuity (which also requires $B_n \neq 0$), distinguished from a shock by involving no change in the plasma density. Shocks and discontinuities are ubiquitous throughout the heliosphere, and are of crucial importance in understanding the interaction between the solar wind and the magnetosphere, as we will discuss later.

1.3 The Solar Wind-Magnetosphere-Ionosphere System

The outermost layer of the solar atmosphere is a freely-expanding, fully ionised magnetised plasma which flows out into interplanetary space, known as the solar wind. When it reaches the magnetised planets, the planetary field forms an obstacle to the solar wind creating a cavity called a magnetosphere. Within this region the planetary field dominates over the interplanetary magnetic field (IMF) carried by the solar wind, and the plasma dynamics within this region are strongly dependent on the dynamics of the planetary system itself.

Whilst each of the magnetospheres of the solar system has been explored in-situ (by instrumentation on-board spacecraft) and remotely (by space or ground-based photon detection at variety of wavelengths), the magnetosphere of Earth is the most well-understood of these systems. Numerous spacecraft missions over the last several decades

have investigated near-Earth space in increasingly great detail, utilising the unique parameter space to study fundamental plasma physics. Combined with ground and remote observations which have revealed the interconnectedness of the magnetosphere and ionosphere, our knowledge of geospace has improved rapidly. However, the mechanisms by which each component of the coupled solar wind-magnetosphere-ionosphere system influences global dynamics are not yet fully understood. The wider relevance to society due to space weather impacts make this an increasingly important field of study.

1.3.1 The Solar Wind

The solar wind is generated in the outer layers of the Sun's atmosphere, in the hot, tenuous solar corona which extends out to several solar radii. The corona is distinguished by its dramatic temperature gradient, where the plasma can exceed $\sim 10^6$K but corresponds to a low-β environment due to the intense magnetic field connecting it to the photosphere. The coronal heating mechanisms responsible for this high temperature are still a topic of much debate, but may be explained by phenomena like wave heating or nano-flare reconnection events between coronal flux tubes (Hansteen, 2009). The resulting gradient in thermal pressure drives a rapid expansion of the outer atmosphere, creating an outflowing stream of highly ionised plasma, mostly hot electrons and protons (H^+).

This 'solar wind' was hypothesised well before it was fully understood theoretically, e.g. due to observations of the Carrington event in 1859 (Green and Boardsen, 2006), and the idea that it is composed of positively and negatively charged particles was proposed after auroral observations by Birkeland (1908). This could not be explained, however, until the discovery of the corona and the theoretical work of Parker (1958). By describing a steady-state outflow using a one-dimensional, spherically-symmetrical hydrodynamic model, a number of solutions for a possible solar wind were found; the solution that later matched observations by Mariner II (Neugebauer and Snyder, 1962) was that of a supersonic outflow, which reaches a constant velocity at $\sim$ 10 solar radii. In reality the solar wind is magnetised, and effects due to e.g. pressure anisotropies and the presence of heavy ions mean that Parker's model is only an approximation to the true solar wind profile - though still a reasonably accurate one.

The solar wind plasma is highly conducting, and hence is frozen-in with the magnetic field embedded into the coronal plasma. As the plasma is accelerated radially outward the dynamic pressure begins to dominate over the magnetic pressure and the solar wind drags this magnetic field with it. Further out in the solar wind the rotation of the Sun, into which the field lines remain anchored, results in an Archimedean spiral-formation in the IMF, called the Parker spiral (see Figure 1.4). As the field propagates into interplanetary space it forms the interplanetary magnetic field (IMF), which reaches out to the edge of the heliosphere where the solar wind reaches dynamic pressure balance with the interstellar wind (Richardson et al., 2019).

However in reality the solar wind outflow is much more complex, and depending on the phase of the 11-year solar cycle the solar wind and IMF can show very different

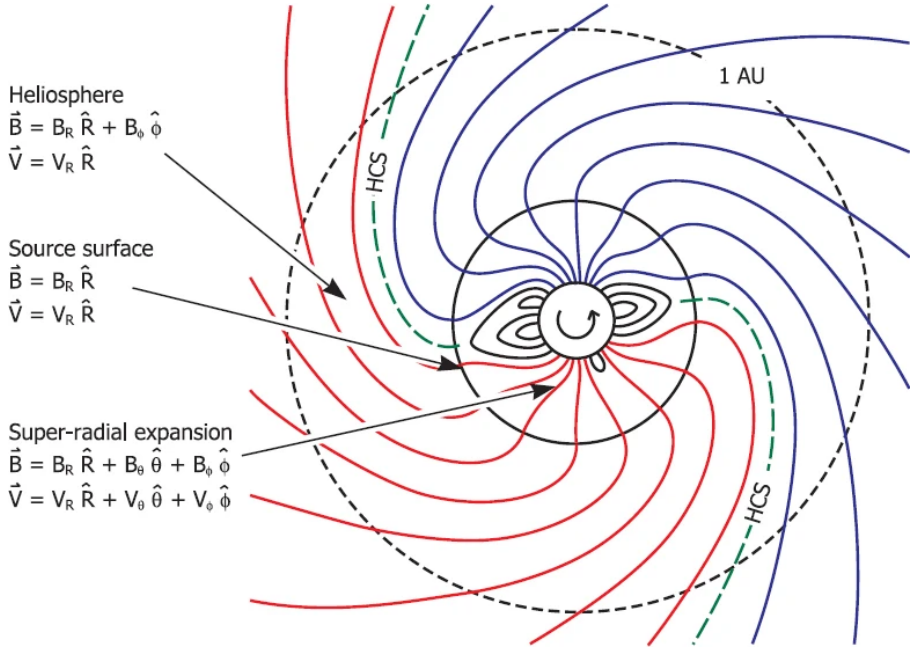

Figure 1.4 – Cartoon showing the evolution of the solar magnetic field radially from the sun, with the changing form of the IMF and solar wind flow labelled at different distances in heliospheric coordinates. The IMF forms the Parker spiral out in the heliosphere, with the heliospheric current sheet (HCS) dividing regions of field with opposite radial components coloured in red and blue. The location of the Earth corresponds to the black dashed circle at 1AU (from Owens and Forsyth, 2013).

behaviour due to the non-uniform nature of the corona. At solar minimum the coronal field is quasi-dipolar with open field lines (coronal holes) typically at high latitudes, and closed field lines (coronal loops) near the magnetic equator which extend out to form the streamer belt (Gosling, 2010). At coronal holes, the plasma is free to flow outward and is associated with faster, less dense solar wind; where the coronal pressure is sufficient to open-up closed arcades of plasma within coronal loops, a slower, denser solar wind is able to stream away. This separation of 'slow' and 'fast' solar wind regions is less clear at solar maximum, where the heliomagnetic field becomes highly inclined to the solar rotation axis and increasingly less dipolar, such that slow wind is able to stream at higher latitudes (Owens and Forsyth, 2013).

Even at solar minimum there remains a non-zero dipole tilt. The opposing polarity of slow solar wind near the magnetic equator results in the formation of the heliospheric current sheet, where the IMF switches sign in the radial direction either side. Due to the tilt, however, the location of this current sheet changes in the ecliptic plane, rippling into a 'Ballerina skirt' formation (see Figure 1.5) such that an observer fixed in the ecliptic plane experiences changes in the IMF polarity over the (synodic) solar rotation period (Alfvén, 1977). At the Earth at 1 AU there is therefore significant variability in the solar wind and IMF over time. For example, the inclination of the Earth's orbit results in a semi-annual variability in the average IMF direction, which is believed to affect the efficiency of coupling to the magnetosphere and the resulting geomagnetic activity (Russell and McPherron, 1973).

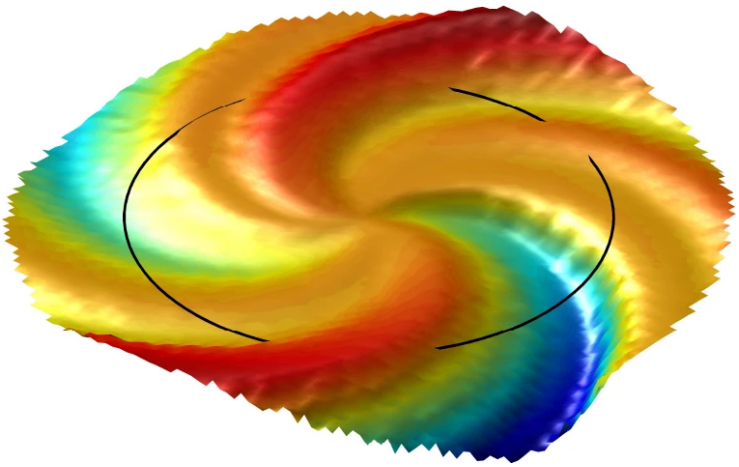

Figure 1.5 – Results from an MHD simulation showing the shape of the heliospheric current sheet (HCS) during solar minimum conditions. The warping of the surface results in multiple crossings by the Earth (which lies along the black line at 1 AU) through the HCS during a single solar rotation (from Owens and Forsyth, 2013).

Such time-variation becomes much more extreme at solar maximum, deviating greatly from the simple Parker model described above. The solar wind is host to various types of transient events which result in shocks and discontinuities as described in section 1.2.4. The most extreme of these are coronal mass ejections (CMEs), eruptions of highly magnetised coronal plasma which propagate through interplanetary space. The mechanisms by which these are formed are still a topic of great uncertainty, but they have been observed to occur most frequently at solar maximum (~ 5/day) compared to solar minimum (~ 1/day), occurring over a broader range of latitudes at maximum and mostly near the equator at minimum (Webb and Howard, 2012). Those observed in-situ, known as interplanetary coronal mass ejections (ICMEs), can have speeds well in excess of the ambient solar wind, and hence are associated with strong shocks at their leading edge.

Magnetic clouds are a subset of ICMEs containing twisted flux rope structures, which can carry large out-of-ecliptic magnetic fields (e.g. Owens, 2016). These can cover an enormous spatial range, and have been observed to have a longitudinal width up to 60° (e.g. Bothmer and Schwenn, 1997, Good and Forsyth, 2016), though this depends on the distinction between the extent of the associated shock and the flux rope embedded within its leading edge. Furthermore, in-situ multi-spacecraft measurements show that properties within these structures vary not only in radial distance as they propagate, but also in longitude (e.g. Winslow et al., 2016, Davies et al., 2020). Shocks in the solar wind are similarly found at corotating interaction regions (CIR), dividing regions of fast and slow solar wind which cannot mix as they are frozen-in to the IMF and thus form shocks at their interface. The sudden enhancement of dynamic pressure associated with interplanetary shocks can have significant societal impacts if they interact with the Earth's magnetosphere.

Understanding how such transients evolve is therefore crucial in predicting conditions at 1 AU. Upstream monitors such as the ACE and Wind spacecraft, positioned at

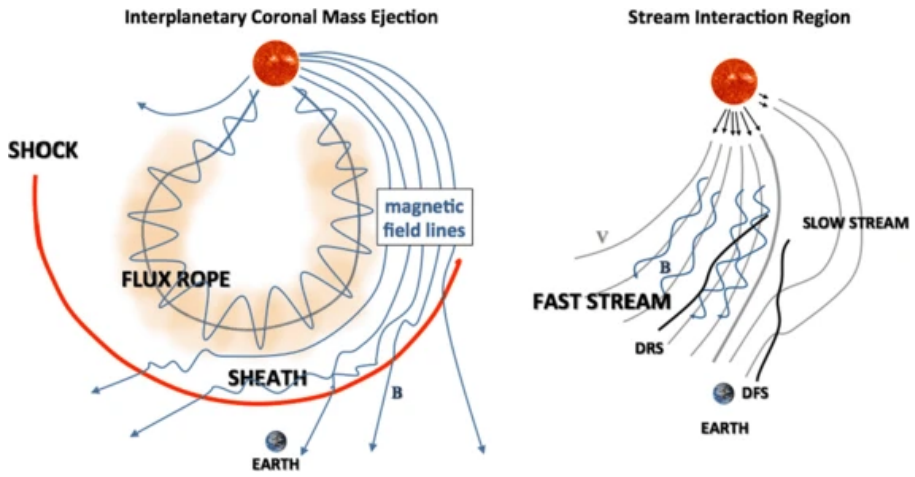

Figure 1.6 – Cartoon showing two types of transient events in the solar wind: an interplanetary coronal mass ejection (ICME) and a corotating interaction region (CIR). A shock forms at the leading edge of the ICME, which is host to turbulence and particle acceleration in the sheath and an embedded flux rope connected to the solar surface. For a CIR, a forward (DFS) and reverse (DRS) shock form at the interface between fast and slow solar wind streams (from Kilpua et al., 2017).

the L1 Lagrange point, provide real-time measurements of the solar wind which are invaluable in forecasting space weather. The properties of the ambient solar wind at 1 AU are therefore well known, with average measured values of $v \approx 450$ kms^{-1}, $n \approx 8$ cm^{-3}, $B \approx 7$ nT, and $T_{p,e} \approx 12$ eV (Hundhausen, 2019, Wilson Iii et al., 2018). However, further knowledge of extreme events at Earth is required to fully predict their frequency and potential impact, particularly the largest group of ICMEs known as Carrington-like events, which currently have an estimated probability of $\sim$1% of occurring over the next decade (Moriña et al., 2019). The recently-launched Parker Solar Probe and Solar Orbiter spacecraft will further improve our knowledge of the origin and evolution of the solar wind, and have already provided in-situ measurements of ICMEs (Davies et al., 2021).

The resulting geomagnetic disturbances are further exacerbated if the enhancement is followed by a period of strong southward IMF, as can occur within e.g. magnetic clouds, which results in geomagnetic storms and substorms as will be discussed later. The complex interaction between the solar wind and the magnetosphere thus determines how changing conditions in interplanetary space affect geospace. Indeed, the solar wind is not a unique feature of our star - the interaction of stellar winds with magnetised exoplanets is similarly expected (e.g. Nichols and Milan, 2016), and has profound implications for potential habitability, making it a topic of growing interest in astrophysics (See et al., 2014).

1.3.2 The Terrestrial Magnetosphere

The Earth's magnetic field is generated by dynamo action due to the convection of conducting material in the planet's core. This magnetic field emanates out into near-Earth space and takes the form of dipole field at large distances from the planet's surface. Closer to the Earth the importance of higher order moments in the magnetic field, e.g.

quadrupole, requires a more detailed description (Thébault et al., 2015). However for the purposes of magnetospheric studies the field is well-described as a geomagnetic dipole with an inclination of $\sim 10^{\circ}$ to the rotation axis, and thus reorients itself diurnally and seasonally. This field inevitably interacts with the interplanetary magnetic field from the solar wind: were near-Earth space a perfect vacuum then these two fields would simply superpose, but due to the frozen-in condition on the solar wind plasma these two fields cannot mix with one-another.

The result is the diversion of the solar wind flow about the planetary field, forming a boundary in space called the magnetopause. This is preceded by a shocked boundary where the solar wind becomes subsonic, known as the bow shock, with the denser, decelerated and heated plasma between the two forming the magnetosheath (Eastwood et al., 2015). On the dayside of the planet the magnetopause has an approximately spherical geometry, but becomes cylindrical further downstream, forming the magnetotail. The magnetosphere is thus shielded from the solar wind plasma and IMF, and if the frozen-in condition holds then the magnetosphere is 'closed', with no normal component of the magnetic field crossing the boundary ($B_n = 0$) forming a tangential discontinuity. This corresponds to a shielding current system flowing along the magnetopause known as Chapman-Ferraro currents. The location of the magnetopause is determined by a mutual pressure balance: on the solar wind side the pressure exerted on the planetary is dominated by the dynamic (or ram) pressure of the solar wind, ρv^2, and on the magnetospheric side by the magnetic pressure, $B^2/2\mu_0$ (Kivelson and Russell, 1995). The magnetosphere thus expands and contracts depending on the time-variation in solar wind dynamic pressure.

Were the magnetosphere always closed and the ideal MHD condition never to break down, the magnetosphere would be largely empty of plasma and the system would reconfigure with the changing orientation of the planetary dipole and the direction of the solar wind inflow. However, as explained in section 1.2.3, this approximation breaks down at intense current sheets where the fields on either side carry anti-parallel components. Magnetic reconnection on the magnetopause thus provides a mechanism for the planetary field and the IMF to diffuse and mix, transferring mass and energy into the magnetosphere. Under southward IMF conditions, field lines that are initially connected to the solar wind reconnect with 'closed' field lines with both ends at the magnetic poles of the Earth, forming 'open' field lines each with one end at the North/South pole and another out in the solar wind. The large tension force in the newly-reconnected field lines, resulting from the stored magnetic energy, accelerates the local plasma forming reconnection jets perpendicular to the plane of reconnection. These field lines are then carried downstream by the solar wind from the dayside, resulting in large-scale convective flows of the magnetospheric field into the long, stretched magnetotail, as shown in Figure 1.7.

The field in the magnetotail is of opposite polarity in each hemisphere, resulting in the cross-tail current sheet separating the low-density magnetotail lobes. This current is carried by plasma in a region of enhanced mass density, called the plasma sheet, which

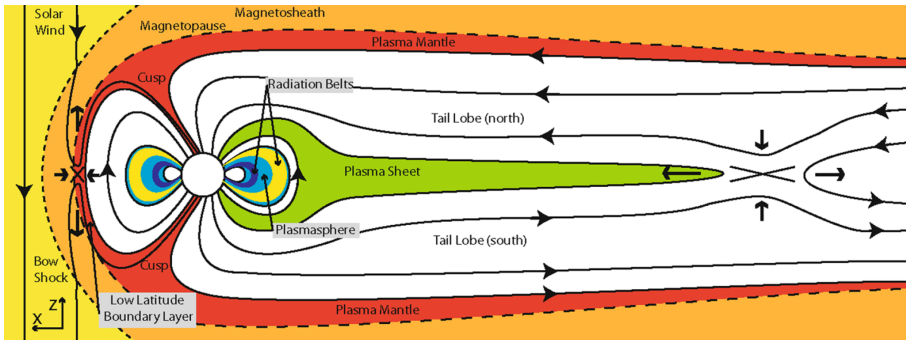

Figure 1.7 – A cartoon showing the different features of the magnetosphere during southward IMF conditions (from Eastwood et al., 2015).

is transported from the solar wind along open field lines. Where the current sheet is intensified and thinned sufficiently by accumulated open magnetic flux, the anti-parallel magnetotail field lines reconnect once more, closing the open field. This is referred to as nightside reconnection, in contrast with dayside reconnection occurring on the magnetopause. The plasma is then accelerated as reconnection jets, sunward on the Earth side and downtail on the other side. The newly-closed field returns to the dayside about dawn and dusk, ultimately reconnecting once more at the magnetopause. This forms a cycle of convection in the magnetosphere, first hypothesised by Dungey (1961) and hence termed the Dungey cycle.

This description implies that global convection proceeds in a steady manner, and whilst the magnetosphere is generally slowly-varying the interaction with the solar wind is never truly steady, leading to an extremely non-linear dynamical system (Eastwood et al., 2015). Indeed, the dayside and nightside reconnection rates are rarely in balance; the location and intensity of reconnection on the magnetopause changes with the upstream solar wind conditions, and the IMF orientation - and particularly its southward component - can vary significantly over timescales of minutes to days. Internal processes can further influence this interaction over convection timescales (Borovsky et al., 2013). The nightside reconnection rate typically responds with a time delay due to reconfiguration of the magnetotail current sheet, though can respond rapidly to a dynamic pressure enhancement due to e.g. an interplanetary shock, and the downtail distance of the reconnection site varies significantly depending on the amount of open flux in the system (Milan et al., 2004). This loading and unloading of flux becomes periodic during strong driving, associated with substorms which pose a significant space weather risk (see section 1.3.4).

A variety of structural features are observed within the terrestrial magnetosphere, often consistent across different planetary systems (see again Figure 1.7). Plasma populations primarily enter the magnetosphere from the solar wind along open field lines, though can also cross the magnetopause via diffusion or due to plasma instabilities, e.g. Kelvin-Helmholtz (Eastwood et al., 2015). Outflows from the high-latitude ionosphere, referred to as the polar wind, also provide a source of heavy ions (e.g. O^+). In the inner

magnetosphere this results in a region of cold denser plasma known as the plasmasphere, which corotates with the planet on closed field lines due to the increasingly high β at small radial distances. The plasma density thus varies significantly throughout the magnetosphere, ranging from $\sim 10^3$ cm^{-3} in the plasmasphere at 3 R_E (Berube et al., 2005), to as low as $\sim 10^{-2}$ cm^{-3} in the lobes (Haaland et al., 2017). The inner magnetosphere also contains trapped populations of higher-energy particles, forming the ring current, which arises from differential drifts of electrons and ions, and the radiation belts, containing relativistic particles. The ring current acts to shield the low-latitude inner magnetosphere and ionosphere from the cross-tail electric field due to magnetospheric convection. It is also responsible for depressing the surface magnetic field on the Earth, whilst the radiation belts pose a significant degradation risk to satellites.

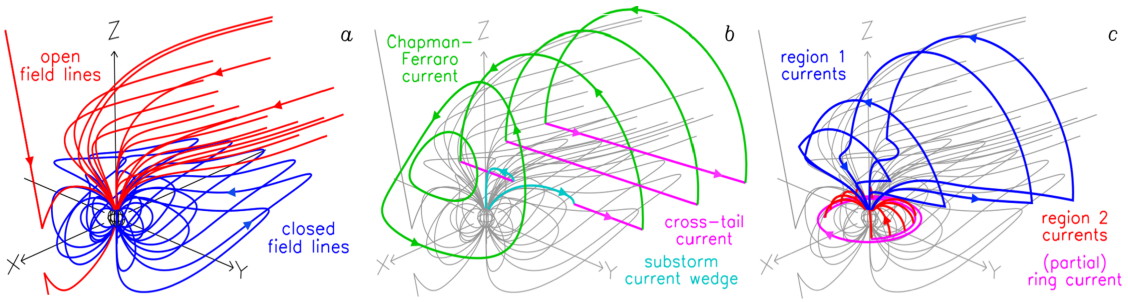

Figure 1.8 – Schematic showing the primary current systems in the magnetosphere during southward IMF. Chapman-Ferraro currents flow on the magnetopause, closing in the magnetotail via the cross-tail current sheet. This can partly close in the ionosphere during substorms, which also closes the Region 1 currents forming at the boundary of open and closed field lines, and the Region 2 currents connected to the partial ring current (from Milan et al., 2017).

Whilst phenomena occurring below fluid scales are therefore important in fully understanding the near-Earth space environment and the risk to society, the global dynamics of the magnetosphere can be well-described by ideal MHD: the large-scale convection of open flux is the primary driver of space weather, since this is responsible for the injection of high energy particles. From the MHD perspective, the boundaries of different regions of plasma are naturally associated with gradients in pressure. One can infer from the momentum equation (1.20) that in a quasi-steady state this must be balanced by a current perpendicular to the magnetic field. However, since electrical charges cannot accumulate locally due to quasi-neutrality, the current is divergence-free and hence must form closed loops; perpendicular currents which are divergent must thus achieve closure via field-aligned currents (FACs). One such example is the Region 1 current system, for which the solar wind is a generator by driving global convection, since this results in a flow shear between plasma on adjacent open and closed field lines. This is connected to both the magnetopause and the outer part of the cross-tail current sheet, and persists under southward IMF, forming a complete circuit via FACs which close in the high-latitude ionosphere (Ganushkina et al., 2018). There also exists the Region 2 current system, which arises due to pressure gradients in the ring current during disturbed times, forming a partial ring current which closes in the ionosphere equatorward

of Region 1. These global current circuits are demonstrated in Figure 1.8.

Magnetospheric current systems are therefore naturally connected to the ionosphere, such that the magnetosphere and ionosphere form an electrodynamically-coupled system. The ionospheric plasma, being resistive due to collisions with neutrals, exerts stress on the magnetosphere achieved by a transfer of momentum between the two. Understanding how currents close in the ionosphere, influenced by the composition and ionisation processes of the ionospheric plasma, is an important requirement to fully explaining global magnetospheric dynamics.

1.3.3 The Terrestrial Ionosphere

The partially-ionised plasma in the ionosphere is, unlike the plasma in the more tenuous magnetosphere, collisional. This plasma essentially lies suspended in the upper layer of the neutral atmosphere, known as the thermosphere. The stratification of the ionosphere is categorised into different regions at increasing altitude: the D, E and F regions, of which the latter is subdivided into the F1 and F2 regions (Solomon, 2010). The typical plasma density varies significantly with altitude, with the peak plasma density found at $\sim$300km within the F2 region. O^+ is generally the dominant ion throughout the F region, though other heavy ions can dominate in lower regions. Since the density of the thermosphere decreases exponentially with altitude, the ionisation fraction of the ionospheric plasma generally increases with altitude: at 100km this is only of order 0.0001% during the day, and only exceeds 50% within the plasmasphere, at altitudes on the order of Earth radii.

The distinction between day and night is important due to the ionisation mechanisms responsible for sustaining the ionospheric plasma. Most of the electron and ion population arises from ionisation of the neutral atmosphere by solar radiation, particularly in the extreme ultraviolet (EUV) range, resulting in both a latitude- and longitude-dependence in the local conductivity. This gives rise to a seasonal and diurnal variability, but also longer-term changes over the solar rotation (27-day) and solar cycle (11-year) periods. The result is that the dayside, sunlit ionosphere is significantly more populated by plasma than the nightside, which essentially depletes to just the F2 region due to recombination of molecular ions at lower altitudes (Solomon, 2010).

However, there may still be some residual plasma in the lower nightside ionosphere, especially at high latitudes. This is due to the existence of the auroral oval, which contains plasma of magnetospheric origin (ultimately injected from the solar wind). Of this plasma, some is precipitated into the ionosphere after being accelerated Earthward along magnetospheric field lines, whilst an additional source comes from scattering (by waves) of magnetospheric plasma which then enters the atmosphere (Moore et al., 2016). The former mechanism occurs when there is insufficient charge density along some portion of the field line, creating a potential drop to accelerate magnetospheric electrons and hence achieve the field-aligned current required for current closure. Within the polar cap, i.e. poleward of the auroral oval, polar rain (precipitation of soft solar wind electrons along open field lines, e.g. Zhang et al., 2011) and precipitation in the polar cusp

(on newly-reconnected field lines mapping out to the magnetosheath, e.g. Russell, 2000) provide another source of ionisation. This is generally lower energy precipitation, of order ∼100 eV, compared to the ∼1-100 keV auroral electrons. Note that ions also play a role in precipitation, though they contribute less energy flux than the much less massive electrons (e.g. Newell et al., 2009).

These precipitating electrons ionise neutral atmospheric gases, in turn producing the aurora (bright displays of visible light emission resulting from molecular excitation) and altering the local conductivity and the atmospheric chemistry due to subsequent recombination. Since precipitation rates are dependent on geomagnetic activity (due to enhancement of field-aligned currents and particle energy fluxes), the resulting conductivity changes can vary significantly over short timescales (hours to days) and show large spatial variation, especially between the dayside and nightside (e.g. Heelis and Maute, 2020).

The resulting complex conductivity distribution relates the horizontal ionospheric current to the field-aligned current via the electric and magnetic fields in the ionosphere. At high latitudes this electric field is imposed by the magnetospheric convection, and at low latitudes by the co-motion of the plasma with the neutral wind with velocity $\mathbf{v}_n$. Whilst the magnetospheric convection is described by the idealised Ohm's law ($\mathbf{E} = -\mathbf{v} \times \mathbf{B}$), in the ionosphere we must use the form of the generalised Ohm's law given by equation (1.14), but also accounting for the effect of the neutral wind such that $\mathbf{J} = \boldsymbol{\sigma} \cdot (\mathbf{E} + \mathbf{v}_n \times \mathbf{B})$. Each contribution to the conductivity tensor, (σ_P, σ_H and $\sigma_{||}$) captures the roles of both electron-neutral and ion-neutral collisions (with frequency ν_{en} and ν_{in}, respectively) in determining the total conductivity and how it varies throughout the ionosphere. Writing these in full, as can be derived by solving (1.8) accounting for collisions, we have (Baumjohann and Treumann, 1997):

$$\sigma_P = \frac{n_e e^2}{m_e}\left(\frac{\nu_{en}}{\nu_{en}^2+\omega_{ge}^2}+\frac{m_e}{m_i}\frac{\nu_{in}}{\nu_{in}^2+\omega_{gi}^2}\right), \tag{1.36}$$

$$\sigma_H = \frac{n_e e^2}{m_e}\left(\frac{\omega_{ge}}{\nu_{en}^2+\omega_{ge}^2}+\frac{m_e}{m_i}\frac{\omega_{gi}}{\nu_{in}^2+\omega_{gi}^2}\right), \tag{1.37}$$

$$\sigma_{||} = \frac{n_e e^2}{m_e}\left(\frac{1}{\nu_{en}}+\frac{m_e}{m_i}\frac{1}{\nu_{in}}\right). \tag{1.38}$$

It is clear that the ratio of the collision frequency to the gyrofrequency $\omega_{ge,i}$ will determine which of these conductivities dominates in a given region, and will vary between species. Since B (and hence the gyrofrequency) is basically constant over several hundred km of altitude, this is determined by the reduction in the collision rate with altitude: in the limit of $\omega_{ge,i} \gg \nu_{e,in}$, both σ_P and σ_H are much smaller than $\sigma_{||}$.

Across most of the ionosphere, except for at the lowest altitudes (where plasma densities are too low to carry significant current), the electrons drift in the $\mathbf{E} \times \mathbf{B}$-direction as $\omega_{ge} \gg \nu_{en}$. In the low-altitude ionosphere, towards the bottom of the E-region, we have

$\nu_{in} \gg \omega_{gi}$ and so the ion motion is coupled to the neutral wind (Fuller-Rowell and Schrijver, 2009). The differential motion of the ions (stationary in the neutral wind frame) and electrons thus results in a Hall current. Within the upper E-region, ν_{in} is comparable to ω_{gi} and the ions decouple from the neutral wind and can travel in the direction of the electric field, resulting in an additional Pedersen current. In the auroral region where **E** dominates the effect of the neutral wind flow, this also occurs in the lower E-region, and the two currents combine to produce the 'auroral electrojet' (see Figure 1.9). In the upper ionosphere, within the F-region, the reduced neutral density and hence collision rates of both species mean that the gryofrequency greatly dominates and both electrons and ions undergo ExB-drift (Cowley, 2000). Since this drift is in the same direction for both species, no current flows as a result of this (considered also by the cancelling of terms in the expression for σ_H above).

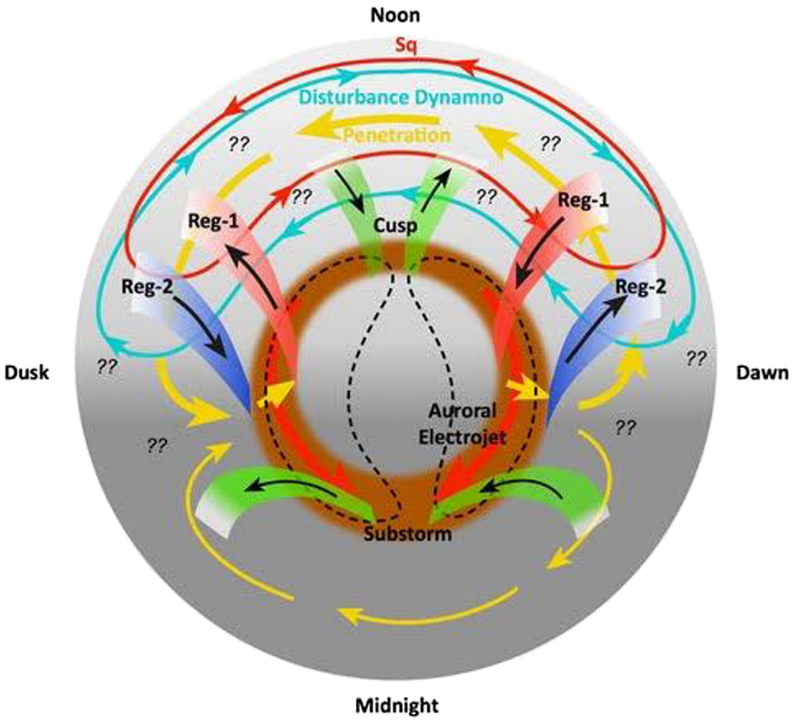

Figure 1.9 – Current systems in the ionosphere, showing the Region 1 and 2 field-aligned currents along with those entering from the cusp and due to substorms. Perpendicular currents include the auroral electrojet and those at lower latitudes, where question marks indicate regions where specific current systems are less well-defined (from Heelis and Maute, 2020).

Hence the closure of the magnetospheric field-aligned current is achieved by horizontal Pedersen and Hall currents flowing in the E-region, at altitudes ∼100km. In fact, the Hall current generally closes within the ionosphere and most of the current closure is achieved by the Pedersen current (Vasyliunas, 2009). The electric field in the ionosphere is predominantly perpendicular to the magnetic field, since the field-aligned component will be negligible due to the high field-aligned conductivity. At low- to mid-latitudes the horizontal electric field may thus have some altitude-dependence if field lines are sufficiently sloped. However, at high latitudes where the magnetic field lines are mostly

vertical it will be effectively constant with altitude in the E-region assuming large spatial scales and slow variations. Thanks to this fact, the horizontal current at high latitudes can then more easily be described by integrating Ohm's law over the height of the ionosphere, yielding a thin-shell approximation. We then obtain height-integrated conductivities Σ_P, Σ_H and $\Sigma_{||}$, which are macro-scale conductances corresponding to the local conductivities σ_P, σ_H and $\sigma_{||}$ respectively. These conductances are of order ~ 10 mho on the dayside and in the auroral region, and ~ 1 mho on the nightside (e.g. Ridley et al., 2004). We also obtain a height-integrated horizontal current density $\mathbf{i}_\perp$, with dimensions current per unit length. Neglecting the parallel electric field $\mathbf{E}_{||}$, this is given by

$$\mathbf{i}_\perp = \Sigma_P \mathbf{E} + \Sigma_H \hat{\mathbf{b}} \times \mathbf{E}. \tag{1.39}$$

Where this horizontal current diverges, current continuity requires the existence of a field-aligned current of density $j_{||}$ into/out of the ionosphere. Hence $\nabla \cdot \mathbf{i}_\perp = j_{||}$, and it follows that the FAC corresponds to gradients in the conductances as well as divergence of the electric field (Baumjohann and Treumann, 1997). Provided the convection is quasi-steady, which is generally the case in the magnetosphere, the ionospheric electric field can be described by an electrostatic potential ψ whereby $\mathbf{E} = -\nabla\psi$. Given some distribution of FAC over the ionosphere with a defined conductance profile, one can solve for this potential, which should then map out along magnetospheric field lines in the absence of inductive effects and parallel potential drops (Hesse, 1997). This provides a means of relating magnetospheric convection directly to the ionospheric convection, since the two are coupled, as is explained in more detail in the following section.

This model is a powerful tool in understanding how stress is transferred between the magnetosphere and ionosphere. Whilst changes in the solar wind driving and consequent magnetospheric dynamics act to alter ionospheric convection via field-aligned currents, changes in the conductance driven by both solar radiation and precipitation from the magnetosphere can likewise alter magnetospheric convection and, ultimately, the solar wind-magnetosphere interaction. The three form a closely-coupled system, and the mechanisms responsible for this coupling is an area of intense and growing research. As well has having fundamental implications for understanding the space environment of all magnetised planets, these geospace phenomena have the potential to severely impact modern society.

1.3.4 Coupling Mechanisms

The connection between the magnetosphere and the ionosphere naturally results in a further, albeit more indirect connection between the solar wind and the ionosphere. Field lines which are open allow transport of plasma from the solar wind into the Earth's upper atmosphere, even directly via the cusps. The motion of open flux driven by the solar wind flow is responsible for currents and electric fields in the high-latitude ionosphere, and the associated thermospheric heating and ground-level geomagnetic perturbations. The solar wind, magnetosphere and ionosphere can in that sense be considered as a

single coupled system under certain conditions, dependent on the extent to which the magnetosphere is open. This corresponds to a region of the ionosphere, called the polar cap, which contains 'open flux' and within which the electrodynamics are dictated by the solar wind interaction. The polar cap is bounded by the 'open-closed boundary' (OCB), which is approximately coincident with the Region 1 current system (Milan et al., 2017).

Open field lines in the polar cap essentially flow with the ionospheric plasma from the dayside towards the nightside where they cross through the OCB. Return flow in the magnetosphere causes the ionospheric plasma to flow via dawn and dusk at lower latitudes towards the dayside, resulting in a twin-cell convection pattern under southward IMF. In the symmetric case this corresponds to a dawn-dusk oriented convection electric field, which is rarely the case since the the IMF takes an arbitrary orientation resulting in asymmetries in convection. The shape and size of the polar cap further varies with time-varying solar wind driving and imbalance between the dayside and nightside reconnection rates, Φ_D and Φ_N, respectively, as demonstrated in Figure 1.10. This is known as the expanding/contracting polar cap paradigm, and can be observed by the migration of the associated current systems and change in shape and size of the auroral oval (Milan, 2015).

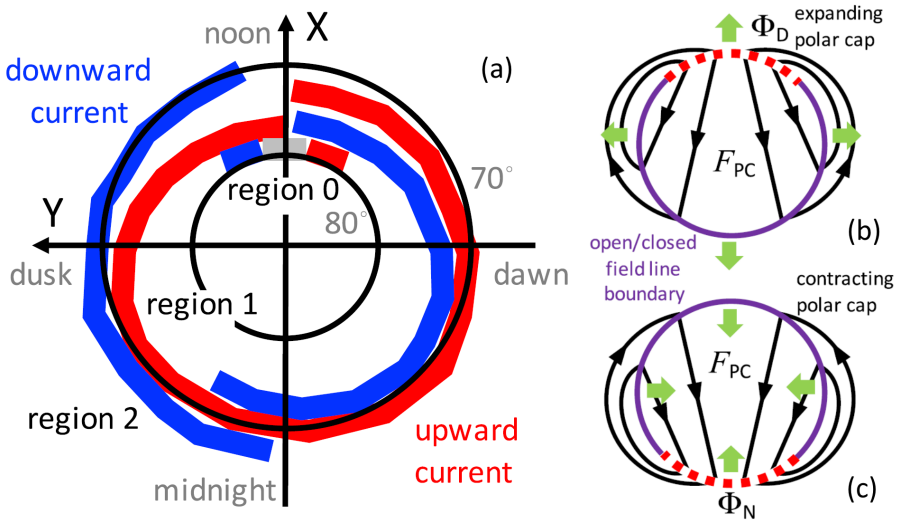

Figure 1.10 – Schematic showing (a) the typical location of Region 0, 1 and 2 field-aligned current systems in the polar cap shown in blue and red. Shown alongside are cartoons of (b) expansion and (c) contraction of the polar cap, containing open flux F_{PC}, due to unbalanced dayside and nightside reconnection rates indicated by the dashed red lines (adapted from Milan et al., 2017).

The focus of southward IMF is due to the requirements of anti-parallel field for reconnection to occur: at the subsolar point and in the plane containing a dipole axis pointing along positive Z, the IMF B_z must be negative. However, the geometry of the dayside magnetosphere is approximately spherical rather than planar, and hence the angle that the magnetospheric field makes with the draped IMF, known as the 'magnetic shear angle', varies over the magnetopause. Strictly the reconnection rate is then optimised where the shear angle is 180°, though it further depends on the local plasma conditions

and is enhanced where the solar wind inflow is normal to the reconnection line close to the subsolar point, where it is often assumed maximal. Reconnection therefore occurs for essentially any orientation of the two fields, e.g. at high latitudes poleward of the cusps for northward IMF. This is also dependent on the inclination of the Earth's dipole to the ecliptic plane, which changes both diurnal and seasonally.

Moreover, magnetopause reconnection occurs not at a single point but rather along an X-line of finite length. Spacecraft observations have provided evidence of reconnection occurring over a significant azimuthal range on the magnetopause (e.g. Hasegawa et al., 2016, Walsh et al., 2017), but single point measurements in space and time are insufficient to determine whether reconnection is truly continuous across the X-line as a magnetic separator. Global simulations have shown the existence of separators on the magnetopause along which reconnection may appear continuous, but which can branch-off into multiple X-lines over a finite extent (Glocer et al., 2016). This more patchy type of reconnection is well-established in the literature and is described in terms of flux transfer events (FTEs). These have been observed ubiquitously by spacecraft such as MMS, Cluster and THEMIS (e.g. Fear et al., 2009, Hwang et al., 2016), as well as in ground-based data (Wild et al., 2003), and FTEs may play an important role in controlling the amount of open flux in the magnetosphere (Fear et al., 2017).

Nonetheless the global rate of reconnection is typically determined by considering reconnection to occur continuously along a single X-line. A common metric used to determine when the solar wind coupling is most efficient is the IMF clock angle, given by $\theta_{IMF} = \tan^{-1}(B_y/B_z)$ for components of the IMF: this varies between 0° - 360°, and is equal to 180° in the southward case. Strictly, capturing the global rate of reconnection requires knowledge about the field and plasma across the magnetopause, but also where the magnetic merging is occurring. However it can be approximated by calculating the geoeffective electric field, i.e. that which is available for the diffusion process, typically given by $E_{geo} = v_x B_z$. If multiplied by some characteristic system scale this becomes a voltage, i.e. total rate of flux opening: this could be the width of the dayside magnetopause L_{MP}, typically $\sim$ 20 R_E, and hence the dayside coupling rate $\Phi_D \sim v_x B_z L_{MP}$. However provided we know where the reconnection line is located we can perform a more exact calculation for the total rate of dayside flux opening.

In 3-D the local reconnection rate at some point on the magnetopause is equal to the electric field parallel to the X-line, $E_{||}$, and the reconnection voltage along the length of the dayside separator S is given by:

$$\Phi_D = -\int_S \mathbf{E}_{||} \cdot d\mathbf{l}, \tag{1.40}$$

where the subscript of Φ_D denotes that this is the dayside reconnection rate. For ideal MHD ($\mathbf{E} = -\mathbf{v} \times \mathbf{B}$) the electric field parallel to the magnetic field must be identically zero. This means that individual magnetic field lines are electric equipotentials, i.e. the voltage is always zero between two points on the field line. In steady-state (i.e. $\frac{\partial \mathbf{B}}{\partial t} = 0$) the electrostatic potential at the ionospheric footpoint of a field line which maps out

to the separator must also then match the potential at the corresponding point along the separator itself. It follows that the reconnection voltage in steady-state is equal to the voltage between the footpoints of field lines terminating the dayside separator. The steady-state condition also requires that the dayside and nightside reconnection rates balance, i.e. $\Phi_D = \Phi_N$, and in the absence of any other contributions to the magnetospheric flow such as viscous interactions with the solar wind, the voltage across the polar cap is $\Phi_{PC} = \frac{1}{2}(\Phi_D + \Phi_N) = \Phi_D$. This is typically referred to as the cross-polar cap potential, or CPCP, and is used as a measure of the rate at which open flux is transported across the polar cap in quasi-steady conditions.

Whilst the Region 1 currents map to the edge of the polar cap, the Region 2 currents, which close via the partial ring current, sit just equatorward of these. The Region 1 FAC flows into the ionosphere on the dawnside (upward electrons) and out of the ionosphere at dusk. The Region 2 FAC is of opposite polarity to the Region 1 FAC, and hence acts to shield the lower latitude ionosphere from the convection electric field. The FAC is of the same sense in each hemisphere, though the direction of the magnetic field $\hat{\mathbf{b}}$ is of opposite polarity. Hence the FAC may be defined as negative if it flows into the ionosphere in the Southern hemisphere depending on convention (if $j_{||} = \mathbf{J} \cdot \hat{\mathbf{b}}$). Provided one knows the distribution of these FACs and the height-integrated conductivities on the ionosphere, then the thin-shell approximation can be applied to obtain the ionospheric electrostatic potential ψ by taking the divergence of equation (1.39):

$$\nabla \cdot \mathbf{i}_{\perp} = j_{||} = \nabla \cdot \left(\vec{\mathbf{\Sigma}} \cdot (-\nabla\psi + \mathbf{v}_n \times \mathbf{B}) \right), \tag{1.41}$$

where we have included the neutral wind contribution to the total electric field, and used a conductance tensor

$$\vec{\mathbf{\Sigma}} = \begin{pmatrix} \Sigma_P & \Sigma_H \\ -\Sigma_H & \Sigma_P \end{pmatrix}. \tag{1.42}$$

In a frame in which the Earth is rotating, the neutral wind term carries the rotation rate of the upper atmosphere as well as local wind speeds. In the Earth's frame however, since electric fields are frame-dependent, this effect disappears and since the local wind speed can be neglected in the high-latitude ionosphere (where convection dominates) the above simplifies to

$$j_{||} = \nabla \cdot (\vec{\mathbf{\Sigma}} \cdot \nabla\psi). \tag{1.43}$$

As mentioned in the previous section, the potential ψ should map out along magnetic field lines and corresponds to the electric field in the magnetosphere. From this perspective it is easy to see the fundamental importance of magnetosphere-ionosphere coupling in dictating global dynamics. The above equation can be understood by considering a simple current-voltage relationship, $I = V/R$, where I is the total field-aligned current

(TFAC) integrated over a chosen hemisphere and V is the CPCP, i.e. the difference between the minimum and maximum of ψ. We see that in the infinitely-conducting limit ($R \to 0$) a finite current is closed via an infinitesimal potential and hence we have a static ionospheric plasma. In such a scenario magnetospheric convection would cease since the magnetic field footpoints would be rigidly tied-in to the ionosphere (Raeder, 2003). In the opposite case where the ionosphere is infinitely resistive ($R \to \infty$), field lines can freely slip through the ionosphere which hence plays no role in the dynamics. Instead, currents would be forced to close in the solid Earth, a phenomenon believed to occur in Mercury's magnetosphere (Anderson et al., 2014). This current-voltage relationship is often used when describing the magnetosphere-ionosphere system in the context of a global electrical circuit; previous studies have found that it acts neither as a voltage generator nor a current generator in steady-state (Ridley et al., 2004).

In the frame corresponding to equation (1.41) collisions with corotating ionospheric neutrals enforce corotation of the the cold plasma in the inner magnetosphere, which is fixed to the planetary field. The dominance of corotation at small distances r from the planet is is clear by considering the ExB-drift, given by $\mathbf{v} = \mathbf{E} \times \mathbf{B}/B^2$, which drops-off linearly as the field strength increases, going as r^3 for a dipole. Meanwhile the corotation flow is simply given by $\mathbf{v} = \mathbf{\Omega} \times \mathbf{r}$, where $\mathbf{\Omega}$ is the rotation vector of the Earth. For a rotation axis roughly aligned with the dipole axis this goes at r, i.e. the growth of the convection dominates by a factor of r^2, especially at higher latitudes. At the gas giants the corotation flow is the dominant source of plasma circulation in the magnetosphere; at Earth this is only true out to a few R_E, forming a stagnation point at dusk and a gradual transition at dawn as shown in Figure 1.11. Nonetheless this is an important effect to include if one is interested in the inner magnetospheric dynamics.

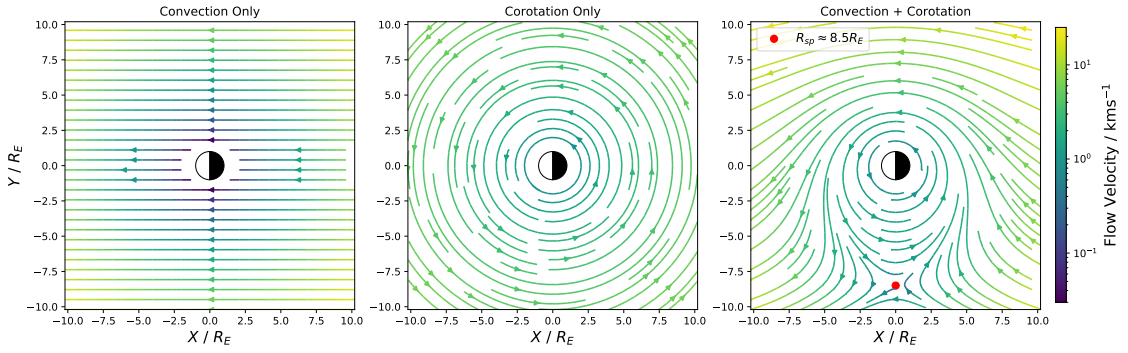

Figure 1.11 – Flow streamlines in the magnetosphere in the presence of (left) an idealised, homogeneous convection electric field of 2×10^{-4} Vm^{-1}, (centre) a corotation electric field and (right) a superposition of the two. The resulting flow stagnation point R_{sp} is indicated.

This two-way coupling between the magnetosphere and ionosphere is more complex during time-dependent conditions. Following a dynamic pressure enhancement, compression of the magnetopause results in strong field-aligned current signatures in the ionosphere, with an associated magnetic perturbation on the ground, known as a sudden commencement (SC) (Smith et al., 2019). This could happen due to e.g. a CME

or a CIR, which if followed by an extended period of southward IMF develops into a geomagnetic storm, in which case it is referred to as a sudden storm commencement (SSC). Storms are characterised by extreme mass and energy transport into the inner magnetosphere, resulting in enhancement of the ring current and hence further ground perturbations. This is measured by the disturbed stormtime (DST) index, and is one of many such geomagnetic indices used to quantify the level of geomagnetic activity in the magnetosphere-ionosphere system.

Strong geomagnetic disturbances are observed much more frequently than storms, however, due to the existence of substorms. As mentioned in section 1.3.2, these arise due to an imbalance between dayside and nightside reconnection resulting in sudden unloading of open flux. A reconnection line is formed much closer to the Earth on closed field lines, corresponding to lower latitudes than the preceding auroral oval, which thus expands equatorward along with enhancements in the FAC, auroral electrojet and ground perturbations. These can occur multiple times per day, whenever the IMF is southward for a prolonged period of time: usually up to hours, rather than hours-to-days for storms (Lyons, 2000). As well as having a clear latitude-dependence, these phenomena can have different impacts in local-time, and show differences between hemispheres due to diurnal and seasonal variations (e.g. Liou et al., 2018). Therefore understanding the coupling timescales involved, as well as accurately predicting the onset time for such events, is crucial in mitigating space weather impacts at a given location on the Earth.

Indeed, these impacts can be profound even if such an event is not particularly extreme. Geomagnetic perturbations on the ground induce a geoelectric field within the conducting Earth. This can drive geomagnetically-induced currents (GICs) in infrastructure such as electrical grids and pipelines, causing significant damage and socio-economic cost (Eastwood, 2008). Enhanced ionospheric electric fields and currents result in increased dissipation into the thermosphere due to collisions with neutrals: this can heat the upper atmosphere, causing expansion and hence increased density and drag at the trajectories low-Earth orbiting satellites. If they are not boosted back into a higher orbit, this will reduce their lifetime as well as pose a risk for possible satellite collisions. At higher orbits, impact ionisation by highly energetic radiation belt particles can damage on-board instruments and permanently damage satellites. It is clear therefore that in order understand better the risk posed to modern society by our geospace environment, the ability to model the solar wind-magnetosphere-ionosphere interaction is a necessary requirement.

1.4 Global Magnetospheric Modelling

Linking the physical processes occurring in the magnetosphere with conditions in the solar wind on a global scale is extremely difficult with sparse spacecraft measurements

and ground-based observations. Data analysis and empirical modelling has led to significant understanding of much of the underlying physical mechanisms, but the time-dependence and complexity of the dynamics means that these empirical models often fall short of fully describing the system (Eastwood et al., 2017). For example, models which aim to predict the size and shape of the magnetopause based on upstream solar wind conditions generally assume that the boundary is in equilibrium, resulting in step changes to solar wind pressure.

Furthermore, the non-linearity in the system means that knowledge about the prior state of the magnetosphere is needed to accurately model its response to a given period of driving. This cannot be provided simply via in-situ measurements, since these only correspond to a single point in space and time: one would require a full constellation of spacecraft to achieve sufficient coverage of the magnetosphere. Furthermore, whilst the magnetosphere can be modelled as a superposition of magnetic fields generated by known current systems (e.g. Tsyganenko, 2002), the evolution of these currents during non-steady conditions means these can be particularly inaccurate for space weather purposes (e.g. during an extreme event). A first-principles approach to modelling the system is therefore necessary, in which computer simulations are employed to solve a set of governing equations for the plasma dependent on the scales of interest.

Ideally we would wish to include effects applicable to all scales, which requires the use of kinetic theory. One method is to simulate the dynamics of a large (but scaled-down) number of 'macroparticles' and their interaction with background electromagnetic fields, known as particle-in-cell (PIC) simulations. Some models instead aim to fully solve the Vlasov equation and hence are referred to as kinetic Vlasov simulations. Whilst these resolve phenomena on the smallest scales, kinetic models are generally the most computationally intensive approaches. To address this problem, 'hybrid' simulations can instead be used which treat one particle species as a fluid and the other kinetically. Whilst kinetic-scale phenomena are not as important when modelling global dynamics, capturing this extra physics is particularly beneficial for studying reconnection, inner magnetospheric dynamics and various aspects of ionospheric coupling (e.g. particle precipitation).

However as explained in section 1.1.2, due to computational constraints such simulations are generally limited to local modelling, or 2-D global rather than 3-D (see Figure 1.12). Instead, global magnetohydrodynamic (GMHD) codes have become the primary tool for simulating the solar wind-magnetosphere-ionosphere interaction, and due to their versatility can be applied to effectively any planetary system.

1.4.1 Global MHD Simulations

Magnetospheric simulation as a field has grown significantly over the past few decades, with substantial advancement in computational power allowing increasingly complex studies to be performed (Raeder, 2003). These predominantly employ the ideal MHD approximation, which has proven effective at reproducing phenomena on applicable scales. Multiple GMHD codes exist in the community, and studies performed using

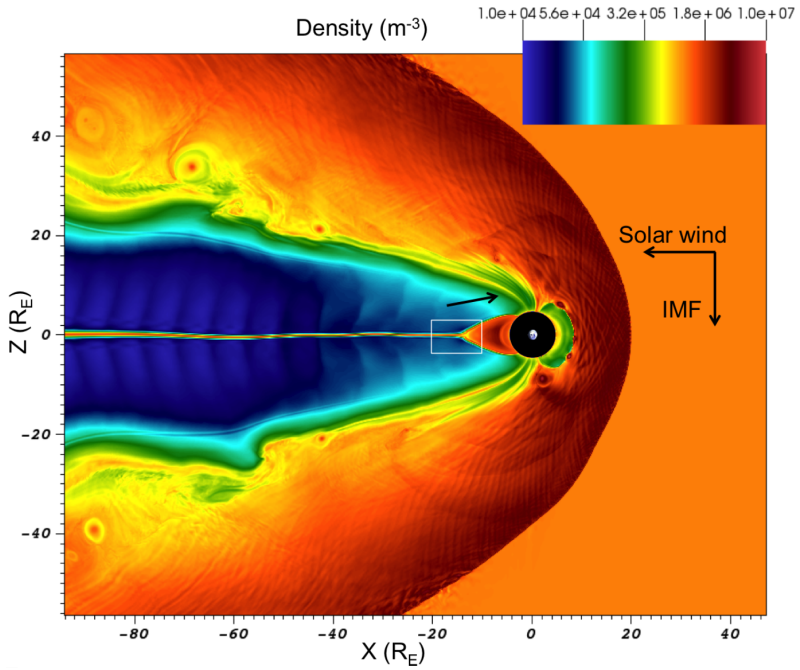

Figure 1.12 – Two-dimensional simulation of the magnetosphere using a hybrid-Vlasov code, which excludes the Y-dimension spatially whilst solving for the y-component of the velocity. The plasma density is shown, revealing smaller scale phenomena like magnetosheath waves and turbulence (from Palmroth et al., 2017).

these form an extensive literature. These models are readily available to run on NASA's Community-Coordinated Modeling Center (CCMC): the four codes hosted on here and with a long heritage in magnetospheric simulations are BATS-R-US (Powell et al., 1999), LFM (Lyon et al., 2004), Open-GGCM (Raeder et al., 2001a), and GUMICS (Janhunen et al., 2012). Further GMHD codes are also used in the international magnetospheric physics community, e.g. PPMLR (Hu et al., 2007), and more recently the Gorgon MHD code (Mejnertsen et al., 2018). Whilst the fundamental approaches to modelling the system are very similar between codes, they all employ different formulations when solving the MHD equations, and deal with various numerical challenges in unique ways.

The generic approach is to place the geomagnetic dipole at the origin of the simulation domain, with the Z-axis set to that of a conventional geospace coordinate system, e.g. Geocentric Solar Magnetic (GSM) in which case the dipole axis points along Z. The solar wind is injected at a single boundary normal to the X-axis, with the Y-axis forming a right-hand set. A variety of simulation grids are used: in the most simple case this is a uniform cartesian grid, though stretched/refined cartesian, spherical and adaptive grids are often chosen to improve efficiency and allow focus on particular regions, as shown in Figure 1.13.

The outer edges of the simulation domain must employ a Neumann boundary (i.e. free-flow) condition on all variables, allowing the solar wind and magnetotail plasma to flow out of the domain. The exception is the sunward edge, where the solar wind inflow is set by a Dirichlet (i.e. hard) boundary condition: parameters are fixed (ρ, $\mathbf{v}$, $\mathbf{B}$, and T) and the solar wind hence flows into the simulation domain where it interacts

with the dipole field. One limitation is in the inability to apply a time-varying B_x, since this cannot propagate in a planar phase front in the X-direction, and hence B_x is either neglected or set to be finite but constant. This sunward edge is usually placed $\sim 30\ R_E$ upstream, with the opposite (downstream) boundary $\sim 100 - 200 R_E$ from the Earth in the distant magnetotail. The remaining boundaries are then $\gtrsim 40\ R_E$ from the Earth in Y or Z, sufficient to fully contain the magnetopause flanks.

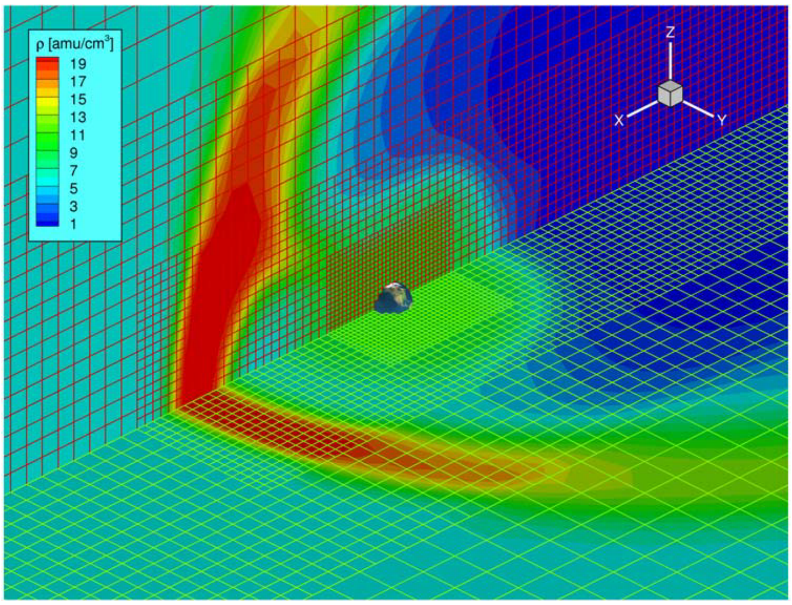

Figure 1.13 – Example of a simulation grid in a GMHD simulation using the BATS-R-US code. The grid is block-refined, with a minimum grid cell size of $1/4\ R_E$ in the inner magnetosphere, increasing to $4\ R_E$ far away from the Earth (from Zhang et al., 2007).

The solar wind can be injected with synthetic conditions for idealised studies, or by using data from an upstream solar wind monitor for simulating a specific event. Whilst in-situ measurements at L1 can be directly applied to the simulation boundary, these correspond to conditions at $200\ R_E$ and so methods are often used to account for the differences arising from the solar wind propagation over this distance (Mailyan et al., 2008). This can be important for forecasting purposes, where small differences in driving conditions can result in significantly different dynamical states of the magnetosphere, though these differences can still manifest even with simultaneous measurements by different spacecraft at L1 (Ashour-Abdalla et al., 2008).

Each of the codes described above use explicit, finite volume solvers which calculate fluxes on the interfaces between adjacent grid cells, but their solvers differ in form depending on approach. For example, some magnetospheric codes solve the ideal MHD equations, whilst some include a finite resistivity which allows for local resistive effects e.g. at reconnecting current sheets. Each code achieves closure through an energy equation that may be solved differently: this would ideally include the effect of magnetic pressure, but this can result in negative internal energies (Raeder, 2003). Some codes instead just solve for the plasma (internal plus kinetic) energy or just the internal energy, which avoids such issues in the resulting thermal pressure but is not strictly conservative

in total energy.

Many efforts have been made to compare and benchmark different MHD codes, which is crucial in being able to properly interpret simulation results in the context of model variance and applicability. For example, Gordeev et al. (2015) performed a broad assessment of the agreement between the codes at the CCMC, showing that key quantities such as magnetopause stand-off distance, lobe magnetic field strength and plasma sheet thermal pressure are generally calculated to at least order-of-magnitude agreement with one-another across a wide range of conditions. In comparing to commonly-used empirical models, some codes appeared to perform better than others for certain purposes, but each appeared to have its own specific strength. Nonetheless, there are challenges and limitations which apply to all of these models that must be carefully considered and, where possible, treated within the numerical approach.

One particular challenge in MHD solvers is in keeping the magnetic field divergence-free, which is limited by numerical errors even if the numerical schemes are designed to be fully conservative. Various techniques are employed to reduce $\nabla \cdot \mathbf{B}$, which carry a necessary computational cost to ensure accuracy, e.g. divergence 'cleaning' in GUMICS-4 which accounts for $\sim$10% of runtime (Janhunen et al., 2012). This can be improved by the use of a staggered grid, where electromagnetic quantities are defined at the edges and faces of grid cells whilst the fluid quantities are defined at the cell centres. With such a grid the issue can even be avoided entirely (to machine precision) by solving for the magnetic vector potential $\mathbf{A}$ in place of the magnetic field, with the caveat that calculations involving spatial derivatives of the field (e.g. Ampère's law) are then second-order derivatives.

Naturally, the use of MHD falls under scrutiny in certain regions of the magnetosphere. One key issue is the nature of magnetic reconnection, which within the ideal MHD formulation should not strictly occur. However, one consequence of solving the MHD equations on a discrete grid is the existence of 'numerical resistivity', which allows diffusion of the field at a rate dependent on the grid resolution and numerical scheme used. However, whilst differing numerics may affect the local reconnection physics, which occur in reality on kinetic scales, the global reconnection process seems to reconfigure to achieve a consistent overall solution between models and hence comparable amounts of magnetospheric convection (Toffoletto and Siscoe, 2009). This is in agreement with the hypothesis that the global reconnection rate is independent of local dissipation mechanisms (Axford, 1984), though recent studies have challenged this idea (e.g. Ouellette et al., 2016).

Some models have begun employing extended MHD phenomena to better capture local reconnection physics, e.g. Hall MHD simulations which include the Hall term in equation (1.26) to simulate the smaller-scale magnetosphere of Ganymede (Tóth et al., 2016). It is also possible to employ either a constant or varying resistivity throughout the simulation domain to dominate the diffusion process and reduce dependence on numerics. Such approaches allow more detailed studies of magnetopause reconnection, though reconnection in the magnetotail, where microscopic phenomena are believed to

be particularly important, is a more contentious issue in MHD simulations. As a result it is not clear to what extent these models can accurately capture substorms (including their frequency and intensity) without additional extended MHD or kinetic effects (e.g. Raeder et al., 2001a).

The inner magnetosphere similarly poses a problem for GMHD codes: beyond hosting important kinetic-scale physics, the $1/r^3$-dependence in the dipole field strength becomes increasingly challenging closer to the planet. Large gradients in the field between adjacent grid cells close to the Earth results in large discretisation errors, and hence strong artificial currents. Furthermore, the stability of an explicit solver is dependent on the Courant-Friedrichs-Lewy condition, which requires that the fastest phenomena be resolved temporally, i.e. the timestep is no larger than the time for the fastest wave speed to propagate across a grid cell. Since this timestep must be the same everywhere in the simulation domain (unless sub-cycling is performed), the sharp increase in Alfvén speed close to the planet slows the computational speed dramatically.

These issues are mitigated by excluding the innermost portion of the magnetosphere, typically no further out than $\sim 3 - 4R_E$, where the MHD equations are not solved and inner boundary conditions are applied. The use of higher-order gradients, or increased resolution in the inner magnetosphere by using a refined or adaptive grid, allows for this boundary to be placed closer to the Earth. Such artificial currents are also reduced by splitting the magnetic field into a curl-free dipole component and a non-dipolar component, where only the latter is used in determining the current (Tanaka, 1994).

1.4.2 Model Coupling and Forecasting

Since the magnetosphere and ionosphere are closely-coupled, any MHD model which is designed to accurately capture global dynamics must include the influence of the ionospheric resistivity. This is achieved through the inner boundary condition, where the plasma flow is determined by the convection in the ionosphere. Typically this is calculated by mapping field-aligned currents from the MHD domain at the inner boundary onto a separate ionospheric grid, and solving for the electrostatic potential using the thin-shell approximation of equation (1.43). As explained in section 1.3.4, the potential can then be mapped-out along magnetic field lines; from this the electric field is obtained in the inner magnetosphere, where the plasma flow is consequently set to $\mathbf{v} = \mathbf{E} \times \mathbf{B}/B^2$. Additional boundary conditions may be set, e.g. a fixed plasma density and temperature, to better replicate the properties in the inner magnetosphere.

Applying this procedure requires the specification of a conductance tensor $\boldsymbol{\Sigma}$ on the ionospheric grid. This can be determined using empirical formulae for the various ionisation mechanisms based on the available parameters, e.g. mapping electron density and temperature from the inner boundary to model particle precipitation (e.g. Raeder et al., 1998, Wiltberger et al., 2009), or using assimilative techniques to specify the conductance based on the FAC distribution (Ridley et al., 2004). However, a simple assumption of constant, uniform conductance is often used to reduce complexity in the global dynamics if one is only interested in a specific phenomenon or for a focussed parameter

study (e.g. Merkin and Lyon, 2010). This further avoids any non-linear feedback arising from changes to the ionospheric conductance due to varying inner boundary quantities.

A more comprehensive approach is instead to couple an MHD code to a separate model which solves the relevant physics. Coupling a thin-shell ionosphere model to a code which solves the fluid equations for the ionosphere and thermosphere allows for direct computation of the conductivity profile in the ionosphere, and the energy transfer with thermospheric neutrals such as Joule heating (Raeder et al., 2001b). This significantly improves estimates of ground magnetic perturbations (and hence GICs) versus the use of empirical conductance formulae, and such coupled thermosphere models can be used to relate Joule heating to observed LEO satellite densities (Connor et al., 2016).

Of further importance to high-latitude ionospheric electrodynamics is the Region 2 current system, which arises due to effects not captured in MHD. Modellers have hence coupled MHD codes to inner magnetosphere models designed to capture multi-species phenomena and pressure anisotropies, such as the Rice Convection Model (RCM) (Welling and Ridley, 2010). Simulations using BATS-R-US have used the current generated on closed inner magnetospheric field lines within RCM for the mapping of FACs onto a thin-shell ionosphere, forming a Region 2 current. This acts to shield the lower-latitude ionosphere from the convection electric field and is therefore of importance equatorward of the auroral region.

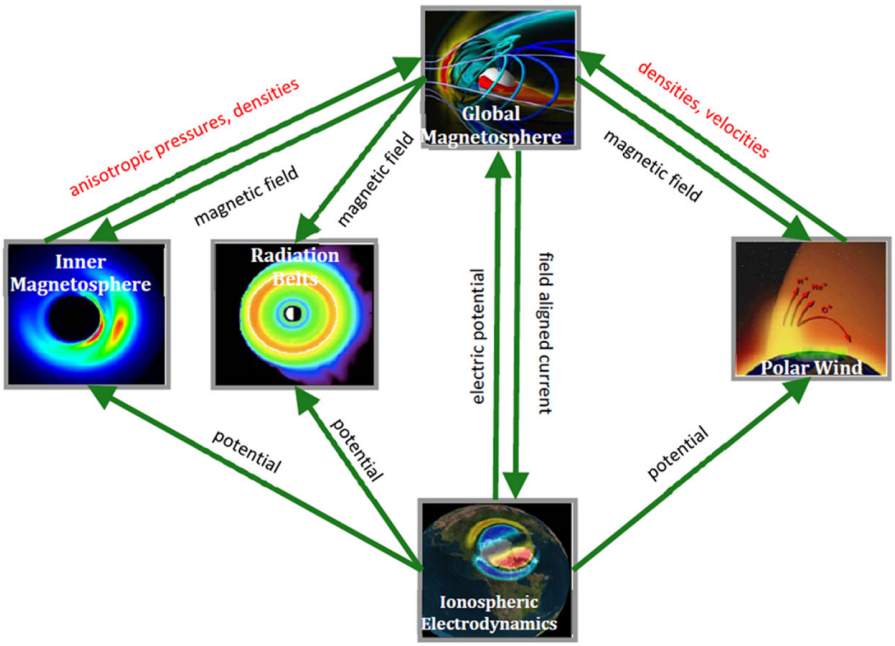

Figure 1.14 – Flow chart showing the coupling of different models for comprehensive simulations of the magnetosphere. The framework is built around a central GMHD code, with the direction of coupling indicated along with the necessary parameters to be exchanged (from Eastwood et al., 2015).

These codes can be further coupled to models of the polar wind and radiation belts to obtain a more complete inner magnetosphere solution, as shown in Figure 1.14; this can

have further feedback into the solar wind-magnetosphere interaction, e.g. reduced reconnection rate due to plasmaspheric plumes (Borovsky et al., 2013). As well as coupling into separate domains, local kinetic simulations can be run within the GMHD domain to capture physics missing from the MHD description. Embedded-particle-in-cell (EPIC) simulations have been employed to study dayside reconnection (Chen et al., 2017), and in the magnetotail for smaller-scale magnetospheres (e.g. Tóth et al., 2016). Though combining many such coupled models into a single computational tool is challenging and requires some simplifications, it allows for a comprehensive approach to simulating space weather, e.g. using the Space Weather Modeling Framework (SWMF) (Tóth et al., 2005). Real-time runs therefore allow for nowcasting and forecasting of space weather impacts by driving these tools with upstream L1 data, though computational cost is a major limiting factor.

1.5 Motivation and Questions

The solar wind, magnetosphere and ionosphere form a closely-coupled system, connected by complex mechanisms that drive space weather and pose genuine risks to society. The system is strongly sensitive to driving conditions, which change over a variety of timescales and are further complicated by internal processes. Changes in the efficiency of solar wind coupling manifest in the varying location and rate of reconnection at the magnetopause, which are challenging to quantify globally with sparse in-situ measurements. The importance of a specific parameter in controlling this coupling is therefore impossible to determine with observations alone. The timescales over which reconnection responds to changes in the solar wind, and the spatial and temporal response of the ionosphere under varying driving conditions, are of particular relevance but remain an open question.

Global magnetospheric modelling has proven to be an invaluable tool in understanding many aspects of this interaction. Through the use of MHD simulations, parameter studies can be performed to reveal the global configuration of the system for any chosen mode of solar wind driving. Combining these simulations to models capturing different components of geospace can allow for a more complete description of the system. These models can also place observations in context, and reveal elusive aspects of the key phenomena of interest that are not captured on a local scale. The versatility and efficiency of these models allows for simulations of real space weather events, and studies of the temporal response of the system over a long time-duration.

The aim of the work in thesis is to perform global MHD simulations of the solar wind-magnetosphere interaction, exploring how magnetopause reconnection evolves spatially and temporally when the magnetosphere is driven under different conditions - including with real solar wind data. This will improve our understanding of reconnection as an inherently 3-D process and place in-situ spacecraft observations in better context. By coupling these simulations to a model ionosphere the resulting changes in associated FACs can be investigated, thus revealing the interdependence of the two systems and

the key timescales of response. This will ultimately contribute to our knowledge of the factors that determine the potential impact of severe space weather events.

In Chapter 2 an overview of the Gorgon MHD code is presented, and the coupling of the code to a thin-shell ionosphere model is described. In Chapter 3 the dependence of magnetopause reconnection on the dipole tilt angle of the Earth is investigated, and related to current systems in the ionosphere. Chapter 4 then focusses attention on the time-dependent aspects of this interaction, and the response of magnetopause reconnection to shock-driven dynamic pressure enhancements. Finally in Chapter 5 the model is extended to accurately simulate real events, and explore the timescales over which the magnetosphere and ionosphere evolve during a geomagnetic storm.

Chapter 2

The Gorgon MHD Code

Some work discussed in this chapter has been published in the following article:
Joseph W B Eggington, Lars Mejnertsen, Ravindra T Desai, Jonathan P Eastwood, Jeremy P Chittenden, Forging links in Earth's plasma environment, *Astronomy & Geophysics*, Volume 59, Issue 6, December 2018, Pages 6.26–6.28, https://doi.org/10.1093/astrogeo/aty275

2.1 Overview

The Gorgon MHD code was originally developed in Imperial College's Plasma Physics Group, for the purpose of simulating laboratory plasmas. Much of its original design is therefore tailored towards collisional, resistive regimes capturing smaller-scale MHD phenomena. In such a treatment, Gorgon employs a fully explicit, Eulerian formulation of the resistive semi-conservative MHD equations, solved in the following form (Ciardi et al., 2007):

$$\frac{\partial \rho}{\partial t} + \nabla \cdot (\rho \mathbf{v}) = 0, \tag{2.1}$$

$$\frac{\partial}{\partial t}(\rho \mathbf{v}) + (\mathbf{v} \cdot \nabla)\rho \mathbf{v} = -\nabla(P_p + P_e) + \mathbf{J} \times \mathbf{B}, \tag{2.2}$$

$$\frac{\partial \epsilon_p}{\partial t} + \nabla \cdot (\epsilon_p \mathbf{v}) = -P_p \nabla \cdot \mathbf{v} - \Delta_{pe}, \tag{2.3}$$

$$\frac{\partial \epsilon_e}{\partial t} + \nabla \cdot (\epsilon_e \mathbf{v}) = -P_e \nabla \cdot \mathbf{v} + \eta |\mathbf{J}|^2 - \Lambda + \Delta_{pe}, \tag{2.4}$$

$$\frac{\partial^2 \mathbf{A}}{\partial t^2} = -c^2 \nabla \times (\nabla \times \mathbf{A}) + c^2 \mu_0 \mathbf{J}, \tag{2.5}$$

$$\eta \mathbf{J} = -\frac{\partial \mathbf{A}}{\partial t} + \mathbf{v} \times \mathbf{B}. \tag{2.6}$$

One can immediately notice the difference between the equations in this form versus those in the ideal MHD case, as shown in section 1.2.1. The momentum equation (2.2) has split proton and electron pressures $P_{p,e}$, with the energy equation (2.3, 2.4) solving for split energy densities $\epsilon_{p,e}$ as well. Gorgon solves the induction equation using a vector potential representation, such that the Ampère-Maxwell law (2.5) and the resistive

Ohm's law (2.6) are expressed in terms of **A**. Additional variables accounting for non-ideal phenomena are the electron-ion energy exchange $\Delta_{p,e}$ and optically-thin radiation losses Λ.

These extended MHD capabilities for laboratory plasma contexts distinguish Gorgon from other codes widely used in magnetospheric physics. The use of separate energy equations for ions and electrons (even when treating the plasma as a single fluid) allows the calculation of independent proton and electron temperatures $T_{p,e}$, which is of value when studying mechanisms of particle acceleration. The energy equations define the general change in internal energy, allowing for complex equations of state, and include the effects of kinetic energy exchange through ion-electron collisions, as well as Ohmic heating and radiative losses for electrons. The use of the vector potential yields a divergence-free magnetic field up to machine accuracy, since $\nabla \cdot (\nabla \times \mathbf{A}) = 0$, removing problematic sources of numerical error found in other codes which solve for **B** instead.

Applying the code for space plasma simulations generally involves setting η, $\Delta_{p,e}$ and Λ to be negligibly small or zero, resulting in an ideal MHD description of a fully-ionised hydrogen plasma. Since most of the terms in the ion and electron energy equations are then negligible, an ideal gas equation of state is assumed as per equation (1.21), i.e. $P_{p,e} = (\gamma - 1)\epsilon_{p,e}$ where $\gamma = 5/3$. Appropriate boundary conditions and choice of simulation domain size are then required to model the magnetosphere, which are essentially as described in section 1.4.1 and shown in Figure 2.1, but are explained again for clarity.

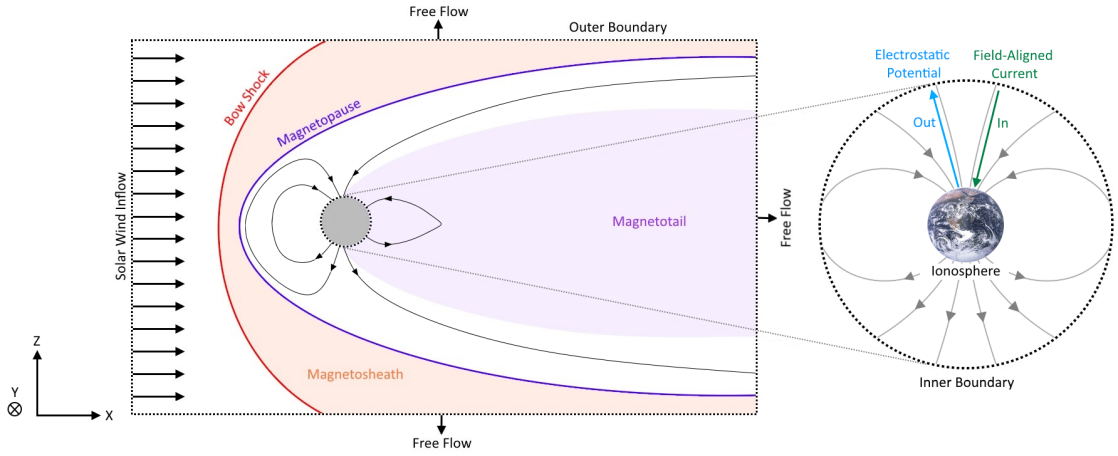

Figure 2.1 – A cartoon showing the outer and inner boundaries of the simulation domain in Gorgon, represented here in the X-Z plane.

At the outer edges of the simulation domain, free-flow is applied to allow the plasma to leave the vicinity of the planet, e.g. when the solar wind is diverted around the magnetopause, or magnetospheric plasma is ejected downtail. The exception to this is at the sunward edge of the box, placed to the left of the Earth, where the solar wind inflow is applied and acts as the primary source of plasma in the simulation. Here we can define ρ, $\mathbf{v}$, $T_{p,e}$ and $\mathbf{B}$ for the inflowing plasma, determining how it interacts with the planetary magnetic field. This is initialised as a dipole with an arbitrary magnitude

and orientation, which can be rotated if the MHD solver does not employ a split dipole representation of **B** and hence is not restricted to simulations of just the terrestrial magnetosphere.

The remaining boundary is the inner boundary close to the planet, within which the MHD equations are not solved for the reasons outlined in section 1.4.1. In previous versions of the code, this region was treated as a vacuum containing the dipole source which carried an effective resistivity of order ~ 1 mho^{-1}. Whilst this therefore played a similar role to the resistive ionosphere, it was not determined by the same coupling mechanisms and the spatial distribution of the resistivity was not well-defined, e.g. it captured no currents or convection asymmetries associated with gradients in Pedersen and Hall conductance. More crucially, the lack of a separate ionosphere model onto which magnetospheric field-aligned currents were mapped precluded the use of Gorgon for space weather modelling purposes.

Previous studies with the code therefore focused on the dynamics of the outer boundaries of the magnetosphere. Mejnertsen et al. (2016) used Gorgon to simulate the magnetosphere of Neptune, employing dipole rotation to explore the reconfiguration of the system under different, highly-inclined orientations of the planetary field with respect to the solar wind inflow. Mejnertsen et al. (2018) later simulated the Earth's magnetosphere in response to a time-varying solar wind using upstream L1 data from the ACE spacecraft, investigating the complex time-dependent motion of the bow shock. However, using Gorgon to study more detailed aspects of the global dynamics, especially with application to space weather impacts such as simulating extreme events, required the addition of a magnetosphere-ionosphere coupling module. This is also necessary for simulations of other planetary magnetospheres where the ionosphere plays a key role, e.g. at the gas giants with their corotating internal plasma sources.

In order to couple the MHD simulation to a thin-shell ionosphere model as is frequently done with other magnetospheric codes, several changes to the numerics and boundary and initialisation conditions have been made from the version of the code used in the above studies. This previous version was described in-depth by Mejnertsen (2018), where numerical tests of the MHD solver are also presented. In the present chapter the details of the updated MHD solver are briefly summarised, with a focus on the changes relevant for the work in this thesis. The procedure for magnetosphere-ionosphere coupling in Gorgon is then described, and appropriate testing and benchmarking is performed to demonstrate its veracity.

For clarity, the work forming this chapter which is original to this thesis is as follows: the testing of a pre-existing solver for the ionospheric potential; the implementation and testing of different conductance models and lower-latitude boundary conditions within said solver; the testing of the mapping of ionospheric variables to and from the magnetospheric domain; the implementation and testing of the inner boundary condition in the MHD solver based on the potential; the benchmarking of the updated code against another GMHD code via a test simulation. All simulations shown throughout this thesis were performed using Imperial College's high performance computing facilities, and the

output data were stored and analysed via remote data repositories.

2.2 MHD Solver

Gorgon takes an Eulerian approach, solving the MHD equations on a uniform, staggered, 3-D cartesian grid, also known as a Yee grid (Yee, 1966). This means the grid resolution is maintained throughout the entire domain, typically between $\frac{1}{4}\ R_E$ and $\frac{1}{2}\ R_E$ in each of the X-, Y- and Z-directions for simulations of the Earth's magnetosphere. The term 'staggered' refers to the relative positions within each grid cell at which different quantities are defined. In Gorgon, the magnetic field is calculated at the centre of the cell faces, the vector potential (and electric field and current) at the cell edges and the fluid quantities like momentum (**p**), mass density and energy at the centres of the cells. This is demonstrated in Figure 2.2. The benefit of this design is in the conservation of magnetic flux, at the cost of having to average across grid cells when combining electromagnetic and fluid quantities.

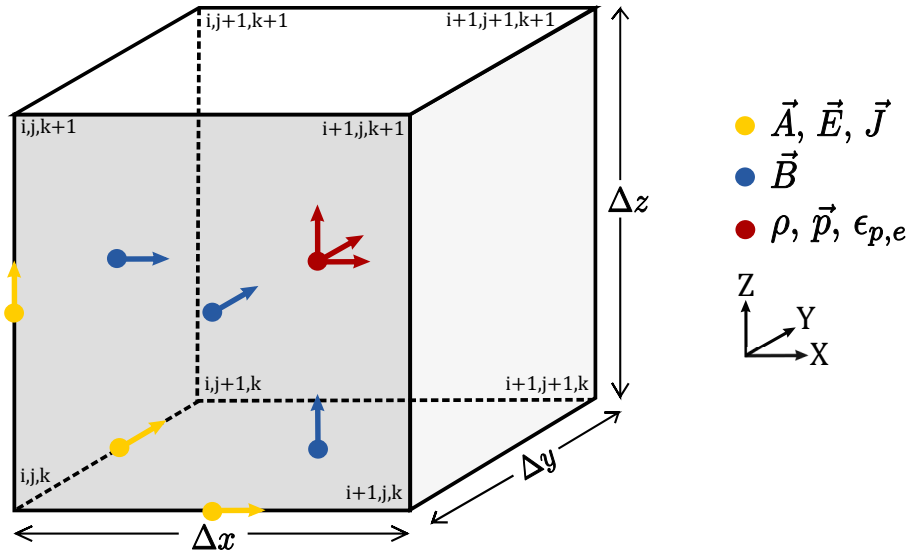

Figure 2.2 – A cartoon showing the placement of different quantities on the staggered grid in Gorgon. The fluid quantities are placed at the cell centres (red arrows) with the electromagnetic quantities at the cell faces (blue arrows) and edges (yellow arrows).

The code is built around a hydrodynamic solver, with a separate magnetic field solver which is optionally switched on for the MHD case. The solvers are iterated every timestep Δt, which is variable and defined based on the CFL condition mentioned in section 1.4.1, given by:

$$\Delta t < \min(\Delta x_i / v_i), \tag{2.7}$$

where Δx_i is the grid cell size and v_i is the sum of the velocity and the fastest wave speed in a given grid cell, i.e. the timestep must not be greater than the minimum transit time of waves within the cell. Since the grid is uniform in Gorgon, the timestep is hence determined by the maximum wave speed anywhere in the simulation domain. This

becomes prohibitive for a code if it uses a grid which is more refined in areas with higher wave speeds, and some codes circumvent the increased global computation time by subcycling within some regions (eg. Janhunen et al., 2012).

The hydrodynamic solver in Gorgon employs a Lagrangian-remap scheme, which first updates fluid quantities based on the pressure and magnetic forces (i.e. 'Lagrangian'), and then advects the expanded fluid by 'remapping' it onto the Eulerian grid. The Lagrangian step solves equations (2.2-2.4) in the absence of advection terms $(\mathbf{v} \cdot \nabla)\rho\mathbf{v}$ and $\nabla \cdot (\epsilon_{p,e}\mathbf{v})$, and is calculated using a second-order Runge-Kutta method (Benson, 1992). The remapping is then performed in the advection step, which utilises a third-order Van Leer advection scheme (Van Leer, 1977).

The MHD equations in Gorgon are represented in terms of conservative quantities: energy $\epsilon_{p,e}$, density ρ and momentum $\rho\mathbf{v}$. However, the energy equation only accounts for the internal energy rather than the total energy and hence neglects the change in magnetic and kinetic energies, though total energy is typically found to be conserved within 10% (Ciardi et al., 2007). Whilst the Lagrangian-remap approach is designed to conserve fluxes at the cell boundaries, kinetic energy is not fully conserved during the momentum remap. This is further exacerbated in the vicinity of shocks, where the advection routine switches to lower order to reduce numerical effects.

Like other MHD codes Gorgon utilises an artificial viscosity, which is required in the presence of shocks to decelerate plasma and provide irreversible heating, but also to reduce numerical overshoots and oscillations downstream of the shock (Arber et al., 2001). Previously this was achieved via a von Neumann artificial viscosity (Benson, 1992), which adds a viscous 'pressure' P_v during the Lagrangian step with a linear form proportional to the local density, sound speed and velocity jump Δv, and was applied anywhere such a velocity jump between adjacent cells was present. This has been modified by replacing the sound speed with the magnetosonic speed, and instead using a Wilkins artificial viscosity combined with a Christensen flux-limited viscosity. The Wilkins artificial viscosity (Wilkins, 1980) is a summation of a linear and quadratic viscosity:

$$P_v = c_1 \rho c_{ms} |\Delta v| + c_2 \rho (\Delta v)^2, \tag{2.8}$$

where the dimensionless coefficients c_1 and c_2 have an arbitrary value. The Christensen flux-limited viscosity further improves on this by calculating Δv to higher order but also effectively switches off the viscosity in regions with smooth solutions (Benson, 1992). Whilst any artificial viscosity results in the shock being spread out over multiple grid cells, the above approach allows the shock to be resolved more sharply than the previous von Neumann viscosity. Note that whilst the DeBar correction (which improves kinetic energy conservation) was previously used, this has been disabled as it was found to introduce errors at the bow shock in the updated version.

The magnetic solver similarly consists of two steps: advection and resistive diffusion. The former is performed using the same third-order Van Leer advection scheme as in the hydrodynamic case, solving the induction equation (1.25) without the diffusive term

in the form $\partial \mathbf{A}/\partial t = \mathbf{v} \times \mathbf{B}$. The resistive diffusion is then calculated by integrating equation (2.5) over a timestep Δt, assuming $\nabla \times \mathbf{B}$ stays constant, and discretising the result to advance $\mathbf{A}$ and $\mathbf{E}$ to the next timestep (Jennings, 2006). In the limit of $\eta \to \infty$, the solution reduces to electromagnetic wave propagation through a vacuum and so the fields are able to advance in the absence of plasma. Where η is finite diffusion dominates the wave propagation, and where η is sufficiently small only the advection step evolves the field.

Since the speed of light has to be resolved according to the CFL condition the resistive diffusion solver is sub-cycled over the fluid timestep, though an artificial cap on the speed of light can placed, e.g. $c \sim 4 \times 10^6$ ms^{-1} (Ciardi et al., 2007), to improve code efficiency. A similar cap is set for the Alfvén speed through the Boris correction (Boris, 1970), which damps Alfvén waves by modifying force terms in the momentum equation (2.2).

To reduce discretisation errors in the magnetic field (and associated artificial currents) in the inner magnetosphere, a split dipole magnetic field has been implemented whereby we replace:

$$\mathbf{B} \rightarrow \mathbf{B}_0 + \mathbf{B}_1, \tag{2.9}$$

$$\nabla \times \mathbf{B} \rightarrow \nabla \times \mathbf{B}_1, \tag{2.10}$$

$$\frac{\partial \mathbf{B}}{\partial t} \rightarrow \frac{\partial \mathbf{B_1}}{\partial t}. \tag{2.11}$$

Here $\mathbf{B_0}$ and $\mathbf{B_0}$ are the dipolar (curl-free) and non-dipolar contributions to the magnetic field, respectively. This is beneficial since $\mathbf{B_0}$ dominates close to the Earth and hence the current is only determined from the significantly smaller $\mathbf{B_1}$. In codes which solve for the total energy, the magnetic pressure contribution can be defined by just using $\mathbf{B_1}$, whilst the advection of the field still requires the use of the total field (i.e. $\mathbf{E} = -\mathbf{v} \times (\mathbf{B}_0 + \mathbf{B}_1)$). Note that (2.11) is only valid if the dipole is static, and including dipole rotation with a split dipole approach requires more complex treatment of the induction equation (e.g. Tóth et al., 2004). This has not yet been implemented in Gorgon, and so the dipole is kept fixed throughout the work in this thesis. Note that we assume a centred dipole, i.e. there is no offset of the dipole axis with respect to the Earth's rotation axis.

In previous simulations, the domain was initialised either filled with low-density plasma or as a vacuum. A vacuum density cut-off was also defined, whereby cells with density below this value were treated as a vacuum where the resistive diffusion solver reduced to the electromagnetic wave solution. Since coupling with an ionosphere model requires defining the flow at the inner boundary, which must then feed-through to the rest of the magnetosphere, a finite density throughout the simulation domain is necessary to achieve this. Furthermore, the presence of the cold plasmaspheric plasma in the inner magnetosphere is often modelled by setting a fixed density and temperature at the inner boundary (e.g. Hu et al., 2007, Ridley et al., 2010). For these reasons, the vacuum

cut-off is thus no longer used when including magnetosphere-ionosphere coupling.

2.3 Inner Boundary Conditions

The treatment of the inner boundary in Gorgon is now similar to that used in other codes which are coupled to a thin-shell ionosphere model. The approach is to define the plasma density, temperature and velocity everywhere inside the spherical region contained within the inner boundary, enforcing these every timestep. The cells for which this is performed are flagged as inner boundary cells if the cell centre lies within the specified inner boundary radius R_{IB}, usually placed at 3 to 4 R_E. Whilst the MHD equations are not fully solved in this region, the cells just outside of the boundary are updated based on the inner boundary properties and thus the cold, dense plasma spreads out to form a plasmasphere and the inner boundary flow feeds-through to the global magnetosphere.

Since the inner boundary density is uniform and constant, any magnetospheric plasma which flows through the inner boundary is effectively removed from the simulation. Conversely, a flow from the inner boundary acts as a plasma source, similar to the polar wind outflow from the ionosphere, though this is not based on the same physical mechanisms. Whilst the inner boundary acts as a dipole source region where the non-dipolar magnetic field component $\mathbf{B}_1$ should be negligible, it is still allowed to advect with the flow to ensure the total field is smooth through the boundary.

To capture the role of the ionosphere in modulating global convection, field-aligned currents must be mapped from the inner magnetosphere onto a separate ionospheric grid, and the thin-shell Ohm's law (1.43) then solved to obtain an electric potential that is mapped back out. A separate ionosphere module in Gorgon performs the necessary mapping, interpolation and calculations that supply the inner boundary condition on the flow, as we will now describe.

2.3.1 Thin-Shell Ionosphere Model

The ionosphere in Gorgon is treated using the standard approximation of a thin conducting shell with height-integrated conductivities, or conductances, as described in section 1.3.3. The goal is to obtain the electric potential ψ on the ionosphere given some field-aligned current distribution $j_{||}$ mapped-down from the magnetosphere. To do this, we solve equation (1.43) on a regular 2-D spherical grid of radius R_{IS} with cell size $(\Delta\theta, \Delta\lambda)$. The colatitude θ and azimuth λ are defined as follows, for ionospheric coordinates x_{IS}, y_{IS} and z_{IS} in the magnetospheric domain:

$$R_{IS} = \sqrt{x_{IS}^2 + y_{IS}^2 + z_{IS}^2}, \tag{2.12}$$

$$\theta = \cos^{-1}\left(\frac{z_{IS}}{R}\right), \tag{2.13}$$

$$\lambda = \tan^{-1}\left(\frac{y_{IS}}{x_{IS}}\right). \tag{2.14}$$

The choice of R_{IS} is arbitrary and depends on the desired height of the ionospheric shell, e.g. 300km, but this is small on the scale of an Earth radius. In the discussion in section 1.3.4 it was assumed that the magnetic field lines in the ionosphere were vertical in the region of interest. We do not make this assumption here, and set $\mathbf{j}_{||} \cdot \hat{\mathbf{r}} = j_{||} \cos\delta$, where $\delta = \delta(\theta)$ is the angle between the radial direction $\hat{\mathbf{r}}$ and the unit dipole magnetic field $\hat{\mathbf{b}} = \hat{\mathbf{b}}(r, \theta)$. Note this correction is not significant at auroral latitudes - and even at 45° colatitude $\cos\delta \approx 0.9$ - but it does provide some improved accuracy, particularly at lower latitudes (Wolf, 1975). We still neglect the neutral wind and model the ionosphere within the frame of the rotating Earth, in which case the form of equation (1.43) remains the same but the conductance tensor is given by:

$$\vec{\mathbf{\Sigma}} = \frac{1}{\cos\delta}\begin{pmatrix} \Sigma_P / \cos\delta & \Sigma_H \\ -\Sigma_H & \Sigma_P \cos\delta \end{pmatrix} \tag{2.15}$$

As explained in section 1.3.3, the Hall and Pedersen conductances are themselves dependent on two key ionisation sources: solar EUV radiation, and electron precipitation. These are defined at each grid cell and can be obtained using empirical formulae or simply set to be uniform, as we will discuss later. Expanding equation (1.43) with the use of (2.15) gives the following partial differential equation (PDE):

$$C_{\theta\theta}\frac{\partial^2\Psi}{\partial\theta^2} + C_{\lambda\lambda}\frac{\partial^2\Psi}{\partial\lambda^2} + C_\theta\frac{\partial\Psi}{\partial\theta} + C_\lambda\frac{\partial\Psi}{\partial\lambda} - f = 0, \tag{2.16}$$

with coefficients

$$C_{\theta\theta} = \Sigma_P\frac{\sin^2\theta}{\cos^2\delta}, \tag{2.17}$$

$$C_{\lambda\lambda} = \Sigma_P, \tag{2.18}$$

$$C_\theta = \left(\frac{\partial}{\partial\theta}\left(\Sigma_P\frac{\sin\theta}{\cos^2\delta}\right) - \frac{\partial}{\partial\lambda}\left(\frac{\Sigma_H}{\cos\delta}\right)\right)\sin\theta, \tag{2.19}$$

$$C_\lambda = \sin\theta\frac{\partial}{\partial\theta}\left(\frac{\Sigma_H}{\cos\delta}\right) + \frac{\partial\Sigma_P}{\partial\lambda}, \tag{2.20}$$

$$f = -j_{||}r^2\sin^2\theta\cos\delta. \tag{2.21}$$

One can see that a uniform Hall conductance drops out of the solution for ψ, consistent with the Hall current closing within the ionosphere unless there are gradients in Σ_H. Each of the coefficients can be readily obtained at each grid cell by calculating

differences between adjacent cells. This PDE is solved for ψ by employing successive over-relaxation (Hadjidimos, 2000), which reaches convergence by taking weighted averages of iterations according to a relaxation factor ω. The choice of ω determines the rate of convergence, which will only occur for $0 \leq \omega \leq 2$. We use a a second-order central finite differencing method to evaluate the partial derivatives in equation (2.16) at a given point on the ionosphere (King et al., 2003). By taking that $\Psi(\theta, \lambda) \approx \Psi_{i,j}$, where $\Psi_{i,j}$ is the value at a discrete point on the grid we have:

$$\frac{\partial \Psi}{\partial \theta} \approx \frac{\Psi_{i+1,j} - \Psi_{i-1,j}}{2\Delta\theta}, \tag{2.22}$$

$$\frac{\partial \Psi}{\partial \lambda} \approx \frac{\Psi_{i,j+1} - \Psi_{i,j-1}}{2\Delta\lambda}, \tag{2.23}$$

$$\frac{\partial^2 \Psi}{\partial \theta^2} \approx \frac{\Psi_{i+1,j} - 2\Psi_{i,j} + \Psi_{i-1,j}}{(\Delta\theta)^2}, \tag{2.24}$$

$$\frac{\partial^2 \Psi}{\partial \lambda^2} \approx \frac{\Psi_{i,j+1} - 2\Psi_{i,j} + \Psi_{i,j-1}}{(\Delta\lambda)^2}. \tag{2.25}$$

A solution is for ψ is determined within a set number of iterations (e.g. 1000) or once it converges to within a certain tolerance level. Periodic boundary conditions are applied azimuthally, and the coordinate singularities at the poles are handled by averaging ψ in λ at the end of each iteration. To validate the solver we now test it using a variety of different conductance profiles, which reflect typical forms used in GMHD simulations and which will be required for future space weather modelling applications.

2.3.2 Conductance Specification

As described in section 1.3.3, there are multiple sources of ionisation in the ionosphere which contribute to the total height-integrated conductivity. That which is responsible for the largest long-term variation is solar EUV ionisation, which results in a strong day-night asymmetry; at solstice, this then also creates a North-South asymmetry due to preferential solar irradiation of the summer hemisphere (Ridley, 2007). Further sources of ionising radiation come from the scattering of sunlight by the atmosphere, and also starlight, both providing some additional nightside conductance (e.g. Ridley et al., 2004). Another important contribution at high latitudes is due to electron precipitation associated with the discrete and diffuse aurorae, but also with lower energy precipitation within the polar cap and polar cusp (e.g. Huang et al., 2014). Any such asymmetries can result in significant changes in the morphology of the ionospheric potential, which will feed-back into the magnetosphere and thus impart asymmetries in global dynamics.

Fully capturing the all of these effects would require modelling not only their dependence on solar and magnetospheric inputs, but also on the atmospheric chemistry and density profile of the ionosphere. Since this would be extremely computationally intensive and require coupling an entirely separate model to Gorgon, it is more practical to make key assumptions (such as the thin-shell approximations) and employ empirical

relations to obtain a series of independent conductances. These can then be added in quadrature, since the production rate of charge-carrying electrons and ions in the ionosphere is proportional to the square of the conductance (Janhunen et al., 2012). We can then obtain total Pedersen and Hall conductances:

$$\Sigma_{P,H} = \left(\sum_i (\Sigma^i_{P,H})^2 \right)^{\frac{1}{2}}. \tag{2.26}$$

Such empirical formulae are well-established in the literature, and are used by other global codes since they depend only on readily available quantities from the MHD simulation. These formulae are often used alongside more thorough techniques, like the Assimilative Mapping of Ionospheric Electrodynamics (AMIE) procedure (Richmond and Kamide, 1988) in which space- and ground-based measurements can be used to more accurately estimate the auroral conductance from the model input. Whilst such techniques yield significant improvement in predictions of ground magnetic field perturbations for severe events (e.g. Mukhopadhyay et al., 2020), implementing such an approach in Gorgon would be a significant undertaking and is reserved for future work. Firstly, we use the Moen and Brekke (1993) empirical relationship for the solar EUV conductances:

$$\Sigma_P = F_{10.7}^{0.53}(0.81\cos\chi + 0.54\cos^{\frac{1}{2}}\chi), \tag{2.27}$$

$$\Sigma_H = F_{10.7}^{0.49}(0.34\cos\chi + 0.93\cos^{\frac{1}{2}}\chi), \tag{2.28}$$

where $F_{10.7}$ is the solar radio flux (in units of 10^{-22} $\mathrm{Wm^{-2}Hz^{-1}}$) at a wavelength of 10.7cm, typically used in this context as a proxy metric for the intensity of EUV radiation, and which varies with solar activity. This can be as low as $\sim 70 \times 10^{-22}$ $\mathrm{Wm^{-2}Hz^{-1}}$ during solar minimum, and up to $\sim 300 \times 10^{-22}$ $\mathrm{Wm^{-2}Hz^{-1}}$ during solar maximum (e.g. Lilensten et al., 1996), but here we will use a fixed value of 100×10^{-22} $\mathrm{Wm^{-2}Hz^{-1}}$ rather than accounting for the $\sim$ 11-year solar cycle. The angle $\chi = \chi(\theta, \lambda)$ is the solar zenith angle, and varies across the ionosphere depending on time of day and season. At noon along the ecliptic, $\chi = 0°$; at the terminator we have $\chi = 90°$, but to avoid negative conductances we simply set $\chi = \min(90°, \chi)$.

As already mentioned, the auroral precipitation contribution to conductance is composed of two sources: the diffuse and discrete aurora. In terms of magnetospheric origin, the former is generated within the inner plasma sheet, forming the lower latitude part of the auroral oval (Nishimura et al., 2020). The latter is found in the poleward part of the auroral oval on the ionosphere and maps to the outer plasma sheet (Lyons and Evans, 1984). The conductance resulting from this ionisation can be described in terms of the precipitating energy using suitable empirical relations, e.g. from Robinson et al. (1987):

$$\Sigma_P = \frac{40\bar{E}}{16 + \bar{E}^2}\sqrt{F_E}, \tag{2.29}$$

$$\Sigma_H = 0.45\bar{E}^{0.85}\Sigma_P. \tag{2.30}$$

Here $\bar{E}$ denotes the mean energy of the auroral electrons in keV, and F_E is their corresponding energy flux in ergs/(cm^{2}s). These can be calculated using parameters obtainable from the MHD simulation, for example by sampling density and temperature at the inner boundary. However, how accurate this is depends closely on the inner boundary condition in the model, as well as being limited by the grid resolution since sharp changes in conductance would yield unphysical potentials and hence electric fields. Including an auroral conductance thus requires careful comparison to data under various driving conditions to ensure the plasma parameters at the inner boundary in Gorgon yield reasonable conductance values, which is a matter for future study. Instead we simply use an idealised, Gaussian profile for the auroral conductance in the demonstration here. The polar conductance due to e.g. polar rain is captured just by including an additional constant, uniform conductance at grid points which are poleward of the auroral oval (Ridley et al., 2004).

2.3.3 Electric Potential Testing and Boundary Conditions

For simplicity we use a synthetic FAC profile in these initial tests. This has the same functional form as the example in Merkin and Lyon (2010), given by

$$j_{||}(\theta, \lambda) = j_0 \sin\theta \sin\lambda, \tag{2.31}$$

with magnitude $j_0 = 1\ \mu\text{Am}^{-2}$ which we only apply for colatitudes θ between 17.5° and 25°. This is shown in Figure 2.3a for the Northern hemisphere, yielding a FAC profile resembling the R1 system. In the first example we use a uniform Pedersen conductance of 10 mho and zero Hall conductance, which is a setup commonly used in GMHD simulations to study magnetospheric dynamics (e.g. Merkin et al., 2003). The resulting potential is shown in Figure 2.3b, which is clearly symmetric about the dawn-dusk and noon-midnight meridians. This profile yields a dawn-dusk oriented electric field over the polar cap, consistent with anti-sunward (Dungey cycle) convection which we would expect for a symmetric R1 current system. We do not show the Southern hemisphere, since this would merely be a mirror image of the North with the same polarity of the potential at dawn and dusk.

We now apply more realistic conductance profiles to test the solver's ability to handle asymmetric cases. First, we use the Moen and Brekke (1993) conductance formula (2.28) to capture the day-night asymmetry in conductance due to solar EUV ionisation. This is shown along with the resulting potential in Figure 2.4. The peaks of the potential have now shifted anti-sunward towards regions of lower conductance, with the day-night gradient in Hall conductance also distorting the pattern such that the dawn convection cell is now smaller than the dusk cell. This will correspond to a dawn-dusk asymmetry in magnetospheric convection, demonstrating the role of conductance gradients in exerting stress and shear on the system. This same effect was demonstrated by Ridley et al. (2004) (see their Plate 6) for a similar conductance profile, confirming that the solver is performing as expected.

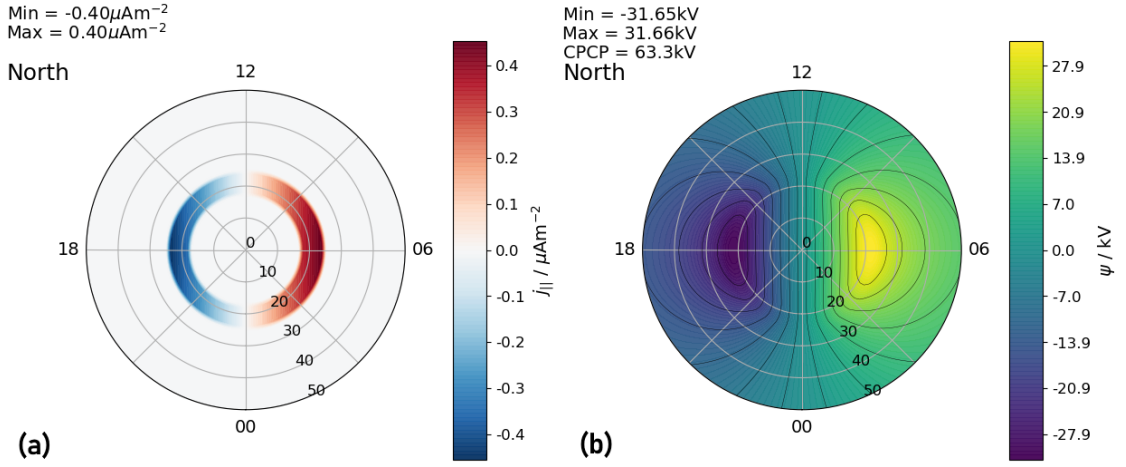

Figure 2.3 – Solution for (a) an idealised Region 1 FAC distribution, showing (b) the potential for uniform conductances of Σ_P = 10 mho, Σ_H = 0mho.

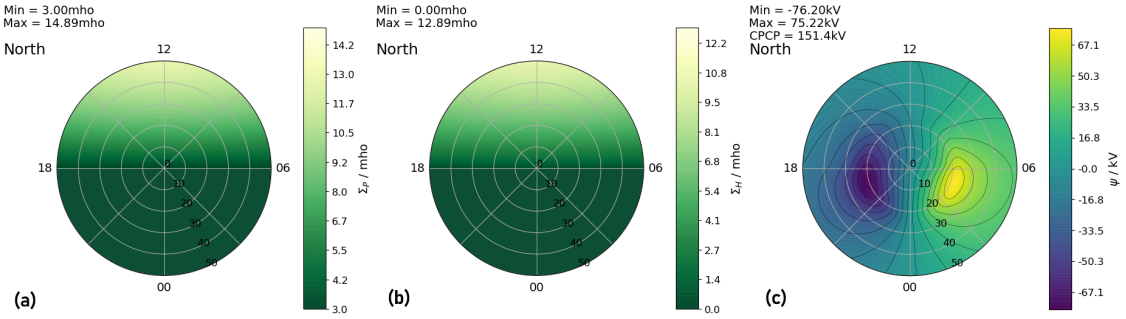

Figure 2.4 – Solution for (c) the potential using the Region 1 FAC distribution shown in Figure 2.3, with (a, b) a conductance profile including ionisation due to solar EUV radiation.

Similar effects arise when including an auroral conductance. Figure 2.5 shows the result of applying an idealised, Gaussian auroral conductance profile centred at 17.5° colatitude with a 1-σ drop-off at 5° latitude either side. The peaks of the conductance have Σ_P = 7 mho and Σ_H = 12 mho, values taken from Coxon et al. (2016). An additional constant polar cap conductance is included poleward of the peak, for which Σ_P = 2.5 mho and Σ_H = 5 mho, as used by Ridley et al. (2004). The sharp gradients in both conductances strongly distort the potential; the dusk cell is slightly larger and shifted anti-sunward towards the pre-midnight sector, whereas the dawn cell now lies in the pre-noon sector. Note there is only a slight mismatch between the maximum and minimum values of ψ in these two examples; the differences between convection cells are primarily morphological changes, which are well-captured by the solver. Again, in these cases there is no North-South asymmetry and hence we do not show the Southern hemisphere.

A more significant mismatch in the potential extrema, as well as a North-South asymmetry, arises if we include seasonal effects on the EUV conductance. The above corresponds to an equinox configuration where each hemisphere is equally sunlit - though even at equinox diurnal variation will cause the dipole tilt angle (and thus solar zenith

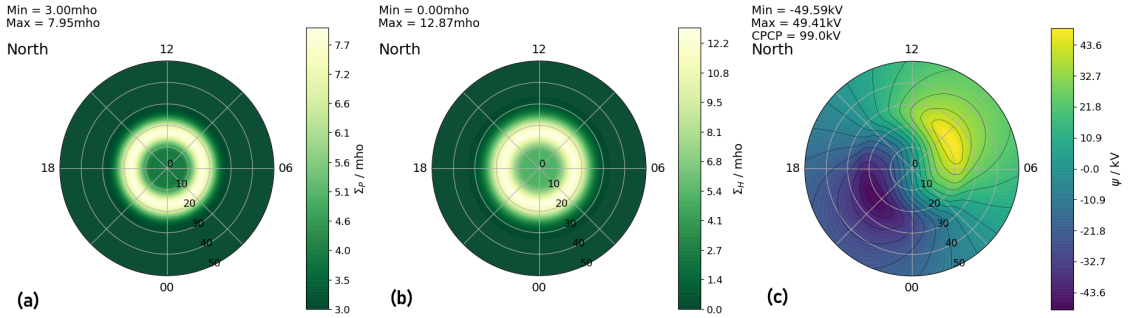

Figure 2.5 – Solution for (c) the potential using the Region 1 FAC distribution shown in Figure 2.3, with (a, b) a conductance profile including ionisation due to idealised auroral and polar cap precipitation.

angle, since the dipole is located at the poles in the model) to vary by $\pm 10^\circ$ and introduce some North-South asymmetry. At solstice, this becomes more extreme and the dipole tilt angle reaches $\sim 30^\circ$, with one hemisphere significantly more sunlit. Capturing such effects is important in simulating space weather events which can have very different impacts in each hemisphere.

This is demonstrated in Figure 2.6, where we include both EUV and auroral/polar cap conductance, as well as introducing a 30° asymmetry in solar zenith angle corresponding to summer conditions in the Northern hemisphere. We therefore also show conditions in the Southern hemisphere, in which the same FAC distribution is applied. In this case the CPCP is significantly lower in the North than the South, due to an overall higher average conductance; the extent of distortion of the Northern convection cells is also lesser in comparison, since the gradients in conductance are smoother around the edges of the polar cap. Hence the solver can also capture seasonal differences in ionospheric convection purely due to conductance asymmetries, as has similarly been demonstrated using other coupled GMHD-ionosphere models (e.g. Wiltberger et al., 2009, Ridley, 2007). Note that this idealised Northern potential profile is comparable in morphology to the mean stormtime convection pattern generated from SuperDARN observations (Walach et al., 2021, see their Figure 3), confirming that the model can produce realistic solutions given some physically representative conductances.

One final issue before coupling this thin-shell model to the MHD code is the option of applying a boundary condition to the ionospheric potential. The mapping between the magnetosphere and ionosphere only occurs within the higher-latitude part of the ionosphere, since the equator of the MHD inner boundary maps to a specific ionospheric latitude which we refer to as the lower-latitude boundary (LLB). In the above examples the potential was solved over the whole sphere: this technically allows for a disparity between non-zero North/South potentials that get mapped out to the neighbouring MHD grid cells in the magnetosphere, resulting in an electric field in the Z-direction if the dipole points in Z. This may not be realistic, since the electric field in the inner magnetosphere is in fact shielded from the cross-tail electric field at low latitudes.

Since the regions within the MHD inner boundary are not properly modelled, the potential at latitudes below the LLB is therefore not fully known unless the MHD code is

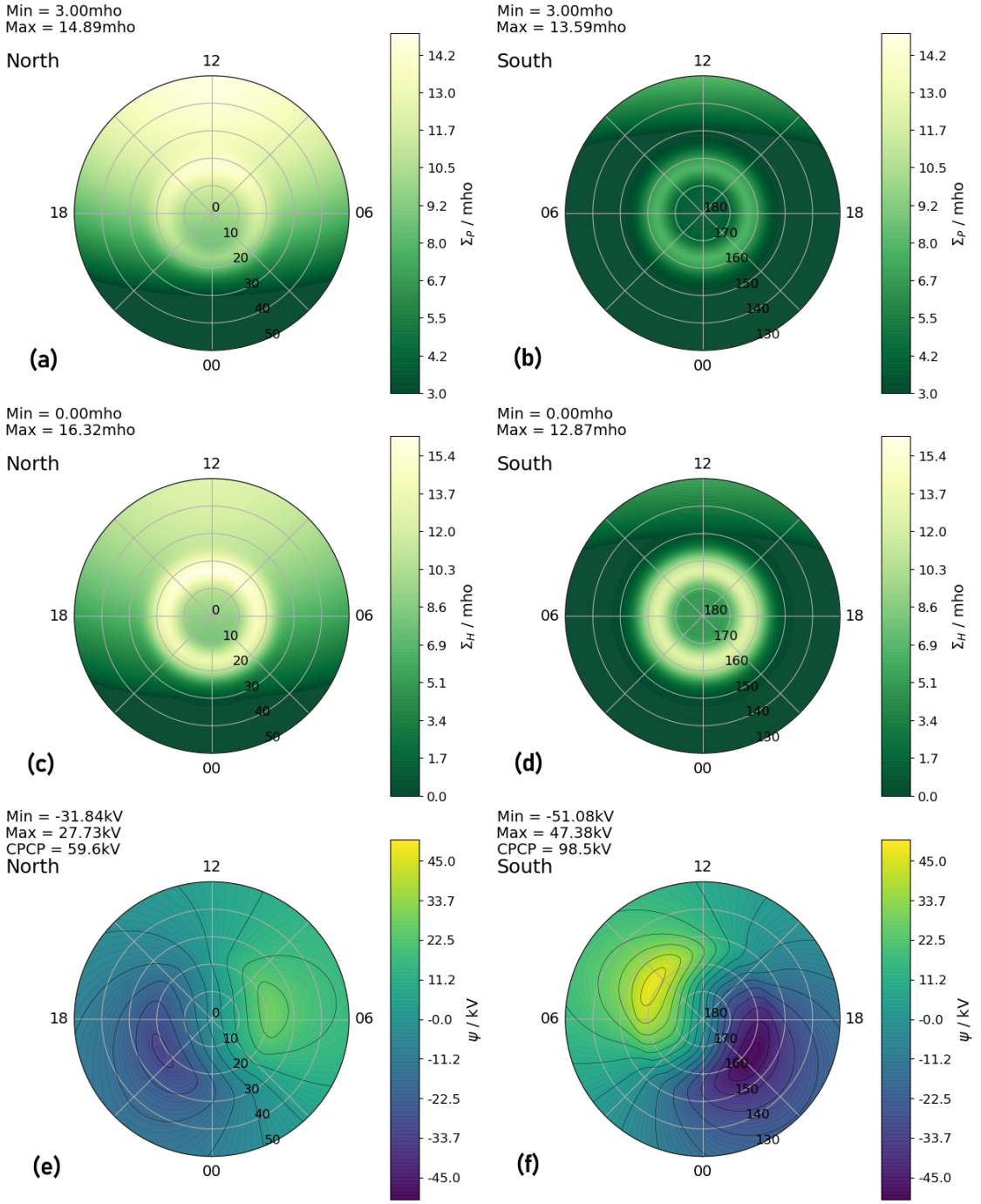

Figure 2.6 – Solution at each hemisphere for (e, f) the potential using the Region 1 FAC distribution shown in Figure 2.3, with (a-d) a conductance profile including ionisation due to asymmetric solar EUV radiation and idealised auroral and polar cap precipitation.

coupled to a separate inner magnetosphere model. An appropriate choice of boundary condition instead allows for better control of the potential, and a prescribed behaviour at the inner boundary. Merkin and Lyon (2010) explored this in detail using the LFM GMHD code, presenting three different types of lower-latitude boundary conditions which led to considerable differences in magnetospheric dynamics.

The first is a hard (Dirichlet) boundary condition where the potential is zeroed at the

LLB, ensuring that the electric field is zero at the equator of the inner boundary, effectively providing the shielding effect of the ring current. It also enforces zero radial flow at the equator, making the inner boundary hard at low latitudes such that 'ionospheric' outflow of cold plasma can only occur at higher latitudes, similar to the polar wind. This is useful in controlling the dynamics in a consistent manner, but it forgoes realistic ionospheric convection at latitudes near the LLB if the potential drops to zero from its maximum over a small latitude range, e.g. if the polar cap is particularly expanded. Furthermore, it may not be accurate to have zero flow through the inner boundary if it is placed at a large radial distances, especially if the magnetosphere is particularly dynamic, or compressed.

Alternatively, one can force the potential to have a value at a particular latitude of interest. This can be useful for e.g. space weather forecasting or data comparison at chosen latitudes, or setting the potential to zero at the ionospheric equator to make the two hemispheres independent in their solutions. The latter option however abandons the close control over the inner boundary flow, since one could then have any potential profile at the MHD equator and the aforementioned Z-directed electric field due to North/South mismatches. Finally, there is the option of a free-flow (Neumann) condition where the latitudinal gradient in the potential (i.e. E_θ) is zero at the LLB. This has a similar effect to the first option, but allows for equatorial electric fields in the azimuthal direction and hence significant flows in the radial direction. This is then more sensitive to boundary conditions in momentum, since mass may be created or lost by radial flows through the inner boundary.

We now demonstrate the influence of these boundary conditions using the same conductance profile as Figure 2.6. We assume an MHD inner boundary of 3 R_E, which corresponds to a colatitude of $\sim 35^\circ$. The hard boundary condition at the LLB is applied by zeroing the potential at this colatitude; the Neumann condition simply sets the North/South LLB potentials to be the same before each solver iteration, i.e. the potential is constant in θ throughout the lower-latitude ionosphere (but varies in λ); the final condition sets $\psi = 0$ at the equator. The resulting potentials in each hemisphere are shown in Figure 2.7.

The equatorial boundary condition appears to give an identical solution in the high-latitude ionosphere to when we applied no boundary condition at all, and is therefore unnecessary if one does not wish to control the solution at lower latitudes. The hard condition at the LLB has confined the convection pattern purely to high latitudes and has yielded notably smaller extrema in the potential, though still captures some distortion and North/South asymmetry in its morphology. The Neumann condition similarly captures this distortion, but underestimates the North/South asymmetry due to the very large potentials near the LLB being mutually enforced between each hemisphere, hence the exaggerated CPCPs. The results are summarised in Table 2.1. The most sensible choice for an inner boundary radius $\gtrsim 3\ R_E$ therefore appears to be either the 'Hard (LLB)' condition, or simply solving over the full sphere as before, i.e. 'None'. Other

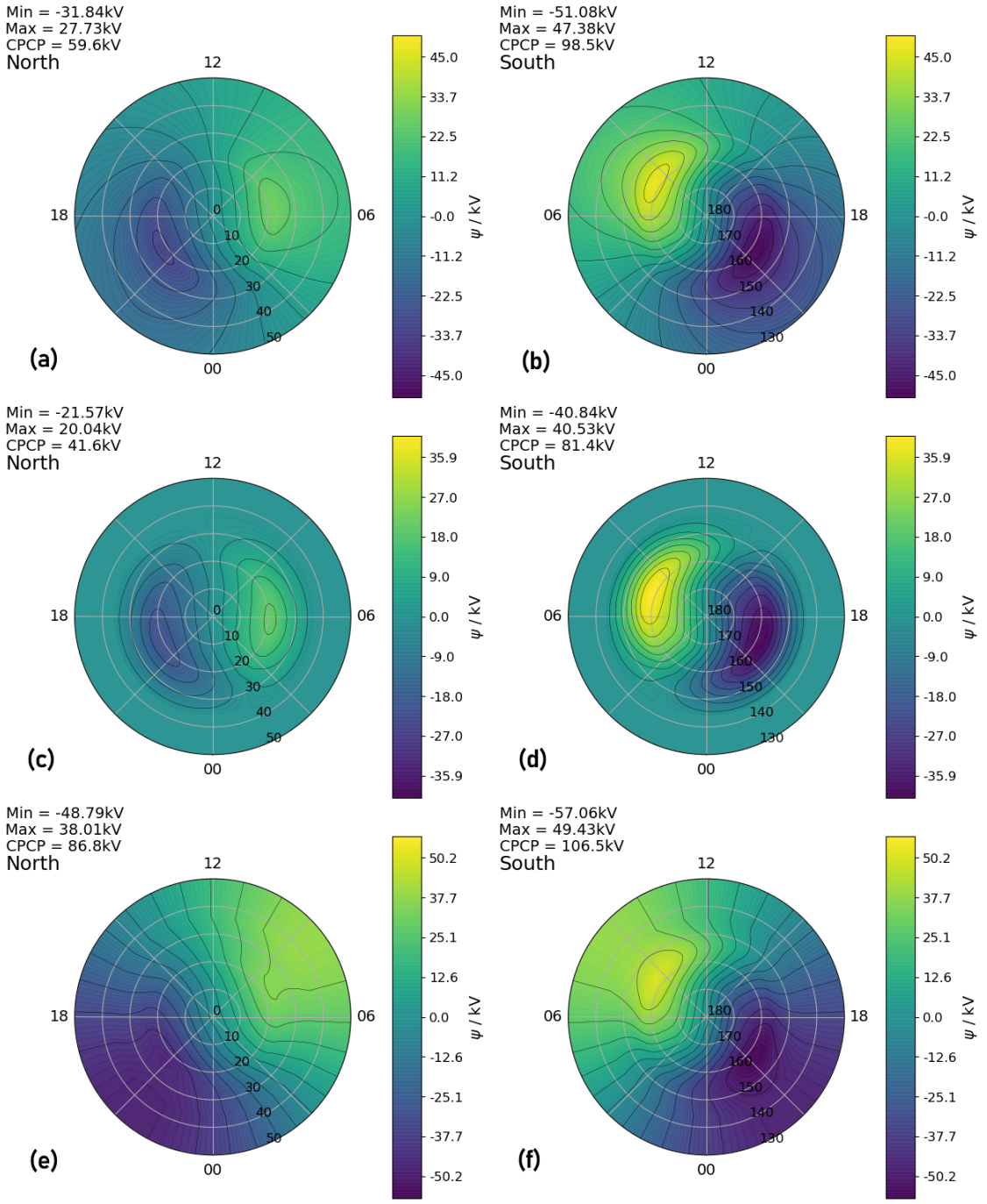

Figure 2.7 – Solutions for the potential for different boundary conditions corresponding to the same FAC and conductances as in Figure 2.6, where (a, b) have a hard boundary condition where the potential is zeroed at the equator, (c, d) have the same except the potential is zeroed at the LLB, and (e, f) have a Neumann boundary condition applied at the LLB.

choices may have some benefit, but only if additional constraints on the potential are required. Throughout this thesis the 'Hard (LLB)' condition is used, in order to ensure that the electric field near the inner boundary is well-behaved. However, for future simulations where an accurate potential is required at lower latitudes - e.g. for data comparison or for forecasting ground magnetic perturbations - it may be preferable to apply no such

boundary condition. The solver has therefore been left adaptable for such purposes.

Boundary Condition	North			South		
	CPCP	ψ_{max}	ψ_{min}	CPCP	ψ_{max}	ψ_{min}
None	59.6	27.73	-31.84	98.5	47.38	-51.08
Neumann (LLB)	86.8	38.01	-48.79	106.5	49.43	-57.06
Hard (eq.)	59.6	27.73	-31.84	98.5	47.38	-51.08
Hard (LLB)	41.6	20.04	-21.57	81.4	40.53	-40.84

Table 2.1 – Values (in kV) for the CPCP and minima/maxima in electric potential at each hemisphere for the different boundary conditions shown in Figure 2.7.

2.3.4 Coupling with the Magnetosphere

We now discuss the coupling of the thin-shell ionosphere model with the Gorgon MHD code. In order to calculate the FAC generated at some position in the magnetosphere that inevitably enters the ionosphere, we apply Ampère's law, i.e.

$$j_{||} = \frac{1}{\mu_0}(\nabla \times \mathbf{B}) \cdot \hat{\mathbf{b}} \tag{2.32}$$

where μ_0 is the permeability of free space. To obtain the ionospheric FAC we perform this calculation at cells just outside of the inner boundary and map it down onto the ionospheric grid. This requires a procedure of identifying the ionospheric footpoints of given magnetospheric field lines; one could numerically trace the simulated field lines down onto the ionosphere at $\sim 1R_E$ to obtain geomagnetic coordinates, but this is computationally demanding. Instead, we assume that the magnetic field in the inner region is perfectly dipolar, yielding a simple mapping relation for our coordinates:

$$\frac{\cos\theta_{IS}}{\sqrt{R_{IS}}} = \frac{\cos\theta_{IB}}{\sqrt{R_{IB}}}. \tag{2.33}$$

Here subscripts IS, IB denote the ionosphere and magnetospheric inner boundary, respectively. This allows us to map elements of $j_{||}$ onto new positions θ at the ionospheric radius R_{IS} (as the dipole field has no λ-dependence). It should be noted that this mapping procedure will project a cartesian grid onto the spherical ionosphere, and as such we must interpolate it onto a spherical grid for the purposes of analysis. Further noting that $j_{||} \propto B$ (Goodman, 1995), we must also scale the mapped FAC as:

$$j_{IS,||} = B_{IS}\frac{j_{IB,||}}{B_{IB}}. \tag{2.34}$$

This FAC gets passed into the ionospheric potential solver, which returns a value for ψ mapped back along the field line. The potential does not need scaling upon mapping: exact values on the spherical mesh remain the same, with the mesh stretched equatorward from the LLB to cover unmapped latitudes. From this we calculate the electric field $\mathbf{E}$ at the inner boundary, by solving for the gradient on the cartesian grid of spacing (Δx, Δy, Δz), whereby

$$\mathbf{E} = -\nabla\psi(x,y,z) = \frac{\psi_{i,j,k} - \psi_{i+1,j,k}}{\Delta x}\hat{\mathbf{i}} + \frac{\psi_{i,j,k} - \psi_{i,j+1,k}}{\Delta y}\hat{\mathbf{j}} + \frac{\psi_{i,j,k} - \psi_{i,j,k+1}}{\Delta z}\hat{\mathbf{k}}. \tag{2.35}$$

Here we evaluate ψ at the faces of the grid cells to obtain a cell-centred **E**, meaning this is a second-order approximation. Combining this with the cell-centred **B** at the inner boundary of the simulation gives the E×B-drift velocity,

$$\mathbf{v} = \frac{\mathbf{E} \times \mathbf{B}}{B^2}. \tag{2.36}$$

The electrostatic approximation neglects any inductive effects by assuming magnetic field variations are negligible on timescales of order ∼10s and under (Lotko, 2004). By default the potential is therefore only calculated every 30s, enforcing the same flow every timestep until it is recalculated - though this can be changed arbitrarily if one wishes to study the FAC response over shorter timescales. The resulting velocity field can then optionally be superposed with a corotation velocity (the dominant flow in the innermost magnetosphere at Earth) to obtain the net flow at the inner boundary. This is necessary in cases where we wish to capture the effect of dipole rotation, since the ionosphere is solved within the (non-rotating) Earth frame. We quickly demonstrate the calculation of the inner boundary flow by solving it analytically using the previously calculated potentials. The electric field is computed on a smooth spherical surface as:

$$\mathbf{E} = -\nabla\psi(r,\theta,\lambda) = -\frac{\partial\psi}{\partial r}\hat{\mathbf{r}} - \frac{1}{r}\frac{\partial\psi}{\partial\theta}\hat{\boldsymbol{\theta}} - \frac{1}{r\sin\theta}\frac{\partial\psi}{\partial\lambda}\hat{\boldsymbol{\lambda}}, \tag{2.37}$$

where the gradients are calculated to second order. This is combined with the dipole magnetic field at the inner boundary (since a dipole is assumed throughout the enclosed region), whereby

$$\mathbf{B} = \frac{\mu_0 m}{4\pi r^3}(-2\cos\theta\hat{\mathbf{r}} + \sin\theta\hat{\boldsymbol{\theta}}) \tag{2.38}$$

with a magnetic dipole moment $m = 7.95\times10^{22}\mathrm{Am}^{-2}$ for the Earth. Figure 2.8 shows the x-component of the inner boundary flow using the idealised FAC and uniform conductance in Figure 2.3 applying no boundary condition on the potential, and also for a 'Hard (LLB)' boundary condition. The inner boundary is placed at 3 R_E, and equation (2.36) is solved on a spherical shell assuming a perfect dipole. It is clear that both solutions correspond to anti-sunward convection (positive v_x) over a circular polar cap, with return flow at mid-to-low latitudes. Where there is no boundary condition there is a component of the flow out of the boundary near the equator, as expected; where we apply the 'Hard (LLB)' boundary condition the radial flow disappears and flow stagnates at noon in the equatorial plane.

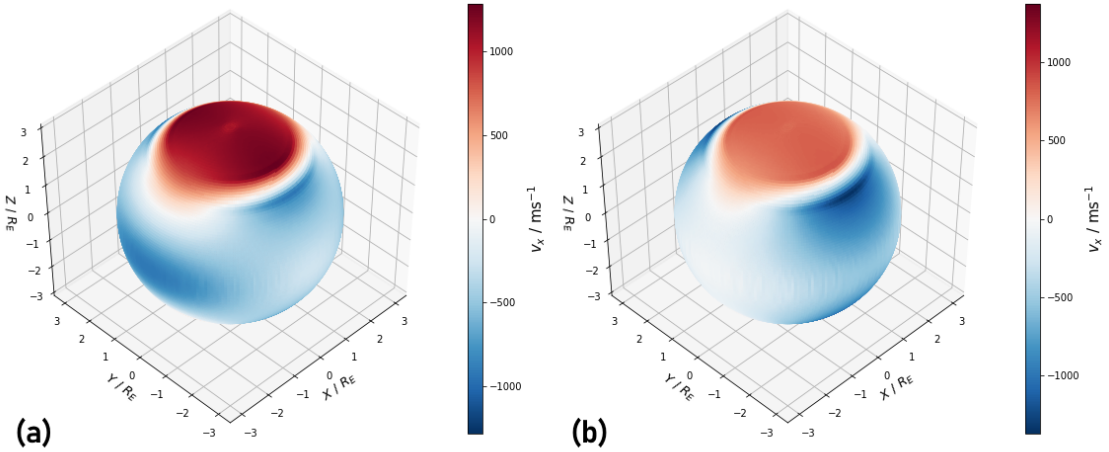

Figure 2.8 – Flow in the x-direction at a $3R_E$ inner boundary, where (a) is the solution corresponding to Figure 2.3b and (b) is the equivalent with a hard lower-latitude boundary condition.

2.4 Testing and Benchmarking

We now test the coupling in Gorgon with a full MHD simulation, by comparing the output to another GMHD code driven with the same solar wind conditions. Our goal is to confirm a good qualitative model agreement in the FAC and potential patterns on the ionosphere, and a broad quantitative model agreement in FAC intensity and CPCP. It should be noted that due to differing numerics and grid specifications, widely-used GMHD models have shown large disagreements in CPCP and total field-aligned current in benchmarking studies, even by up to an order-of-magnitude (Gordeev et al., 2015, Honkonen et al., 2013). We do therefore expect some differences in these values, and a comparison serves the further purpose of identifying these to place any Gorgon results in the context of existing models in the community.

To this end we recreate a run performed by Merkin and Lyon (2010) using the MIX magnetosphere-ionosphere coupling module, coupled with the LFM MHD code (LFM-MIX). This involves driving Earth's dipole field in a zero-tilt, non-rotating configuration. An idealised solar wind input is used with the following parameters: $v_x = 500$ kms^{-1}, $|B| = |B_z| = 5$ nT, $T_i = T_e = 5$ keV, $n = 5$ cm^{-3}. The IMF is southward for the first 2h, northward from 2h to 4h, and southward again until the end of the run at 9h. The cartesian grid has a resolution of 0.5 R_E and dimensions X = (-30, 90) R_E, Y = (-40, 40) R_E, Z = (-40, 40) R_E. The inner boundary is placed at 4 R_E, at which the number density and ion/electron temperature are fixed to n = 370 cm^{-3} and $T_{i,e}$ = 0.1 eV, respectively. The ionospheric grid has size 64 $\times$ 128 (latitude by longitude), and as in the MIX model we use a constant, uniform Pedersen conductance of 10 mho and zero Hall conductance.

The initialisation and time-evolution of the magnetosphere is demonstrated in Figure 2.9. The magnetosphere is formed between panels (a-d), reaching a quasi-steady state between 1-2h where the nightside field has become less dipolar with the formation

of a high-pressure plasma sheet. The thinning of the magnetotail current sheet corresponds to the the onset of tail reconnection in panel (d). In panel (e) the IMF has been northward for 2h, and hence the dayside topology is significantly different to panel (d) with less flux loaded in the tail. In panel (f) the IMF has then been southward for 1h, and is continuously driven with these conditions for the remainder of the simulation; the gradual growth of the Region 1 current system which connects to the ionosphere results in some erosion of the dayside magnetopause. Driving the system with such a highly geoeffective solar wind for the final 5 hours thus provides a fairly challenging initial test for the ionospheric coupling as we expect strong Region 1 FACs and an expanded polar cap.

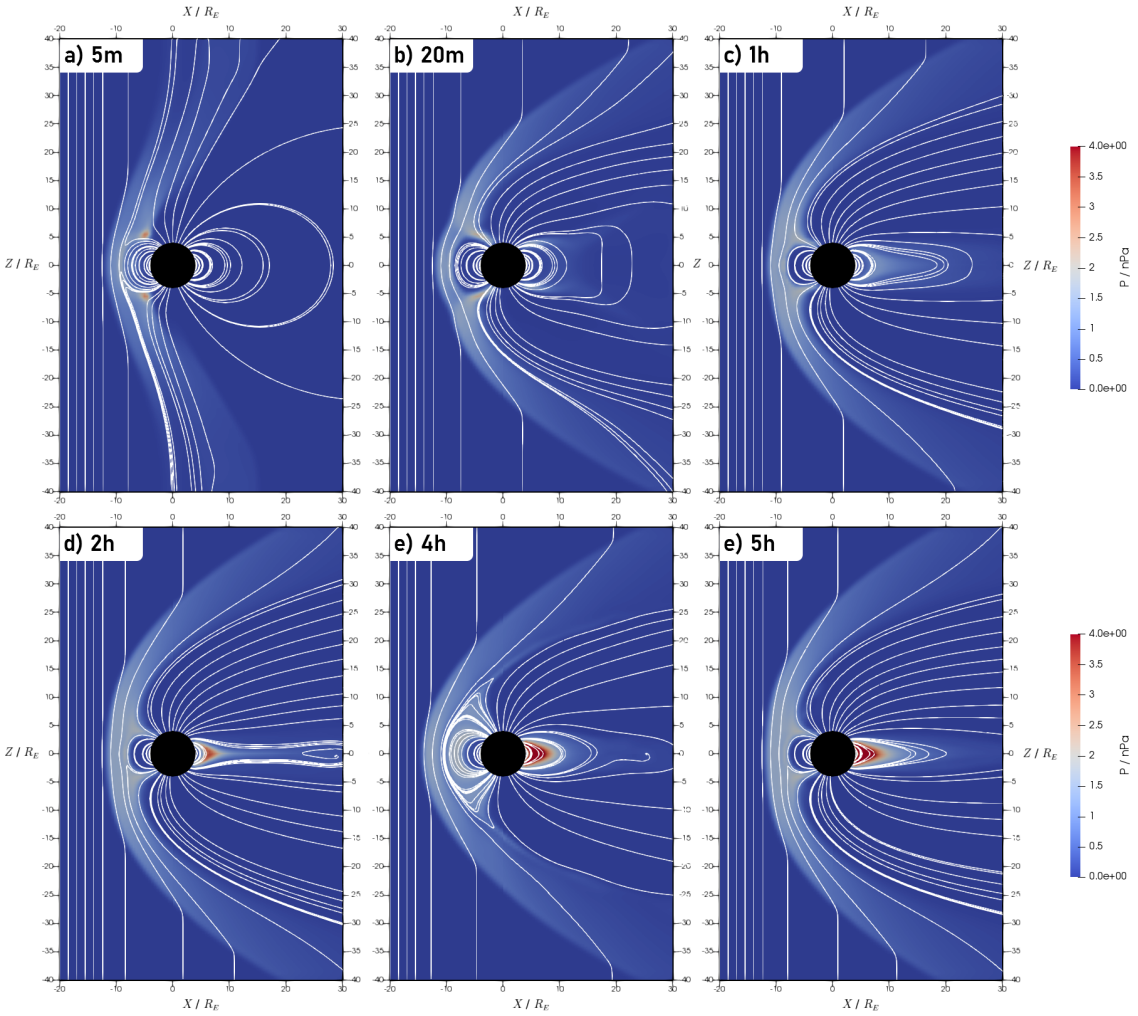

Figure 2.9 – Slices in the X-Z plane of the magnetosphere showing the plasma pressure and magnetic field lines over time.

Figure 2.10 shows the ionospheric conditions at the end of the simulation in Gorgon, and the results from LFM-MIX from Merkin and Lyon (2010) (using the same boundary condition on the potential) for comparison. The Region 1 current system is prominent in both models, peaking at $\sim 20^\circ$ colatitude, with oppositely-directed currents visible immediately equatorward, though these lie only on the nightside and are weaker in LFM-MIX. The FAC in Gorgon reaches higher maximum magnitudes, about twice that

of LFM-MIX. The Region 1 FAC also appears to be distributed across thinner range in latitudes in Gorgon, with both models showing a difference in minimum/maximum FAC. Conversely, the Gorgon CPCP (72 kV) is actually less than that of LFM-MIX (95 kV), likely due to the more localised FAC profile and the zeroing of the potential at a more poleward LLB. Gorgon also shows a larger dawn-dusk disparity in peak potential, though such differences are typically temporal deviations from an average symmetric state. Most importantly, both models have similar overall morphologies between $0° - 30°$ colatitude which is crucial in determining the global dynamics.

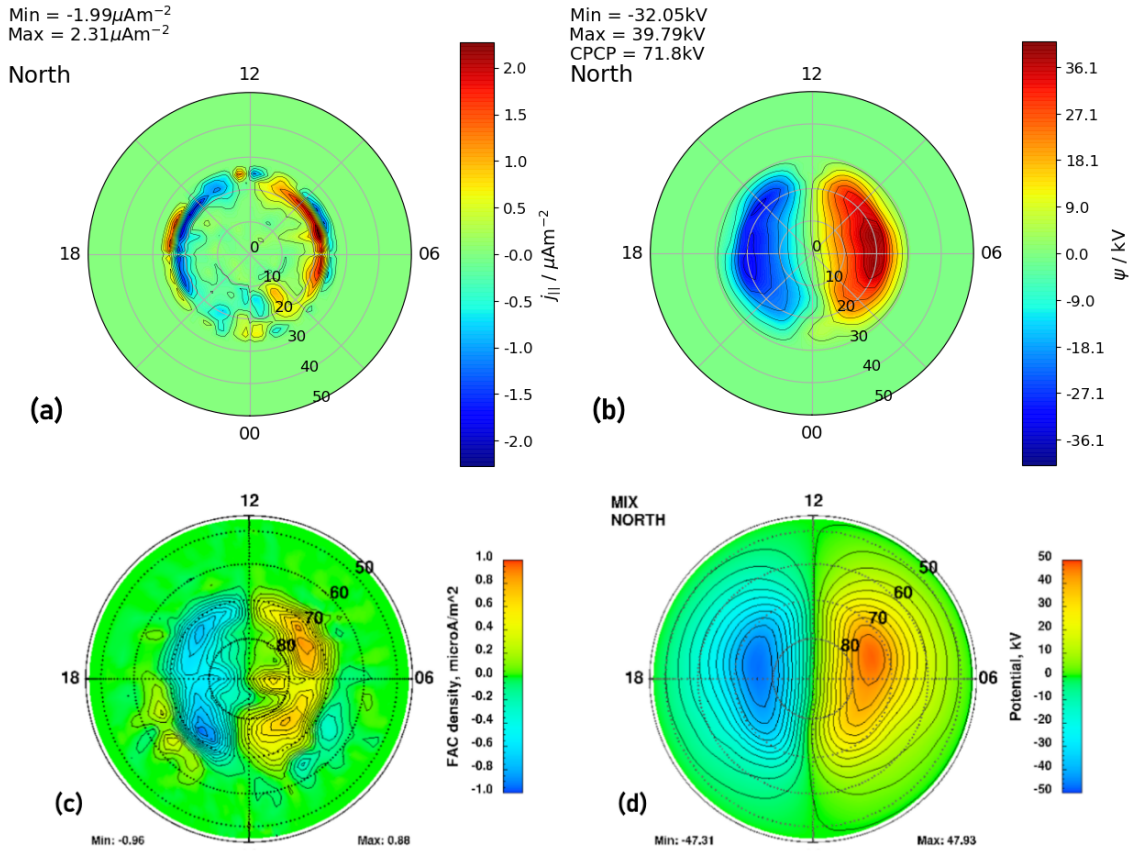

Figure 2.10 – Ionospheric FAC (a,c) and potential (b,d) at the Northern polar cap after 9h of simulation time using (a,b) Gorgon and (c,d) LFM-MIX (Figure 6 of Merkin and Lyon, 2010). The minimum/maximum values are indicated in each plot.

It is worth noting that the CPCP is a much more common benchmarking metric than the maximum intensity of the FAC, which is likely more sensitive to the numerics used by the model. Ridley et al. (2010) demonstrated that decreasing the resolution in the inner magnetosphere tends to reduce the CPCP; LFM employs a deformed spherical grid providing higher resolution at the inner boundary, which in this case was placed at 2 R_E. Hence as well as explaining the lower CPCP, the larger and less diffuse FAC in Gorgon may result from the coarser grid used versus LFM since the FAC is calculated over fewer grid cells; this is then mapped and interpolated at a lower resolution and within a smaller mapping region. Therefore whilst repeating the simulation with a higher resolution and smaller inner boundary in Gorgon would likely yield closer agreement, it is reassuring

that the CPCPs and underlying FAC patterns are similar after 9 hours of varying strong and weak solar wind driving.

To provide a clearer quantitative picture of the ionospheric conditions in Gorgon, as well as any North-South differences, Figure 2.11 shows the relationship between the FAC and the potential plotted as a function of colatitude through a dawn-dusk meridian slice. The location of the LLB is clear to see, with the FAC and potential zeroed everywhere beyond 30° colatitude. Whilst there is a small North-South FAC asymmetry, this is primarily due to the slice passing through different current peaks, and the much smoother potential profile shows very little asymmetry. Whilst one should be careful not to ascribe too much meaning to a single cut through the ionosphere at a single point in time, we do note the better agreement versus the LFM-MIX FAC magnitudes in Figure 2.10 when sampling away from the Gorgon FAC extrema.

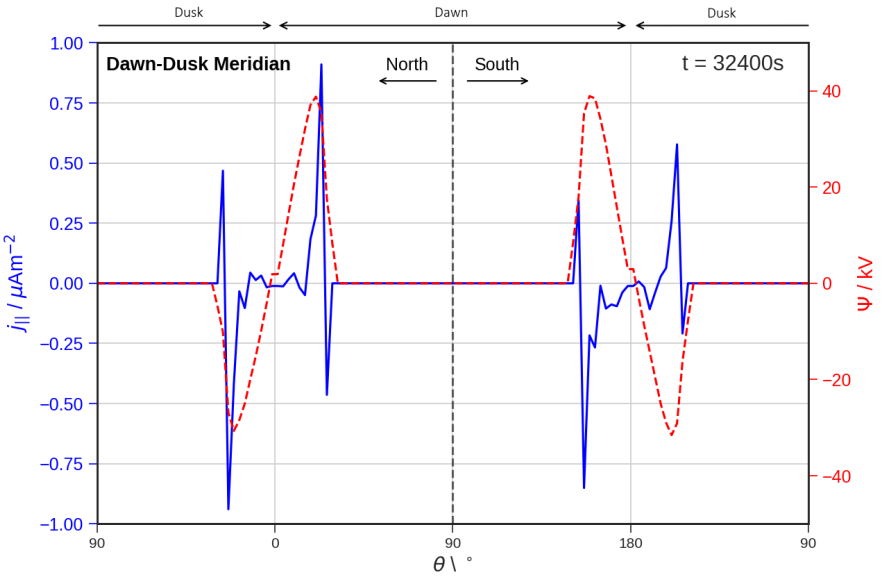

Figure 2.11 – A slice through the dawn-dusk meridian showing the FAC (blue) and potential (red) across the whole ionosphere.

Now that we have verified that the ionospheric conditions agree with expectations, we must test the behaviour at the MHD inner boundary to ensure the ionosphere is influencing the magnetosphere as desired. Figure 2.12 shows the x-component of the inner boundary flow, comparing the solution calculated on a spherical shell as in Figure 2.8 and the actual MHD values sampled on the Gorgon cartesian grid. There is good general agreement between the flow patterns and range of values for v_x, suggesting the mapping procedure and calculation of $\mathbf{v}$ is performing well on the cartesian grid. The flow is similar to the idealised solutions shown in Figure 2.8, with anti-sunward flow over the polar cap and return flow at lower-latitudes, weakest at the equator at noon. Note the solution in Figure 2.12b is not as smooth as the ideal cases, but this is to be expected given that the potential in Figure 2.10b is not perfectly smooth either, and due to the limitations of interpolating between a cartesian and spherical grid.

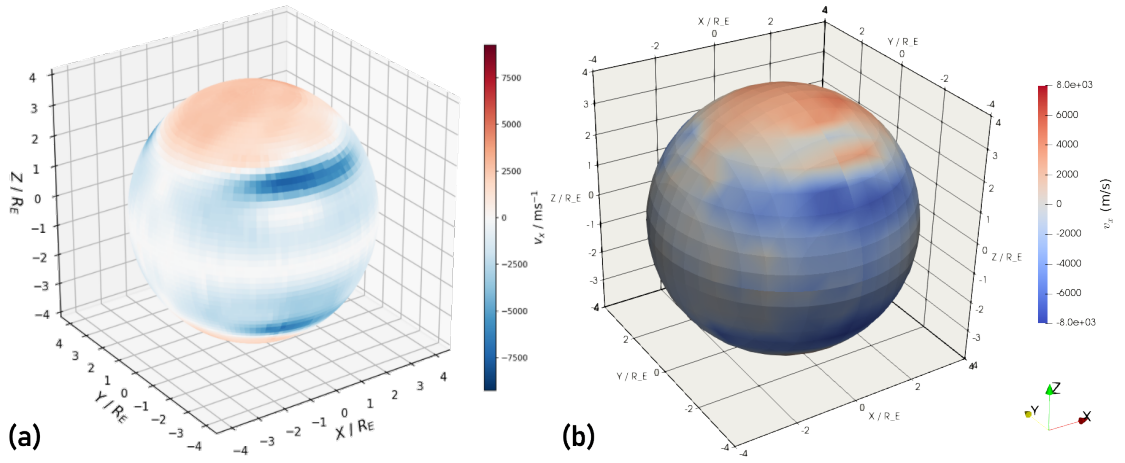

Figure 2.12 – Flow in the x-direction at the inner boundary at the end of the simulation, where (a) is the solution computed on a smooth spherical surface and (b) is the actual flow in the MHD domain interpolated onto a sphere.

The overall behaviour is consistent with Dungey cycle dynamics under strong southward IMF driving, and shows that the MHD simulation is properly capturing magnetosphere-ionosphere coupling and is able to model the response of the terrestrial ionosphere to a given set of solar wind conditions. This opens the possibility for a much broader range of studies using the code than previously possible, such as seasonal and diurnal variations in the M-I system, and the response to severe space weather events using both synthetic and real solar wind input.

Chapter 3

Dipole Tilt Effect on the Magnetosphere-Ionosphere System

The work presented in this chapter has been published in a peer-reviewed journal article:
Eggington, J. W. B., Eastwood, J. P., Mejnertsen, L., Desai, R. T., & Chittenden, J. P. (2020). Dipole tilt effect on magnetopause reconnection and the steady-state magnetosphere-ionosphere system: Global MHD simulations. *Journal of Geophysical Research: Space Physics*, 125, e2019JA027510. https://doi.org/10.1029/2019JA027510

3.1 Introduction

The evolving solar wind is the key source of short timescale variation in the magnetosphere, due to changes in coupling at the magnetopause. Whilst this is important over minutes to hours, longer timescale variability arises not only from the solar wind but also from internal dynamics. The orientation of the Earth's rotation axis to the Sun-Earth line, i.e. the X-axis of the Geocentric Solar Ecliptic (GSE) coordinate system, varies between seasons due to the obliquity of the planet and the eccentricity/inclination of its orbit with an amplitude of $\sim 23.5^\circ$. The resulting changes in solar zenith angle across the ionosphere cause a diurnal and season dependence of conductance, as discussed in the previous chapter, which will affect ionospheric conditions and magnetospheric dynamics.

In addition, the Earth's geomagnetic dipole axis is offset from its rotation axis by $\sim 10^\circ$, and hence the combined diurnal and seasonal variation of the dipole orientation is even greater with an amplitude of $\sim 34^\circ$. This is typically defined within the Geocentric Solar Magnetic (GSM) coordinate system, which shares its X-axis with the GSE system but is rotated from GSE such that the dipole axis is contained within the X-Z plane. The 'dipole tilt angle' μ is then defined as the angle between the dipole axis and the Z-axis of the GSM system, and its variation over a single year is demonstrated in Figure 3.1. The diurnal amplitude of $\sim 10^\circ$ is fairly constant, being slightly larger around solstice, where the seasonal variation reaches its peak. Hence at solstice the tilt angle ranges from $\sim 14^\circ - 34^\circ$, and at equinox is between $\pm 10^\circ$.

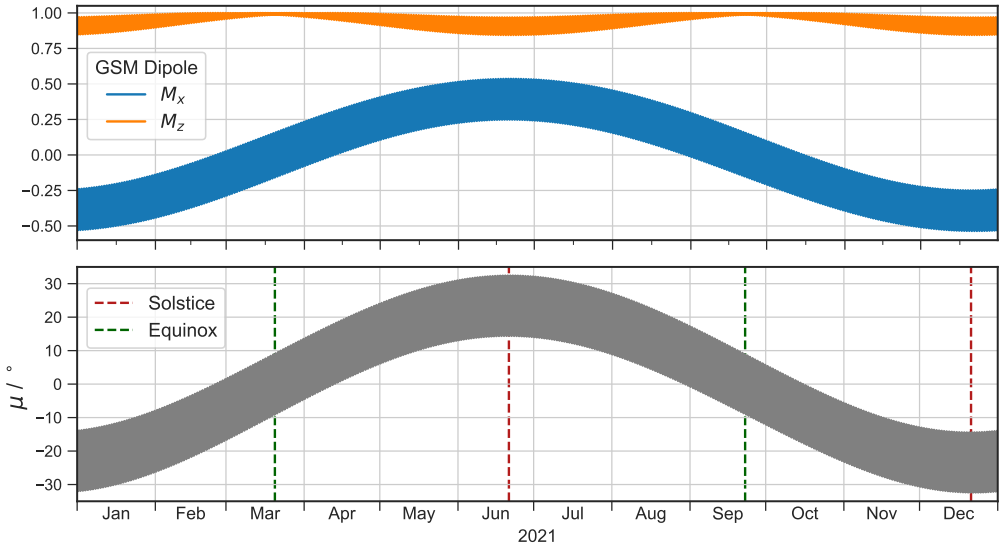

Figure 3.1 – Variation in the geomagnetic dipole orientation over one year (2021) showing the change in (top) the $x-$ and $y-$ components of the unit dipole axis **M** in GSM coordinates, and (bottom) the dipole tilt angle μ. Equinox and solstice are indicated, when the tilt angle is at its minimum and maximum, respectively. The width of the signals represents the diurnal variation.

3.1.1 Seasonal Variation in Dayside Coupling

The effect on the magnetosphere of a varying dipole tilt angle is significant, and naturally influences the coupling with the solar wind since the rate and location of reconnection on the magnetopause is determined by the relative orientation of the IMF and the magnetospheric field. As explained in section 1.3.4, magnetopause reconnection occurs predominantly along the magnetic separator: a continuous line along which differing magnetic topologies meet and which is terminated by magnetic null points (where $|\mathbf{B}| = 0$) (Dunlop et al., 2011a). The reconnection rate at some point along this line is closely determined by the angle between the field either side the magnetopause, i.e. the magnetic shear angle, and is maximised for the given local plasma conditions where the shear angle is 180°. However, since regions of antiparallel field typically exist only locally on the magnetopause, the location and extent of the reconnection line is a complex issue.

One description which attempts to predict the X-line location on the magnetopause is antiparallel reconnection, in which reconnection occurs where the shear angle is largest (Crooker, 1979). This angle depends on the relative orientation of the IMF and the planetary dipole axis, and therefore is sensitive to the dipole tilt angle. For purely southward IMF and a small tilt angle, antiparallel reconnection should occur anywhere along a line across the magnetic equator, and for purely northward IMF at high latitudes in the noon-midnight plane. Introducing an arbitrary and non-zero IMF B_y component splits the reconnection line at noon, with antiparallel regions in each of the dawn and dusk hemispheres.

However, in general magnetic reconnection does not require anti-parallel fields (e.g.

reviews by Hesse et al., 2011, Paschmann et al., 2013, Eastwood et al., 2013, Cassak and Fuselier, 2016), leading to the concept of guide-field, or component reconnection, where the out-of-plane magnetic field is non-zero at the X-line (Sonnerup, 1974, Gonzalez and Mozer, 1974). This permits an extended continuous X-line across the dayside magnetopause for non-southward IMF, which has been observed using multi-spacecraft observations (e.g. Dunlop et al., 2011b).

Various models have been developed to predict the orientation and location of the X-line as a function of upstream conditions, in particular the magnetic field orientation in the magnetosheath (e.g. discussion by Komar et al., 2015), which have also been tested against observations (Walsh et al., 2017, Souza et al., 2017). Furthermore, spacecraft data has shown that (except in cases where the IMF B_x is large) the reconnection line is continuous during southward IMF and generally follows the ridge of maximum magnetic shear, but does not necessarily cross the subsolar point (Trattner et al., 2007). This complication in the component description arises due to seasonal variations in the mean dipole tilt angle, since the region of maximum shear shifts southward during Northern summer and northward during Northern winter. The maximum magnetic shear model has also been applied to observations from the THEMIS mission (Trattner et al., 2012), showing this same seasonal dependence, and a similar effect was found by combining THEMIS and Cluster data (Zhu et al., 2015).

Global MHD simulations have been used to explore the effect of dipole tilt angle on reconnection in more detail. The location of the separator has previously been shown for tilt angles between -20° and +20°, showing the X-line as continuous and shifting with tilt angle in the same fashion as described above (Hoilijoki et al., 2014). The inclusion of an IMF B_x component also contributes to this shift, as demonstrated in previous simulations (Peng et al., 2010). However, a recent survey of THEMIS data revealed that the seasonal (tilt angle) control of the X-line location tends to dominate that of B_x (Hoshi et al., 2018). This seasonality may contribute to semi-annual variations in geomagnetic activity (Russell and McPherron, 1973). Indeed, MHD simulations have shown that for increasing tilt angle and during southward IMF, the region of antiparallel magnetic field decreases in size (Russell et al., 2003) and changes location (Komar et al., 2015). Whilst this may reduce the global rate of reconnection on the magnetopause, i.e. the dayside coupling rate Φ_D, no such dependence has yet been quantified in simulations for the full range of tilt angles.

Additionally, this presumes that the reconnection location corresponds closely to these antiparallel regions, whilst in fact the full 3-D geometry and length of the X-line will depend on more than just the location and size of the antiparallel regions but also the local plasma conditions and particular shape of the magnetopause for some given configuration. MHD simulations have shown that the magnetopause topology is highly sensitive to dipole tilt angle, with the location of the magnetopause nose (the point of first contact of the solar wind) shifting northward (southward) for a positive (negative)

tilt angle, thus affecting the location of first contact with the solar wind and the predictions of component reconnection (Liu et al., 2012, Lu et al., 2013). Furthermore, observations have shown that the tilt introduces asymmetries in the bow shock (Jelínek et al., 2008, Lu et al., 2019a). Extending such a study beyond the terrestrial parameter range may reveal even more complex behaviour.

3.1.2 Seasonal Ionospheric Asymmetries

In addition to altering the rate of open flux production, the tilt angle may introduce asymmetries in magnetospheric convection which would affect the global dynamics. Park et al. (2006) showed that during southward IMF and for a static dipole with a 30° tilt angle, the dayside reconnection location (inferred by antiparallel regions) shifts to roughly follow the magnetic equator, whilst the nightside reconnection location follows the shift of the magnetotail current sheet. The latter is hinged by the magnetotail geometry towards the ecliptic plane, such that convection in the Northern hemisphere is forced to follow a longer pathway than in the South. Similar hinging effects have been found in spacecraft data, showing a clear seasonal dependence (Xiao et al., 2016). Any such dynamical changes in the magnetosphere will also manifest in the ionospheric convection: Park et al. (2006) suggested that a North-South asymmetry in CPCP develops since the convection electric field is stronger on average in the Northern hemisphere. Similar asymmetries were also seen in simulations using duskward IMF with a non-zero dipole tilt angle (Park et al., 2010).

Ridley et al. (2004) investigated the control of conductance in models on the magnetosphere under southward IMF, showing that at solstice during Northern summer the Northern field-aligned currents are significantly stronger than at the South. This has similarly been shown in simulations of the IMF switching from Northward to southward (Lu et al., 2019b), which also found differences in the Northern and Southern polar cap sizes due to the dipole tilt angle having an asymmetric impact on the cusp in each hemisphere. However, the inclusion of non-uniform conductance (accounting for enhanced solar EUV ionisation in the sunlit hemisphere) has been shown to be largely responsible for disparities in Northern and Southern FAC in simulations (Ridley, 2007). Simulations of the role of conductance during real events on both the CPCP and reconnection rate, inferred separately in each hemisphere, found hemispheric asymmetries in both parameters as well as differences between the CPCP and Φ_D, which was attributed to viscous interaction with the solar wind and/or saturation of the potential whereby it reaches a maximum sustainable value (Jensen et al., 2017). Simulating instead with a uniform conductance - and for the full range of tilt angles - would isolate the contribution of any asymmetries that arise purely due to changes in the location of reconnection.

Observations have noted clear North-South asymmetries in CPCP, attributed to asymmetric convection due to dipole tilt, though some studies have found larger values in both summer (e.g. Pettigrew et al., 2010) and winter (e.g. Zhang et al., 2007). Differences in observed FAC are more consistent, with data showing that the maximum summer FAC can be roughly twice the maximum winter FAC (Papitashvili et al., 2002, Wang et

al., 2005). Recent AMPERE data even shows stronger average Region 1 FACs driven in the Northern ionosphere independent of season (Coxon et al., 2016). Any such asymmetries are of consequence for the potential impact of a severe space weather event, since the onset time will closely determine which locations on the Earth experience the strongest ground perturbations.

As already noted, $\sim 10^\circ$ of the amplitude of the dipole tilt angle variation arises from the offset of the geomagnetic dipole to the rotation axis. Cnossen and Richmond (2012) explored the impact that more extreme offsets might have on ionospheric conditions, showing variations over 24h periods for tilt angles up to 60° at both solstice and equinox. Whilst at equinox a trend of decreasing daily-average CPCP was seen for increasing tilt angle in both hemispheres, such a clear trend was not seen at solstice. Later simulations using the true offset showed that changes in solar wind coupling can account for up to 90% of CPCP variation, and conductance effects as little as 10% (Cnossen et al., 2012b). However, daily averaging will smear-out much of the magnetospheric response to dipole orientation, making it difficult to distinguish between driving factors.

3.1.3 Motivation and Outline

Overall it is clear that the dipole tilt introduces significant asymmetries in the magnetosphere-ionosphere system, but the exact tilt angle-dependence is not fully understood. By eliminating various factors like dipole rotation and non-uniform conductance, and focusing on static, steady-state configurations, we can demonstrate with more clarity the fundamental impact of a varying tilt angle arising solely from changes in magnetopause reconnection and magnetospheric convection. In fact, whilst the Earth's tilt angle variation is limited to a range of $\pm 34^\circ$ at present, this has not always been the case. The internal magnetic field is known to vary significantly over geological timescales, often undergoing full reversals every few hundred-thousand years (Gubbins, 2008). Additionally, between these dramatic reconfigurations there are periods of temporary migration known as 'geomagnetic excursions'. Noticeable tilt angle variations can occur even on decadal timescales, with a total change of $\sim 1^\circ$ over the last half a century (Korte and Mandea, 2008, Amit and Olson, 2008). This is demonstrated in Figure 3.2, which shows 500 years of geomagnetic pole motion; the North magnetic pole (where the field points into the Earth) has been accelerating dramatically over the last 30 years (Livermore et al., 2020). Hence, more severe dipole tilt configurations could one day represent a realistic scenario for a severe space weather event.

Highly-inclined dipoles are also a feature of interest outside of the terrestrial context. In particular, the dipole axes of Uranus and Neptune are offset by large angles to their rotation axes (by 60° and 47° respectively, Russell and Dougherty, 2010). Coupled with their severe obliquity to the ecliptic plane, these magnetospheres undergo significant reconfiguration both diurnally and seasonally as shown in both observations (e.g. Cowley, 2013) and simulations (e.g. Mejnertsen et al., 2016, Cao and Paty, 2017). More exotically, cases of tidally-locked exoplanets and direct evidence of exoplanet magnetic fields suggest the possibility of magnetospheres which, as well as being highly inclined to the

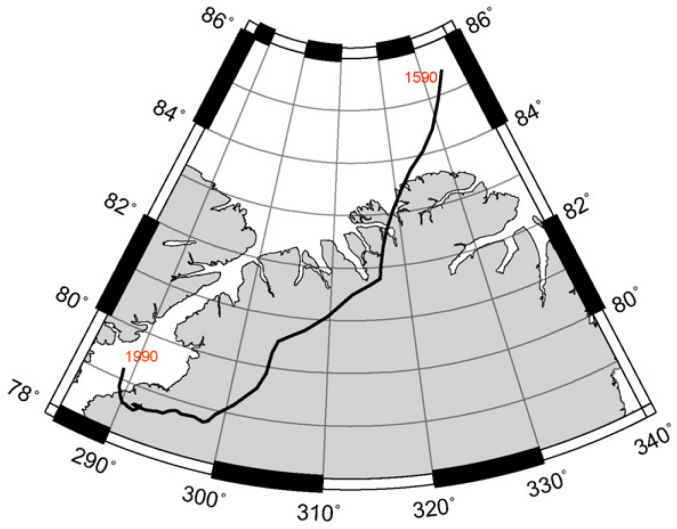

Figure 3.2 – Migration of the North geomagnetic pole over the last 500 years calculated using the CALS7K archaemagnetic field model. Since the geomagnetic dipole axis passes through the centre of the planet, the migration path of the South pole is a mirror-image of the North (from Amit and Olson, 2008).

stellar wind, are locked-in to this extreme tilted configuration - though such a slow rotation rate might not support a strong planetary dynamo (Grießmeier et al., 2004). Thus, understanding the behaviour of the magnetosphere-ionosphere system for larger tilt angles is important not only for revealing the key parameter dependencies of the terrestrial space environment, but also in exploring the various cases which may indeed exist in nature.

In this study we investigate differences in the steady-state magnetosphere-ionosphere system for the full range of dipole tilt angles from 0° to 90°, in each case tilting the Northern hemisphere to face sunward and keeping the dipole static. Changes in the location and intensity of dayside magnetopause reconnection are investigated in each case, to reveal the key determining factors in the case of southward IMF. We thus explore how changes in coupling with the solar wind affect magnetospheric dynamics, and the asymmetries that develop in the convection due to the tilt angle effects in more detail than has been shown before. Finally, these results are used to explain the various impacts on ionospheric conditions, revealing the key role of tilt angle on modulating the location, strength and morphology of the Region 1 current system, and thus the importance of this parameter in determining potential impacts as a function of onset time for a given severe space weather event.

3.2 Methodology

3.2.1 Simulation Set-up

The simulation domain is the same as in section 2.4: we employ a domain of dimensions X = (-30, 90) R_E, Y = (-40, 40) R_E, Z = (-40, 40) R_E and a grid of resolution 0.5 R_E. Note this

coordinate system essentially corresponds to GSM but is positive in the anti-sunward direction, i.e. $(X, Y, Z) = (-X_{GSM}, -Y_{GSM}, Z_{GSM})$. For consistency with previous studies, we therefore define the tilt angle as $\mu = \tan^{-1}(-M_x/M_z)$ such that it is positive in the sunward direction. The same inner boundary conditions are applied as in section 2.4, set at a radius of 4 R_E. The ionospheric potential is zeroed at the lower-latitude boundary at 30° colatitude (in the frame of the tilted ionosphere).

In each of our runs, we initialise the magnetosphere with 4h of purely southward IMF ($B_z = -2$ nT) driving using a synthetic, steady solar wind of velocity $v_x = 400$ kms^{-1}, number density $n = 5\,\text{cm}^{-3}$ and ion/electron temperature $T_{i,e} = 5$ eV. This gives time for the magnetosphere to enter a quasi-steady state to minimise any time-dependence in the results. The same simulation is performed for a series of dipole tilt angles from $0° - 90°$ in steps of 10°, whereby a positive dipole tilt angle denotes the Northern magnetic pole (i.e. at positive Z in GSM coordinates) pointing towards the Sun.

We take the approach of using a uniform Pedersen conductance of 10 mho, and zero Hall conductance, meaning we do not include the effects of EUV ionization and auroral precipitation. In reality these will be altered by the dipole tilt angle due to changes in the solar zenith angle and would create further asymmetries in the system. Furthermore, it has been shown that changes in ionospheric conductance can impart changes in the reconnection rate in models by affecting the magnetopause geometry (Merkin et al., 2003). However, coupled with the already complex geometric effects of dipole tilt, the exact effect of a changing conductance profile on the global dynamics is hard to diagnose separately, and is outside the scope of this study.

3.2.2 Numerical Resistivity

Whilst reconnection strictly should not occur in collisionless MHD (as an electrical resistivity is required to allow diffusion of the magnetic field), one consequence of solving the MHD equations on a discrete grid is that the field will numerically diffuse to an extent that is determined by the coarseness of the grid and the numerics of the code. Reconnection in simulations will therefore occur numerically wherever there is a sufficiently strong current layer, its rate dependent on the grid resolution chosen. In the specific case of Gorgon, $\mathbf{A}$ is updated using the electric field $\mathbf{E}$, which is calculated as $\mathbf{E} = -\mathbf{v} \times \mathbf{B}$. To do this, $\mathbf{v}$ is interpolated from a cell-centred position to a face-centred one, introducing some error, along with that associated with the van Leer advection scheme. The use of a uniform grid resolution in this study ensures no a priori assumption is required about where numerical reconnection is likely to occur on the magnetopause, since the grid effects will be consistent across all tilt angles.

One way to more closely control reconnection in simulations is by artificially setting either an explicit (uniform) or anomalous (current-dependent) resistivity, independent of the numerics. Various other studies exploring dayside reconnection in MHD simulations have employed such resistivity models throughout the entire simulation domain, with values often orders of magnitude greater than the actual resistivity in the magnetosphere. This acts to smooth the magnetopause current sheet, making it more stable

to reconnection and reducing the occurrence of flux transfer events (FTEs), such that reconnection occurs steadily along a single X-line. Raeder (2006) showed that for a tilted dipole, FTEs are more likely to occur in simulations due to flux piling-up at the dayside magnetopause, provided the grid resolution is sufficiently high (or else strong numerical diffusion prevents sufficient flux pile-up). However, Dorelli and Bhattacharjee (2009) showed that FTE generation can still occur with zero tilt angle, suggesting FTE generation may be more closely related to movement of the flow stagnation point away from the magnetic separator. Glocer et al. (2016) traced magnetic separators in simulations for cases of small and large uniform resistivity, showing splitting of the separator into multiple X-lines due to FTE occurrence where the resistivity was small.

Whilst our resolution of 0.5 R_E results in a relatively coarse magnetopause, it ensures that (at least for the smaller tilt angle cases) FTEs are less likely to develop. This is beneficial since it becomes more straightforward to quantify the reconnection rate where there is a single well-defined X-line. Setting a large explicit or anomalous resistivity (e.g. Uzdensky, 2003) would also aid in this. However, in our runs reconnection is essentially entirely driven by numerical diffusion, with the resistivity several orders of magnitude below those required to compete with numerical effects.

3.3 Magnetospheric Dynamics

To explore how the dipole tilt angle affects the field topology in the magnetosphere, we focus on the example cases of 0°, 30° and 90°. We have chosen these as they represent the symmetric (untilted) case, the realistic extreme case at present (i.e. the approximate tilt angle at Northern summer solstice), and the limit of the parameter space. Figure 3.3 shows plots of the current density and open magnetic field lines in the magnetosphere in the X-Z plane for each of these tilt angles, shown after 4h of simulation. The field lines have their seed points at the edges of the plotting domain, and so their density does not necessarily represent the local magnetic field strength. The location of the magnetopause is shown, defined as the boundary at which there is minimum solar wind entry into the magnetosphere, similar to the method of Palmroth et al. (2003). We launch a large number of flow streamlines (∼40,000) from the sunward edge of the simulation box, and identify the boundary about which they are diverted by finding voids (minima) in the streamline density (Mejnertsen, 2018). These voids are binned onto a parabolic grid, as this effectively captures the spherical dayside and cylindrical nightside geometries. The approximate dayside and nightside reconnection sites are indicated, located by inspection.

For 0° tilt angle, the dayside reconnection site, nightside reconnection site and magnetotail current sheet all lie in the equatorial plane. For 30°, the dayside reconnection site is found to have moved southward, roughly aligned to the magnetic equator on the magnetopause. Notably, the magnetotail current sheet does not lie in the same plane as this point, and is hinged downwards due to the magnetotail geometry being dominated

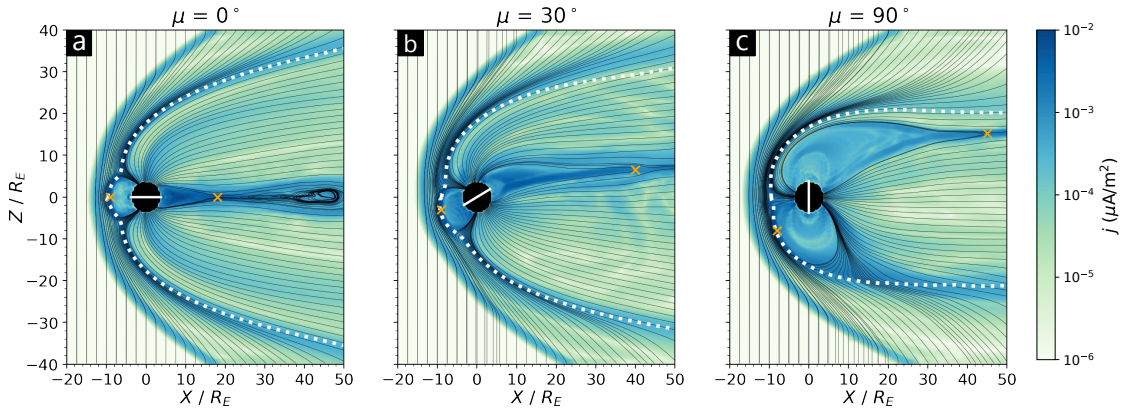

Figure 3.3 – The current density j and open magnetic field lines (in black) in the noon-midnight plane for 0°, 30° and 90° dipole tilt angles, shown after 4h of simulation. The solid white line denotes the magnetic equator, the dotted white line represents the magnetopause, and the orange crosses mark the approximate location of the reconnection site.

by the solar wind pressure at large downstream distances, as found in other simulations (Park et al., 2006). This appears to offset the tail reconnection site, with the closed field lines tilted away from the magnetic equator, the implication being that field lines opened in the Northern hemisphere must cover a longer convection path before again reconnecting on the nightside. In a steady configuration where Northern and Southern magnetic field lines open and close at equal rates (and each hemisphere contains equal amounts of open flux), the result will be a stronger convection electric field on average in the Northern hemisphere than the Southern.

In the more extreme 90° case, the dayside reconnection region has moved yet further southward on the magnetopause, and the same hinging effect is present at the tail reconnection site, with the current sheet slightly northward of the 30° configuration. However, the dayside reconnection site is no longer located close to the magnetic equator, but lies roughly half-way down from the subsolar magnetopause. Extending the tilt angle range to more extreme values has thus revealed a more complex dependence than is initially apparent. Notably, for 0° we see a plasmoid being ejected downtail from the near-Earth neutral line, suggesting that (numerical) reconnection in the magnetotail is time-dependent. As a result the magnetosphere can only be quasi-steady, to an extent determined by the variability in dayside and nightside reconnection.

Another key effect is in the changing size and shape of the magnetopause and bow shock, with the tail magnetopause shrinking in its Z-dimension and the subsolar bow shock moving upstream with increasing tilt angle. The magnetopause nose is shifted southward for 30°; at 90° the nose has returned to the subsolar point, and the dayside magnetopause appears flatter and larger overall than for 0°. This is a result of the dipole field strength being greatest at the magnetic pole, which for 90° directly faces the solar wind. This pole-on configuration has further consequences for the newly-reconnected dayside magnetic field, as the reconnection outflow south of the subsolar magnetopause will be largely in the z-direction. For newly opened magnetospheric field lines connected

to the North pole, the resulting convection will be mostly perpendicular to the magnetic field in the subsolar region, generating a strong electric field here. If the electric field is stronger on the dayside than the nightside, this may influence the Region 1 field-aligned currents towards noon on the ionosphere, since footpoints here connect to regions in the magnetosphere with stronger flow shear (see section 3.5).

This effect is demonstrated in Figure 3.4, which shows the electric field interpolated onto a large number of field lines traced from conjugate North/South seed points on the inner boundary, including only those which exit the simulation domain. As well as highlighting the 3-D topology, the large density of field lines yields regions of darker shading which indicate more clearly where the electric field has a greater magnitude. As suggested, it is slightly larger on average in the Northern hemisphere for 30°, particularly close to the Earth and in the distant tail. This is more pronounced for 90° where the Northern field lines close to the Earth map directly into the magnetosheath, whilst the conjugate Southern field lines show a much weaker electric field, mapping directly into the magnetotail. Note that in the extreme 90° case the 'Northern' hemisphere refers to regions connected to the pole which faces the Sun and which was initially aligned with the positive Z-axis.

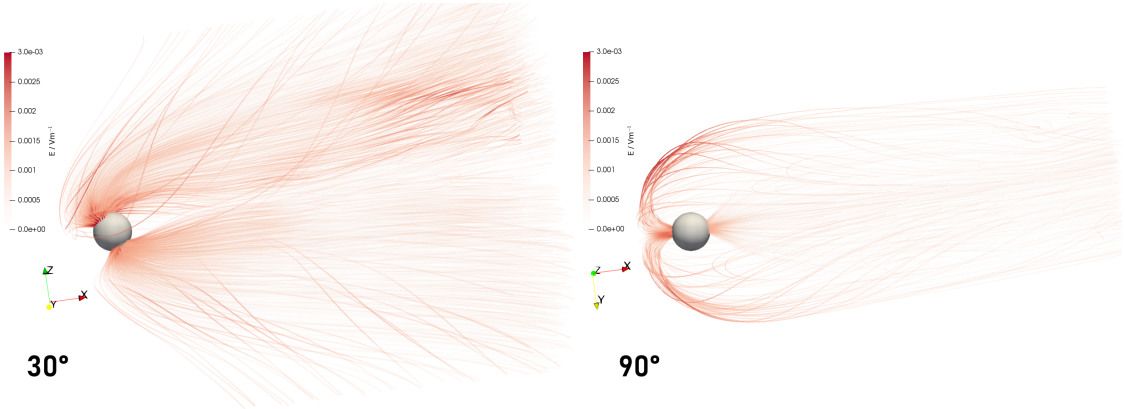

Figure 3.4 – The magnitude of the electric field on conjugate North/South open magnetic field lines for 30° and 90° dipole tilt angles.

The closed field regions grow in size on both the dayside and nightside as the tilt angle increases, due to a reduction in open flux content in the magnetosphere, as shown in Figure 3.5. The consequences should thus be reduced geomagnetic activity and smaller ionospheric polar caps, supporting the notion that these are seasonally modulated due to changing tilt angle. The reduced open flux content suggests an associated drop in the reconnection voltage, despite the upstream solar wind conditions being identical in each case. To understand this in more detail, we now look more closely at the nature of dayside reconnection and how the rate of flux transfer varies with tilt angle.

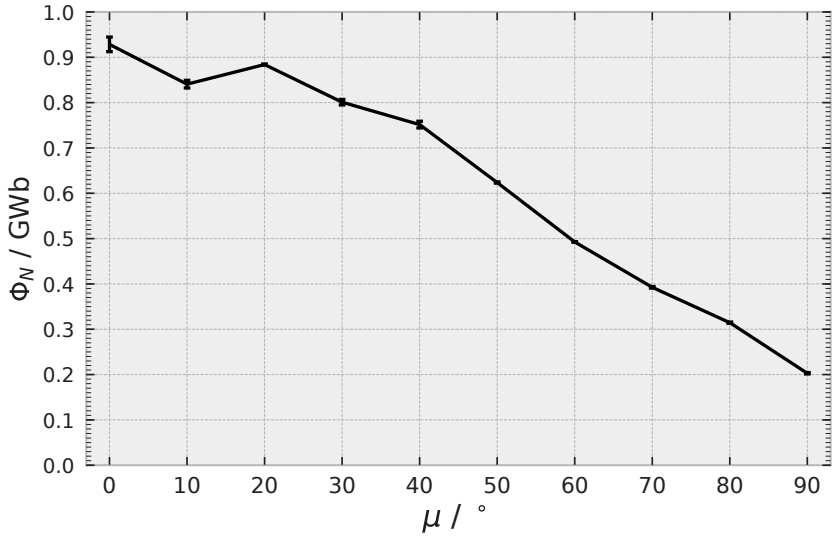

Figure 3.5 – Northern open flux content in the magnetosphere for each dipole tilt angle, averaged over the final 30 minutes of simulation. The error bars show the standard deviation during that period, in which the flux was sampled every 5 minutes.

3.4 Magnetopause Reconnection

3.4.1 Dayside Topology and FTE Generation

The motion of the reconnection site for a varying tilt angle arises due to changes in the magnetic topology at the dayside magnetopause, since the X-line is located at the intersection of magnetic domains. These domains can be identified in the simulation by tracing field lines in both directions from various points in the magnetosphere. Where the field lines terminate defines the magnetic connectivity of these points, i.e. 'solar wind', 'closed', 'North-open' or 'South-open'. In the solar wind case, both ends exit the simulation box; in the closed case, both ends terminate at the dipole source; in the North/South-open cases, one end exits the box and the other terminates at the North/South pole of the Earth. The field line may fail to terminate; this either indicates a magnetic island, or can occur spuriously due to interpolation errors. Structures of this connectivity (rather than isolated points) imply time-dependent, patchy reconnection consistent with FTE generation, and thus we label this domain as 'FTE'. Such structures have been investigated in Gorgon before, revealing complex interwoven flux ropes spanning the magnetopause (Mejnertsen, 2018), though we do not explore their topology in detail here. Figure 3.6 shows magnetic connectivity and flow streamlines around the dayside magnetopause in the noon-midnight meridian plane for each tilt angle at a single point in time, with each domain coloured according to the key.

At 0° we see evidence of an FTE being formed around the subsolar region. The steady X-line is diverted into two separate X-lines at $\pm 2\ R_E$, and the flow streamlines terminate within this structure, possibly due to vortical flow inside the FTE. This is consistent with the findings of Dorelli and Bhattacharjee (2009), in that a dipole tilt is not required in the

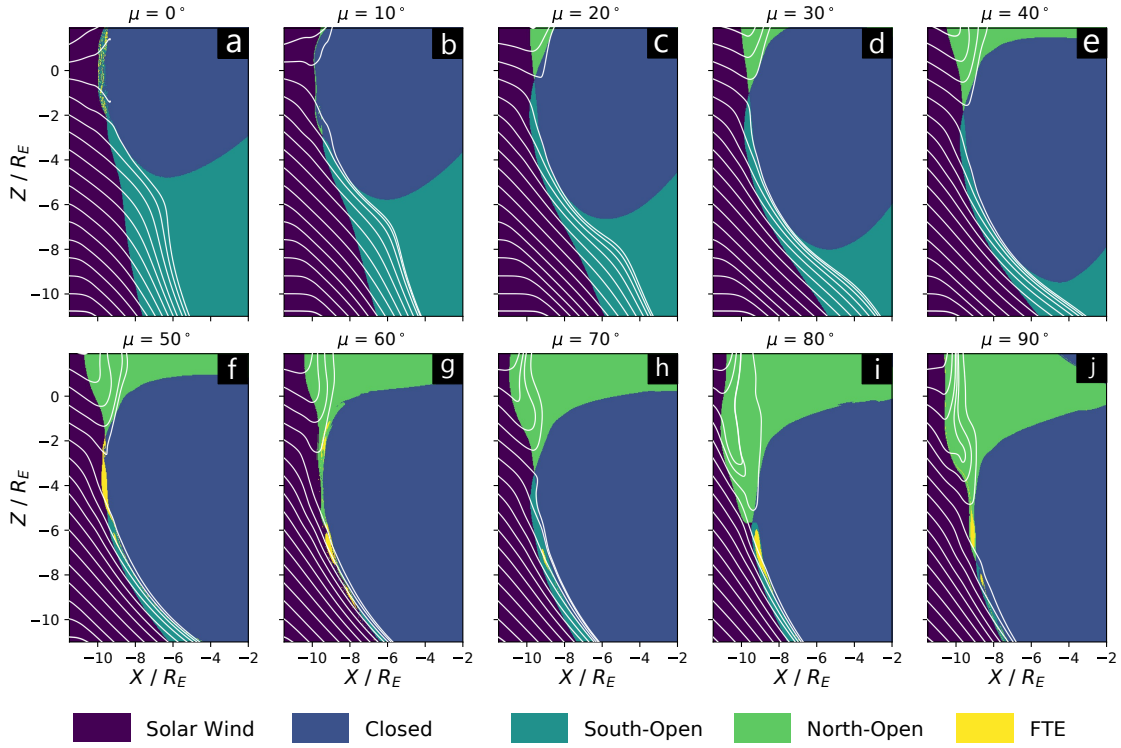

Figure 3.6 – Magnetic topology at the dayside in the noon-midnight meridian plane for successive dipole tilt angles after 13800s of simulation. Shown as white lines are streamlines calculated from the bulk velocity projected onto the X-Z plane.

formation of an FTE even if there is a tilt angle-dependence to their formation rate. In this case however, the FTE may be a result of erosion of the subsolar magnetopause due to strong anti-parallel reconnection, making the current sheet thin and less stable (exacerbated by the coarse grid resolution). Indeed, from 10° to 40° there are no FTEs around the reconnection region at this specific point in time, implying reconnection is generally more steady for the smaller tilt angles. This reflects the fact that the 0° case is unique in that reconnection is completely antiparallel along the equatorial plane, whereas the antisymmetry between the IMF and magnetospheric field breaks down the moment a tilt is introduced.

For tilt angles of 50° and above, there is persistent evidence of FTEs on the magnetopause, though not necessarily located at the separator. This indicates that the steadiness of magnetopause reconnection may depend on the tilt angle, in agreement with Raeder (2006), and that the separator location becomes more time-dependent with increasing tilt angle. For these large tilt angles, the flow streamlines are diverted far from the subsolar region, and can be almost parallel to the magnetopause at the separator location. Whilst the stagnation point (where the streamlines diverge, though the flow may still have some y-component) is coincident with the steady X-line for $20° - 40°$ tilt angles, it appears to be the source region for FTEs at large tilt angles. This is consistent with the FTE generation mechanism of Dorelli and Bhattacharjee (2009), whereby diversion of the magnetosheath flow away from the separator renders the flow unstable.

Thus, from the perspective of this 2-D projection, the tilt angle dependence in FTE occurrence may be due to the independent motions of the flow stagnation point and the steady X-point with an increasing tilt angle. Nonetheless, this view only represents a single snapshot in time, whilst FTEs are an inherently transient phenomenon. Furthermore, our understanding of these structure is limited within this 2-D view, since the global 3-D X-line configuration may be much more complex. To determine the relative stability of the separator and the extent of its deviation for different tilt angles, we must trace-out its location over a long time period and thus examine its full 3-D motion.

3.4.2 Location of the X-Line

Since reconnection predominantly occurs along the magnetic separator - which demarcates different magnetic domains - locating it does not require any a priori assumption about whether reconnection is of antiparallel- or component-type. To trace-out its location in Gorgon, we adopt an approach derived from that of Komar et al. (2013). Magnetic null points (which terminate each end of the separator) are found using the method of Haynes and Parnell (2007), i.e. we search for all grid cells containing reversals in each component of **B** and perform a trilinear interpolation to obtain sub-grid coordinates. For a given IMF clock angle, the terminating nulls at dawn and dusk can be selected by finding those closest to the vacuum superposition solutions (Yeh, 1976), with positions $\mathbf{r}_n = (x_n, y_n, z_n)$ given by:

$$r_n = \left(\frac{M}{2B_{IMF}}\right)^{\frac{1}{3}} \left(\cos\theta_{IMF} + \sqrt{8 + \cos^2\theta_{IMF}}\right)^{\frac{1}{3}}, \tag{3.1}$$

$$y_n = r_n \left(\frac{3 + \sin^2\theta_{IMF} - \cos\theta_{IMF}\sqrt{\cos^2\theta_{IMF} + 8}}{6}\right)^{\frac{1}{2}}, \tag{3.2}$$

$$z_n = r_n \left(\frac{2 + \cos^2\theta_{IMF} + \cos\theta_{IMF}\sqrt{\cos^2\theta_{IMF} + 8}}{6}\right)^{\frac{1}{2}}, \tag{3.3}$$

where M is the Earth's magnetic dipole moment (8×10^{22} Am^{-2}), θ_{IMF} is the IMF clock angle, and $x_n = 0$ in the terminator plane. The use of this method is demonstrated in Figure 3.7, alongside an alternative but less efficient approach used later in Chapter 4 for cases where the null point is not easily identified.

The vacuum solution becomes non-trivial in the case of a dipole tilt or non-zero B_x, since the dipole axis and IMF cannot be treated as coplanar. Since we are driving with due southward IMF, there are an infinite number of nulls in the equatorial plane for the 0° tilt angle case; for small tilt angles the null locations remain close to those in the 0° case. For larger tilt angles ($\gtrsim 30°$) the number of dayside nulls decreases dramatically and regular FTE generation leads to splitting of the separator into multiple X-lines. This forms additional nulls around noon; as a general solution for all tilt angles, we thus select the dayside nulls closest to dawn and dusk, and trace from these. If the nulls in

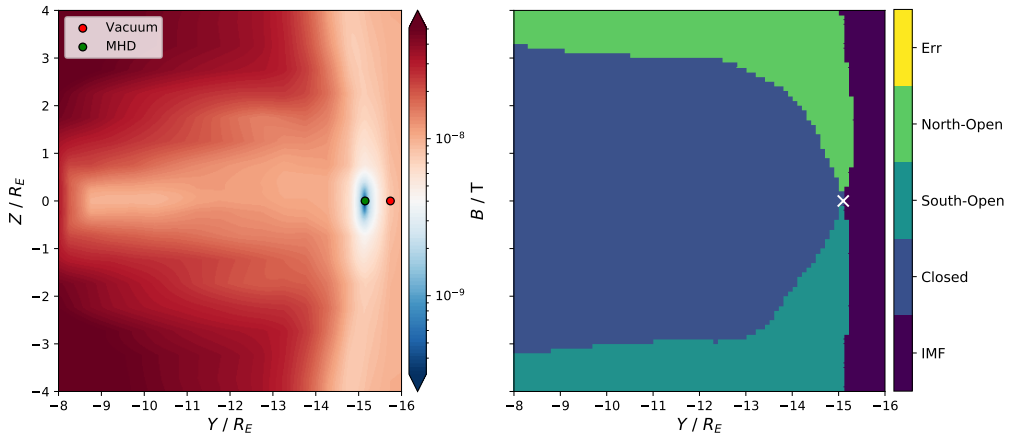

Figure 3.7 – Two methods used throughout this thesis to locate the intersection of the separator with the terminator plane. Shown (left) is the technique whereby the MHD null lying closest to the vacuum superposition solution is identified, and (right) an approach in which the magnetic connectivity is sampled close to the vacuum null. The view is from the Sun towards the Earth and for the 0° tilt angle case.

question do not lie along the terminator plane, we trace in both directions to terminate the separator where $X = 0$, so that the entire dayside magnetopause is covered and the length of the separator is independent of the choice of nulls. Where there are multiple X-lines formed, we simply allow the trace to follow only the one which is the least diverted from the steady X-line. Whilst tracing all of them is possible, these are only transient features and do not represent the average location of the separator, and are not always well resolved with a coarse grid at the magnetopause.

To locate the separator about a chosen null point, we draw a hemispheric grid (oriented sunward) and trace magnetic field lines in both directions from each grid point to determine the magnetic connectivity. These hemispheres are of arbitrary size and resolution; for most of our traces we have used radii of 1 R_E and 50×50 grids. From these connectivities we construct a map of the magnetic domains about the vicinity of the null. We then employ image processing algorithms using the Python SciKit package (Walt et al., 2014) to identify where the four domains converge, which defines the location of the separator on this grid. Using edge detection the boundaries of the connectivity structures (e.g. the closed region) are identified and uniquely labelled by which domains lie on either side. We sample through the grid and count how many such edges lie within a given region; the sample area that contains all four edges of the half-open domains is determined to contain the separator. We then draw a line straddling this sample area, and interpolate along it to find the exact location of the convergence point. A new hemisphere is then drawn around this point, and the process repeated until the opposite null point is reached (see Figure 3.8).

We perform our trace in 5 minute intervals for the final 30 minutes of the simulation and calculate the average separator location over this period, which should smooth-out transient changes in its configuration. To reliably find the time-averaged separators for a given dipole tilt angle, the separator arrays need to be of a common length and share

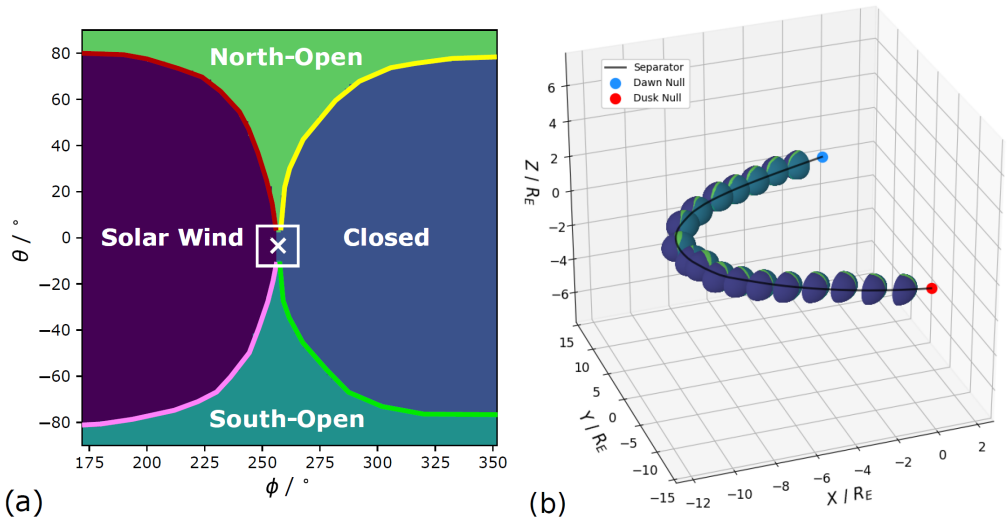

Figure 3.8 – A schematic showing the advancement of the separator tracing algorithm. A hemispheric grid is initially constructed around a chosen magnetic null point, on which magnetic connectivity (a) is determined. The convergence point of the magnetic domains is then set as the next point along the separator using edge detection methods, on which a new connectivity map is constructed. This is repeated until a second, terminating magnetic null point is reached (b).

the same values in at least one dimension. Since the separators are always oriented in a dawn-dusk sense for southward IMF, we linearly interpolate the traced positions onto a fixed set of regularly-spaced Y-values, found by calculating the average Y-coordinate of the dawn/dusk terminating points over the 30 minute period, then choosing Y-values in intervals of 0.75 R_E bounded by these end points. We note that in cases where the nulls identified lie upstream of the terminator plane, we simply trace beyond the nulls so that all the separators terminate around $X = 0$ and the length of the separator is independent of the terminating points used. Extrapolation is performed for the final point if needed (e.g. if the traced separator extent at a given timestep is 0.2 R_E short of the average final Y-value) but this is minimal and any resulting error is small since the separator geometry becomes more linear around $X = 0$. This also reduces possible undershooting/overshooting in X since using the minimum/maximum out of all Y-values would result in the other interpolated separators stopping before/after the terminator plane. Once this is done, we average across X and Z for the fixed set of Y-values, repeating this process for each tilt angle. The standard deviation of the Z-values for the interpolated separators gives the range of positions. Figure 3.9 shows the resulting magnetic separators for each tilt angle. In panel (a) we have also displayed the range in traced positions across the magnetopause in each case.

For 0°, the average separator lies roughly along the equatorial plane, deviating slightly at the subsolar point by about 1 R_E. For 10°, the terminating points of the separator have moved southward of their original locations, whereas in the subsolar region there is a large southward deviation, consistent with the observed topology in Figure 3.6b. For 20° to 60° this deviation is not seen, and the separators are shifted more weakly at the subsolar magnetopause than at the flanks. We note the similarities in this trend to the

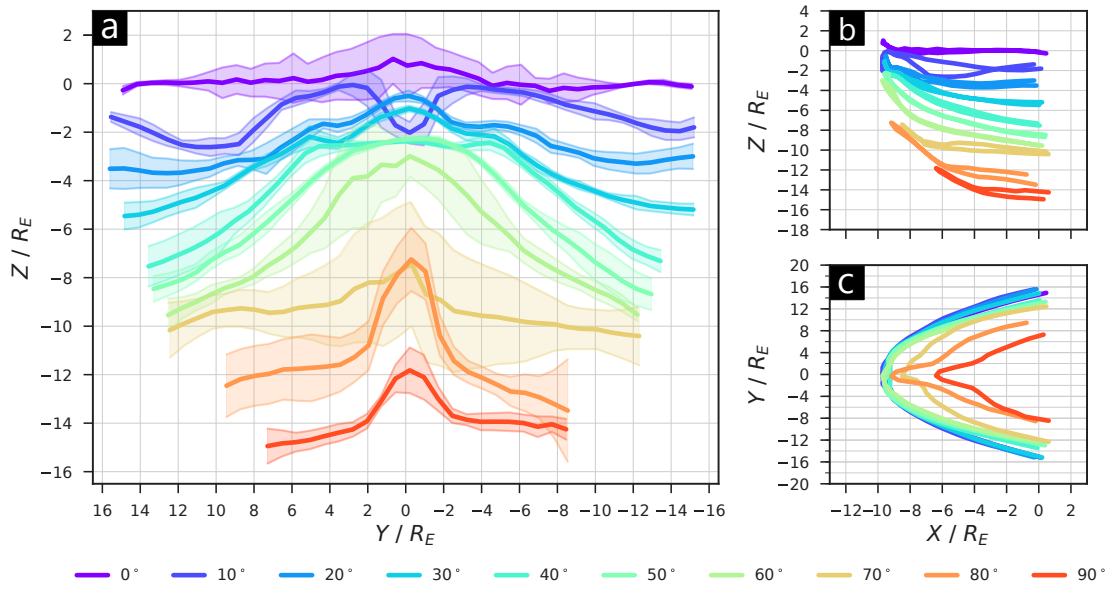

Figure 3.9 – Traced magnetic separators at the dayside magnetopause for different dipole tilt angles, plotted in the Y-Z (a), X-Z (b) and X-Y (c) planes. Shown is the average location of the separator over the last 30 minutes of simulation, with the shaded regions representing one standard deviation in the Z-direction.

results found by Hoilijoki et al., 2014 up to 20°; our results show that this still holds for larger tilt angles. At 70° we see that the separator suddenly shifts more strongly at noon, creating a flatter average profile. At 80° and 90°, it continues to migrate southward at the flanks, but is deviated northward at noon, creating a narrow profile that increases the effective length of the X-line. In general, the location of the dawn and dusk terminating points are shifted southward (in Z) and Earthward (in Y) in a consistent manner, but it is the central portions that show a complex tilt angle-dependence.

In the purely antiparallel case of 0°, there is a range of deviation of up to 1 R_E in the separator location over this interval, largest at noon. There is less deviation at 10°, and it remains relatively stable across its extent (with more motion at the flanks) up to 50°. However, the separator becomes significantly more time-dependent from 60° onwards, varying most at 70° by ± 3 R_E over the 30 minute interval. This is consistent with the observed prevalence of FTE generation for large tilt angles in Figure 3.6, which will significantly alter the dayside topology over short timescales. Overall, though the X-line does not appear perfectly steady for any tilt angle, the degree to which it is stable appears to depend closely on the tilt angle.

To help explain the southward migration of the separator, we calculate the magnetic shear angle on the dayside magnetopause for 0°, 30° and 90° tilt angles. This requires sampling properties immediately either side of the magnetopause, for which we need to know the distribution of surface normals everywhere on the boundary. To obtain this for each set of magnetopause coordinates, we use a procedure similar to that described by Komar et al. (2015), based on the method of Hoppe et al. (1992). As previously mentioned, the magnetopause is constructed in paraboloidal coordinates (u, v, ϕ),

where ϕ is the angle perpendicular to and cyclical about the X-axis; u and v are opposite parabolic dimensions but v is not needed to describe the surface coordinates. For each point $\mathbf{r}_{MP}(u,\phi) = (X_{MP}, Y_{MP}, Z_{MP})$ on the surface we find the (3×3) covariance matrix for cartesian vectors $\mathbf{d} = \mathbf{r}_k - \mathbf{r}_{MP}$ connecting said point with its four nearest neighbours $\mathbf{r}_k$, separated on the magnetopause grid by $(\Delta u, \Delta\phi)$:

$$\mathbf{r}_k \in \{\mathbf{r}(u-\Delta u,\phi), \mathbf{r}(u+\Delta u,\phi), \mathbf{r}(u,\phi-\Delta\phi), \mathbf{r}(u,\phi+\Delta\phi)\}. \tag{3.4}$$

The matrix is thus defined for each $\mathbf{r}_{MP}$ as:

$$M_{i,j}(\mathbf{r}_{MP}) = \sum_k d_i d_j \tag{3.5}$$

for cartesian components i, j of $\mathbf{d}$. The normal $\hat{\mathbf{n}}(\mathbf{r}_{MP})$ is defined as the eigenvector of M whose eigenvalue is minimal, oriented towards the solar wind by default. To validate this procedure, we show in Figure 3.10 the components of $\hat{\mathbf{n}}$ on the magnetopause for the 0° tilt angle case. Clearly the magnetopause is normal to the solar wind inflow at the magnetopause nose (where $\hat{\mathbf{n}} = -\hat{\mathbf{x}}$), and points increasingly towards $\pm\hat{\mathbf{y}}$ and $\pm\hat{\mathbf{z}}$ at the flanks, all as expected. The method also resolves the concave divot in the surface around the cusps (seen in Figure 3.3), where the normals are rotated towards $\pm\hat{\mathbf{z}}$. Hence this approach properly captures the magnetopause geometry and is appropriate for determining the local variation in properties either side of the magnetopause.

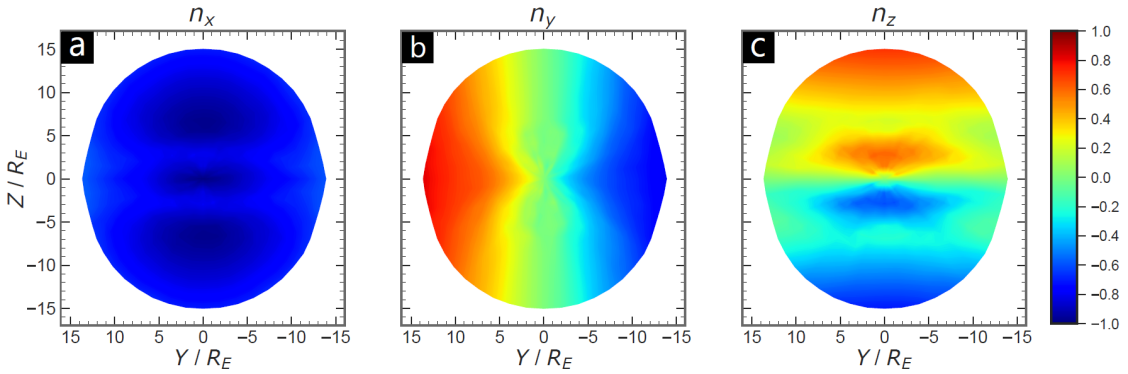

Figure 3.10 – Components of the dayside magnetopause normals calculated across the surface for the 0° dipole tilt angle case.

To calculate the shear angle the magnetic field is sampled either side of the boundary, stepping perpendicularly from the magnetopause coordinates to obtain the fields $\mathbf{B}_{SW}$ and $\mathbf{B}_{MS}$ in the solar wind and magnetosphere, respectively. The angle between the sampled fields is then given by $\cos^{-1}(\mathbf{B}_{SW} \cdot \mathbf{B}_{MP} / B_{SW} B_{MS})$. Figure 3.11 shows the result of this method for 0°, 30° and 90° dipole tilt angles. In the 0° case the separator can be seen to follow the region of antiparallel field, which covers the entire equatorial plane. For 30° this region has shrunk in size, and the separator is draped southward at the flanks towards where the shear is largest. For 90° the antiparallel region is reduced to essentially a single point about which the separator is approximately hinged. This suggests that, at least for purely southward IMF, the separator tends to reconfigure with

tilt angle so as to maximise the shear angle along its extent, though it can deviate around the subsolar region. This is consistent with the findings of Komar et al. (2015) for a 15° tilt angle, where the maximum magnetic shear model provided the most accurate prediction of X-line location out of several tested models for southward IMF. However, we note that unlike in the present study the IMF used in their simulations was not purely southward, i.e. it was southward-oriented with a non-zero B_y.

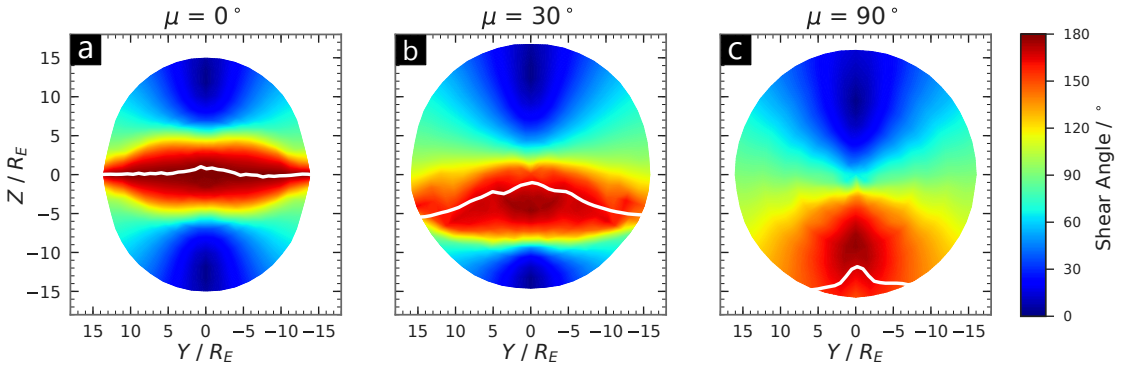

Figure 3.11 – The magnetic shear angle on the dayside magnetopause for 0°, 30° and 90° dipole tilt angles, shown here in the Y-Z plane after 4h of simulation. The white lines are the average locations of the separator over the final 30 minutes, as shown in Figure 3.9.

3.4.3 Variation in Reconnection Rate

Whilst informative of the magnetic topology, the separator geometry alone does not reveal information about the location or intensity of reconnection itself. To infer this, we must calculate the electric field parallel to the separator ($E_{\parallel}$) along its full extent, which provides the local reconnection rate. Various methods have been employed in simulations to determine the global reconnection rate, such as tracing streamlines back into the solar wind to determine the geoeffective potential (Merkin et al., 2003), integrating the parallel electric field along all open field lines to get the global potential extrema (Jensen et al., 2017), and calculating it from the CPCP based on assumptions of negligible potential drops (Connor et al., 2014). However this does not provide local information about reconnection, and some potential drop between the magnetopause and the ionosphere is inevitable in simulations which may be hard to quantify. Studies using an explicit resistivity typically calculate the reconnection rate as $\mathbf{E}_{\parallel} = \eta \mathbf{J}_{\parallel}$, which is not possible for collisionless simulations unless the numerical resistivity is assumed to have some value. In this study, we instead output $\mathbf{E}$ from the MHD solver at every timestep, capturing the numerical errors which then modify the induction equation and correspond to numerical diffusion.

Studies using the GUMICS code have shown that such an approach can pick-up significant noise if the flow stagnation line does not coincide with the magnetic merging line, since flow reversals can occur between adjacent cell-centres (Laitinen et al., 2006, Janhunen et al., 2012). However we combine temporal averaging along with the use of a staggered grid, which reduces sensitivity to anomalous numerical noise and has

been performed in similar studies when showing $E_{\parallel}$ along the separator (Cnossen et al., 2012b). Nonetheless, we stress that any such method is not perfect and may not be fully capturing the global rate of flux transfer and energy conversion, but serves to show the general spatial and tilt-angle dependence of the reconnection rate. To calculate $E_{\parallel}$, we perform a trilinear interpolation to find **E** at every point along the separators and temporally average to yield the same loci of points shown in Figure 3.9. We then average between successive points to get **E** half-way along the connecting segments to obtain a second-order representation. Integrating this (to second-order) over the length of the separator provides the approximate average dayside reconnection voltage, i.e. global rate of flux transfer into the magnetosphere.

Figure 3.12 shows the resulting $E_{\parallel}$ for each tilt angle. For 0-50°, the electric field intensity is focused around the central point, whilst it becomes much weaker for 60° and above. Where the separator is strongly deviated around noon (most notably at 10° and 80°), the electric field appears to drop, as was found by Glocer et al. (2016) during FTE generation. We note that for 0-30° tilt angles (where the separator crosses close to the Sun-Earth line) the enhanced reconnection rate around the subsolar region would yield a view consistent with component reconnection if measured locally. However, this electric field is non-zero elsewhere along the separator, which itself extends far away from the subsolar point. Similarly the electric field is non-zero in regions of small magnetic shear for both 30° and 90° - in contrast to the predictions of antiparallel reconnection. Furthermore, whilst for 0° and 90° it reaches a maximum where the shear is largest, for the 30° case this occurs just northward of the region of maximum shear. As pointed out by Glocer et al. (2016), these paradigms may only present a local perspective of 3-D dayside reconnection, and could lend to misleading conclusions if applied to a global context such at that shown here.

The reconnection voltage obtained by integrating these parallel electric fields is shown in Figure 3.13a. From 10° onwards the overall trend is that the average voltage decreases with increasing tilt angle for steady southward IMF. The calculated voltage for 0° is in fact 15 kV lower than at 10°, which may contrast with expectations for the optimised shear angle along the separator at 0°. However, there is still a greater open flux content at 0° during this interval (0.93 GWb versus 0.84 GWb for 10°), which suggests a larger reconnection voltage on average. If this is true then the lower value may be a result of more persistent FTE generation during the sampled period, reduced accuracy in sampling the electric field due to erosion of the magnetopause (see Figure 3.6a), or unique effect of the purely anti-parallel field along the equatorial plane for 0° which could limit numerical diffusion. Some of these effects, if present, could be rectified by the use of a large explicit resistivity to minimise dependence on the numerics, but we reserve this for future study since it precludes meaningful analysis of the FACs. If the calculation is instead accurately capturing the dayside coupling for 0°, the greater open flux content could instead be a consequence of complex magnetotail dynamics, such as bursty (substorm-like) tail reconnection, by which open flux is stored for some time before being rapidly released (consistent with the plasmoid ejection in Figure 3.3a).

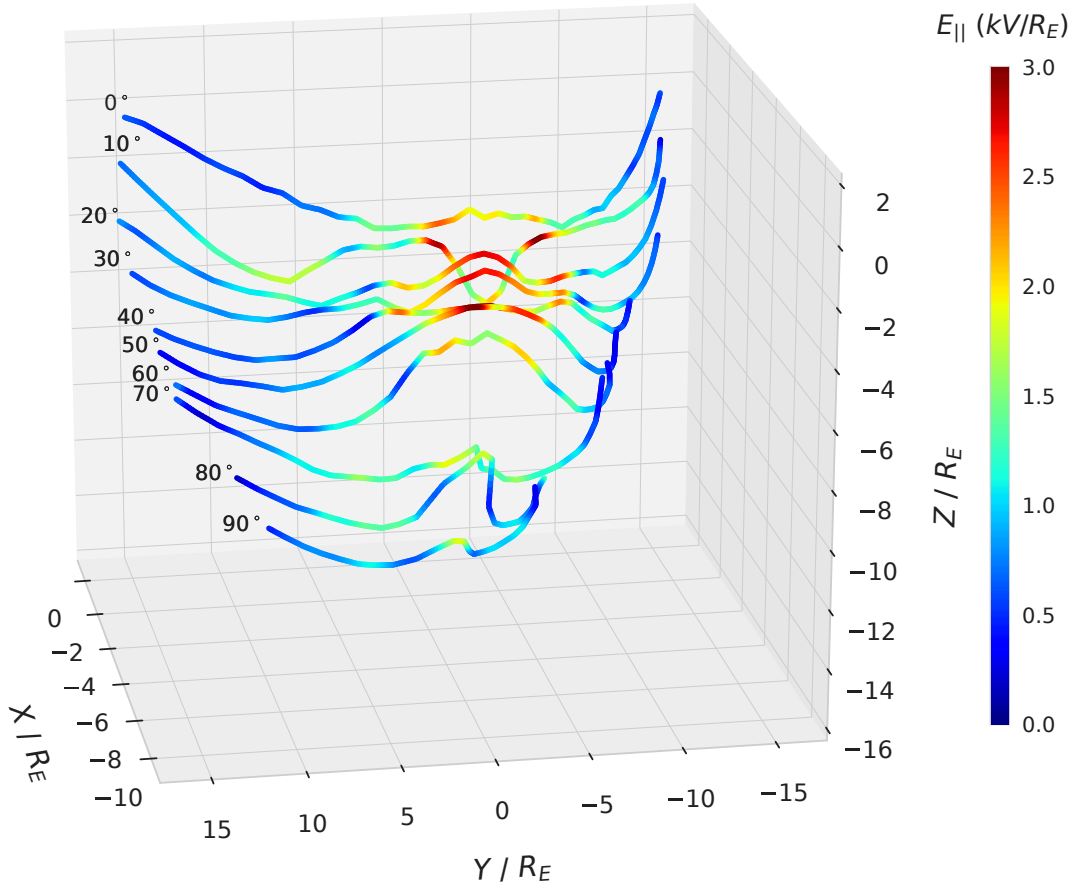

Figure 3.12 – The electric field parallel to the magnetic separator for successive dipole tilt angles, averaged over the final 30 minutes of simulation.

For all tilt angles the reconnection voltage is strongly time-dependent - most notably at 40° where it varies by ±7 kV over this interval. Note that although we have not traced out all X-lines where multiple were formed, the local reconnection rate tends to drop in the vicinity of the FTEs that they flank. Furthermore, Glocer et al. (2016) found that the calculated reconnection voltage was the same regardless of which separator branch was traced in their simulations, and so tracing other branches should not significantly affect our calculations. The shorter timescale behaviour seen in the reconnection voltage should average-out to achieve the global quasi-steady state, since the total flux is the time-integral of the reconnection rate. The polar caps should therefore shrink with increasing tilt angle due to reduced open flux content, altering the location of ionospheric Region 1 currents. Additional changes in the currents such as emerging North-South asymmetries may also lead to a more complex tilt angle-dependence, which we now investigate.

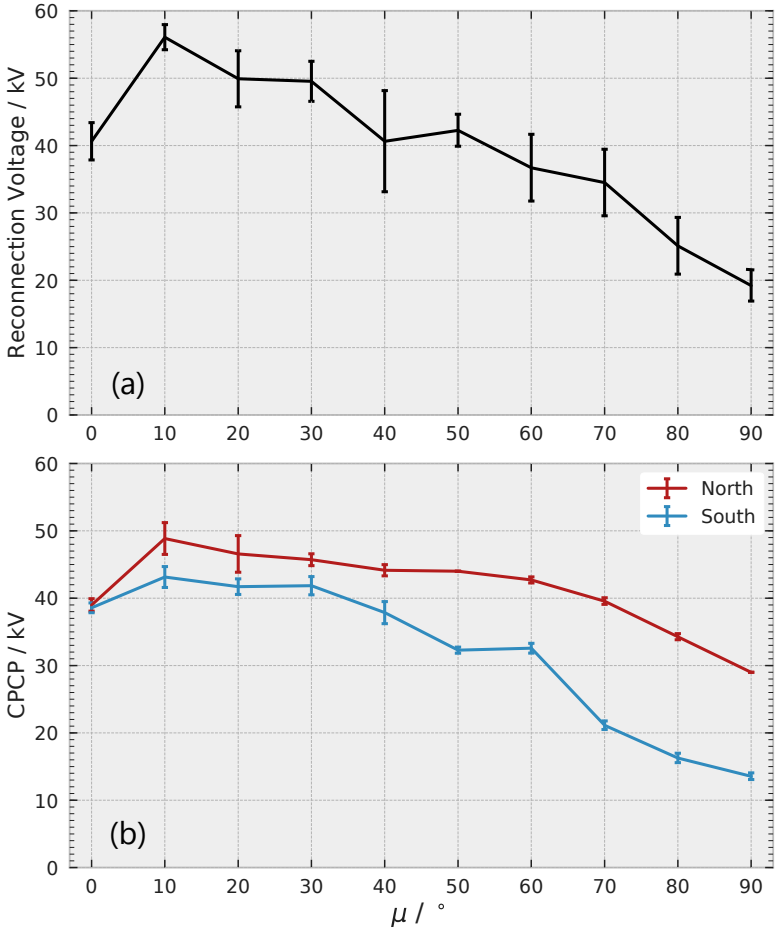

Figure 3.13 – The dayside reconnection rate (a) integrated along the traced separators, and the ionospheric cross-polar cap potential (CPCP) (b) at each hemisphere for successive dipole tilt angles averaged over the final 30 minutes of simulation, with error bars representing one standard deviation.

3.5 Ionospheric Convection and Currents

To explore how the tilt angle effects manifest in the ionosphere, we first examine the polar caps in more detail. In ideal MHD ($\mathbf{E} = -\mathbf{v} \times \mathbf{B}$) and in steady-state ($\partial \mathbf{B}/\partial t = 0$), the parallel electric field $E_{||}$ along magnetic field lines is zero. Thus, the electrostatic potential on closed field lines should be identical at conjugate North/South ionospheric footpoints (Hesse, 1997), and the reconnection voltage should map down as the CPCP assuming the potential extrema lie along the OCB.

Figure 3.13b shows the CPCP at North and South for each tilt angle. On both hemispheres the overall trend in the CPCP matches that in the reconnection voltage, as expected, supporting our conclusions about reduced dayside coupling with increasing tilt angle. The reduced CPCP at 0° versus 10° is notably also in agreement, though it remains possible that the actual dayside rate for 0° is higher than for 10° since the CPCP depends on both Φ_D and Φ_N. An imbalance between dayside and nightside reconnection, which is likely given the plasmoid evident at 0°, would also result in a reduced amount of flux being circulated back to the dayside during this time and hence a weaker CPCP.

The Northern CPCP is generally comparable to the reconnection voltage, with some differences seen in each case. At the South, however, there is a larger drop in CPCP with growing tilt angle, introducing a North-South asymmetry that becomes significant at large tilt angles. Thus, the breaking of a global North-South symmetry in the magnetosphere also breaks the symmetry in the simulated North/South CPCPs, even with a uniform conductance profile, as also found by Park et al. (2006) for a 30° tilt angle. Since the constraint of matching potentials does not apply to open field lines, as these only map to one hemisphere, the additional Northern potential must be provided within the polar cap and have its roots in the solar wind interaction. This is consistent with the greater convection path lengths in the Northern hemisphere, and hence electric field, shown in Figure 3.4. A tempting conclusion based purely on the mismatch in CPCPs is that the magnetosphere is not actually in steady-state, which is perhaps only established over a much greater simulation time if there are strong asymmetries in the system. In such a scenario the path lengths would eventually settle to be equal in each hemisphere and the CPCPs would then reach conjugacy. However this is contradictory with the hinging of the magnetotail current sheet, also seen in other simulations (Park et al., 2006, Ridley et al., 2004) and in observations (Xiao et al., 2016).

A further issue unexplained by this interpretation is that the CPCP in the North is actually higher than Φ_D for the largest dipole tilts; some mechanism other than reconnection must be contributing to the increased potential. A process often attributed to increases in CPCP in both simulations and observations is viscous interaction with the solar wind, arising due to velocity shears between plasma elements either side of the magnetopause. This is usually considered in terms of closed field lines, whereby the interaction causes circulation of the magnetospheric field in the same sense as reconnection-driven convection even during northward IMF. In fact, this still occurs in the presence of reconnection, and has been proposed to contribute to differences in CPCP and Φ_D in other simulations (e.g. Jensen et al., 2017, Connor et al., 2014), and may contribute tens of kV to the CPCP for driving conditions such as these (Bruntz et al., 2012). However the effect of this process is less clear for large tilt angles. As shown in Figure 3.6, as the tilt angle increases the flow on newly-reconnected North/South-open field becomes very different; it reverses either side of the magnetopause close to the subsolar point on Northern field lines, which constitute a growing portion of the dayside field, but becomes tangential to the magnetosheath flow in the South.

Thus whilst the the presence of a viscous potential can explain the differences between the CPCP and the reconnection potential, this could also contribute to the different North/South CPCPs if additional momentum is being transferred onto open flux tubes in the North pole - particularly for extreme cases like a 90° tilt angle. This would still be consistent with the greater convection path length in the North, and without any contradiction to the expectations of steady-state. However this is difficult to distinguish from purely numerical explanations - for example it may be that the Φ_D calculation is an underestimate of the true value for large tilt angles, perhaps due to increased error where the separator is shorter and less steady. There will also exist some potential drop

along field lines due to numerical diffusion ($E_{||} \propto J_{||}$), which could introduce asymmetry due to a differing FAC morphology on each hemisphere. However the North/South CPCP disparity is clearly growing with tilt angle whilst the typical FAC strength should be decreasing, making this unlikely to be the only cause. Future work could distinguish these effects through the use of a much higher resolution grid and/or an anomalous resistivity along the separator. Regardless, the CPCP is only a single metric, and does not determine any morphological changes occurring due to the tilt, which we now turn our attention to.

Before showing the full ionospheric conditions, we first identify the location of the open-closed boundary (OCB) in the simulations which will help to explain the evolution of the polar cap. The magnetic connectivity is sampled at the inner boundary at 4 R_E. Here the field is either fully closed, or North-open/South-open yielding three possible domains. The Scikit-Image package is used to identify the boundaries of the sampled domains, giving a set of coordinates of the OCB in colatitude and longitude which is then mapped down onto the ionospheric grid using dipole mapping. This is demonstrated in Figure 3.14 for a 60° dipole tilt.

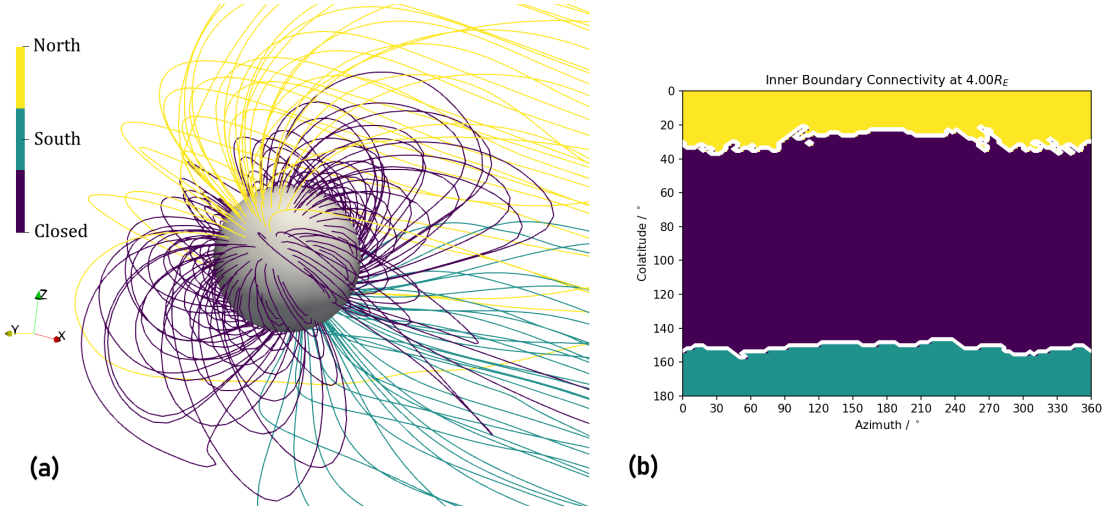

Figure 3.14 – Method for identifying the open-closed boundary (OCB) in Gorgon, showing (a) the tracing of field lines from the simulation inner boundary which are labelled according to their connectivity, and (b) finding the locus of OCB points dividing each domain, shown in magnetic coordinates with the North pole at 0° colatitude.

If the reconnection line were perfectly static and continuous on both the dayside and nightside, then the shapes of the two OCBs would be close to mirror images of one-another in steady-state, since they must enclose the same amount of flux. However, previous simulations using Gorgon have shown that flux ropes formed on the dayside magnetosphere can be connected to just one pole and carry open flux towards the nightside before dissipating (Mejnertsen, 2018). Hence the results in this study showing non-steady reconnection at both the dayside and nightside suggest that some North/South asymmetry, as well as a complex irregular OCB morphology, may be expected.

Figure 3.15 shows the ionospheric potential profiles at North and South after 4h, with the OCB indicated. Once again we focus on 0°, 30° and 90° as our example cases.

For 0° the Northern and Southern conditions match, with the OCB sitting at 5° higher in latitude on the dayside such that the polar cap is shifted slightly to the nightside. Around dawn and dusk, small regions of open field are impinging from the nightside polar cap towards the dayside, which may be signatures of the plasmoid ejection in Figure 3.3 or instabilities at the flanks. The twin-cell convection pattern in the potential is as expected for southward IMF, with conditions almost identical in each hemisphere.

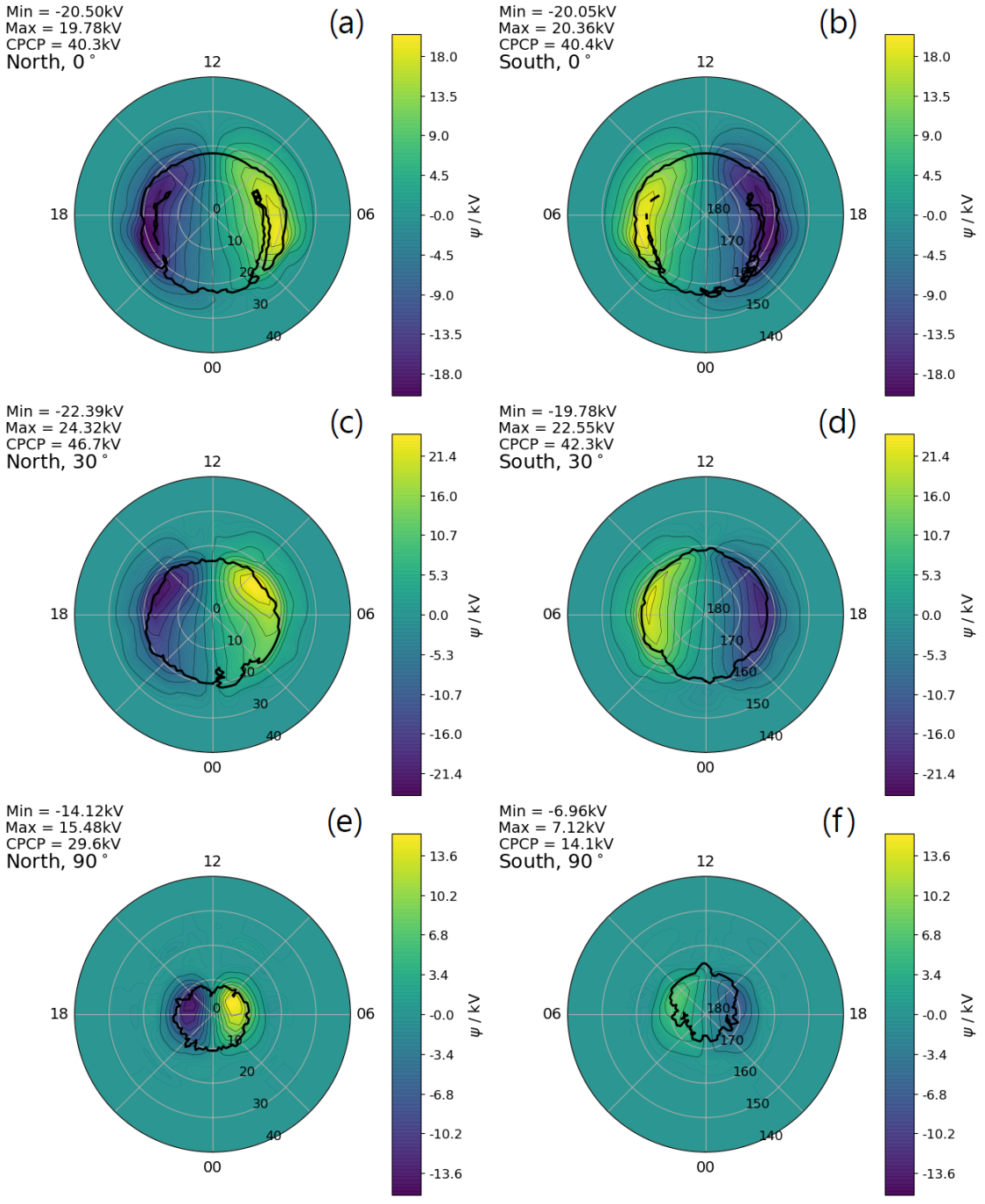

Figure 3.15 – Electric potential ψ at the Northern (a, c, e) and Southern (b, d, f) ionosphere after 4h of simulation for 30° (a, b), 60° (c, d) and 90° (e, f) dipole tilt angles. The black lines mark the location of the open-closed boundary. The corresponding minimum/maximum potential and CPCP is shown in each case.

For the 30° tilt angle the polar caps have begun to shrink in size, and the Northern OCB is slightly eroded at noon compared to the South. The Northern convection cells are focussed on the dayside, whilst in the South they are marginally weaker and show more day-night symmetry. For 90° the polar caps are now considerably smaller, again slightly eroded at noon in the North whilst in the South it is shifted slightly sunward. The convection cells are also much weaker, and there appears to be very little flow at mid-to-high latitudes which now map to closed, inner magnetospheric field lines. In the North the potential is once again strongest on the dayside, and roughly twice as large as in the Southern hemisphere.

It is noteworthy that the peaks of the potential do not lie perfectly along the OCB but are slightly poleward in each case. To some extent any agreement will be limited by the timescale over which the ionosphere is updated in the simulation ($\sim$ 30s) versus any changes in the OCB, but the lack of coincidence of the two reinforces the notion of an additional contribution to the potential, particularly in the North. Regardless, the results seen here show that North-South asymmetries can arise in the potential due to asymmetries in the convection in the magnetosphere. This disparity suggests that the FAC may differ significantly on each hemisphere at large tilt angles, even though the OCBs should enclose effectively the same amount of flux in a quasi-steady-state. The Region 1 current system is generated along this boundary due to flow shear (Cowley, 2000), and thus any flow asymmetries on open field lines will give rise to asymmetries in the FAC at each hemisphere and in local time.

Figure 3.16 shows the FAC for the same example tilt angles. For 0° the Region 1 FAC profiles extend to noon, being weaker at midnight; for 30° the Northern FAC profile is broadened on the dayside, where the two bands of Region 1 current reach maximum amplitudes. In the South this day/night asymmetry is not seen, and though Region 1 currents reach slightly larger maximum values than in the North, they are thinner than in the 0° case and the total upward field-aligned current (TFAC) is now lower. For 90° the smaller polar caps result in a strongly localised current system with a much lower TFAC on both hemispheres. However, in the North the maximum FAC value is still comparable to the 0° case, and is clearly offset towards the dayside. At the South a slight dayside bias is seen, but this is much less significant than in the North and the currents are approximately half as intense at their peak.

Thus, as the tilt angle increases, a growing North-South asymmetry in each of the FAC and potential emerges, despite our use of a uniform conductance profile. This asymmetry must therefore originate in the convection electric field itself, and is explained by our findings in section 3.3, i.e. that the convection path length for Northern open field lines becomes longer than the Southern field lines as the tilt angle increases. To sustain this configuration in steady-state, faster flows in the Northern hemisphere - especially at the dayside where newly-reconnected field flows strongly perpendicular to the polar cap surface - must thus drive stronger currents than in the South, and with an increasing bias towards noon.

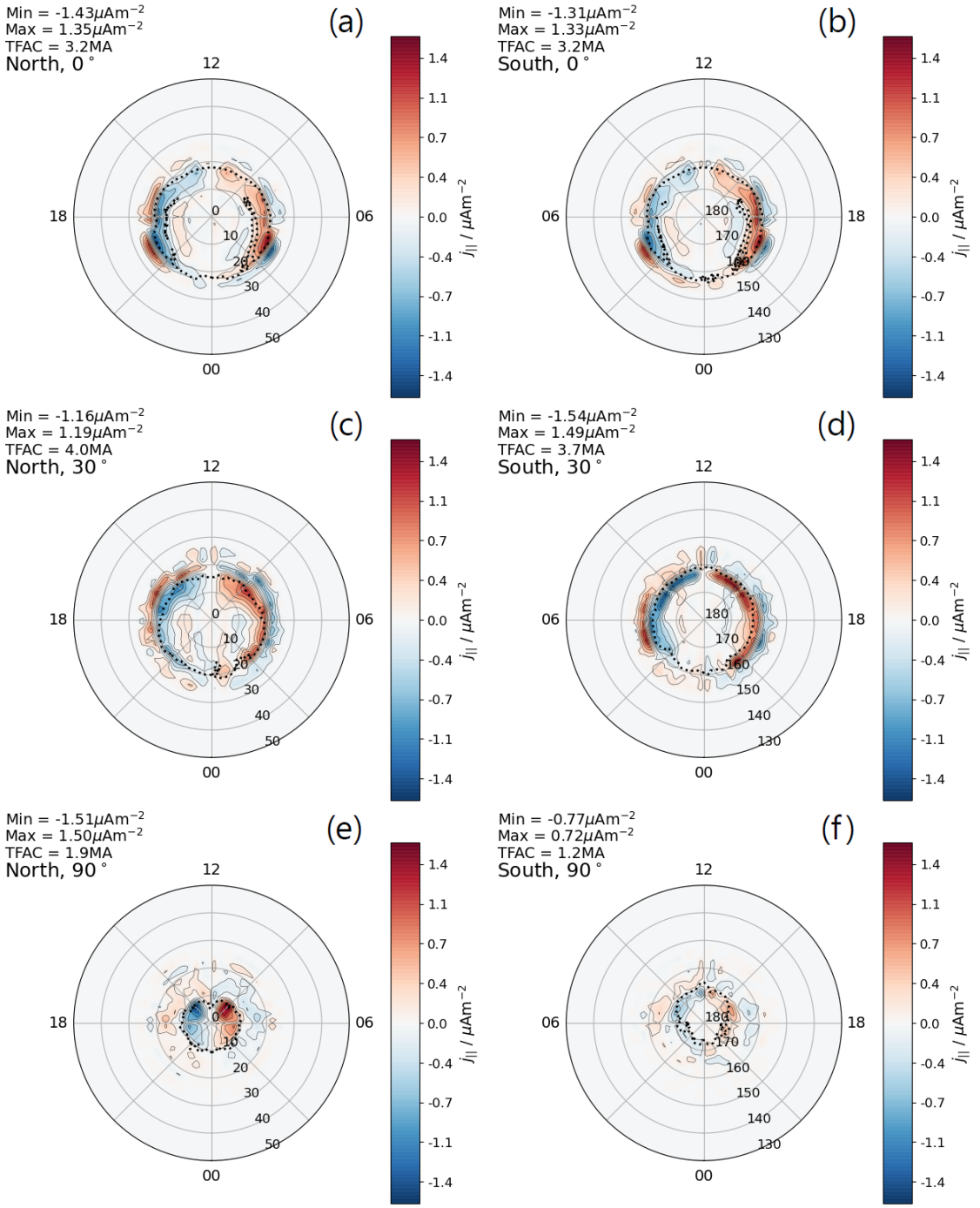

Figure 3.16 – Field-aligned current $j_{||}$ at the Northern (a, c, e) and Southern (b, d, f) ionosphere after 4h of simulation for 0° (a, b), 30° (c, d) and 90° (e, f) dipole tilt angles. The dotted black lines mark the location of the open-closed boundary. The corresponding minimum/maximum FAC and TFAC is shown in each case.

3.6 Discussion and Future Work

In this Chapter we have investigated the effect of an increasing dipole tilt angle on the global magnetosphere and its coupling with the solar wind and ionosphere, during a period of steady southward IMF. We find that the reconnection line on the magnetopause

shifts southward with increasing tilt angle, in agreement with findings from previous studies. However, in extending the survey to larger angles than has previously been investigated we have revealed that the reconfiguration of the magnetic separator is complex and time-dependent, especially for larger tilt angles. Even for a 90° tilt angle, the separator is continuous across the entire dayside magnetopause, and reconnection appears active along its extent.

The magnetosphere is thus still 'open' for an arbitrarily large tilt angle, with the reconnection voltage dropping (above 10°) with increasing tilt angle and the polar cap contracting. We find that a 0° tilt angle presents a unique case compared to non-zero angles, as the strong antisymmetry in the system renders both dayside and nightside reconnection to be less stable than at 10° and show a more complex time-dependence. We emphasise that steady-state represents a special case, and that a more smooth trend in dayside reconnection voltage may be seen if driving with a varying IMF, rather than with the steady conditions for several hours. However, this would introduce more complex responses in the global system such that the effect of the dipole tilt angle alone would be hard to diagnose.

The reduced geoeffectiveness at large tilt angles may be a result of strongly diverted magnetosheath flow where the separator is offset far from the subsolar region. Reconnection is also increasingly unsteady as the tilt angle becomes large, with FTE generation becoming more persistent, thus making the rate of flux transfer highly time-dependent. This appears to be associated with an offset of the magnetosheath flow stagnation point from the separator location. Away from noon, the separator is more steady, but the reconnection rate generally lower due to reduced magnetic shear angle. This has implications for reconnection at magnetospheres with highly inclined dipoles, e.g. at the ice giants where observations are extremely limited. For example, it has been shown that seasonal modulation in magnetic shear angle at Neptune's magnetopause is likely to strongly alter where reconnection occurs (Masters, 2015), whilst simulations reveal that reconnection can locally 'switch-off' for certain periods of planetary rotation (e.g. Mejnertsen et al., 2016, Cao and Paty, 2017). An investigation into the separator location for the various extreme configurations of the ice giant magnetospheres could thus reveal to what extent reconnection can be globally active even where the shear angle is small, and whether it is strongly FTE-driven.

In our terrestrial context the drop in reconnection voltage is associated with a contracting ionospheric polar cap, and shrinking Region 1 current systems and CPCPs. However, the strength of these currents shows a more non-linear dependence on tilt angle. We have shown that as the tilt angle increases, an asymmetry between the convection path lengths of Northern and Southern open magnetospheric field lines emerges. In order to sustain a steady-state, Northern ionospheric currents can thus reach larger intensities than their Southern counterparts, despite equal polar cap flux content, and the CPCP becomes larger in the North even without including conductance changes. The morphology of these currents also begins to vary significantly, showing a bias on the

dayside in the North but more day-night symmetry in the South. Whilst this static configuration does not reflect a realistic scenario for the terrestrial magnetosphere (since dipole rotation and non-uniform conductance will act to smooth out some of the asymmetry over hours), the existence of this asymmetry has implications for the potential impact of a severe space weather event. For example, at the onset of a geomagnetic storm, the hemisphere which preferentially faces the solar wind may experience more intense and/or localised FAC (and thus ground magnetic perturbations) close to solstice and affect sudden commencements (see Eastwood et al., 2018 and references within) even despite any differences in conductance.

It is important to point out that migration of the geomagnetic poles over geological timescales would re-map the ionospheric coordinates onto lower geographic latitudes. The severe tilt angle cases presented here thus reveal that in this scenario, lower latitude regions may become susceptible to increasingly significant space weather impacts, but constrained to a smaller polar cap region. Furthermore, periods of geomagnetic reversal are associated with changes in the strength of the Earth's dipole moment, which will give rise to additional changes in ionospheric coupling (e.g. Cnossen et al., 2012a). Our study could thus be extended further to explore how various changes in the internal magnetic field affect the impact of a given severe event.

Finally, there are a number of caveats in our study that could be addressed in future investigations. The inclusion of a high resolution magnetopause and a more physics-based resistivity would allow more detailed investigation into the local behaviour along the separator, rather than just its global configuration. Similarly, using a highly refined inner magnetospheric grid would better resolve local variations in FAC and potential, and help to elucidate the exact mechanism generating the differences in North/South CPCPs. Employing such a setup to simulate a severe space weather event would reveal the extent to which these asymmetries can influence impacts at different locations on the Earth.

Extending the model to include Hall-MHD would directly affect the local reconnection rate via the Hall electric field, and it is not known if this affects the location of the separator. Exploring various additional IMF orientations may reveal further complex dependencies on the tilt angle, as has previously been done in the case of a 15° tilt angle and 30° IMF clock angle (Komar et al., 2015). For example, by breaking the antisymmetry between the IMF and magnetospheric field in the 0° case, a different trend from 0°-10° could be seen. Whilst these additional factors are all fundamental and help to build the overall picture, the study presented here demonstrates that the underlying trend driven by the dipole tilt alone has a significant impact on the global magnetosphere-ionosphere system, that varies strongly over the full range of tilt angles.

Chapter 4

Time-Varying Reconnection during Sudden Commencement

4.1 Introduction

Geomagnetic storms are a temporary disturbance in the geomagnetic field due to enhanced energy exchange between the solar wind and magnetosphere (and thus ionosphere), and are responsible for the most significant space weather impacts (Akasofu, 2018). These arise during periods of extended southward IMF, and are typically associated solar wind transients such as coronal mass ejections (CMEs) and corotating interaction regions (CIRs). These can contain large out-of-ecliptic magnetic field components, and carry shocks at their leading edge. At 1 AU these shocks are generally fast mode, and can mostly be treated as planar on the scale size of the magnetosphere (e.g. Russell et al., 1983). For most CMEs the leading shock has its normal orientated along the Sun-Earth line (Richter et al., 1985), whilst CIR shocks have relatively inclined normals (Pizzo, 1991).

Sudden increases in solar wind density and/or velocity are characterised as dynamic pressure enhancements (DPEs), which result in strong compression of the magnetopause. Such an event can be identified by a bipolar signature in the horizontal ground magnetic field due to the compression (Smith et al., 2019). This is termed a sudden commencement (SC), which if it develops into a geomagnetic storm is known as a sudden storm commencement (SSC). SSCs are increasingly recognised as a space weather threat to power systems, as they can induce particularly large GICs (Eastwood et al., 2018).

4.1.1 Shock Impact on the M-I System

Interplanetary (IP) shocks represent an extreme type of DPE, and their effect on the magnetosphere has been widely studied in simulations. Once a fast forward IP shock front reaches the Earth's bow shock it is decelerated within the dense magnetosheath, forming a curved front which then compresses the magnetopause (Samsonov et al., 2006). Waves are consequently launched into the magnetosphere, which have been shown to propagate faster than the shock front in the solar wind, especially on the nightside as they travel into the magnetotail (Andréeová et al., 2008). Faster propagation speeds have

been found in simulations when the shock has a higher dynamic pressure (Andreeova et al., 2011a).

Studies have further shown that the reflection of fast mode waves off the GMHD simulation inner boundary (representing reflection by the ionosphere) acts to decelerate the compression of the magnetosphere and bow shock, and which further reflects back towards the inner boundary (Samsonov et al., 2007, Andréeová et al., 2008, Yu and Ridley, 2011). Similar simulations have been performed for dynamic pressure decreases (Ozturk et al., 2019), e.g. due to fast reverse shocks, which have the opposite effect of causing expansion of the boundaries. Theoretical studies predict that oscillations in the magnetopause position occur when it is displaced (Freeman et al., 1995), which has also been shown in recent MHD simulations (Desai et al., 2021). Any such oscillations may also modulate the local reconnection rate along the dayside magnetopause.

It is the initial fast mode shock wave, transmitted through the magnetopause, which first triggers ground signatures defining the SC. Two distinct phases are seen in these signatures, called the preliminary impulse (PI) and main impulse (MI) (Araki, 1994). These are understood (in the post-noon sector) in terms of a downward FAC during the PI phase and an upward FAC during the MI phase. Global MHD simulations have been used to explore the response of the ionosphere to a sudden pressure pulse in the solar wind (e.g. Slinker et al., 1999, Keller et al., 2002), finding that the response of the FAC does indeed occur in two phases: one at higher latitudes followed by another at lower latitudes. The first PI phase currents were shown to result from the propagation of a compressional wave along the magnetopause flanks (Fujita et al., 2003a). The MI phase currents have been shown to occur in two separate phases (Fujita et al., 2003b): firstly due to deceleration of plasma behind the wavefront, generating (in the post-noon sector) a downward nightside FAC and upward dayside FAC; and secondly due to enhanced magnetospheric convection, generating upward duskside FAC that forms a Region 1-like system.

In a similar study, Samsonov et al. (2010) described these currents in terms of transient systems resembling the NBZ FAC (which occurs under northward IMF) and Region 1 FAC, which then decay to whatever conditions arise due to the post-shock solar wind driving. The Region 1-like FAC system has been attributed specifically to equatorial flow vortices in the outer magnetosphere rather than being reconnection-driven. These have been explored in detail in simulations (e.g. Samsonov and Sibeck, 2013) and have been observed in-situ for both pressure increases (Tian et al., 2016) and decreases (Zhao et al., 2016), as well as remotely in convection data (Kim et al., 2017). Note the above simulations used a northward IMF, and a two-phased FAC response has also been seen in simulations using southward IMF (Yu and Ridley, 2009). However, convection-driven FAC signatures may be stronger if the reconnection dynamo is enhanced by the DPE.

4.1.2 Dayside Coupling after Dynamic Pressure Enhancement

The enhanced reconnection rate following the onset of a geomagnetic storm leads to increased open flux content, expansion of the polar cap and thus migration of the FAC to

lower latitudes. This arises since a larger stormtime IMF strength B and inflow speed v raise the local electric field along the X-line; for a southward IMF-dominated storm of duration Δt, the total open flux generation can be approximated using average stormtime values as $\overline{vB_z} L_{MP} \Delta t$, where L_{MP} is the approximate width of the magnetopause (see section 1.3.4). A survey of past geomagnetic storms has shown that $\overline{vB_z}$ is more important than Δt in determining the intensity of the storm (Wang et al., 2003). Thus, an intense event with a short duration could lead to more severe space weather impacts than a weaker (but longer) event.

Palmroth et al. (2007) showed that events similar to slow shocks (i.e. with a reduction in B_z) have a higher coupling efficiency than events where B_z increases. This is defined as the efficiency at which the available convection electric field generates an increase in a chosen geomagnetic index, and has a more complex dependence than the reconnection rate, though the latter should be dominant over convection (rather than compression) timescales. Similarly, Andreeova et al. (2011b) showed by combining observations with simulations that solar wind discontinuities with a smaller E_y actually have a higher coupling efficiency. If this is related to dayside reconnection it may suggest that whilst Φ_D still increases with a greater B_z or E_y, it may do so by a smaller factor than with the dynamic pressure. Alternatively, reconnection may simply be less important than compressional signatures in determining the geomagnetic response to some DPEs. Note that there is also a distinction between a dynamic pressure increase and a velocity increase; the latter is explicitly contained in most solar wind coupling functions (e.g. Milan et al., 2012), but the former may be dominated by density changes. Nonetheless a greater velocity is strongly correlated with the geoeffectiveness, and simulations have shown that the solar wind speed is more important in determining the intensity of ground signatures from a DPE than the density (Kubota et al., 2015).

The response of the polar cap size to a DPE is in fact complicated. Using the OpenGGCM code, (Oliveira and Raeder, 2014) studied the geoefficiency of frontal and inclined shocks. The dayside showed strong FAC enhancement due to compressional signatures, whilst frontal shocks were more geoeffective than inclined shocks as they triggered the closure of magnetotail flux, i.e. substorms. The inclined shocks generated a North-South asymmetry in the response, which was less effective at closing nightside flux. Similar results were found using the same model to simulate the FAC response (Shi et al., 2019). Such nightside flux closure is associated with contraction of the polar cap, which has been widely observed for DPEs (Milan et al., 2004, Hubert et al., 2006). Studying three different DPEs during southward IMF, Boudouridis et al. (2005) found that the polar cap generally contracted due to strong magnetotail reconnection. An increase in coupling efficiency was seen after arrival, but was mainly attributed to nightside reconnection.

Nonetheless, this does not preclude the enhancement of dayside reconnection following the arrival of a shock. Boudouridis et al. (2007) used SuperDARN data to show increased convection on the dayside following DPEs associated with magnetopause reconnection. The dynamic pressure was mostly dominated by the jump in density for southward IMF cases. Hence both dayside and nightside reconnection may be enhanced,

competing to determine the change in polar cap and auroral oval shape and size in the short time following a DPE. Boudouridis et al. (2011) later showed immediate dayside convection response under southward IMF, which is slightly delayed and weaker but longer lasting for northward IMF, with the nightside response only seen ~ 10 minutes after the dayside. Observations have also found enhanced particle fluxes on the dayside during weakly southward IMF after a DPE, with some luminosity increase in the dayside auroral oval (Borodkova, 2010).

Similar conclusions have been made in simulations. Using OpenGGCM, Connor et al. (2014) estimated separate dayside and nightside reconnection rates using the ionospheric potential, assuming some linear combination of Φ_D and Φ_N with a viscous potential to produce a total CPCP. For southward IMF they showed clear enhancement of Φ_D after the Alfvén wave transit time into the ionosphere, being 2 to 4 times the contribution to CPCP than Φ_N which is enhanced several minutes later. This delay causes initial dominance of the dayside rate due to compressed magnetosheath field by the pressure enhancement, and hence expansion followed by eventual contraction of polar cap. However for northward IMF they found that Φ_N dominates, reduced by the effect of sunward convection due to high latitude reconnection, consistent with an overall contraction of the polar cap, but still permitting some enhanced dayside reconnection. Similarly for northward IMF, Samsonov et al. (2010) suggested that the transient NBZ FAC occurring during shock propagation is due to enhanced cusp reconnection - this has also been proposed to explain ground magnetic observations after a sudden impulse (Han et al., 2010).

4.1.3 Motivation and Outline

It is clear that dynamic pressure enhancements, especially IP shocks, may result in immediate enhanced dayside reconnection. By using a metric to estimate the dayside reconnection rate based on a catalogue of geomagnetic storms, Guo et al. (2011) found that the solar wind pressure makes a significant contribution to solar wind coupling, moreso for storms driven primarily by the compressed sheath regions between an ICME leading edge and the shock ahead of it. Thus the effect of a DPE in compressing the magnetosheath field may be crucial in determining the dayside coupling during SC, and the resulting space weather impacts e.g. injection of high-energy particles and enhanced FAC signatures.

The response of the dayside field topology during SC is also interesting from a reconnection perspective. The compression of the magnetopause will influence where reconnection occurs, since the separator should evolve with the deformed surface. The distortion of the X-line may alter the local reconnection rate due to changes in the field orientation, and the extent to which the separator - and reconnection itself - can evolve dynamically over a given timescale has further implications for studies of reconnection at the magnetopause. This is very difficult to verify observationally with in-situ measurements; observations of reconnection X-lines by MMS have shown stationarity of the X-line over several minutes, but these were for steady conditions (Fuselier et al., 2019).

Global MHD simulations provide an ideal means to investigate this, given their ability to capture the dynamical changes in the global system in the short time following impact. In this study, we will simulate the response of the separator and the associated M-I coupling due to a variety of shocks impacting the magnetosphere. By simulating a series of different clock angles, dipole tilt angles and solar wind dynamic pressures we can determine how these parameters control the response of the dayside coupling. Furthermore, by use of an explicit resistivity in Gorgon, we can investigate in close detail how the reconnection rate is altered locally as the shock propagates over the magnetopause.

4.2 Simulation Set-up

We employ a high-resolution grid of spacing 0.25 R_E everywhere in the simulation domain, which as in the previous Chapter spans X = (-30, 90) R_E, Y = (-40, 40) R_E, Z = (-40, 40) R_E. The inner boundary is placed at 3 R_E rather than 4 R_E, though as before has plasma parameters of n = 370 cm^{-3} and $T_{i,e}$ = 0.1 eV. Whilst this smaller radius can lead to prohibitively slow timestep effects due to extremely fast shock-induced Alfvén waves, it allows for more realistic reflection of waves off the inner boundary and more accurate mapping of FACs in case of reduced dipolarity resulting from compression.

The magnetosphere is initialised using the same solar wind conditions as in the previous section, except that in some cases we change the IMF clock angle. A shock is then injected from the sunward edge of the box by introducing a jump in solar wind parameters that satisfies the Rankine-Hugoniot (RH) jump conditions, discussed in section 1.2.4. The solar wind conditions are then kept at the post-shock values for the remainder of the simulation, which continues for 10 minutes after the jump is applied. Since the shock must be injected as a single solar wind phase front propagating in one direction, we stick to the simple case of a perpendicular shock ($B_n = 0$, $v_t = 0$), which is a reasonable approximation for a typical ICME shock. The jump conditions then reduce to

$$[\rho v_n] = 0, \tag{4.1}$$

$$\left[\rho v_n^2 + p^2 + \frac{B_t^2}{2\mu_0}\right] = 0, \tag{4.2}$$

$$\left[\left(\frac{\gamma}{\gamma-1}\frac{p}{\rho} + \frac{v^2}{2}\right)\rho v_n + \frac{v_n B_t^2}{\mu_0}\right] = 0, \tag{4.3}$$

$$[\mathbf{v_n} \times \mathbf{B_t}] = 0. \tag{4.4}$$

Denoting the inflow velocity in the simulation coordinates as $v'_{1,2}$, where 1 and 2 correspond to sunward and anti-sunward of the shock, respectively, we can calculate the normal velocity in the rest frame of the shock as $v_n = v' - v_s$, where v_s is the shock speed. Substituting this into equation (4.1), we have

$$v_s = \frac{n_1 v_{n1} - n_2 v_{n2}}{n_1 - n_2}. \tag{4.5}$$

From this the shock speed can be calculated to obtain the values for v_n, and substituted into equation (4.2) to solve for one of either the thermal pressure $n_1 k_B T_1$ or magnetic pressure $B_1^2/2\mu_0$, provided the other is prescribed. Thus for a chosen jump in density, velocity and magnetic field we can find the jump in temperature required to satisfy the RH conditions. For the majority of the shocks in this study, we use jumps of n = 5 cm^{-3} $\rightarrow$ 10 cm^{-3}, v_x = 400 km^{-1} $\rightarrow$ 600 kms^{-1} and B_z = -2 nT $\rightarrow$ -4 nT; the resulting temperature jump is $T_{i,e}$ = 5 eV $\rightarrow$ 417 eV, providing the full set of solar wind conditions required to simulate the shock.

To investigate the clock-angle dependence of the separator response, as well as the geoefficiency of the shock for different clock-angles, we use three different orientations of θ_{IMF} = 180° (due southward), 135° (equally southward and duskward) and 90° (due duskward). Due to the coplanarity theorem (see section 1.2.4) the field orientation cannot vary either side of the shock and so the magnetosphere is initialised with the different θ_{IMF}. We do not investigate northward IMF orientations, since we are interested in sudden commencements which would be most likely to develop into geomagnetic storms. We then simulate a θ_{IMF} = 180° shock with 30° dipole tilt angle, representing an event occurring during Northern summer, revealing any seasonal dependence. Finally, we simulate a much stronger shock for the purely southward IMF case, for which n = 5 cm^{-3} $\rightarrow$ 20 cm^{-3} and v_x = 400 kms^{-1} $\rightarrow$ 1000, such that $T_{i,e}$ = 1250 eV. The jump in IMF is kept the same, so as to isolate the effect of the dynamic pressure. The full set of different simulation conditions is shown in Table 4.1.

Shock	θ_{IMF} / °	μ / °	n_2 / cm^{-3}	v_2 / kms^{-1}	$T_{i,e}$ / eV	B_2 / nT
1	180	0	10	600	417	4
2	135	0	10	600	417	4
3	90	0	10	600	417	4
4	180	30	10	600	417	4
5	180	0	20	1000	1250	4

Table 4.1 – Upstream jump conditions for each simulated shock, along with the different IMF clock angles and tilt angles with which the magnetosphere is initialised.

Shock 5 presents the limit of a four-fold increase in density allowed by the RH conditions for the $\gamma = 5/3$ case. Previous studies have identified typical compression ratios between 1.2 and 2 for fast forward shocks at 1 AU, and shock speeds of 50-200 kms^{-1} (Berdichevsky et al., 2000). The jump conditions in this study all yield shock speeds of 200 kms^{-1} in the upstream solar wind frame and hence are representative of real events, though significantly greater shock speeds are possible for the most extreme events (Tsurutani and Lakhina, 2014). Furthermore, the results should be generalisable as we are only focussing on the dayside magnetosphere, meaning any conclusions should not be too dependent on the system being in steady-state for driving under the given IMF clock

angle. This would be less true if we were interested in the nightside reconnection response, since it would be sensitive to the particular configuration of the magnetotail. Furthermore, assuming the IMF orientation is unlikely to change significantly either side of the shock over the timescales of interest, the synthetic conditions should still be broadly representative of impact by an ICME-driven shock that generates a sheath-driven geomagnetic storm (at least for southward IMF).

4.2.1 Explicit Resistivity

The shocks are simulated first with no explicit resistivity included, such that the magnetosphere is collisionless and the compression of the magnetopause is physically accurate. In order to closely examine the evolution in the reconnection electric field along the separator, we then repeat Shocks 1, 3 and 5 with an explicit resistivity of $\eta/\mu_0 = 5 \times 10^{10}$ $\mathrm{m^2 s^{-1}}$. This ensures smoothness of current sheets for ease of tracing the dynamic separators, as well as a means to accurately quantify the local reconnection rate. This also reduces any model-dependence in the results, hence improving reproducibility.

Whilst the full electron energy equation (2.4) in Gorgon includes Ohmic heating due to resistivity, this is switched off in all of the runs to reduce the effect of non-ideal phenomena. Indeed, a resistive magnetosphere is a significant deviation from reality even in steady-state, and so we only focus on the dayside reconnection region during compression when analysing the results. To first verify that the explicit resistivity is performing its intended role, we plot the magnetic connectivity in the X-Z plane, as well as the magnetopause current sheet which should show clear differences versus the numerical resistivity case.

The effect on the global magnetic connectivity is shown in Figure 4.1. Most notable is the location of the tail reconnection site, which is far downtail in the collisionless case, and has moved Earthward to $X \sim 14\ R_E$ in the resistive case. Some spurious patches of open field leak onto the nightside closed field in the collisionless simulation, but disappear in the resistive case. This suggests less bursty reconnection in general with a large η, meaning FTEs will be less likely to occur on the dayside, as desired. The dayside topology has changed significantly, containing more closed flux which balances the reduced closed flux content on the nightside. The separatrices bounding the IMF and the open field now appear rounder on the dayside in general, but the magnetopause stand-off distance is roughly the same along the subsolar line. Whilst these topological changes will likely affect the shape of the separators, our goal with the resistive runs is not to compare the geometric evolution but rather the electric field across the reconnection line during the shock propagation, the timescales of which should be consistent.

The impact on the magnetopause current sheet is shown in Figure 4.2, where the bow shock current is also visible. The effect of the resistivity is to smooth these out, resulting in a thicker and larger overall magnetopause current sheet in the resistive case. However, the collisionless simulation yields larger peak current densities of order $\sim$20 $\mathrm{nAm^{-2}}$

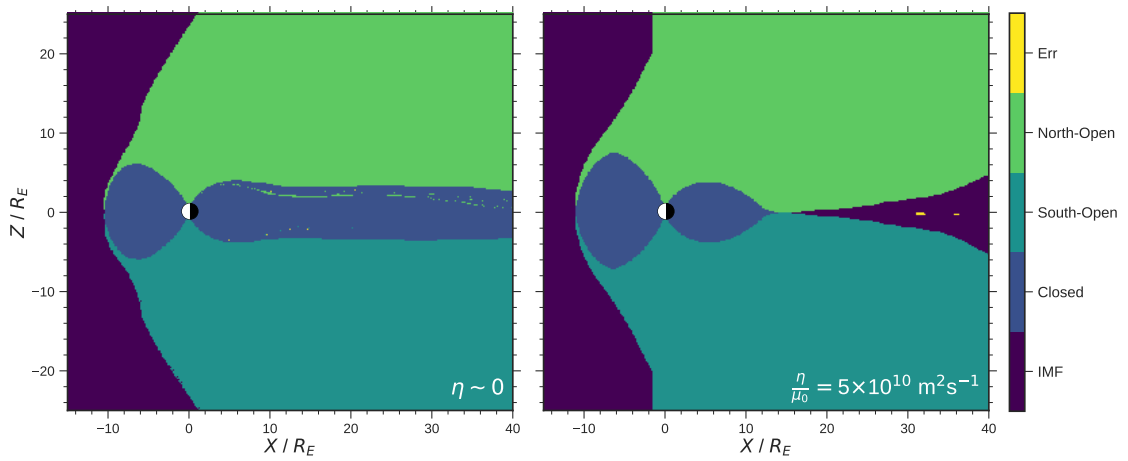

Figure 4.1 – Magnetic connectivity in the X-Z plane of the magnetosphere for different resistivities η at 2h, prior to the arrival of Shock 1.

which is consistent with typical values in literature (e.g. Ganushkina et al., 2018). Therefore whilst numerical diffusion still allows for a more physically representative boundary, as expected, the resistive diffusion is achieving its intended purpose of stabilising the current sheet and improving ease of analysis.

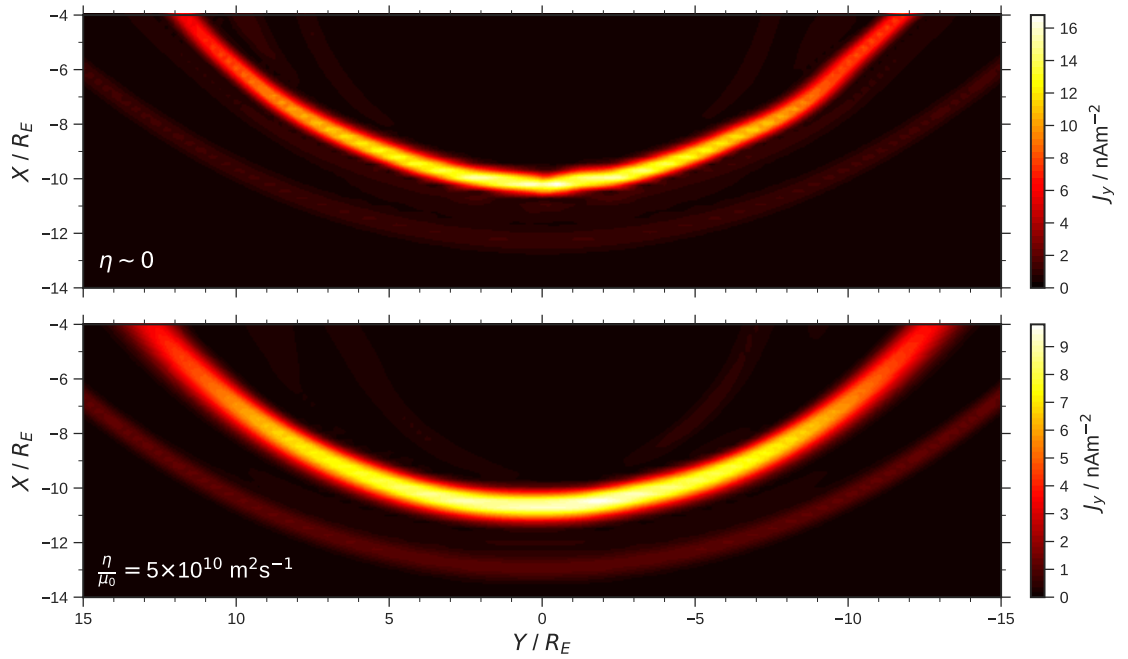

Figure 4.2 – Magnitude of J_y in the equatorial dayside magnetosphere for different resistivities η at 2h, prior to the arrival of Shock 1. The magnetopause is the band of most intense current, with the bow shock visible just below in each plot.

This also demonstrates that the explicit diffusion is dominating over the numerical diffusion: in principle the global reconnection rate should remain broadly the same despite whatever is causing the dissipation along the separator, as the same geoeffective electric field is being provided by the solar wind. In the southward IMF case the reconnection line will lie essentially along the equatorial magnetopause. Since the current

density is weaker in the resistive simulation, the explicit resistivity must be larger than the numerical resistivity to achieve the same local reconnection rate $E_{\parallel} = \eta J_{\parallel}$ at a given point.

4.3 Global Topology and Shock Propagation

We first examine the response of the magnetosphere to the shocks, to demonstrate the compression of the magnetopause and the propagation of shock-driven disturbances through the system. Figure 4.3 shows the evolution of the thermal pressure during the period of propagation just after arrival. The shock can be seen coming in from the left-hand edge, making contact with the bow shock at around 7340s and the magnetopause at $\sim 10R_E$ at around 7360s. Since the solar wind conditions prior to contact are time-constant, the system is initially in a quasi-steady configuration. By 7380s the jump in dynamic pressure has compressed the bow shock and magnetopause, and the shock begins to advance along dawn and dusk towards the flanks, distorting the magnetopause surface at the shock front. By 7480s the shock has passed the terminator plane, and the magnetopause is at its minimum stand-off distance.

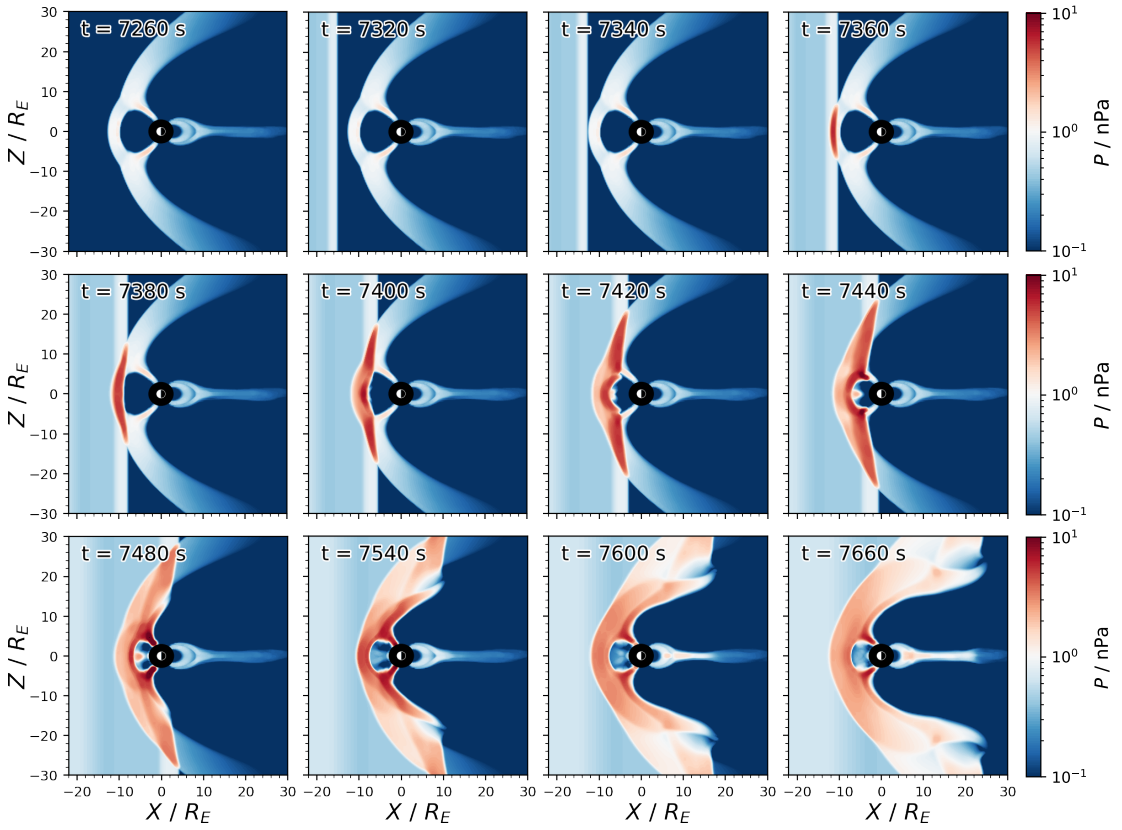

Figure 4.3 – Slices in the noon-midnight plane for Shock 1 showing the thermal pressure P over time as the shock propagates through the magnetosphere.

A fast wave is seen propagating throughout the dayside magnetosphere from 7420s

onwards as a pressure front, which reflects off the inner boundary and arrests the compression of the magnetopause. By 7540s the stand-off distance has returned to $\sim 8\ R_E$, where it then remains relatively steady (except for some lower-amplitude oscillations) and relaxes to balance the post-shock driving conditions. This motion will drastically change the magnetosheath flow in the frame of the magnetopause, and thus should modulate the coupling with the solar wind. However, separating the different enhancements in dayside and nightside reconnection in these simulations - which requires accurately quantifying the nightside rate - is extremely difficult.

On the nightside, the plasma sheet pressure is enhanced from $\sim$ 7600s which may trigger the occurrence of nightside reconnection, roughly 5 minutes after dayside reconnection should be enhanced. However we note the location of the tail reconnection site far downtail in the initial configuration, which may delay the closure of tail flux. This distance will depend on the grid resolution in the tail and the numerics of the model, as well as being highly sensitive to the preceding driving conditions. It is therefore difficult to generalise the effect on tail reconnection, and the characteristic timescales over which it is enhanced purely based on the observed enhancement of the plasma sheet pressure. In order to gain a purely qualitative understanding, we instead analyse the resistive simulation of Shock 5, in which the tail reconnection site is much closer to the Earth and for which the shock propagates more quickly than Shock 1. Figure 4.4 shows the connectivity in the X-Z plane during the propagation of the shock.

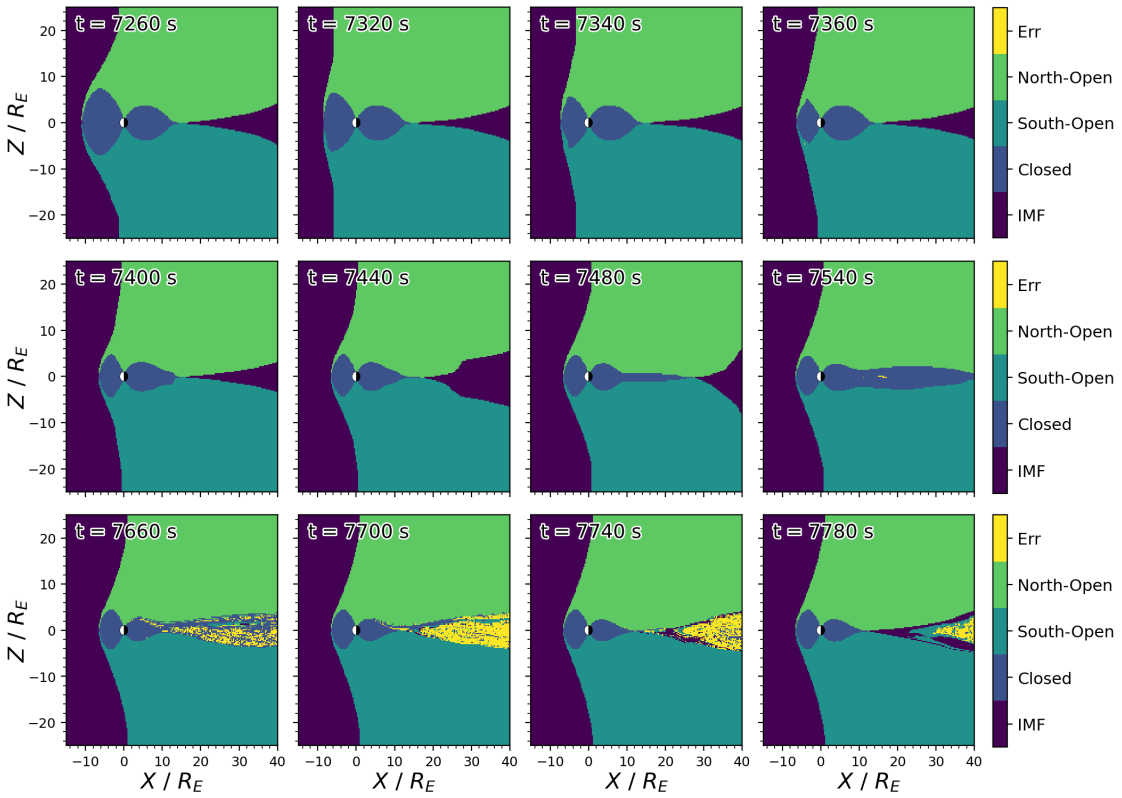

Figure 4.4 – Slices in the noon-midnight plane for Shock 5 using an explicit resistivity, showing the magnetic connectivity over time as the shock propagates through the magnetosphere.

The shock impacts the magnetopause at $\sim$ 7280s, rapidly compressing the dayside before influencing the nightside closed field region at $\sim$ 7400s. Rather than immediately triggering reconnection, the closed field is in fact dragged downtail by the shock front, stretching and thinning the current sheet. The sudden growth of disconnected field coloured in yellow (which does not terminate at any boundaries) indicates the formation of a plasmoid due to the eventual triggering of reconnection at separate locations both near and far from the Earth. The plasmoid is then ejected and the nightside field is dipolarised, reforming a reconnection line near the Earth at $\sim$ 7740s.

These dynamics are generally consistent with the triggering of a substorm, with the distinction that the nightside closed field is stretched out and the current sheet is thinned by the shock, rather than by the build-up of open flux over an already distant reconnection line which then triggers the formation of a new near-Earth neutral line. Therefore whilst the shock clearly acts to close a significant portion of open flux, thus contracting the polar cap, the timescale over which this happens is heavily dependent on the initial configuration of the tail and location of nightside reconnection. A more canonical substorm mechanism (as described in section 1.3.4) may be found under different tail configurations, but we reserve this for future study. In any case, it is clear that there will be an initial period prior to the triggering of nightside reconnection where any enhancement in dayside reconnection will increase the amount of open flux in the system, expanding the polar cap. Thus, we can focus our analysis on this time period.

Before turning our attention to dayside reconnection and the location of the magnetic separators, we first examine the behaviour of magnetic null points (which mark the end points of the dayside separators) at the terminator plane in response to the shock. For the $\theta_{IMF} = 180^\circ$ runs, these should lie everywhere along the equatorial plane and so do not present a convenient means to select the start point for the separators. For the 135° and 90° clock angle cases, as well as the 30° tilt angle case, the nulls seem the natural place to trace from. However due to the compression of the magnetopause the vacuum superposition solutions become unreliable as a means to identify the terminating nulls. To determine if the nulls do indeed remain relatively anchored during the shock propagation we plot their location in Figure 4.5 during the passage of Shock 3. Only nulls close to the magnetopause are shown (excluding any in the magnetotail current sheet), and the 'terminating' nulls, i.e. those closest to the vacuum predictions, are coloured in red and green. The approximate location of the magnetopause at $X = 0$ is inferred from Figure 4.3.

Prior to the shock arrival the terminating nulls lie along the terminator plane, as expected, sitting at high latitudes in both dawn and dusk. Additional spurious nulls are seen, but we find these only exist in pairs and so do not contradict with the topological order required for the labelled terminating nulls to be connected by a single separator. By 7480s contact with the dawn and dusk null points is made; these are then dragged downstream as the shock front propagates, and proceed into the nightside over the following minute. This must arise from the deformation of the magnetopause and the resulting change in the orientation of the magnetospheric field, as well as the draped

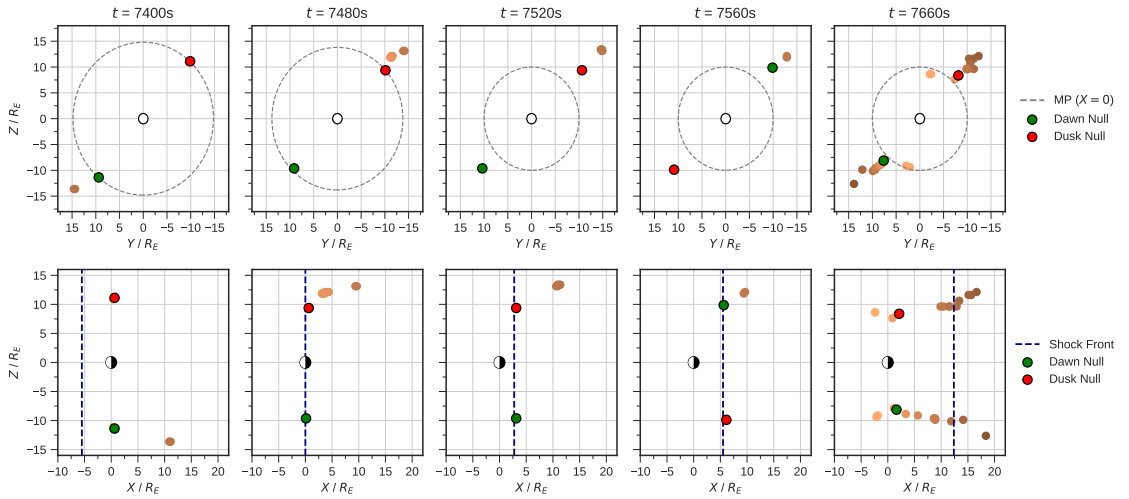

Figure 4.5 – Magnetic null points near the magnetopause during the propagation of Shock 3. The nulls at dawn and dusk closest to the vacuum superposition solutions are labelled in green and red, respectively. The intersection of the magnetopause with the terminator plane and the location of the shock front are indicated, and are approximated.

magnetosheath field.

The implication is that the length of the dayside portion of the separator connecting these nulls is be extended. This does not automatically imply magnetopause reconnection is active over the nightside portion, since the electric field could be negligibly small over this additional extent given that the field and flow are quasi-parallel here. However, the flattening of the surface and enhancement of plasma properties in the vicinity of the shock may permit some reconnection in regions where it is not typically thought to occur. We note that the resistive runs do not reproduce such a large displacement of the nulls; this suggests either that a large resistivity allows diffusion of the field in such a way that the topology is better preserved, or that the null motion could be a peculiarity of the grid effects. However, since the magnetosphere is essentially collisionless it cannot be assumed that the resistive results are more representative of reality.

By 7660s new nulls have appeared near the terminator plane, closer to the vacuum predictions, though a large number of nulls still exist trailing the shock front as far as 20 R_E downtail. Two pairs of nulls are seen at high latitudes around $Y \sim \pm 2\ R_E$, which may indicate high-latitude reconnection typically associated with northward IMF. This may also represent the formation of new, steadier dayside separator that remains in place during the post-shock conditions. Note that this analysis has not been repeated for the other shocks as individual nulls are significantly harder to track for mostly southward IMF, since they exist in much greater number. However we have found in internal investigations that they are indeed initially carried downstream even for 180°, before being repopulated on the dayside. Thus this topological phenomenon does seem to pervade for a variety of IMF orientations.

Overall the results show a highly complex topological behaviour along the shocked magnetospheric boundary, which is a significant deviation from the typical steady picture of reconnection. Whether this does indicate magnetopause reconnection occurring

within the nightside is unclear and is difficult to determine, and is a topic for future investigation. For now we turn our attention to just the dayside portion of the separator, and explore how the total reconnection rate is impacted.

4.4 Magnetopause Reconnection Impact

4.4.1 Separator Response

For a 180° clock angle, i.e. purely southward IMF, the separator lies essentially along the equatorial plane. Its location can therefore be approximated simply by finding the locus of points where $B_z = 0$, which effectively corresponds to the magnetopause. Though it strictly may deviate somewhat in the Z-direction, as seen in Figure 3.9, we are not initially concerned about sampling the reconnection rate locally along the separator and therefore there is little benefit in attempting to trace it out in fine detail. The evolution of the dayside separators during the initial phase of compression - and prior to any subsequent expansion of the boundary - is shown in Figure 4.6 for Shocks 1 and 5.

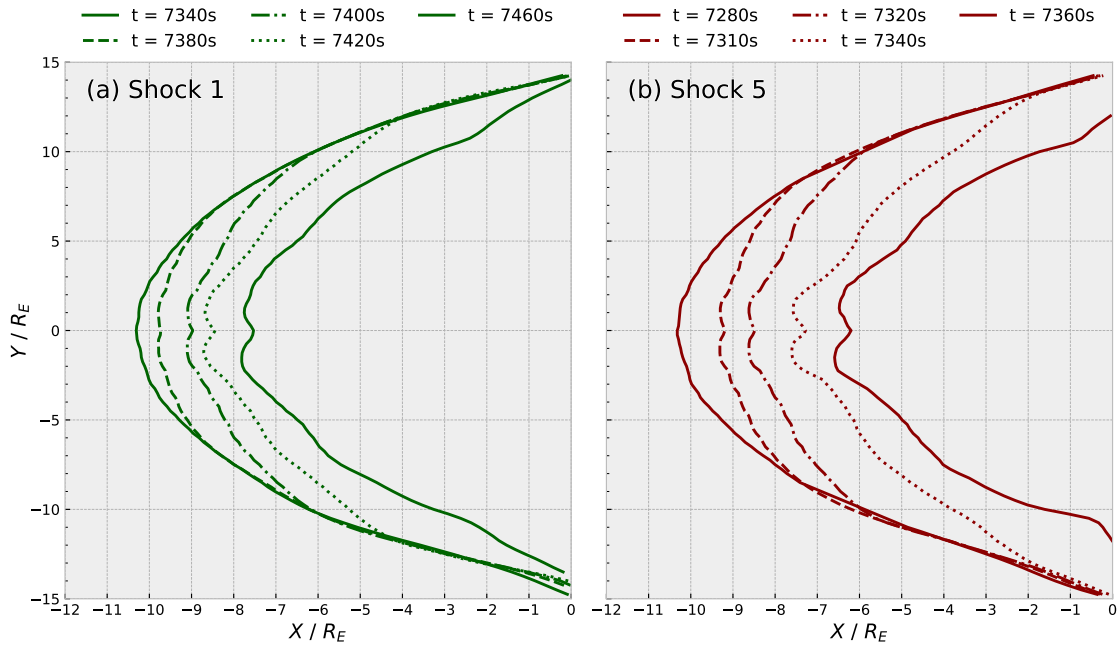

Figure 4.6 – Evolution of the approximate dayside magnetic separator over time for Shocks 1 and 5 during the initial compression phase.

The portion of the separator in contact with the shock is compressed immediately, whilst the regions downstream of the shock front remain in their initial configuration until it gradually propagates into the nightside. This incoherent motion results in a relatively sharp gradient at the shock interface which will be associated with a strong current. In both cases the subsolar magnetopause begins to erode, which suggests that a large amount of flux is being opened. This is particularly severe in the final timesteps. The region around noon continues to move inwards despite the passage of the shock, and the displacement is greater for Shock 5, due to its much greater dynamic pressure.

Since the separator is in motion during the compression phase (with an average subsolar speed of $\sim$ 130 kms^{-1} in the case of Shock 1) we should expect some effect on the magnetosheath electric field which is frame-dependent. This suggests there is likely to be a non-linear behaviour in the reconnection rate. This will be further complicated for the other simulated shocks, since the separators will lie out of the equatorial plane.

The geometry of the separator is closely controlled by the orientation of the fields either side of the magnetopause. As shown in the previous Chapter, the dipole tilt has a significant effect on the length of the separator, causing it to shift from the subsolar magnetopause. Other simulations have shown that the IMF clock angle causes it to rotate about the subsolar line, such that it points along Z for a purely northward IMF if there are no other asymmetries in the driving (Komar et al., 2013). Since this will also control the local and total reconnection rate on the magnetopause, the geoefficiency of a shock during the propagation phase is likely to be controlled by the clock and tilt angles as well. For example, the IMF orientation controls the configuration of the magnetotail current sheet (e.g. Case et al., 2018) which may also affect the impact on tail reconnection.

To identify the location of the dayside magnetic separator during SC, we start by determining its intersection with the terminator plane. Since the method of tracing from terminating nulls is no longer reliable due to the presence of the shock, we simply sample the connectivity close to the vacuum null predictions and find the convergence point of different domains, as shown in the right-hand panel of Figure 3.7. In order to track the separator motion during the magnetopause compression phase we choose only a few sample timesteps: these are prior to the shock impact, during the propagation along the dayside, and just before magnetopause begins to move outwards again. We employ the same separator tracing algorithm as in the previous Chapter, and in the majority of cases use hemispheres of radius 0.5 R_E and resolution 50×50. The results for Shocks 2-4 are shown in Figure 4.7.

The overall motion of the separators is similar to that of Shock 1. For both shocks 2 and 4 the same erosion of the subsolar magnetopause is seen, but this is not present for Shock 3. The implication is that there is less flux being opened for the 90° clock angle case, which is to be expected since this IMF orientation is less favourable for reconnection. For Shock 2, the separator is bent in the Z-direction at the shock front at 7400s and 7420s, which is a significant deviation from the steady configuration as this will dramatically alter the field orientations either side of the magnetopause, and hence the local reconnection electric field. A similar effect is seen at 7460s for Shock 3. Based on these results we expect the reconnection rate to be enhanced immediately at the shock interface.

For Shock 4 the trend is more comparable to Shock 1, with the exception that it is hinged from the subsolar point and shifts southward towards the flanks, as explored in the previous chapter. At the subsolar region the separator deviates downwards initially, indicative of an FTE. The compression of the magnetopause does not process this feature away, but rather it is seen for the subsequent timesteps. This suggests that more complex magnetic field structures may survive this relative short time-period evolution,

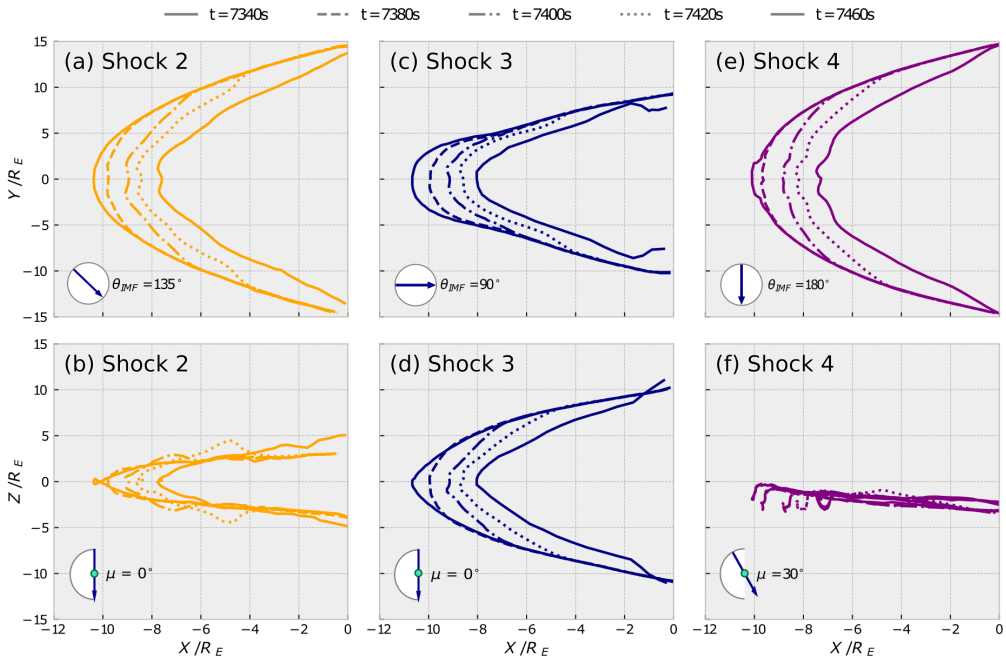

Figure 4.7 – Evolution of the dayside magnetic separator over time for Shocks 2, 3 and 4 during the initial compression phase. The IMF clock angle θ_{IFM} and tilt angle μ is indicated in each case.

regardless of how much reconnection is occurring.

4.4.2 Dayside Reconnection Rate

Unlike in the previous simulations in Chapter 3, there is no clear expectation that the voltage across the separator maps down onto the ionosphere as the CPCP; this is a result of the strong compression of the magnetosphere, meaning the system is far from steady-state. The presence of induced magnetospheric electric fields and time-delays in the ionospheric response may result in a mismatch with the electrostatic potential; quantifying the dayside reconnection rate is therefore difficult. Since the magnetosphere is initially quasi-steady prior to the shock arrival, the dayside and nightside reconnection rates are largely in balance and the dayside rate Φ_D can be taken as roughly constant over a few minutes. For the value at some general time t_1 after the time of impact t_0 - and prior to the compression of the magnetotail current sheet - the dayside rate can then be approximated as

$$\Phi_D(t_1) \approx \Phi_D(t_0) + \frac{dF_{PC}(t_1)}{dt}, \tag{4.6}$$

where we can estimate

$$\frac{dF_{PC}(t_1)}{dt} \approx \frac{F_{PC}(t_1 + \Delta t) - F_{PC}(t_1 - \Delta t)}{2\Delta t}, \tag{4.7}$$

for some sampling cadence Δt. Note that we expect the initial dayside reconnection rates to be $\lesssim 40$ kV as per the voltages found in the previous Chapter, and so the total dayside rate should be dominated by dF_{PC}/dt. Figure 4.8 shows the value of dF_{PC}/dt in the

Northern hemisphere over the first 5 minutes of shock propagation for each event. The flux is calculated in the same way as in the previous Chapter, sampled every 10s, and the time t is zeroed at 7340s for Shocks 1-4 and at 7280s for Shock 5 (which propagates more quickly). In each case the arrival of the shock results in a sharp increase in the dayside reconnection rate, which then drops from its peak as the magnetopause is compressed. This must result from the initial pile-up of shocked magnetosheath plasma and magnetic field, in agreement with findings by previous studies (e.g. Connor et al., 2014).

For Shocks 1-4 this peak is followed by another increase after 2-3 minutes, which is most pronounced for Shock 1. This timing roughly corresponds to the expansion of the magnetopause following the reflection of a pressure wave off the inner boundary as seen in Figure 4.3; it therefore appears that the expansion and contraction of the boundary modulates the reconnection rate, since the inflow speed of the magnetosheath plasma varies in the rest frame of the separator. Further smaller-scale oscillations are seen, which may correspond to higher order oscillations in the magnetosheath plasma e.g. waves reflecting between the bow shock and the magnetopause, as well as further oscillations in the magnetopause. Shock 5 does not show the same behaviour, which we attribute to the triggering of nightside reconnection after 2-3 minutes which then dominates the dayside rate, leading to negative rates of change of flux after 5 minutes.

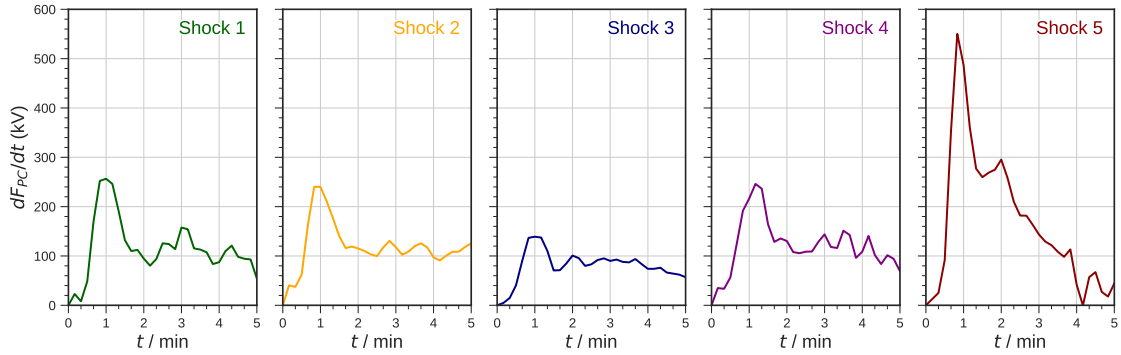

Figure 4.8 – Rate of change of open flux F_{PC} in the Northern hemisphere for each Shock, during the first 5 minutes of propagation.

One important caveat to address when quantitatively interpreting the results is in the conservation of an injected shock as it propagates through the simulation box. In order to properly treat shocks - especially the bow shock - an artificial viscosity is used in the code (see section 2.2), which confines them to a few grid cells and removes spurious oscillations. However this is naturally limited by the grid resolution, and some spreading of a propagating shock is inevitable unless one employs an adaptive grid which greatly enhances the resolution local to the shock front (Torrilhon, 2003).

The consequence for this study is that the conditions in the magnetosheath are to some extent dependent on the grid resolution, and may slightly over- or under-exaggerate the magnetosheath field strength and flow speed in the cells containing the propagating shock over dynamical timescales. Furthermore, the pile-up of shocked magnetosheath plasma may be broader than in reality. The use of an artificial viscosity minimises these

effects, as well as the choice of a high resolution (0.25 R_E) solar wind compared to simulations where the grid is designed to be more coarse in the solar wind to save computation time. The results should also be general to other models, since the same effect will be present to some extent in any simulations of events like these. Nonetheless we must be careful when comparing the exact values between the weaker and denser shocks, and primarily focus on the overall behaviour.

To aid with this, the trend between the different shocks is summarised in Table 4.2, which shows the open flux content in the Northern hemisphere prior to and 5min after the arrival of each shock, along with the peak and average rates of change in open flux. Examining Shocks 1-3, the peak change in reconnection rate during SC instead seems to show a much weaker clock-angle dependence than the $\sim \sin^4(\theta_{IMF}/2)$ assumed in many commonly-used coupling functions (e.g. Milan et al., 2012 and references therein), which also assume a (generally) linear trend in velocity. A more physically motivated coupling function may thus be required for this dynamic scenario. A similar conclusion can be made from the tilted dipole case, where the flux content is smaller but the peak rates are comparable to Shock 1. Note that other simulation studies have also found a weaker clock-angle dependence than expected by some empirical and theoretical formulae (e.g. Wang et al., 2014, Komar and Cassak, 2016), so this is likely not a unique effect of the compression. Nonetheless the fact that a strong enhancement is seen for all orientations and persists for some time after impact shows that the jump in dynamic pressure has a significant control over the strength of coupling, which is not greatly limited by the clock angle.

Shock	F_{PC} (GWb)		dF_{PC}/dt (kV)	
	$t = 0$	$t = 5$ min	Average	Peak
1	0.65	0.68	118	257
2	0.55	0.59	122	240
3	0.33	0.36	82	139
4	0.56	0.60	123	246
5	0.65	0.70	169	550

Table 4.2 – Open flux in the Northern hemisphere before and after the dayside shock propagation, along with the peak and average rates of change of Northern open flux.

Finally, Shock 5 has a substantially greater peak dF_{PC}/dt than Shock 1, with the sole distinguishing factor between each event being the dynamic pressure jump. However whilst the speed of post-shock solar wind differed by a factor of 1.67, the ratio of the peak rates is clearly greater at 2.14. Since the upstream density in Shock 5 is twice that of Shock 1, this may suggest that the density of the DPE is also important during compression, even if density is not expected to play a role in dayside coupling in more steady conditions. However this is difficult to distinguish from other non-linear dependencies in the magnetosheath field strength and flow speed. Note that the factor of 2 increase in the jump in IMF strength will also contribute to the increase in the reconnection rate, but this is consistent across all of the shocks.

Overall whilst the clock (and tilt) angle does clearly control the dayside coupling, this dependence is smaller than expected and the jump in dynamic pressure is highly effective at enhancing the peak and average reconnection rates for all orientations. This may be related to the distortion in the magnetopause as the shock is propagating; the separator is flattened and reduces in extent, which will greatly alter the relative orientation (i.e. shear angle) between the IMF and magnetospheric field and the total integrated voltage. This may reduce the geoefficiency for mostly southward IMF cases, and/or increase it for orientations closer to a 90° clock angle, which could help to explain trends seen in previous studies of dynamic pressure enhancements (e.g. Andreeova et al., 2011b).

We note that the average reconnection rates show a weaker trend than the peak rates. In part this can be explained by an increase in nightside reconnection prior to t = 5 min, which may be more intense for more geoeffective cases and close more of the newly opened flux. This is especially true for Shock 5 where it has clearly been triggered earlier due to the greater shock speed. Furthermore the effect of oscillatory behaviour at the magnetopause may be to limit the total flux that can be opened during this initial period. This would complicate the picture at the polar cap, where there is already some time delay before it is seen to expand, and faster shocks would also lead to an earlier contraction which may be more easily observed than an initial expansion.

4.4.3 Local Electric Field

We now utilise our resistive runs to more closely examine how the pressure enhancement generates an increased reconnection electric field. The local reconnection rate is calculated as $\mathbf{E}_{\parallel} = \eta \mathbf{J}_{\parallel}$, ignoring any motional electric field component ($\mathbf{E} = -\mathbf{v} \times \mathbf{B}$) which would be frame-dependent and require transforming into the local inertial frame along the moving separators. This negates any contributions due to numerical diffusion, but as explained earlier this is dominated by the resistive diffusion and would introduce further model-dependence in the results. Over dynamical timescales and without temporal averaging, any calculations based purely on numerical diffusion may also be significantly erroneous. It should be stressed once again that the magnetosheath conditions depend on the conservation of the shocks, and that we are interested only in the general trends seen. We do not compute any voltages to compare to the earlier values, since the resistivity will likely result in significant topological differences during compression, but rather use the resistive simulations to provide further insight into the results.

Figure 4.9 shows the reconnection rate along the separator for Shock 1 as the shock propagates over the dayside. At $t = 0$s the rate is just dependent on the preceding quiet solar wind conditions, showing symmetry about the subsolar point where it peaks at $\sim$ 0.4 mVm^{-1}; after the shock reaches the magnetopause after 20s the electric field is amplified and the peak value at 40s is almost twice as large. The propagation of the shock is associated with a pair of local peaks in the electric field at dawn and dusk, due to compression of the magnetosheath magnetic field, which then travel down the flanks and into the nightside after 120s.

Thus the local reconnection rate is clearly enhanced at the shock front, and may even trigger reconnection at locations on the dayside magnetopause where it would not normally be expected. For example if the amplitude of these peaks remains sufficiently high in the nightside, then the observed tailward offset of the nulls could allow for magnetopause reconnection past the terminator plane, though it is not clear if this topological phenomenon is a result of grid effects or if it does reflect reality. Another amplification up to $\sim$ 1.2 mVm^{-1} is then seen at 160s, which coincides with the secondary peak in Figure 4.8 due to the expansion of the compressed magnetopause. After this the reconnection rate begins to relax as the magnetopause motion is slowly arrested (as seen in Figure 4.3.

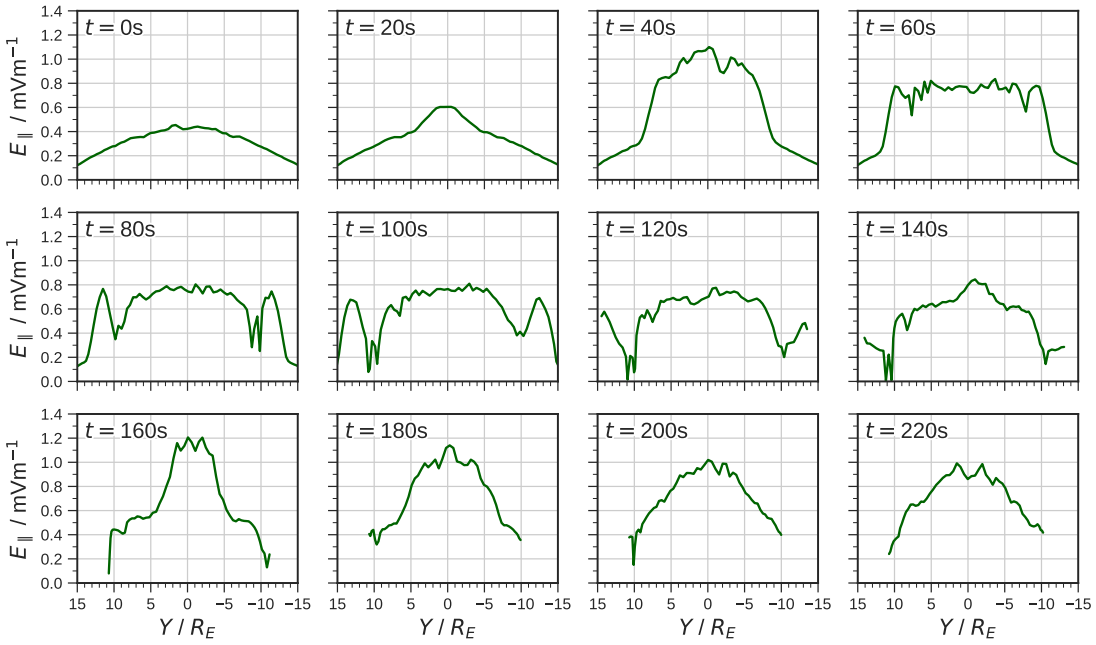

Figure 4.9 – Local reconnection rate $E_{||} = \eta J_{||}$ along the dayside separator for Shock 1 (due southward IMF) over time, where $t = 0$s corresponds to 7340s.

We note the appearance of spikes in the electric field profile around the subsolar region at later timesteps, as well as some dawn-dusk asymmetry despite the inherent symmetry in the setup. These are not present between 0-20s; the spikes are therefore likely a result of perturbations on the magnetopause resulting from the compression, with wavelengths which are not well captured by the 0.5 R_E separator resolution. The dawn-dusk asymmetry can also be attributed to limited spatial sampling, though this may also arise due to the breaking of symmetry by numerical instabilities along the compressed boundary. Since these resistive conditions do not correspond to a realistic magnetopause, we do not investigate the nature of these effects any further in the present study, though locating and analysing the magnetopause (or fluopause) during the compression could be a topic of future work.

We now look at the 90° clock angle case shown in Figure 4.10 for Shock 3. The initial state prior to the shock arrival has a weaker reconnection electric field than for purely

southward IMF, and shows a smaller enhancement from 20-40s, but like before reaches approximately 3 times the peak amplitude. The same effect of enhanced electric field along the propagating shock front is seen up to 120s, as well as a sudden rise at 160s which again as for Shock 1 is roughly triple the initial intensity. Therefore the local enhancement of the reconnection rate appears to depend solely on the increase in dynamic pressure, and is not unique to the most geoeffective IMF orientations. Furthermore the fact this is restricted to the vicinity of the shock front reinforces that the enhancement is not totally dependent on the conservation of the shock and is ultimately driven by the sudden jump compared to the preceding conditions.

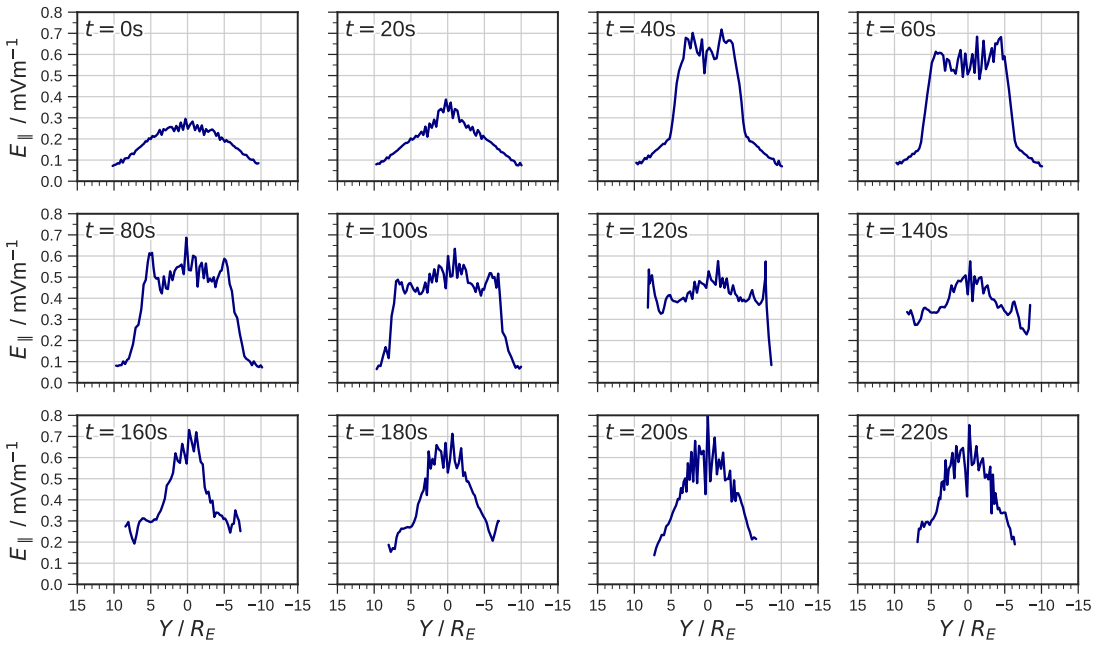

Figure 4.10 – Local reconnection rate $E_{||} = \eta J_{||}$ along the dayside separator for Shock 3 (due duskward IMF) over time, where $t = 0$s corresponds to 7340s.

Finally in Figure 4.11 we examine the case of the higher dynamic pressure Shock 5. Once again due to the greater shock speed we begin from an earlier time window starting at 7280s. The later timesteps also represent a more relaxed state where the magnetopause is relatively static, with $t = 140$s corresponding roughly to $t = 220$s in the previous two Figures in terms of the position of the shock front. This means that individual stages in the evolution are not directly comparable to before, but still demonstrate the same trends. As before the reconnection rate is enhanced at 20s, and the shock propagation generates the same local peaks down the flank magnetopause; during this phase the peak amplitude is ~ 1.2 mVm^{-1}, compared to ~ 0.8 mVm^{-1} for Shock 1. The sudden spike following the departure of the shock front into the nightside reaches ~ 2.4 mVm^{-1}, which is twice that seen for Shock 1. Since the ratio between the dynamic pressures of Shock 1 and Shock 5 is only 3:10, this suggests that the enhancement in the reconnection rate may be limited somewhat by the inertia of the preceding magnetosheath plasma, though the scaling likely depends on the spreading of the shock front prior to impact.

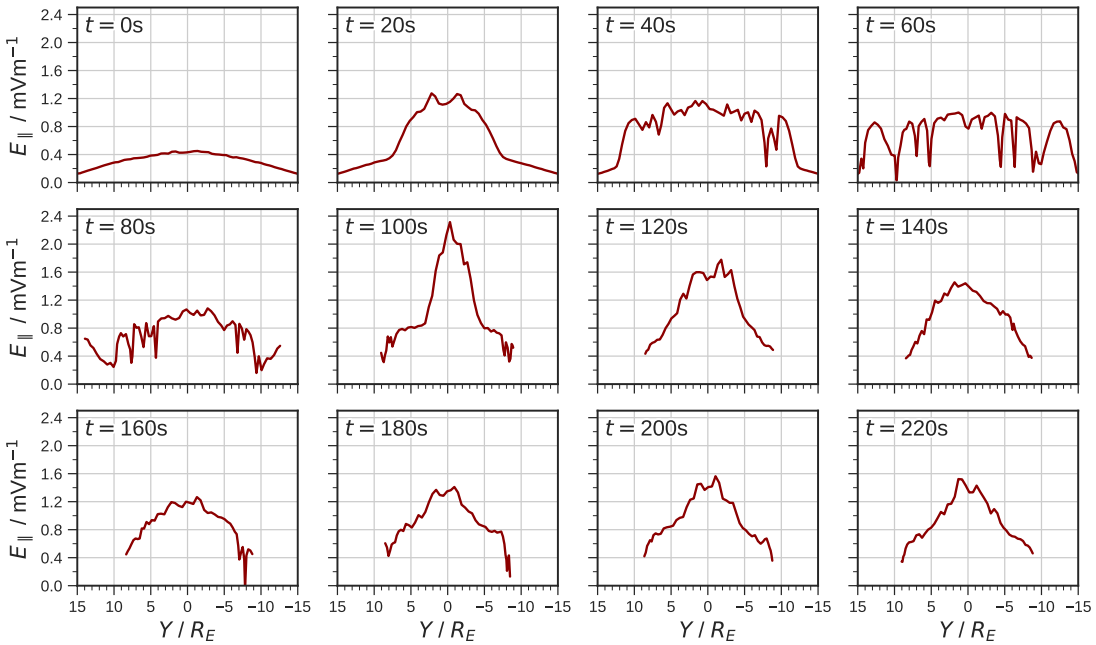

Figure 4.11 – Local reconnection rate $E_{||} = \eta J_{||}$ along the dayside separator for Shock 5 (due southward IMF, greater jump in dynamic pressure) over time, where $t = 0$s corresponds to 7280s.

4.5 Polar Cap and Ionospheric Signatures

The results described above all suggest that there should be clear ionospheric signatures showing the opening of flux in the polar cap and enhanced ionospheric convection associated with dayside reconnection. This should manifest as an expansion of the dayside OCB, and strong Region 1 FACs. Whilst the ionospheric response to sudden commencements has been widely studied in the literature, we will focus here on the aspects specific to our interests and only during the first several minutes after onset.

Figure 4.12 shows the Northern ionospheric FAC during the propagation of Shock 1, with the OCB given by the black line. Note that since there is no dipole tilt the Southern conditions should be a mirror image of those in the North. The first signatures are seen at 7440s, 100s after the shock arrival. At pre-noon and post-noon, the current profile becomes bipolar, with oppositely-directed FAC appearing at lower latitudes just outside of the polar cap region. These are in the same sense at the expected additional FAC signatures during the preliminary impulse (PI) phase (e.g. Fujita et al., 2003a).

The higher latitude sections grow in intensity, reaching $\sim 2\ \mu\text{Am}^{-2}$ in magnitude at 7520s, at which point the first compression signatures move into the nightside, consistent with the first set of main impulse (MI) phase FACs. An additional pair of oppositely-directed currents appear equatorward of these and eventually merge into the original Region 1 FACs by 7700s. The result is a much stronger Region 1 system lying at about 5-10° lower in latitude than in pre-shock conditions, and represents the second set of MI phase FACs, which remain steady unlike the transient current systems associated with

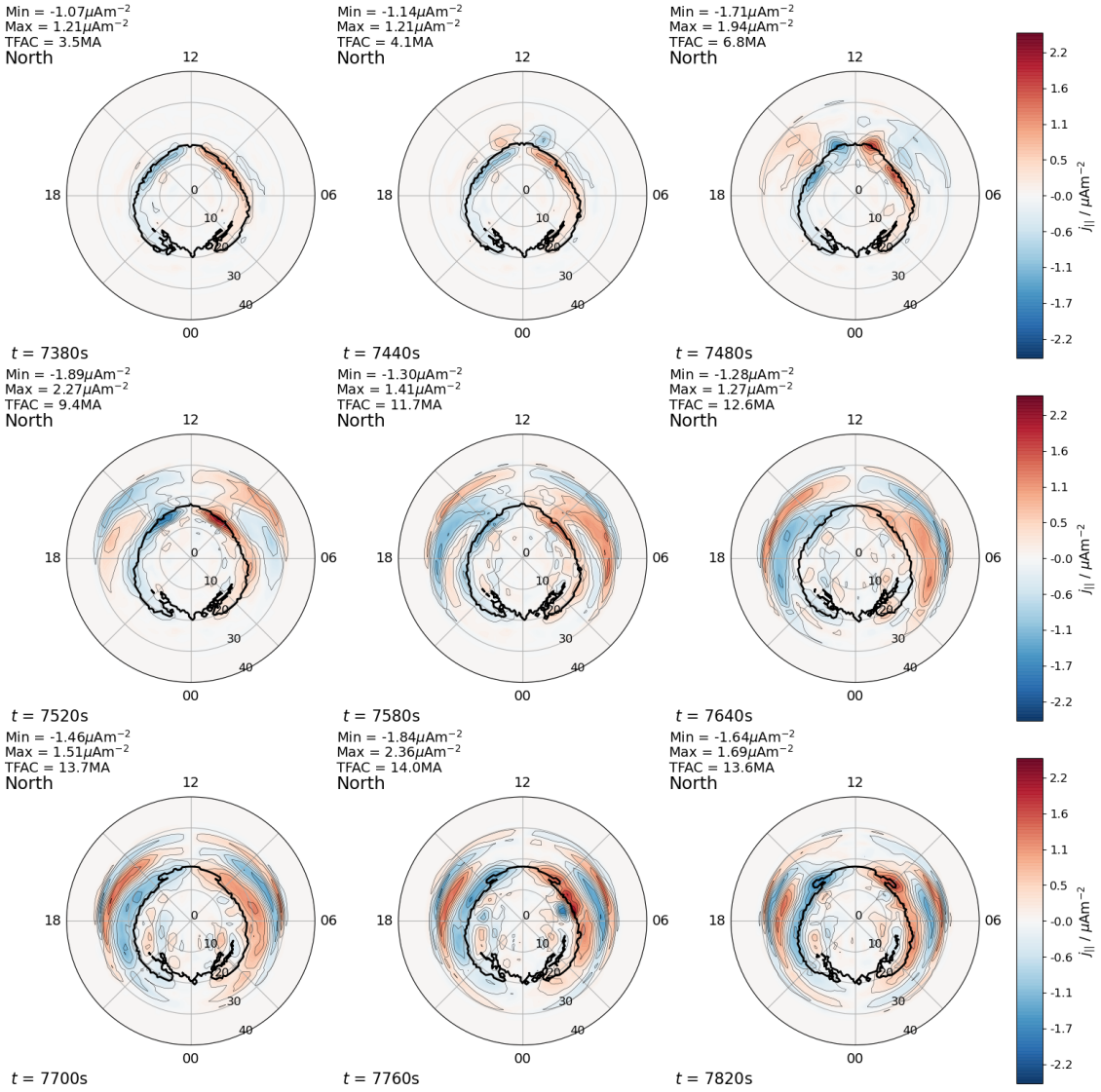

Figure 4.12 – Ionospheric field-aligned current in the Northern hemisphere during the propagation of Shock 1. The open-closed field line boundary is indicated by the black line each case.

the compressional wave at the front of the shock. Further examples of these appear equatorward even as late as 7820s, likely resulting from higher-order reflections of pressure waves off the inner boundary, as suggested in other simulations (Yu and Ridley, 2011).

The signatures in the OCB are minimal at first, though its morphology is slightly changed either side of noon at 7480s coincident with enhancement in the Region 1 FAC. Clearer effects are seen between 7580s-7640s, where it begins to flatten around noon and grow down to slightly lower latitudes. Between 7700s-7820s this expansion of the OCB proceeds into dawn and dusk, where finger-like structures of OCB attached to strong Region 1 signatures appear at both dawn and dusk. This is consistent with the expectations of enhanced dayside reconnection generating stronger convection and hence Region 1 FACs. No clear nightside OCB signatures are seen until after the final timestep shown here. This is consistent with our results, since we only expect nightside reconnection to

occur from 7600s onwards, and with a delay in the FAC comparable to the 100s delay on the dayside.

Overall whilst the immediate ionospheric response is dominated by the effects of the compression of the magnetopause, the underlying reconnection-driven FAC signatures continue to manifest and form a clearly recognisable Region 1 system after about 5 minutes. The expansion of the polar cap occurs over even longer timescales, but is still consistent with enhanced reconnection immediately after the arrival of the shock. Whilst the change in size of the OCB may be small over this initial time period, and indeed may be dominated by later nightside reconnection, attributing the effect of pressure enhancements as simply a contraction of the auroral oval may neglect key dynamics in the dayside ionosphere.

4.6 Discussion and Future Work

In this Chapter we have explored in detail the response of dayside reconnection during a sudden commencement, immediately after the arrival of an interplanetary shock. The shock-induced signatures which compress the magnetosphere and propagate through the system are consistent with those in previous studies using other GMHD codes. The evolution of the magnetic separator during the compression has been shown for a variety of different IMF clock angles, tilt angles and dynamic pressure enhancements. The reconnection line responds dynamically to the distortion of the magnetopause, reducing in extent as it is compressed and moving incoherently as the shock front propagates through the dayside magnetosphere. The separator is strongly bent at the shock interface for clock angles that are not purely southward, and magnetic null points which terminate the separator have been shown to be displaced tailward briefly after the point of contact. These complex topological phenomena demonstrate the extreme non-linearity of the dayside magnetosphere during such events.

The reconnection rate is enhanced after the arrival of the shock, increasing to a sharp peak value in excess of that for the eventual post-shock solar wind conditions which we attribute to piling up of the magnetosheath flow and magnetic field. The subsequent motion of the magnetopause and oscillations within the magnetosheath plasma appear to modulate the reconnection rate before it eventually settles into a steady-state once the magnetopause relaxes. The time-evolution of the reconnection rate shows a clear clock-angle dependence, but this is weaker than that predicted by typical coupling functions and a strong intensification is seen for all IMF orientations. This suggests the enhancement in coupling is driven mostly by the dynamic pressure, and is likely dominated by the velocity jump. This may help explain results in previous studies showing a reduced coupling efficiency during solar wind discontinuities for larger E_y (e.g. Andreeova et al., 2011b).

By complementing our results with resistive MHD simulations we have found that the local electric field along the magnetic separator is increased at the shock interface,

leading to an enhanced reconnection rate at regions away from the subsolar magnetopause. Our results also suggest this effect may even briefly spread to the nightside magnetopause. Thus we may expect reconnection to occur at different locations on the boundary than usually expected, though this should only occur briefly and may be difficult to verify with observations.

The signatures of the enhanced dayside coupling can be seen in the open-closed boundary in the ionosphere. An expansion of the OCB occurs near noon shortly after the onset of the SC, which spreads out to dawn and dusk and is closely associated with enhanced FACs. Transient current systems are seen resulting from the compression of the magnetosphere which generally agree with previous studies (e.g. Fujita et al., 2003a, Samsonov et al., 2010). One such system is in the same sense as the Region 1 FACs, and merges into the pre-existing Region 1 system to form steady bands of FAC that match the post-shock conditions. Signatures of enhanced nightside reconnection are not seen until several minutes later, but are likely to dominate the changes in the dayside polar cap if significant amounts of open flux are closed, as found in observations (e.g. Milan et al., 2004). Future investigation into the effects of compression of the tail would shed further light on this.

As with any simulation study there are a number of caveats to address. The dissipation mechanism responsible for reconnection in most of these runs was numerical diffusion, which will inevitably be sensitive to the grid and numerics of the model being used. Similar studies with other codes would help to generalise the results. However the use of resistive MHD simulations in this study does reproduce the same enhancement in reconnection and replicates the key trends, so we expect these to be reliable. A further issue is the conservation of the shock front as it propagates through the box, which will inevitably influence our results. However whilst the exact magnitude of any effects may differ between grid resolution and numerics - and indeed versus reality - the overall results should remain the same, and are explained in terms of dynamics which should be consistent. Finally, precipitation of particles in the ionosphere resulting from the compression of the system may locally enhance the ionospheric conductance on the dayside, whereas we have kept this uniform throughout. Nonetheless precipitation effects should be most prevalent following the triggering of nightside reconnection and hence are not as important for the period of interest.

Overall the results are in stark contrast to expectations from a steady model of reconnection according to commonly used coupling functions. Our simulations show that the dayside magnetosphere undergoes highly non-linear behaviour in the several minutes after the arrival of a dynamic pressure enhancement, and so attempts to use these functions when estimating the rate of change of open flux during SC may not be reliable. Recent studies in Gorgon have similarly shown that empirical magnetopause models fail to capture the complex motion of the magnetopause during such events (Desai et al., 2021). Care should therefore be taken when attempting to quantify the role of enhanced reconnection in driving geomagnetic activity shortly after onset, which we also expect to

be true for other discontinuities such as dynamic pressure decreases. This has implications not only for our understanding of magnetopause reconnection, but also for space weather impacts in general.

Chapter 5

Coupling Timescales during a Geomagnetic Storm

5.1 Introduction

Geomagnetic storms generate a complex and highly time-dependent response in the magnetosphere-ionosphere system. These are typically characterised by an enhancement of the ring current, measured by the disturbance stormtime (DST) index; only events with a DST of less than -50 nT, as inferred from ground magnetometers, are classified as storms (Lyons, 2000). They occur on average 1-2 times per month, and can be broken down into three phases: initial, main and recovery. The ring current grows during the initial phase, with the DST index dropping below -50 nT during the main phase which can last several hours. The subsequent recovery phase sees the ring current decay over as long as several days.

Fundamentally storms are driven by enhanced dayside reconnection due to prolonged periods of southward IMF, which also results in strong FACs and particle precipitation on the dayside ionosphere. Injection of high-energy particles into the ring current occurs via tail reconnection, which energises the plasma sheet after open field lines convect into the nightside. Tail reconnection during storms is associated with strong substorm activity, through which these events are responsible for the most intense space weather impacts, posing a significant societal risk. Understanding the timescales over which storms evolve is therefore crucial in mitigating their impact, and is strongly dependent on the global convection process.

5.1.1 Global Convection Timescales

As discussed in section 1.3.4, the sequence of dayside and nightside reconnection and global convection can be described according the the expanding/contracting polar cap (ECPC) paradigm (Cowley and Lockwood, 1992). From the ionospheric perspective, the opening of flux on the dayside causes the growth of the open-closed boundary (OCB) around noon, and the resulting flows lead to an expansion of the polar cap. Field lines then convect anti-sunward towards the nightside where they reconnect in the magnetotail, causing ionospheric flows opposite to those at the dayside and hence resulting in a contraction of the polar cap. This transport of open field lines to the nightside can occur

over a period of up to ∼1h, and hence changes in solar wind driving are communicated gradually throughout the magnetosphere by convection.

However, as seen in the previous Chapter, changes in the magnetosphere can also be communicated by MHD waves over seconds to minutes. Studies have shown that ionospheric convection can fully reconfigure over 10-20 minutes in response to the onset of magnetopause reconnection, but also quasi-instantaneously if there is already existing flow (see Morley and Lockwood, 2006 and references therein). In this sense there can be considered two aspects to the response timescales: first that associated with the typical wave transit time for communication to be transmitted along field lines from the solar wind to the ionosphere and nightside magnetosphere, and secondly the convection timescale through which flux is circulated from the dayside to the nightside, and then back to the subsolar magnetopause. Ionospheric signatures have been observed almost immediately on both the dayside and nightside in response to southward IMF turnings (Snekvik et al., 2017), consistent with the first, shorter timescale type of response. However large-scale current systems have been shown to take ∼ 1h or longer to be fully established on the nightside, compared to tens of minutes on the dayside, indicative of convection gradually proceeding throughout the system and triggering the onset of substorms and their subsequent evolution (Milan et al., 2018, Anderson et al., 2014).

Since the dayside and nightside reconnection rates are generally not in balance, the polar cap tends to evolve continuously in response to solar wind driving. The regular occurrence of substorms reflects the gradual accumulation and bursty reconnection of open flux in the magnetotail, leading to periodically intense ionospheric signatures. However during prolonged periods of southward IMF there is enough time for the dayside and nightside rates to reach a relative balance, such that tail reconnection can proceed in a laminar fashion and the flux content evolves uniformly, not requiring flux to be closed suddenly in large quantities (see Figure 5.1). This is known as steady magnetospheric convection (SMC) (DeJong et al., 2009). SMC events can simply be periods of enhanced convection (Walach and Milan, 2015), but have also been shown to evolve from high-latitude substorms through a prolonged expansion phase (Figure 5.1b) if the IMF remains southward (Milan et al., 2019), becoming substorms if the IMF then turns northward. These can persist for several hours, and are associated with intense auroral signatures (Walach et al., 2017).

Since during geomagnetic storms the IMF can remain southward for long periods of time, they can be host not only to substorm activity but also SMCs and other associated phenomena. However the driving conditions can be highly variable, resulting in a particularly complex magnetospheric and ionospheric response over a variety of timescales. For example, multiple IMF switches from northward to southward and vice-versa can occur, as can periods with strong dawn-dusk oriented IMF (B_y) components.

5.1.2 System Response to the IMF

The response of the magnetosphere-ionosphere system to changes in the IMF can be decomposed into to a separate dynamical dependence on each component, particularly B_y

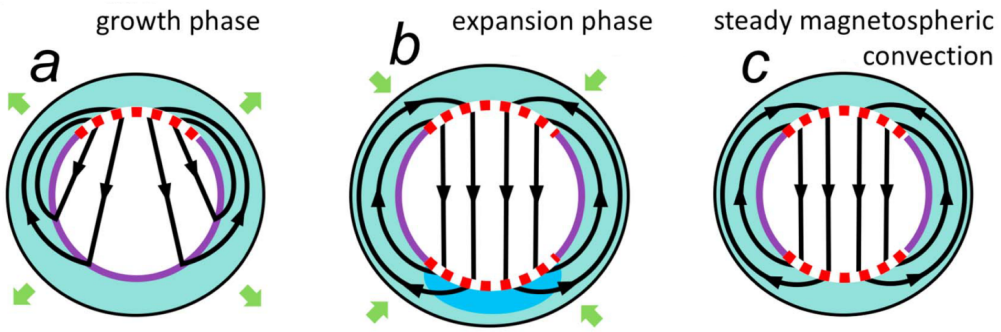

Figure 5.1 – Schematic showing the development of steady magnetospheric convection after an enhancement in dayside reconnection (upper dashed red line). The polar cap (purple circle) expands (green arrows) as in (a) the substorm growth phase, and flux flows (black lines/arrows) towards the nightside where it reconnects (lower dashed red line and blue shaded region) once more as in (b) the substorm expansion phase. However if the dayside rate remains high then nightside reconnection can proceed in a steady fashion (c) where dayside and nightside reconnection are balanced (adapted from Milan et al., 2019).

and B_z. This depends further on the overall driving conditions and hence the particular configuration of the system at a given time. Coxon et al. (2019) employed statistical techniques to study the spatial and temporal response of Birkeland currents to changes in the IMF using AMPERE data. For the IMF B_z they found a 10-20 min dayside response to IMF variation, suggesting a direct driving of the dayside Region 1 FACs. The strongest correlations of the nightside FAC were at timelags of 60-90 min, consistent with the timescale of the expansion of the polar cap and the onset of nightside reconnection, with comparable timescales seen in similar studies (Anderson et al., 2014, Shore et al., 2019). Even longer timescales of 120-150 min were also seen on the nightside, possibly corresponding to the end of the substorm cycle.

In a similar study using AMPERE data, Milan et al. (2018) showed that following southward IMF turnings the Region 1 FACs responded with a 10 min delay on the dayside that maximised after 30 min, whereas on the nightside they maximised after around 90 min. Conversely for northward IMF turnings the dayside Region 1 FACs decayed over 60 min as substorms subsided, but were sustained for longer on the nightside suggesting gradual contraction of the polar cap due to residual nightside reconnection. In both the above studies asymmetries were found between day-night and dawn-dusk, which is not explained purely by the ECPC paradigm; instead, these were attributed to the effect of IMF B_y.

The existence of an IMF B_y results in the asymmetric loading of flux between the dawn and dusk hemispheres, since it exerts a torque on newly-reconnected field lines. This results in a 'twisting' of the magnetotail lobes, and hence a rotation of the magnetotail current sheet out of the equatorial plane due to asymmetric lobe pressure (Cowley, 1981, Xiao et al., 2016). Due to shear flows arising in the magnetosphere, this twisting proceeds onto closed field corresponding to an induced B_y, which has been shown via simulations to arise on the order of tens of minutes (Tenfjord et al., 2015). In response to

a step-like increase in IMF B_y, the induced B_y appeared on closed field lines prior to the response of nightside reconnection, consistent with MHD wave propagation rather than convection timescales. These effects are demonstrated in Figure 5.2. This induced B_y was associated with well-established asymmetries in ionospheric convection under non-zero IMF B_y (Tenfjord et al., 2015), argued in terms of the displacement of field line footpoints which has been used to explain asymmetric auroral observations (Motoba et al., 2011).

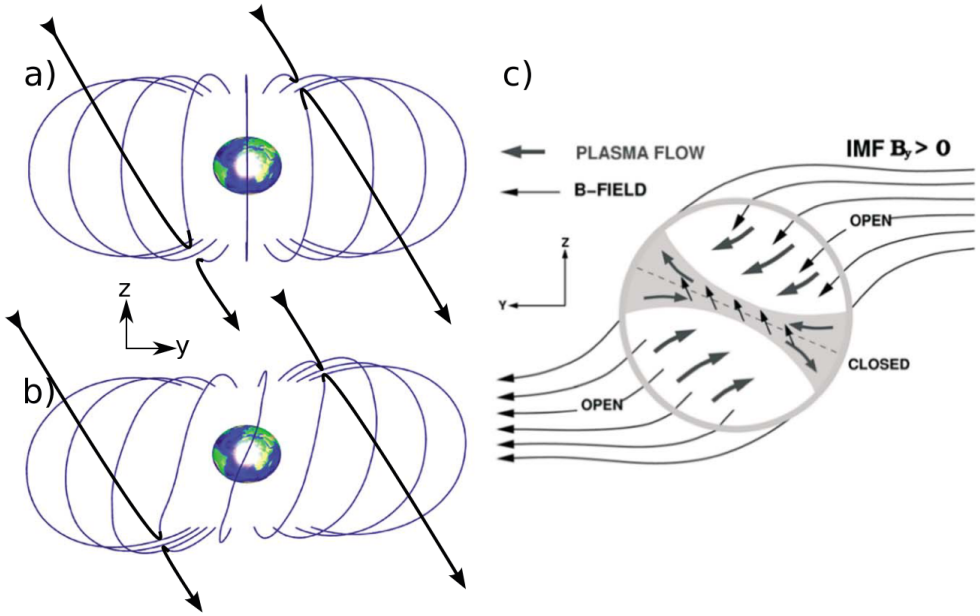

Figure 5.2 – Schematic showing the effect of a B_y component in the IMF (black lines) on (a) closed magnetospheric field, which (b) following reconnection induces a B_y on the closed field lines (in blue). The effect of B_y in (c) the magnetotail lobes (enclosed by the magnetopause and closed field in grey) is a twisting of the current (neutral) sheet (grey dashed line), due to asymmetric flux loading and flow shears (grey arrows) in the lobes which induce a B_y (short black arrows) in the closed field (from Tenfjord et al., 2015).

This contradicts with observations suggesting longer timescales of $\sim$ 1h are required for a B_y to be generated in the tail (Rong et al., 2015, Browett et al., 2017), which are more indicative of convection timescales. Other sources of plasma sheet B_y also exist, such as due to the hinging of the current sheet due to a dipole tilt (Petrukovich, 2011). However, the distinction between an initial response to a change in IMF and a full reconfiguration of the system may complicate any deduced timescales; a later study by Tenfjord et al., 2017 using GOES observations during IMF B_y reversals suggested response times of <15 min and reconfiguration times of <45 min. Similar delays were seen when investigating northward IMF conditions (Tenfjord et al., 2018).

Other observations of these reversals have shown a rotation of the current sheet in the (anti-)clockwise direction for a (positive) negative IMF B_y, occurring over timescales of tens of minutes rather than the expected 60-90 minutes for convection timescales (Case et al., 2018). The rotation was more easily observed during northward IMF, possibly because the current sheet is more disturbed during southward IMF conditions. A separate study finding a longer twisting timescale of 1-3h also showed that the delay was

longer in the inner magnetosphere, i.e. it propagated inward from the middle magnetotail (Pitkänen et al., 2016). A global MHD simulation using idealised IMF variations showed that the outer portions of the current sheet near the magnetopause respond more promptly after ∼15 min at a distance of 20 R_E from the Earth, compared to a response of up to 1h at the inner current sheet (Walker et al., 1999). The timescale of response was slower further downtail, and the twisting more exaggerated. This wide disagreement between studies suggests there may be a strong sensitivity to the particular state of the magnetosphere.

The shorter timescales also disagree with delays seen in large-scale Birkeland currents. Coxon et al. (2019) found the strongest nightside response to IMF B_y to occur between 90-150 min, consistent with timescales attributed to southward IMF driving by Browett et al. (2017) who also found the response in the plasma sheet B_y to be best correlated over longer timescales (up to 4h) for northward IMF. Milan et al. (2018) found that dayside responses to IMF B_y were prompt, but were delayed on the nightside by up to an hour and developed further over up to 4h. This can be interpreted in terms of convection timescales, and suggests the response is generally shorter during strong driving. Thus whilst the effect of an induced B_y may be prevalent in the magnetosphere, this may not be too important for ionospheric coupling or is simply dominated by global convection signatures.

5.1.3 Motivation and Outline

Intensification of field-aligned currents can be very localised, and so accurately predicting the stormtime response of the ionosphere is crucial in forecasting the potential impacts of a severe space weather event at a given location on the Earth. Global MHD simulations provide the means to model ionospheric conditions in real-time for arbitrary driving conditions, and by running with actual upstream solar wind data we can attempt to reproduce the state of the system during a real event. This then allows direct comparison to space- and ground-based observations (e.g. FAC data from AMPERE), from which the observations can be placed in global context to better understand the physical drivers behind the system's response, and the characteristic timescales.

Simulating a real geomagnetic storm therefore provides a meaningful case study to investigate how changes in IMF are propagated through the magnetosphere during non-idealised conditions. During such an event the dynamics are particularly time-dependent, and the strength of driving can greatly vary. This would complement previous simulations using synthetic conditions where the timescales are sensitive to the choice of setup, and provide further physical insight into studies based on in-situ observations. For meaningful results however, a model should be carefully designed to fully capture the spatio-temporal aspects of the driving which can influence the coupling.

For Gorgon, this involves extending the code to simulate the system in a frame which accounts for the proper orientation of the solar wind inflow and the rotation of the Earth. In this chapter, we develop a technique to implement a varying solar wind inflow for a given time period in accurate GSM coordinates to aid comparison to data. We further

include the effect of corotation in the inner magnetosphere, and apply gradients in the conductance based on solar EUV ionisation that are important in generating asymmetries in the system. Using this tailored version of the code we simulate a real geomagnetic storm, and analyse the response timescales of the magnetosphere and ionosphere to varying strength of driving and changes in the IMF orientation. The results are then compared to observations of the ionospheric FACs during the same event, to further elucidate the source of the different timescales. These developments also build the foundations for future space weather modelling efforts using the code.

5.2 Improving the Forecasting

Up to now the model setup has been idealised for the purposes of exploring the system response to specific changes in driving conditions, so as to isolate the effect of a given parameter. To accurately simulate a real event, additional dynamical effects will need to be included. Firstly, the Earth's dipole tilt is not static and varies both diurnally and seasonally; for a simulated period of several hours, this could result in a tilt angle shift of $\sim 10^{\circ}$. Including the time-dependent behaviour in the dipole field in the simulation can be important in capturing changes in the location of reconnection, and asymmetries in magnetospheric convection and ionospheric conductance (and thus FAC signatures).

This issue could be corrected by rotating the dipole from its initial orientation during the simulation. However, this is currently not possible in Gorgon due to the splitting of the magnetic field into dipolar (curl-free) and non-dipolar components, originally required to more accurately calculate field-aligned currents (see section 2.2). Whilst rotating a single magnetic field component is straightforward (as was done in previous versions of the code, e.g. Mejnertsen et al., 2016), the split dipole case presents a significantly more complicated numerical problem.

Instead, we implement a method to capture the effects of dipole rotation by proxy. Since the model is essentially composed of two separate components - a dipole source and an inflowing solar wind - the rotation of the dipole can instead be projected onto the solar wind. This approach is used in other global simulations (e.g. Sorathia et al., 2019). By switching into a frame where the dipole always points along the Z-axis (known as 'Solar Magnetic' coordinates, or SM), the solar wind vectors will be rotated through those same angles of rotation. If we then calculate the dipole orientation as a function of time in the GSE or GSM frames (in which the X-axis points towards the sun), we can transform into SM and obtain a fully rotating solar wind. Doing this requires accurate calculation of the dipole tilt angle μ at a given point in time. In reality the Earth's magnetic field is not perfectly dipolar, and the North and South magnetic poles do not sit at conjugate points. However, for modelling purposes we can approximate the field by using a 'best-fit' dipole which passes directly through the centre of the Earth.

Taking data from the IGRF model (Thébault et al., 2015) for a given year, we calculate the North and South geomagnetic pole location in geographic longitude and latitude

from which we can transform into the GSE/GSM frame. This requires a set of coordinate transformations that take into account the effects of the Earth's rotation and orbital motion (including eccentricity and inclination), so as to fix the Sun's position relative to the Earth (Hapgood, 1992). The result is a vector representing the dipole orientation in cartesian coordinates; the angle between this and the Z-axis is that which we use to rotate the solar wind. An example of applying this method is shown in Figure 5.3. Here the initial dipole orientation is close to Northern summer solstice, showing solar wind vectors with generic GSE components $v = v_x$ and $B = B_z$ that are then rotated into the SM frame. The result is that the solar wind vectors now point out of the noon-midnight meridian plane, and the rotation axis is offset by $\sim 10^\circ$ from the Z-axis (which is now parallel to the dipole axis). In this way any arbitrary pair of solar wind vectors can be rotated into the SM frame. Upstream solar wind monitor data (e.g. from ACE or Wind, propagated from the L1 Lagrange point to the Earth's bow shock) can then be transformed into SM coordinates and hence injected directly into Gorgon via the final transformation $(X, Y, Z) = (-X_{SM}, -Y_{SM}, Z_{SM})$.

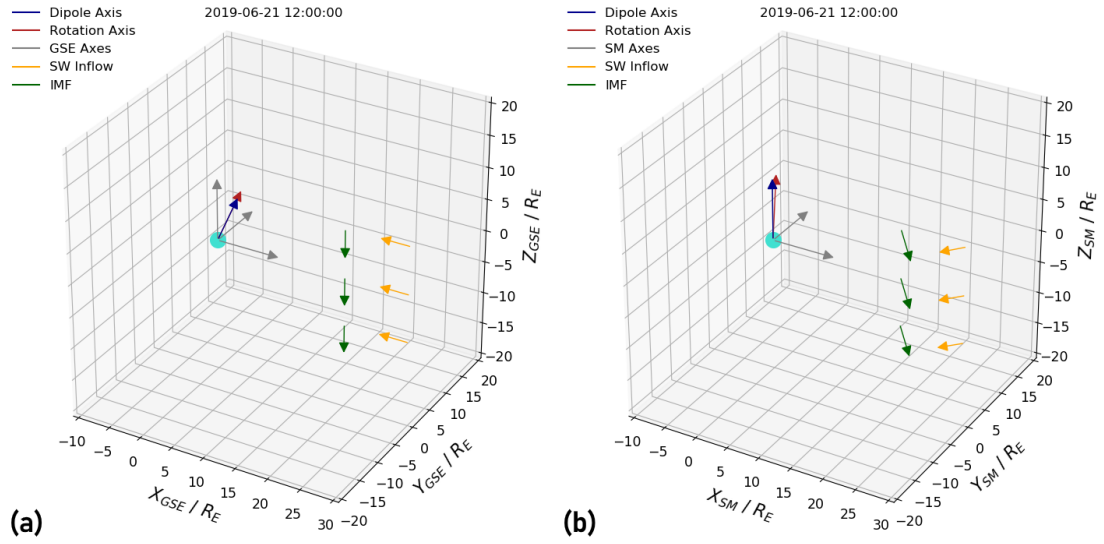

Figure 5.3 – Schematic showing the coordinate transformation from the geocentric solar ecliptic (GSE) frame to the solar magnetic (SM) frame. The dipole and rotational axes are shown and are exact of the time indicated, at Northern summer solstice. The solar wind inflow and IMF vectors are shown before and after, and correspond to a purely southward IMF and radial inflow in GSE.

The rotation of the Earth exhibits a further influence on the magnetosphere in the form of a corotation electric field; magnetospheric plasma tied-into closed flux tubes are forced to rotate with the Earth, the residual momentum for which is provided by collisions with neutrals in the ionosphere. This phenomenon is especially important in the low-β inner magnetosphere, where the transport of cold plasmaspheric electrons and ions are dominated by the corotation flow up to a distance R_{sp} known as the corotation stagnation point (see section 1.3.4). This distance depends on the balance between convection and corotation, which can vary dramatically depending on the strength and rotation rate of the planetary field and the driving solar wind conditions, but generally

extends to several R_E at dusk. For corotation-dominated magnetospheres like that of Jupiter, the stagnation point may lie even beyond the magnetopause and hence convection plays little role.

Thus, including this effect in Gorgon could significantly alter the flow close to the inner boundary. This can be implemented by introducing a neutral wind term to the ionospheric solver, generating an additional corotation electric field as an inner boundary condition, but is most simply included just by adding a corotation term $\mathbf{v_{rot}} = \mathbf{v_{rot}}(t)$ to the plasma flow at the boundary which is expressed analytically as:

$$\mathbf{v_{rot}}(t) = \frac{2\pi}{T_{rot}}\hat{\mathbf{R}}(t) \times \mathbf{r}, \tag{5.1}$$

for a given position $\mathbf{r}$, rotation period T_{rot} and rotation axis $\hat{\mathbf{R}}$. The only variable Gorgon input here is the orientation of the rotation axis at a given point in time, which depends on the specific coordinate system used and can be provided with the solar wind parameters for the SM frame by transforming the vector $\hat{\mathbf{R}} = (0, 0, 1)$ from geographic coordinates. The components of $\hat{\mathbf{R}} = (R_x, R_y, R_z)$ are then updated every timestep, and the corotation flow is calculated for each point $\mathbf{r}_i = (X_i, Y_i, Z_i)$ for cells within the simulation inner boundary.

The second dynamical effect is a more representative treatment of the ionosphere. Including non-uniform ionospheric conductances will introduce further important asymmetries in the system. For a more general study of the dynamics of the system during a specific event, rather than for detailed forecasting purposes, it is sufficient to rely entirely on simple empirical formulae to construct a conductance profile. As discussed in section 2.3.3, without extensive data comparison and sufficient tuning of the inner boundary conditions, a parametrised auroral conductance is likely unreliable. Rather than assuming an unrepresentative synthetic auroral profile we simply include the conductances due to EUV ionisation, specified by the solar zenith angle which is calculated based on the angle between the X-axis and the Sun-Earth line in SM coordinates, i.e. $90^\circ - \mu$. The polar cap conductances, containing auroral contributions and those due to e.g. polar rain, are then just set as constant and uniform to broadly capture their control of convection timescales at the cost of their morphological effects.

To test this implementation, we simulate solar wind driving using the following conditions: n = 5 cm^{-3}, v_x = 400 kms^{-1}, $T_{i,e}$ = 5 eV, B_z = -5 nT. The grid is the same as in Chapter 3, with the rotation and dipole axes pointing along Z. To verify also that the conductance gradient is having an effect on the magnetospheric flow, we perform two separate runs in which one includes a uniform conductance profile (the same as in Chapters 3 and 4), and the other includes the solar EUV ionisation contribution as per equation (2.28) with background conductances of $\Sigma_{P,H}$ = 1 mho. The pressure and flow streamlines in the fully-formed equatorial magnetosphere are shown in Figure 5.4. The existence of closed flow streamlines near the inner boundary demonstrates that the corotation is dominating close to the Earth, as expected. In contrast to the idealised picture shown in Figure 1.11, there exist two stagnation points in each case. This reflects the

more complex convection profile arising due to the geometry of the shielded magnetospheric field, as well as departures from a pure steady-state.

The offset of the flow stagnation points to greater distances in the non-uniform conductance case occurs due to the greater dayside conductance and thus weakened convection, causing corotation to dominate further out. Additional differences are seen in the nightside pressure and magnetopause stand-off distance, as well as the existence of a flow vortex on the dawnside flank with the uniform conductance. We note the strong agreement in the pressure and flows patterns with other MHD simulations shown in Plate 5 of Ridley et al. (2004), which used a similar setup. Overall it is clear that both the corotation flow and ionospheric conductances are strongly influencing magnetospheric convection with this implementation, and so we proceed with simulating a real event with a more detailed simulation setup.

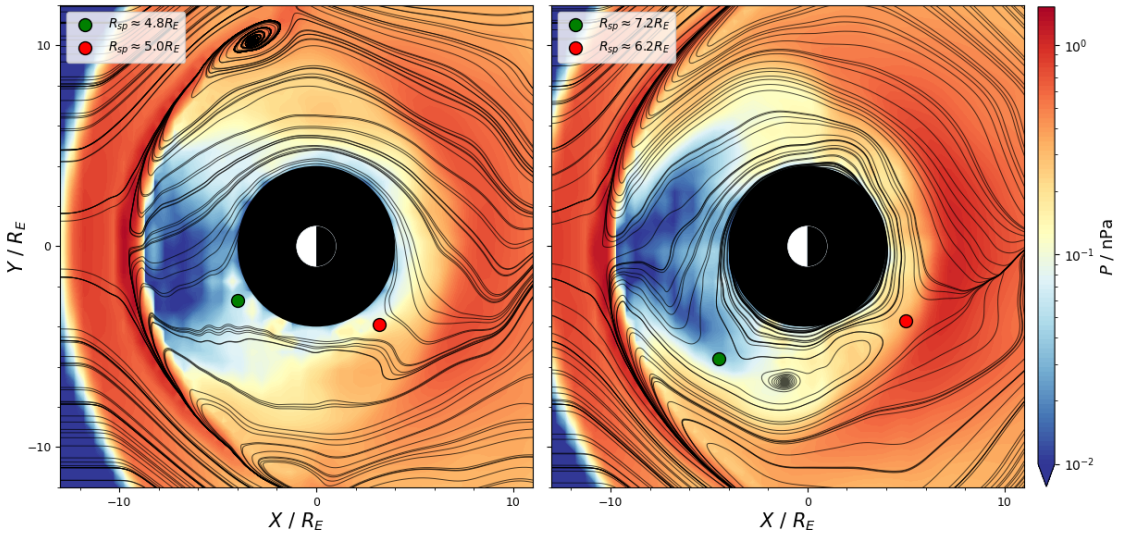

Figure 5.4 – Thermal pressure contours and flow streamlines in the equatorial dayside magnetosphere during southward IMF and with a corotation flow, for (left) a uniform ionospheric conductance and (right) a day-night conductance gradient due to solar EUV ionisation. Approximate flow stagnation points, located by inspection, are indicated.

5.3 Simulating a Real Event: Storm of 3rd May 2014

5.3.1 Solar Wind Conditions

Selecting an appropriate event to simulate requires pre-storm conditions that can be accurately reproduced. This ensures the stormtime response of the system - which is highly non-linear and thus depends closely on the system's state at storm onset - is reflective of reality. There is thus a preference to a storm preceded by steady, quiet solar wind conditions, such that the magnetospheric dynamics are themselves steady. One such candidate occurred in May 2014, between 14:00UT on 3rd and 11:00UT on 7th. This event was preceded by several hours of weak, predominantly northward IMF, for which the

magnetosphere is relatively closed. This event was identified from the list of geomagnetic storms given in the supporting information of Murphy et al., 2018, and corresponds to storm number 34 in said list. There is also good observational coverage of this event from AMPERE and SuperMAG for future comparison to the simulation (J. C. Coxon and R. P. Shore, private communication).

Figure 5.5 shows the solar wind conditions during the first 24h of the storm, which contained the period of longest continuous southward IMF and hence geomagnetic activity. These data were obtained via NASA/GSFC's OMNIWeb service, propagated from L1 to the Earth's bow shock. The shock front associated with the storm is seen to arrive at around 17:50 UT on 3$^{\text{rd}}$, when the number density in the solar wind suddenly increases by about a factor of 2. The IMF also grows and turns southward, remaining so for essentially all of the following 15h and hence presents favourable conditions for steady magnetospheric convection to occur. The IMF then switches northward at around 09:00UT on 4$^{\text{th}}$, and is rarely southward for the remaining 7h shown here. A pair of prominent IMF B_y reversals are also seen between 05:00UT and 07:00UT on 4$^{\text{th}}$, which presents an ideal opportunity to study the response of the magnetotail current sheet. In fact, B_y is strongly negative for almost all of the time for which the IMF is southward, which should generate strong asymmetries in the system and twisting in the magnetotail. Note the dipole tilt angle ranged from $\sim 6^\circ - 25^\circ$ for this period, and hence there should be a noticeable but varying hinging effect in the current sheet as well.

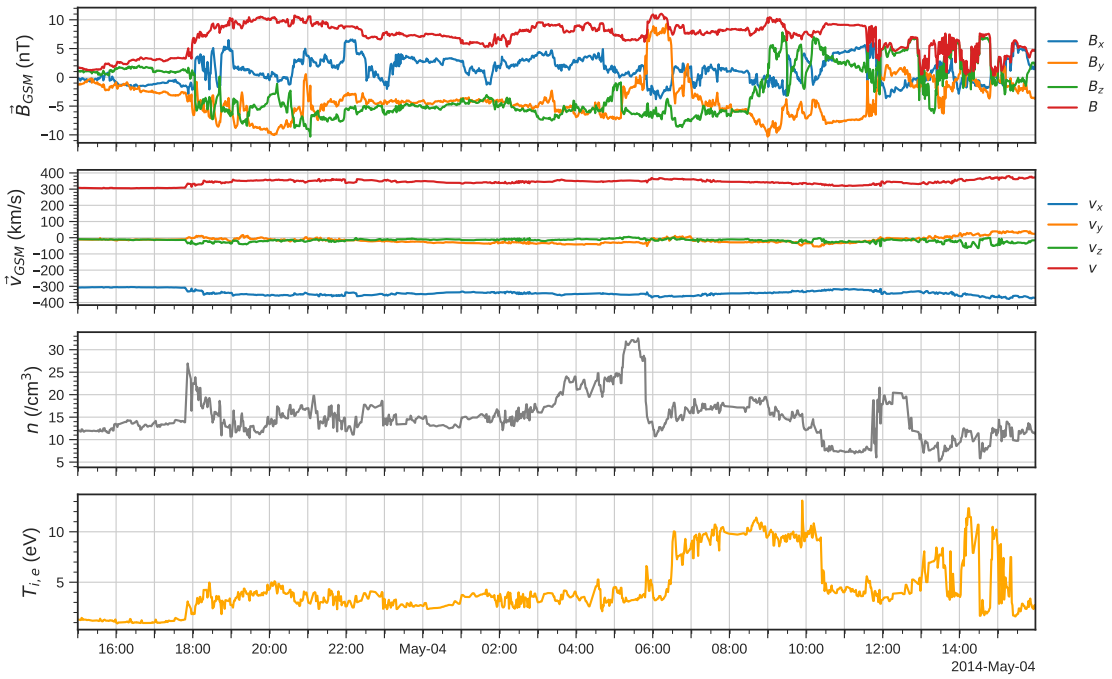

Figure 5.5 – Solar wind conditions from OMNI used to drive the simulation in GSM coordinates. Shown is the IMF **B**, solar wind velocity **v**, number density n and ion (and electron) temperature $T_{i,e}$.

The velocity increases slightly with the initial shock, but is then relatively constant during the event, meaning that timescales associated with convection should depend

primarily on the IMF orientation and can be more easily inferred. However, the density varies significantly; a large dynamic pressure enhancement is seen at 17:50UT on 3rd and is followed by a climb in density and then a sharp dynamic pressure decrease at around 05:50UT on 4th. The proton temperature is also strongly enhanced following both of these spikes, suggesting that the former is a forward shock and the latter a reverse shock. Figure 5.6 shows the results of a simulation using the ENLIL heliospheric MHD code (Odstrcil, 2003), displaying conditions in the ecliptic plane around the onset of the storm as well as those at Earth during the month of May 2014. There is no Earth-bound CME injected into the simulation at this time or indeed during the entire event, whereas one is predicted several days later on the 7th which is consistent with a separate geomagnetic storm identified in the same list from Murphy et al., 2018. Though it is difficult to be certain given the weak variation in v_y, this event could instead be be a CIR, consistent with the region of faster radial flow propagating towards the Earth in the simulation, as well as a spike in density correctly predicted.

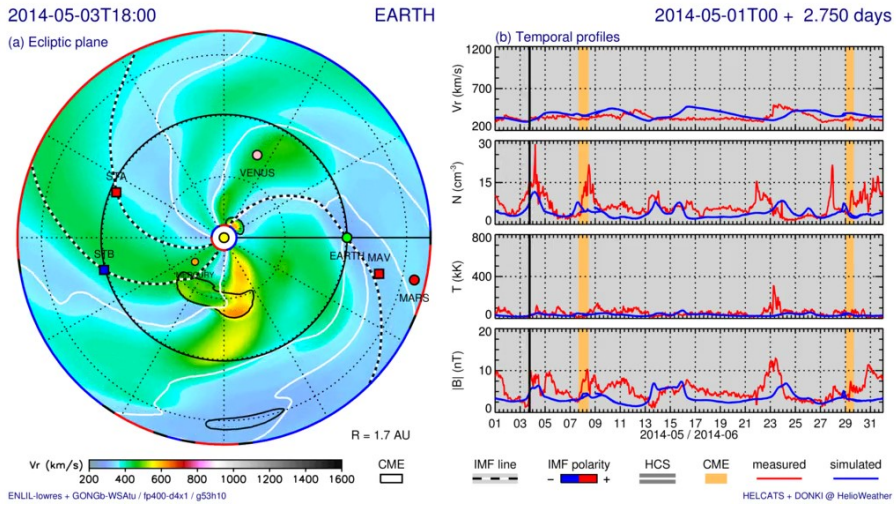

Figure 5.6 – Simulation of the solar wind from the ENLIL heliospheric MHD code showing (left) the radial flow speed and locations of the IMF lines, HCS and CME boundaries in the ecliptic plane and (right) the conditions at Earth during the month of May 2014 (taken from `www.helioweather.net`).

5.3.2 Simulation Setup

We use a grid resolution of 0.5 R_E and inner boundary radius of 4 R_E; the ionospheric potential is zeroed at the lower-latitude boundary (30° colatitude) and is recalculated every 30s. The solar EUV conductances of equation (2.28) are used assuming $F_{10.7}$ = 100×10^{-22} Wm^{-2}Hz^{-1} (i.e. we neglect solar cycle variation), and uniform background polar cap conductances of Σ_P = 7 mho, Σ_H = 12 mho are defined as per Coxon et al., 2016. The solar wind data from OMNI are then transformed into simulation coordinates. We inject solar wind for a total of 24h, using the relatively quiet first 3h of driving to initialise the magnetosphere so that the focus of the analysis is from 17:00 UT on 3rd May onwards. The solar wind input also provides the angle to the Sun-Earth line (which is

always in the X-Z plane) and the components of the rotation axis, from which the solar EUV conductances and the corotation flow are calculated. Note that since a varying IMF B_x cannot be injected into the box, we simply set $B_x = 0$ during the entire simulation.

The spatial domain is extended to accommodate the oblique inflow of the solar wind, which must make contact with the entire flank magnetopause to avoid artefacts of the planar inflow. Since the flow in the SM frame has a large component in the Z-direction we extend the Z domain to ± 80 R_E, whereas the Y-axis spans ± 50 R_E. We employ a longer simulation box of extent X = (-30, 110) R_E to capture as much of the tail dynamics as possible. Note that for an inflow speed of 400 kms^{-1} it takes ~ 5 min for the solar wind to reach the magnetopause from the edge of the box; we do not attempt to account for this in the timing analysis, so any inferred response timescales should be considered to include some additional inflow delay (as well as any errors in the propagation of the data from L1). The simulation data are transformed from Gorgon coordinates into the GSM frame for analysis, which facilitates direct comparison to other studies. This is demonstrated in Figure 5.7; the transformation amounts to a rotation by the dipole tilt angle in the X-Z plane, which will vary during the simulation and limits the maximum value of X_{GSM} near the sunward edge, though this is always well beyond the bow shock radius. Crucially, the plasma sheet lies close to the Z-axis in the GSM frame, which facilitates analysis of the current sheet location and is necessary for comparison to observational studies.

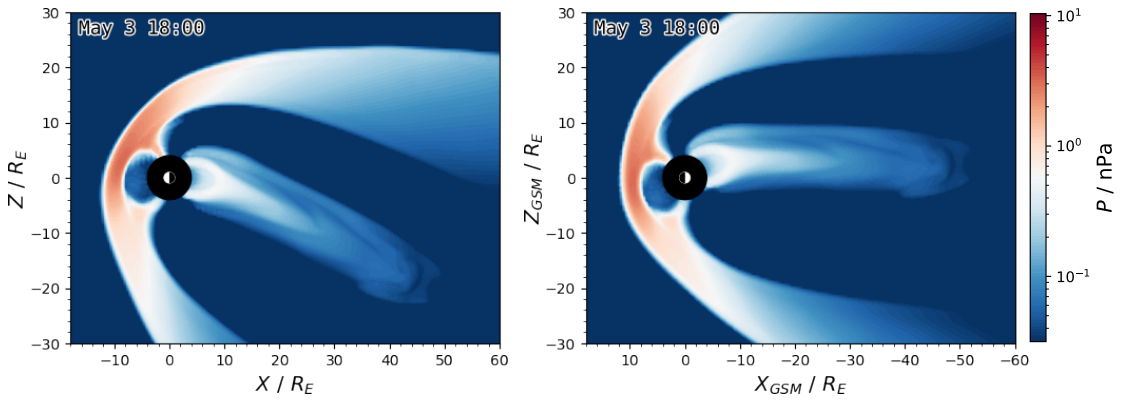

Figure 5.7 – Thermal pressure P in the magnetosphere for an example timestep, showing the transformation from the simulation frame into accurate GSM coordinates at a specific point in time.

5.4 Solar Wind Coupling Timescales and Global Dynamics

5.4.1 Dayside vs Nightside Reconnection

To investigate the balance between dayside and nightside reconnection we first need to establish the key trends in dayside driving during the event. The dayside reconnection rate can be estimated using the solar wind coupling function of Milan et al. (2012), which has the form:

$$\Phi_D = L_{eff}(v_x) v_x B_{yz} \sin^{9/2}(\theta_{IMF}/2), \tag{5.2}$$

$$\text{where } L_{eff}(v_x) = 3.8 R_E \left(\frac{v_x}{4 \times 10^5 \text{ms}^{-1}} \right)^{\frac{1}{3}}. \tag{5.3}$$

The assumption is that reconnection occurs over some effective length L_{eff} in the solar wind, which depends on the inflow speed. Whilst this is empirical and hence fitted to observations, L_{eff} may differ in the simulation and hence we do not expect absolute values of the reconnection rate to match; our purpose is rather just to demonstrate easily how the strength of driving differs over time. Figure 5.8 shows the value of this coupling function during the first 24h of the storm. The main points to highlight are the initial switch from northward to southward IMF at 18:00 UT on 3rd, the signature of the B_y spike at 05:00UT on 4th and the switch back to northward at around 09:00 UT towards the end of the simulated period. The driving is relatively strong for the entire period between 18:00-09:00UT.

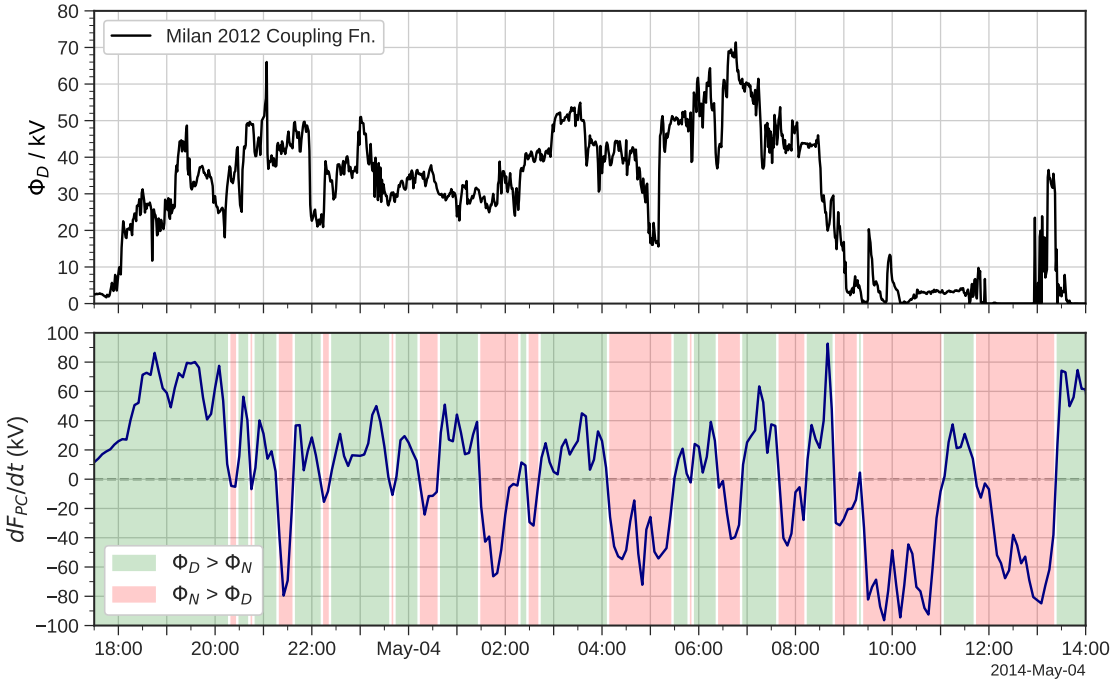

Figure 5.8 – Time-series of (top) the estimated dayside reconnection rate Φ_D using the coupling function of Milan et al. (2012), and (bottom) the rate of change of Northern open flux dF_{PC}/dt in the simulation. Green shading indicates where the dayside rate dominates the nightside rate Φ_N, with red indicating the opposite.

Also shown in Figure 5.8 is the rate of change of flux over time in the simulation, calculated by the same approach as in Chapters 3 and 4. Green shading indicates where dayside reconnection is dominant, and red where nightside reconnection is dominant. Generally the voltages are slightly larger than would be expected based on the coupling function, especially towards the start of the event, which suggests the solar wind is more geoeffective in the simulation. This may correspond to reconnection occurring

over a longer effective X-line than predicted empirically. We also note that the coupling function does not account for the effect of the density, which varies dramatically during this period and hence the associated dynamic pressure increase may amplify the initial growth in open flux.

The dayside rate dominates during the initial few hours, with the nightside rate only catching-up to the jump in the dayside after 2-3 hours when a large amount of flux is rapidly closed. Between 22:30-01:30UT the dayside and nightside rates are relatively balanced, showing much less variance than during the first few hours of driving. However despite steady driving on the dayside a large spike in the nightside rate occurs after 01:30UT, suggesting the occurrence of a substorm-like event. Another period of relatively steady flux follows this from 02:00-04:00UT, after which another spike in the nightside rate occurs about 1h after a rise in the dayside coupling rate. The remainder of the southward driving from 05:00-09:00UT is then marked by periodic behaviour where the dayside and nightside rates are highly unbalanced, switching with a period of 1-2h, possibly induced by the spike in IMF B_y after 05:00UT. After the switch to northward IMF at 09:00UT, the nightside dominates as expected, only closing the remaining open flux after about 2h.

Thus whilst some periods may be consistent with the model of steady magnetospheric convection, these are punctuated by bursty substorm-like activity either side, and the behaviour is especially time-dependent and unbalanced in response to sharp changes in the IMF. We note that other studies have shown the conductance to be important in determining whether the magnetosphere can enter SMC (DeJong et al., 2018). The inclusion of an auroral conductance may therefore influence the steadiness of the total flux content, although the response timescales are unlikely to be affected. Overall, the nightside response timescales indicate a roughly 2h lag behind the dayside response when the IMF B_z switches sign, and shorter timescales when the system is being strongly driven.

5.4.2 Magnetotail Configuration

To examine the behaviour of the magnetotail in response to changes in the IMF, we take slices in the Y-Z plane at a given downtail distance. We choose $X_{GSM} = -20R_E$ since this is likely to contain both open and closed nightside field on average, as well as a strong, thin current sheet. Figure 5.9 shows B_x in the tail over time, with blue indicating field directed sunward in the Northern lobe, and red indicating anti-sunward field in the Southern lobe. The increasing field strength over time demonstrates the loading of open flux in the magnetotail, until the final three panels at 10:00UT, 12:00UT and and 14:00 UT, which are 1h, 3h and 5h after the IMF has turned northward, respectively. The tail field remains relatively strong at 10:00UT, suggesting a slow delay for nightside reconnection to close remaining open flux since the magnetotail is still large in size with a strong B_x at 09:00 UT.

The current sheet is also indicated in green in these plots, defined as the $B_x = 0$ contour, showing a varying dawn-dusk asymmetry due to twisting of the magnetotail.

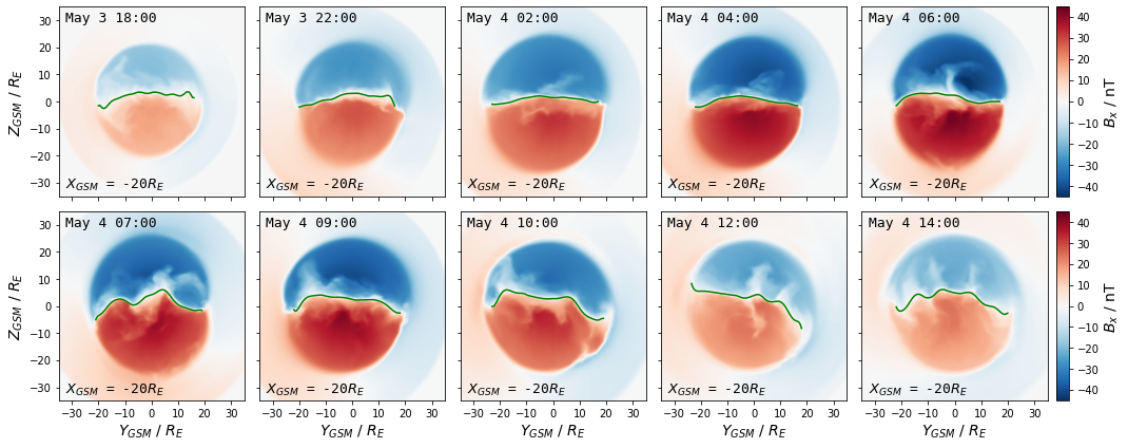

Figure 5.9 – Slices of the magnetotail at $X_{GSM} = -20R_E$ showing the lobe field strength B_x over time. The location of the magnetotail current sheet is shown by the green line.

From 06:00-07:00UT the current sheet begins to rotate incoherently along its extent due to the sharp variations in IMF B_y during this period. The current sheet is notably flat for periods when the tail B_x is strongest, and shows a more complex and irregular morphology during weaker driving. In all cases the current sheet is hinged towards the Northern hemisphere, as expected due to the dipole tilt, though this is also less prominent in the intermediate panels.

To investigate the response of the current sheet in more detail, we identify its location in 5 min intervals at X_{GSM} = -20 R_E over the duration of the event. Only the portion in the range of Y_{GSM} = $\pm$15 R_E is sampled, so as to accommodate the changing size of the magnetotail. The twisting of the current sheet due to changes in B_y is difficult to quantify given its complex shape as seen in Figure 5.9. This can be considered a combination of separate effects: these include the hinging due to the dipole tilt, the twisting due to the IMF and disturbances due to time-dependent tail reconnection, all of which may influence the current sheet incoherently at different Y-positions. In order to extract the first two effects, we fit a second-order polynomial to the current sheet coordinates (Y_{CS}, Z_{CS}) of the form:

$$Z_{CS} = aY_{CS}^2 + \tan(\theta_{CS})Y_{CS} + h_{CS}, \tag{5.4}$$

for some 'rotation' angle θ_{CS} and hinging distance h_{CS} (inferred at $Y_{CS} = 0$). The choice of a simplistic parabolic fit differs from other elliptical models (Xiao et al., 2016 and references therein) which have performed well for small dipole tilt angles at capturing the average current sheet configuration based on large observational datasets. However, the time-dependent behaviour of the magnetotail in this case study, combined with the large tilt angle, mean a more complex fit is unlikely to provide much benefit and would require more free parameters. Instead, we are mostly interested in deducing the response timescales rather than obtaining a perfect model for the current sheet. The uncertainty in this fit is found from the root-mean squared error, which represents the deviation from an idealised, parabolic current sheet, from which we determine the error in both θ_{CS} and

h_{CS}.

The fit is repeated for each sampled timestep to produce a time-series in the current sheet parameters. We then perform a Pearson cross-correlation of these against time-lagged IMF parameters to determine the timelag yielding the strongest correlation, representing the characteristic response time of the current sheet. Specifically we correlate θ_{CS} to B_y and h_{CS} to Φ_D, the latter being estimated using the function in Figure 5.8. The assumption behind these choices is that the rotation - even if weak compared to other effects - depends only on B_y, whilst the hinging depends on the amount of magnetic pressure exerted on the current sheet by the lobes, which increases with a growth in open flux, i.e. due to Φ_D. The dipole tilt angle does also change during the simulation and will vary the hinging, but only over slower timescales than Φ_D. Furthermore whilst different portions of the current sheet may respond at different times, a fitting provides a measure for the overall dominant orientation, whilst a greater error also reveals when this effect is most prominent. Figure 5.10 shows these parameters over time, and the results of the cross-correlation.

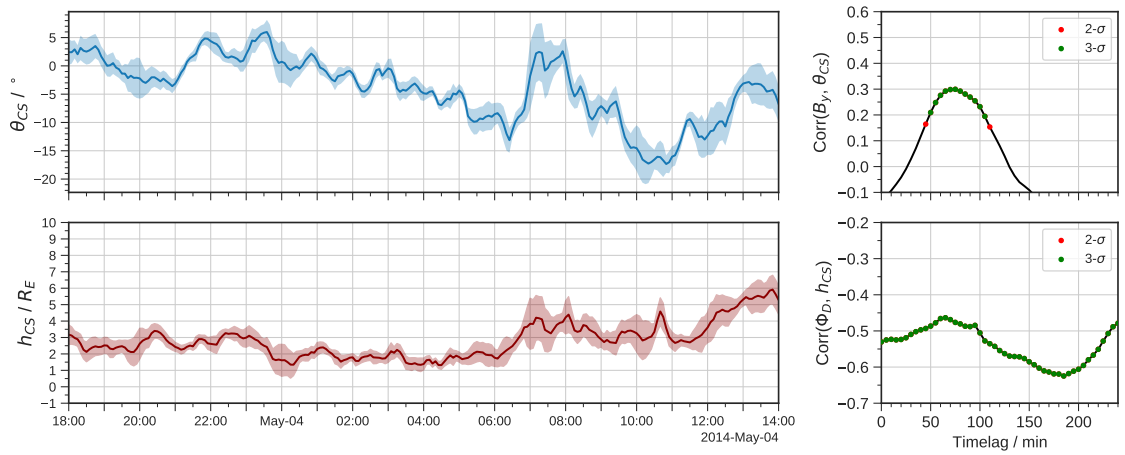

Figure 5.10 – Current sheet rotation θ_{CS} and hinging distance h_{CS} over time during the simulation sampled at $X_{GSM} = -20\ R_E$, with the shading indicating the uncertainty due to error in the parabolic fit. The Pearson correlation coefficient is shown for each timelag of the IMF variables, with statistically significant results indicated in red and green for 2-σ and 3-σ significance, respectively.

During the initial period of driving the rotation is fairly weak, being mostly positive (anti-clockwise) until 01:00UT on 4$^{\text{th}}$ despite the IMF B_y being largely negative. Only after several hours of negative B_y driving does the rotation angle become negative as expected, indicating some other source of rotation counteracting the effect of the IMF. This in fact agrees with observations, which have shown a weaker rotation for negative IMF B_y than for positive (Pitkänen et al., 2021). Dawn-dusk asymmetries in convection can also arise due to day-night gradients in conductance - as present in this simulation - and hence might result in a similar twist which offsets the rotation to positive angles in the presence of weakly negative IMF B_y, though this is a point for future investigation. Regardless, the sense of the twisting becomes more as expected after this time, with a sharp rise and subsequent fall in θ_{CS} in response to the pair of B_y reversals between

05:00-07:00UT. The rotation reaches its greatest amplitude after 10:00UT after the IMF has turned northward, suggesting a more prominent twist during northward driving as also seen in observations (Case et al., 2018). This may indicate that active nightside reconnection tends to remove asymmetries from the system, although they can still develop and grow.

The peak correlation of 0.3 is relatively weak, suggesting the presence of other more significant effects on the current sheet morphology, or possibly an incoherent response as outer portions of the current sheet respond earlier than the innermost region (as shown by Walker et al., 1999). This is apparent in the much greater uncertainty in θ_{CS} at later times when the current sheet is rapidly reconfiguring. The timelag of the peak correlation at 75 min is broadly consistent with the delay of the nightside response to B_y in both the magnetotail and ionospheric FACs observed in other studies and which was attributed to convection timescales (e.g. Milan et al., 2018, Coxon et al., 2019, Browett et al., 2017). Statistically significant timelags are found either side of the peak from 60-105 minutes, ruling out any dominant effect from shorter timelags associated with wave propagation. However shorter timelags of 10-20 min have been noted in observations of B_y reversals (Case et al., 2018); it may be that rapidly-induced B_y is important for periods of weaker driving (i.e. without the need for gradual accumulation of flux), or that the twisting is observed more easily at portions of the current sheet which respond earlier. Alternatively the response to a sharp reversal may be more prompt than for a large but steady B_y, though this is difficult to determine from the single case study here.

The value of h_{CS} remains generally small until the sharp change in B_y, after which it becomes much larger, especially under northward IMF. It should be noted that the dipole tilt angle was smallest during the intermediate period of the simulation, being maximal at $\sim 25^\circ$ at 18:00UT on 3$^{\text{rd}}$ and minimal at $\sim 6^\circ$ around 05:00UT on 4$^{\text{th}}$. This will complicate some of the trend seen here, though the hinging is still much more prominent under northward IMF than southward IMF for times when the tilt angle is large. Furthermore, the uncertainty is lowest during steady southward driving from 03:30-05:00UT, which is also true of the error in θ_{CS}; the implication is that steady, continuous nightside reconnection results in a relatively smooth current sheet which evolves more coherently along its width. The correlations are statistically significant at all timelags, and are much stronger than for θ_{CS}, being anti-correlated such that stronger driving reduces the hinging effect. In contrast to θ_{CS} the strongest correlation for h_{CS} is at 185 min, with the weakest at 70 min. Since the most exaggerated response was under northward IMF, we interpret this as the timescale for nightside reconnection to cease and the magnetotail to reconfigure after the period of strong driving has ended. Indeed, this is similar to timescales in response to B_y under northward IMF indicated by Milan et al. (2018) and Browett et al. (2017).

To infer whether this behaviour is sensitive to our choice of downtail distance, we repeat the analysis at $X_{GSM} = -30\ R_E$ as shown in Figure 5.11. The primary trends are essentially the same, with the rotation being more exaggerated and reaching larger peak values. Notably, the twist in response to the IMF B_y reversal is much more prominent,

suggesting this effect is stronger further downtail, in agreement with previous studies (Walker et al., 1999). The uncertainty is also greater, implying the current sheet is more disturbed here. These differences may be due to a greater portion of open flux which responds more readily to the IMF orientation, and a more incoherent response from the flanks into the centre of the magnetotail. This is reinforced by the much stronger correlations which remain statistically significant. Reassuringly the key timescales remain essentially the same, further confirming that these correspond to convection which influences the current sheet more gradually than inductive effects.

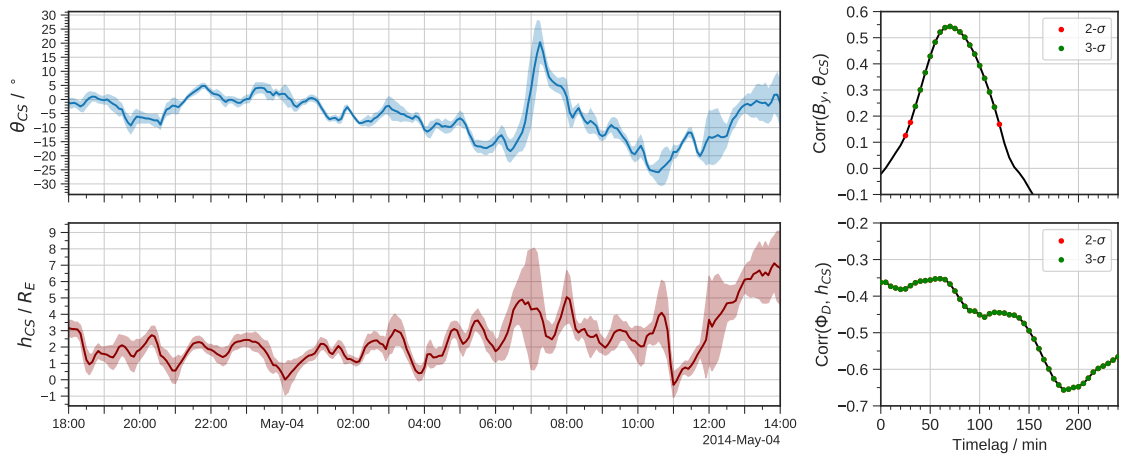

Figure 5.11 – Current sheet rotation θ_{CS} and hinging distance h_{CS} over time during the simulation, sampled at $X_{GSM} = -30\ R_E$. The format is the same as in Figure 5.10.

Overall the current sheet response appears to be bimodal - changes in the morphology due to loading and anti-sunward transport of open flux then accumulating in the tail lobes over convection timescales, and more exaggerated responses under northward IMF driving which are established over $\sim$ 3h after the IMF turns northward. Both the hinging and rotation of the current sheet appear minimised if reconnection in the tail is steady. The response is clearer further downtail, possibly due to the weaker and more open field, though the current sheet is more disturbed here and less resembles an idealised parabolic profile.

5.5 Ionospheric Response Timescales

The key timescales in the magnetospheric dynamics should also dictate to the evolution of global current systems in the ionosphere. We can gain an overview of the response by taking a slice through the ionosphere over time and plotting it as a time-series, known in auroral studies as a keogram. Figure 5.12 shows the FAC in the dawn-dusk meridian at both hemispheres over the duration of the simulation. The Region 1 currents respond almost immediately after the IMF turns southward at 18:00UT, and these gradually migrate equatorward and grow in intensity over the following 2h. The slightly weaker driving around 20:00UT appears to be associated with a temporary poleward shift of the

FACs, around which they reach their peak intensity in the North. These then move equatorward again and remain relatively fixed in latitude after this time; these are essentially skirting the edge of the mapping region which confines the possible range of latitudes. Implementations of the code for future space weather forecasting purposes may therefore require a slightly smaller inner boundary if the FACs would otherwise move further equatorward, though the key changes in location and intensity are still well-established here.

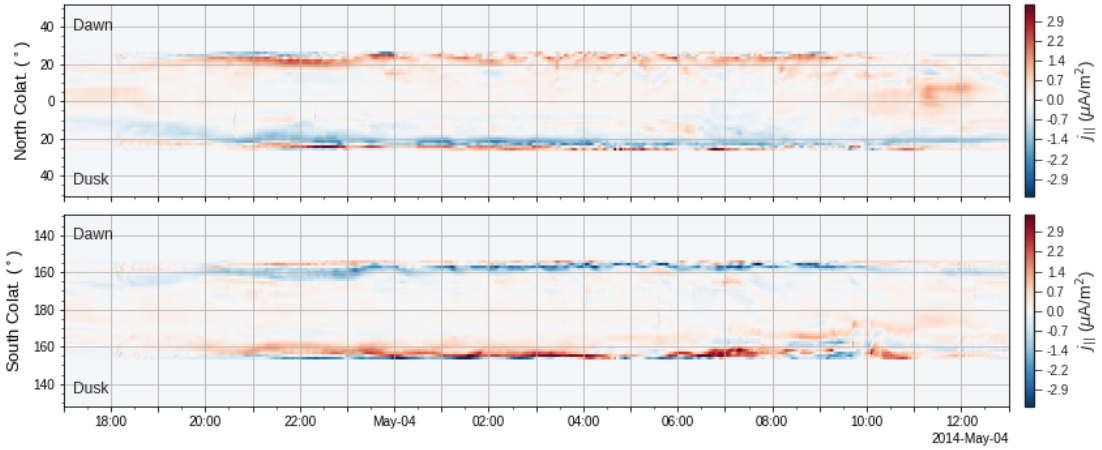

Figure 5.12 – Keogram (time-series) of the ionospheric FAC in the dawn-dusk meridian during the simulation, shown for each hemisphere.

The IMF B_y reversal does appear to yield some signatures at higher latitudes, particularly in the Southern hemisphere, though the Region 1 system seems fairly unperturbed from this perspective. The switch to northward IMF around 09:00UT causes the Region 1 FAC to dissipate fairly quickly. The Southern FAC reaches greater intensity than in the North at later times - possibly due to the slightly weaker conductance - but responds essentially over the same timescales.

To demonstrate in more detail the differences between the dayside and nightside response, Figure 5.13 shows the open-closed field line boundary and electric potential at the same time frames as the magnetotail slices in Figure 5.12. The complex magnetic topology indicates highly time-dependent behaviour during the simulated period. There is a large expansion of the polar cap following the southward turning over the first 4h, and the polar cap remains large even until 09:00 UT despite weaker dayside coupling. Only after 2-3 hours of this weaker driving at 11:00 UT has the dayside polar cap fully contracted, and an extended region of open field still exists at the nightside, once again consistent with a 2 hour delay to the IMF turning.

Figure 5.14 provides a broader overview, showing the cross polar cap potential and total upward field aligned current over time. Similar trends are seen versus the keograms above, with prompt growth in both quantities following the southward turning at 18:00UT on 3rd and gradual growth over about 2h. Both the CPCP and TFAC decrease following the northward turning at 09:00UT, but with a clear time delay that is much less sharp than the drop in the dayside coupling rate in Figure 5.8. The largest drop in the CPCP

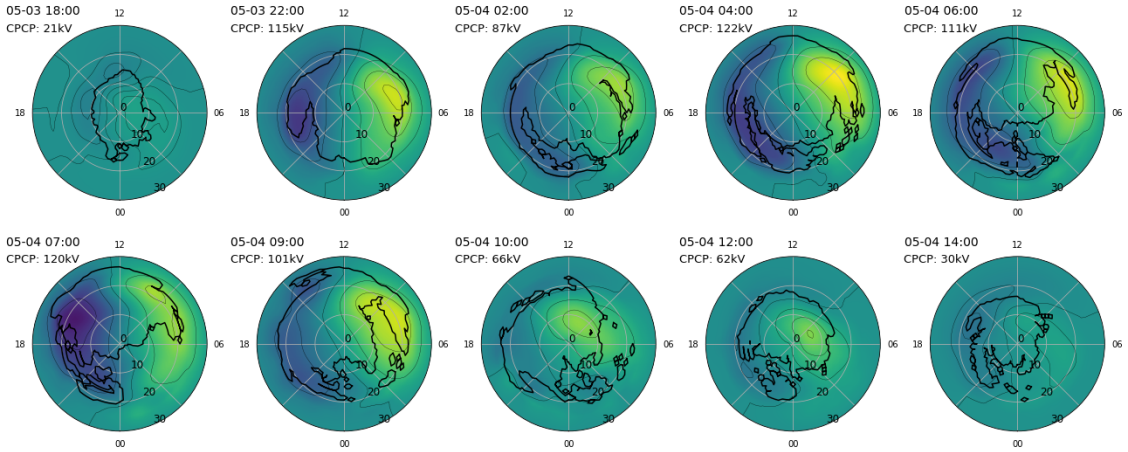

Figure 5.13 – Ionospheric potential in the Northern hemisphere at the same timesteps as the frames in Figure 5.9. The open-closed boundary is indicated by the thick black lines.

occurs after 12:00UT, roughly 3h after the northward turning and consistent with the timescale identified in the current sheet response to this same turning. Thus whilst the dayside response is prompt, the nightside response is determined by the time required for tail reconnection to close remaining open flux, which influences the nightside FACs and potential for up to 3h after subsolar reconnection is reduced.

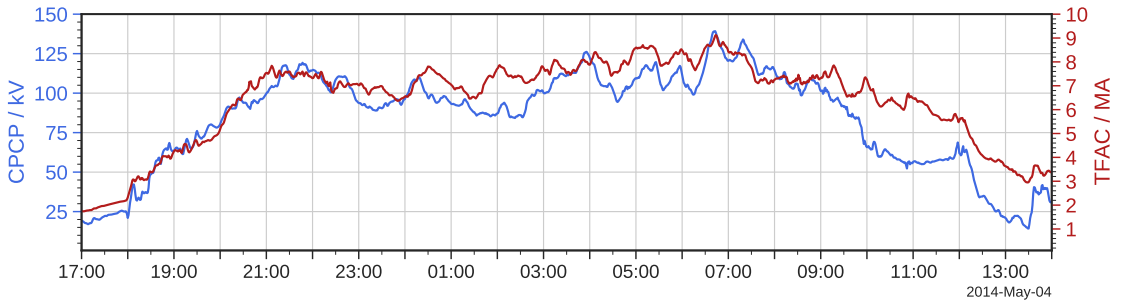

Figure 5.14 – Cross-polar cap potential (CPCP) and total upward field-aligned current (TFAC) in the Northern hemisphere over time.

To validate the trends seen in the simulation and shed further light on the response timescales, we now compare the results to observations by the AMPERE experiment during the same storm. The AMPERE data is generated from on-board magnetometer measurements by commercial satellites in the Iridium constellation, providing a global view of FACs at low-Earth orbit (Anderson et al., 2000). The data are binned by latitude and longitude to form an ionospheric grid similar to that in the simulation. A Pearson cross-correlation of the FAC with the IMF B_z is performed for each bin, and the timelag yielding the strongest correlation (for timelags up to 90 min) is obtained (J. C. Coxon, private communication). The peak correlation coefficients and corresponding timelags are then plotted spatially to yield maps of the FAC response. This technique is described in more detail in Coxon et al. (2019) and is based on the method of Shore et al. (2019) developed for analysing ground magnetometer data. The data covers the entire storm in order to maximise statistical significance, i.e. it includes the following 3 days, though

the strongest FACs and hence correlations occurred within the simulated period.

Figure 5.15 shows a keogram of the AMPERE data analogous to that in Figure 5.12, and maps of the correlations and timescales over the first 24h of the storm. The Region 1 FACs in the keogram show similar trends to that in the simulation, starting with an initial enhancement shortly after the IMF turns southward, seen at dusk in the North at 18:00UT on 3rd. The absence of FACs in the South and at Northern dusk at the same time is likely due to difficulties in detection during the initially weak driving, and similar responses should still be present here. The same temporary equatorward shift in the Region 1 system is seen after 20:00UT on 3rd due to weaker driving, suggesting the simulated FACs are properly capturing the changing influence of the solar wind. Similarly, the Region 1 FACs dissipate at around the same time as in Figure 5.12. Whilst the Region 2 FACs reach latitudes not captured in the simulation, these form a current system that is physically absent in Gorgon, and the latitudes of the Region 1 FACs are generally in agreement.

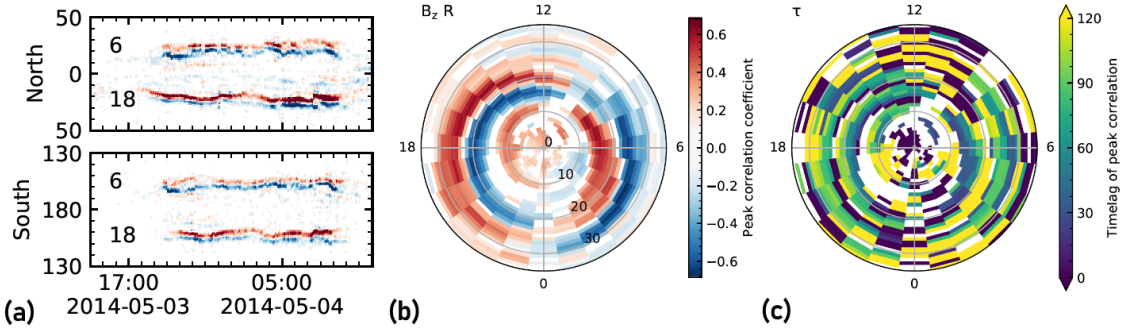

Figure 5.15 – AMPERE data during the first 24h of the storm. Shown are (a) keograms of the FAC in each hemisphere as per Figure 5.12. Also shown are the results of cross-correlating binned FAC at each (Northern) ionospheric coordinate against the IMF B_z, with (a) the peak correlation coefficients and (b) the corresponding timelags shown (Figure courtesy of J. C. Coxon, data from the AMPERE team and the AMPERE Science Center).

Regarding the cross-correlation analysis, we note that an opposite polarity in FAC will result in an opposite correlation coefficient. In other words, a positive correlation coefficient implies that an increase in B_z drives a positive field-aligned current at that point on the ionosphere, and vice-versa. The correlations patterns reveal distinct ionospheric current systems – the Region 1 system lies between $\sim 15 - 25^{\circ}$ colatitude, with the Region 2 system just equatorward. To identify the role of the expanding/contracting polar cap we focus on the timelags at the bins containing the Region 1 FACs.

A range of timescales are seen for the Region 1 system in response to B_z, from direct driving up to indirect driving at 120 minutes. For timelags in the midnight-dawn sector, banding is observed from 15 to 20 degrees colatitude, where shorter timescales are poleward and long timescales are equatorward. This banding is consistent with an expansion of the polar cap, since the equatorward latitudes will only experience a strong response to the solar wind driver once the Region 1 currents have migrated to these latitudes. In the afternoon sector the timescales reach up to 60-90 min, but on the nightside these are

>120 minutes. This suggests a timescale of $\sim$ 1h for the polar cap to fully expand, and a longer period of >120 min for nightside reconnection - via substorms or SMC - to cause a subsequent contraction. This agrees with the 2-3h timescales identified in the simulation for the closure of flux after a change in sign of B_z.

In general we find that the ionospheric response to the dayside driving is prompt, but effects on the nightside can be delayed by up to 2-3 hours as open flux is gradually closed in the magnetotail. These timescales also agree with those identified in the response of the current sheet to northward IMF turning. This delay appears to be shorter when the system is strongly driven. The ionospheric response is therefore consistent with an expanding and contracting polar cap over the same timescales. General agreement in timescales is found with the observations, and we see similar trends in the location of Region 1 field aligned currents.

5.6 Discussion and Future Work

In this chapter we have investigated the response of the magnetosphere and ionosphere to strong, highly variable driving by the solar wind during a geomagnetic storm. The event in question hosted several key features in the IMF, including a switch in B_z from northward to southward and vice-versa, sharp reversals in B_y, and prolonged period of southward IMF that lasted several hours. This makes the event ideal to study the response timescales of the system, both in terms of the opening and closing of flux in the nightside, the configuration of the magnetotail current sheet and associated asymmetries, and the expansion and contraction of the polar cap on the ionosphere.

The nightside reconnection response to dayside driving is delayed by up to 2 hours when the IMF B_z switches sign, due to the gradual accumulation of open flux in the magnetotail due to global convection. Periods are seen where the dayside and nightside reconnection rates are relatively balanced, indicative of the system approaching steady magnetospheric convection, though substorm-like activity is present whereby the two appear to vary periodically over $\sim$ 1h. This suggests the response may be shorter whilst the system is strongly driven, simply reflecting the time taken for field lines to cross a fixed polar cap. Further investigation could involve separating the dayside and nightside rates explicitly, which would require developing a technique to reliably infer the dayside reconnection rate under varying conditions in the simulation.

Similar timescales are seen in the magnetotail current sheet, which rotates in response to variations in IMF B_y, and is hinged by the dipole tilt to an extent dependent on the pressure accumulated in the lobes due to strong dayside driving. The rotation is most strongly correlated to B_y at a timescale of 70-75 min, though it becomes more exaggerated under northward IMF in agreement with previous observations. The effect of the switch to northward IMF is well-established after $\sim$3h, as inferred by the correlation of the hinging to the dayside coupling rate. This corresponds to the reduction of magnetic pressure in the tail as open flux is closed, being slightly longer than the inferred response timescale for nightside reconnection. The current sheet has a more idealised profile and

is much flatter when the driving is stronger, with the variance from a parabolic fit increased when the IMF rapidly varies suggesting an incoherent response across its Y-extent. The rotation is clearly stronger further downtail, but the current sheet is more disturbed here and still reconfigures over essentially the same timescales.

The ionospheric conditions evolve similarly during the storm. The Region 1 FACs respond promptly to changes in dayside coupling, expanding in size over a period of 2h after the switch to southward IMF. These remain at lower latitudes until the eventual switch back to northward IMF. The CPCP then decays gradually, only returning to small values after 3h which agrees with the magnetotail response. A comparison to data from AMPERE shows similar results, with agreement in the latitudes of the Region 1 FAC. Analysis of the observations shows timescales of 60-90 min for the expansion of the polar cap, and >120 min for eventual contraction, consistent with those in the simulation.

These results have implications for the understanding of magnetosphere-ionosphere coupling and the characteristic timescales over which the system evolves. Whilst previous work has shown that changes in the IMF can be communicated into the nightside and onto the ionosphere more quickly (over 20-40 min, Tenfjord et al., 2018), other studies have identified longer timescale responses indicating that the effect of global convection dominates over these inductive effects. Our results support the latter point, and further show that the timescales are sensitive to the particular mode of driving (i.e. northward versus southward IMF), effectively being bimodal if the IMF B_z switches sign regularly. The inferred timescales of $\sim$ 70 min and $\sim$ 3h agree with previous observations regarding the response of the tail to IMF B_y under southward vs northward IMF, respectively (e.g. Browett et al., 2017, Milan et al., 2018). The configuration of the current sheet closely reflects the magnetotail dynamics, and evolves over timescales which match the ionospheric response. This suggests the orientation of the current sheet may act as an effective proxy for the asymmetries being generated in the nightside ionosphere.

The study has also shown that Gorgon is capable of generating a complex magnetospheric and ionospheric response for a range of driving conditions and with real solar wind data. Nonetheless, improvements can be made to the setup which may further affect the results. The effect of the ring current in establishing the Region 2 current system can play an important role in inner magnetospheric dynamics and in more comprehensive comparison to data. However, excluding it does not preclude the use of Gorgon in exploring the behaviour of Region 1 currents and global convection, since the behaviour of the system and its response timescales at high latitudes can still be well modelled. Another limitation is the inability to inject a varying IMF B_x with the perpendicular solar wind phase fronts currently being used, and hence asymmetries arising from its influence on dayside open field are not captured here. Injecting solar wind with a slight phase delay along the sunward edge depending on the value of B_x, such that the phase fronts propagate in at an oblique angle, could be one approach to solve this. Finally, simulating with non-uniform grid geometries, such as a stretched/refined mesh (where the resolution is set to be higher in certain regions of interest) or a spherical grid, would allow for a smaller inner boundary which resolves FACs at lower latitudes.

Chapter 6

Conclusions

The interaction between the solar wind and the terrestrial magnetosphere-ionosphere system is the primary influencing factor controlling the complex and highly dynamic near-Earth space environment. This interaction is dependent on conditions in the solar wind, the orientation of the Earth's magnetic field and the plasma-neutral interactions in the ionosphere. These all vary over a broad range of timescales; transient changes in the solar wind occur over seconds to minutes, whilst diurnal and seasonal variations introduce asymmetries in the magnetosphere and alter the coupling with the solar wind. Over much longer periods, the 11-year solar cycle affects the frequency of transient structures such as CMEs, which drive extreme space weather events. The societal impacts of these events can be severe, and so understanding this interaction is vital in the increasingly technology-dependent world.

In Chapter 2, an updated version of the Gorgon MHD code for simulating the terrestrial magnetosphere is described. This includes a model ionosphere in which the continuity equation is solved on a separate spherical grid, providing an inner boundary condition for the MHD solver. The model is tested with a variety of solver inputs, and the coupling with the magnetospheric part is benchmarked against an existing GMHD code by performing a simulation with the same conditions. The dynamics agree with theoretical expectations, opening the door to a much broader range of studies using the model. The ionosphere plays a key role in influencing global dynamics, and hence its inclusion allows for a more representative magnetospheric state. Furthermore, the ionospheric signatures of various magnetospheric phenomena which were already well-reproduced by the code can now be investigated in detail. This is therefore a crucial step in extending Gorgon's capabilities for the studying of space weather, and for future forecasting applications.

In Chapter 3, the model is applied to study the effect of the Earth's dipole tilt angle on solar wind-magnetosphere-ionosphere coupling. Simulating with steady solar wind inflow and southward IMF, the location of the magnetic separator (i.e. the reconnection line) on the magnetopause is identified in each case, and found to shift southward across its full extent as the tilt angle increases. The length of the dayside separator consequently decreases, and it becomes increasingly unsteady around the subsolar magnetopause due to FTE generation which is more frequent for large tilt angles. As a result the global reconnection rate generally decreases as the tilt angle increases, and the ionospheric polar

cap shrinks in size due to a reduced open flux content. A North-South asymmetry arises in global magnetospheric convection, and is found to generate differences in the morphology of ionospheric field-aligned currents between each hemisphere. Stronger FACs are seen in the Northern (sunward-facing) hemisphere, where the ionospheric potential reaches larger peak values which are found to correspond to a longer convection path length in the Northern hemisphere.

These results have implications for the diurnal- and seasonal-dependence of space weather impacts, since the onset time of a given event will determine the particular orientation of the Earth's magnetic field and hence which hemisphere preferentially faces the solar wind. A prediction error of several hours could yield significant differences in the possible impacts at a given location on the Earth, due to the associated ionospheric asymmetries. Over geological timescales, the migration of the dipole will also result in changes in the size of the polar cap. However, our results suggest that the magnetosphere can remain open under southward IMF regardless of the extent of the tilt, and hence space weather effects - whilst more localised for a smaller polar cap - could still be significant and may shift to lower-latitude regions not typically affected at present. Simulations of the magnetosphere during a severe event under a variety of possible orientations, e.g. the present day versus known historical dipole parameters, are a future point of study to determine more closely the sensitivity to changes in the tilt angle.

In Chapter 4, the ability of Gorgon to model such events is demonstrated. A combination of higher-resolution and resistive simulations are used to study solar wind-magnetosphere-ionosphere coupling during sudden commencement. The system is impacted by a fast-forward perpendicular interplanetary shock. A series of shocks with different IMF and dipole orientations and varying dynamic pressure are simulated to identify what most closely controls the strength of dayside coupling. Features are seen during the shock propagation which agree with previous studies, such as the reflection of a pressure wave off the ionospheric boundary which modulates the motion of the shocked magnetopause. The location of the separator is identified over time for each shock and is highly dynamic in each case, showing a complex geometry due to incoherent motion and strong distortion at the shock front.

By calculating the change in open flux content during the propagation, it is found that the dayside reconnection rate is strongly enhanced by the passage of the shock over the dayside. This is initially driven by pile-up of the magnetosheath plasma and a sharp enhancement of the reconnection electric field local to the shock front, which could lead to reconnection occurring at regions of the magnetopause where it is not usually expected. Whilst the enhanced reconnection rate shows some dependence on the IMF and dipole orientation, it appears to depend more closely on the jump in dynamic pressure and primarily the solar wind speed. Signatures are seen in the ionospheric open-closed boundary, which expands slightly on the dayside for several minutes prior to any eventual closure of flux in the magnetotail induced by the compression of the magnetosphere.

This work helps to explain previous observations suggesting enhancement of dayside reconnection in response to a dynamic pressure enhancement (e.g. Boudouridis et

al., 2007), as well as a greater coupling efficiency during such events where the associated E_y is relatively weak (e.g. Andreeova et al., 2011b). More fundamentally, it suggests that widely-used dayside coupling functions which assume steady conditions, strong scaling with the IMF orientation and generally linear scaling with solar wind speed may underestimate the strength of coupling during sudden commencement, and may fail to capture the actual trend between different events. The behaviour of the reconnection line also demonstrates the difficulty in studying reconnection using in-situ measurements during such events, due to the challenge of separating the large-scale magnetopause motion with local reconnection dynamics. Further investigations could include simulating a reverse shock (i.e. dynamic pressure decrease), and a focus on the subsequent, delayed enhancement of nightside reconnection.

In Chapter 5, Gorgon's capability is extended to simulate the state of the magnetosphere-ionosphere system during a real space weather event. A methodology is developed to drive the model in Solar Magnetic coordinates, and for the inclusion of corotation flow and non-uniform ionospheric conductances to capture more complex dynamics. The use of well-defined geospace coordinates allows for closer comparison to observations, and is an important step towards operational space weather forecasting. This tailored version of the code is then applied to a case study of a real geomagnetic storm which occurred from 3$^{\text{rd}}$-7$^{\text{th}}$ May 2014. The initial 24h of this event was marked by a prolonged $\sim$ 15h period of southward IMF driving either side of sharp transitions from northward to southward IMF and vice-versa. During this periods the IMF B_y was strong, and reversed sharply on two occasions. However the solar wind speed remained relatively constant, such that the characteristic timescales of global convection were determined primarily by the behaviour of the IMF. The simulated event was therefore used to study the timescales over which the magnetosphere-ionosphere system responds to changes in the IMF.

The time-delay of nightside reconnection to changes in dayside coupling is investigated by calculating changes in the total open flux content. After the IMF B_z switches from northward to southward (or vice-versa) the dayside (nightside) rate dominates for up to 2 hours. This corresponds to the gradual build-up of open flux in the magnetotail under southward IMF, and the delay over which this flux is eventually closed under northward IMF. The effect is visible in the strength of the tail lobe B_x which maximises after several hours of southward conditions, and slowly reduces towards the end of the simulation. The location and orientation of the magnetotail current sheet shows a complex time-dependence, being much flatter during strong driving and showing a dawn-dusk asymmetry in response to the large IMF B_y. Further analysis is performed by cross-correlating the current sheet rotation angle and hinging offset from the ecliptic plane with IMF variables. It is found that the current sheet rotation responds with a delay of $\sim$ 70min during southward IMF, whilst the hinging responds most strongly under northward IMF with a delay of $\sim$ 180min. These timescales are consistent with the reconfiguration of the magnetotail due to global convection rather than inductive effects due to propagation of MHD waves, and agree with the findings of observational studies

of ionospheric FACs (e.g. Milan et al., 2018, Coxon et al., 2019).

The ionospheric conditions follow similar trends in the simulation, with the FACs in the dawn-dusk plane responding promptly to changes in the IMF, but the polar cap size and CPCP showing a much slower response. The simulated FACs are compared to contemporary observations by AMPERE and the keograms show good overall agreement in the location of the Region 1 current system. Cross-correlation of the AMPERE FACs reveal timescales in agreement with the response of the magnetotail in the simulation, supporting the role of nightside reconnection and the expanding-contracting polar cap in controlling the location of ionospheric FACs and their associated asymmetries. These results demonstrate Gorgon's value as a space weather modelling tool - however, there are various possible improvements to the code that would greatly benefit any future forecasting efforts.

Foremost of these is the simulation grid, which at present is regular throughout the simulation domain. Whilst the code is highly parallelised and can be scaled to accommodate higher resolutions, this comes at a great computational cost when using a large simulation domain which may be prohibitive for some forecasting requirements. A stretched cartesian grid would allow for higher resolution in regions of interest, e.g. in the inner magnetosphere, and lower where a coarse grid is sufficient, e.g. the solar wind or distant magnetotail. This would also permit a smaller inner boundary at $\sim 3\ R_E$ for relatively little computational overhead, capturing lower-latitude FACs during periods of strong driving, and would also be of benefit for including a ring current, which is responsible for the Region 2 current system. Recent particle tracing efforts in Gorgon provide one avenue for including this, since test particles embedded within the MHD solver can be used to organically generate a ring current.

Such efforts should also be combined with a more complete ionospheric conductance model which accounts for auroral conductance. This could be calculated empirically based on MHD parameters as described in section 2.3.2, or defined via an assimilative approach by fitting to real data. Recent modelling work has included using the Gorgon outputs to produce basic estimates of the ground magnetic field at a given high-latitude geomagnetic station. The above improvements would greatly improve predictive capability, and allow for better coverage at lower latitudes e.g. within the UK. Finally, the Gorgon simulations can be used to aid existing and future space missions. For example, the MHD output has recently been used to generate model images based on X-ray emission within the magnetosphere, which is the goal of the upcoming SMILE mission; such efforts can provide a basis for future model-data comparisons.

The work in this thesis has shown the deep complexity at play in the coupling between the different components of the solar wind-magnetosphere-ionosphere system. At the magnetopause, reconnection is highly sensitive to the orientation of the IMF and terrestrial magnetic field, and its 3-dimensional behaviour can vary significantly whether the system is being driven by a steady or dynamic solar wind. The great utility of global MHD simulations in studying such phenomena has been demonstrated with a range

of studies. Changes in the coupling can generate asymmetries in the global magnetosphere, resulting in signatures on the ionosphere which are important in influencing space weather. These effects are communicated throughout the system over a variety of timescales, from those of rapid compressional signatures to those of slower, large-scale convection. Which of these dominates depends on the specific mode of driving, and may be difficult to predict using purely empirical models which do not take into account the prior state of the system. Such sensitivities demonstrate the difficulty in accurately predicting space weather impacts. Simulations are a invaluable tool for understanding these, and will be central to future efforts to unpick the mysteries of near-Earth space and its unique and growing relevance to society.

Bibliography

Abramowicz, M. A. and P. C. Fragile (2013). "Foundations of black hole accretion disk theory". In: *Living Reviews in Relativity* 16.1, pp. 1–88. DOI: 10.12942/lrr-2013-1.

Akasofu, S.-I. (2018). "A Review of the Current Understanding in the Study of Geomagnetic Storms". In: *International Journal of Earth Science and Geophysics* 4.1, pp. 1–13. DOI: 10.35840/2631-5033/1818.

Alfvén, H. (1977). "Electric currents in cosmic plasmas". In: *Reviews of Geophysics* 15.3, pp. 271–284. DOI: 10.1029/RG015i003p00271.

Amit, H. and P. Olson (2008). "Geomagnetic dipole tilt changes induced by core flow". In: *Physics of the Earth and Planetary Interiors* 166.3-4, pp. 226–238. DOI: 10.1016/j.pepi.2008.01.007.

Anderson, B. J., C. L. Johnson, H. Korth, J. A. Slavin, R. M. Winslow, R. J. Phillips, R. L. McNutt, and S. C. Solomon (2014). "Steady-state field-aligned currents at Mercury". In: *Geophysical Research Letters* 41.21, pp. 7444–7452. DOI: 10.1002/2014GL061677.

Anderson, B. J., K. Takahashi, and B. A. Toth (2000). "Sensing global Birkeland currents with iridium® engineering magnetometer data". In: *Geophysical Research Letters* 27.24, pp. 4045–4048. DOI: 10.1029/2000GL000094.

Andreeova, K., T. I. Pulkkinen, L. Juusola, M. Palmroth, and O. Santolík (2011a). "Propagation of a shock-related disturbance in the Earth's magnetosphere". In: *Journal of Geophysical Research: Space Physics* 116.A1. DOI: 10.1029/2010JA015908.

Andreeova, K., T. Pulkkinen, M. Palmroth, and R. McPherron (2011b). "Geoefficiency of solar wind discontinuities". In: *Journal of Atmospheric and Solar-Terrestrial Physics* 73.1, pp. 112–122. DOI: 10.1016/j.jastp.2010.03.006.

Andréeová, K., T. I. Pulkkinen, T. V. Laitinen, and L. Přech (2008). "Shock propagation in the magnetosphere: Observations and MHD simulations compared". In: *Journal of Geophysical Research: Space Physics* 113.A9. DOI: 10.1029/2008JA013350.

Araki, T. (1994). "A Physical Model of the Geomagnetic Sudden Commencement". In: *Solar Wind Sources of Magnetospheric Ultra-Low-Frequency Waves*. American Geophysical Union (AGU), pp. 183–200. DOI: 10.1029/GM081p0183.

Arber, T. D., A. W. Longbottom, C. L. Gerrard, and A. M. Milne (2001). "A Staggered Grid, Lagrangian-Eulerian Remap Code for 3-D MHD Simulations". In: *Journal of Computational Physics* 171.1, pp. 151–181. DOI: 10.1006/jcph.2001.6780.

Ashour-Abdalla, M., R. J. Walker, V. Peroomian, and M. El-Alaoui (2008). "On the importance of accurate solar wind measurements for studying magnetospheric dynamics". In: *Journal of Geophysical Research: Space Physics* 113.A8. DOI: 10.1029/2007JA012785.

Axford, W. I. (1984). "Magnetic Field Reconnection". In: *Magnetic Reconnection in Space and Laboratory Plasmas*. American Geophysical Union (AGU), pp. 1–8. DOI: 10.1029/GM030p0001.

Baumjohann, W. and R. A. Treumann (1997). *Basic Space Plasma Physics*. Vol. 78. Imperial College Press, p. 329. DOI: 10.1142/p015.

Benson, D. J. (1992). "Computational methods in Lagrangian and Eulerian hydrocodes". In: *Computer Methods in Applied Mechanics and Engineering* 99.2, pp. 235–394. DOI: 10.1016/0045-7825(92)90042-I.

Berdichevsky, D. B., A. Szabo, R. P. Lepping, A. F. Viñas, and F. Mariani (2000). "Interplanetary fast shocks and associated drivers observed through the 23rd solar minimum by Wind over its first 2.5 years". In: *Journal of Geophysical Research: Space Physics* 105.A12, pp. 27289–27314. DOI: 10.1029/1999JA000367.

Berube, D., M. B. Moldwin, S. F. Fung, and J. L. Green (2005). "A plasmaspheric mass density model and constraints on its heavy ion concentration". In: *Journal of Geophysical Research: Space Physics* 110.A4. DOI: 10.1029/2004JA010684.

Birkeland, K. ((1908). *The Norwegian aurora polaris expedition, 1902-1903. Volume I, On the cause of magnetic storms and the origin of terrestrial magnetism*. eng. Open Collections Program at Harvard University. Expeditions and discoveries. Christiania (Oslo) : London ; New York: H. Aschelhoug & Co. ; Longmans, Green & Co.

Boris, J. P. (1970). *A physically motivated solution of the Alfvén problem*. Tech. rep. 2167. Washington, DC: Naval Research Laboratory.

Borodkova, N. L. (2010). "Effect of large and sharp changes of solar wind dynamic pressure on the earths's magnetosphere: analysis of several events". In: *Cosmic Research* 48.1, pp. 41–55. DOI: 10.1134/S001095251001003X.

Borovsky, J. E., M. H. Denton, R. E. Denton, V. K. Jordanova, and J. Krall (2013). "Estimating the effects of ionospheric plasma on solar wind/magnetosphere coupling via mass loading of dayside reconnection: Ion-plasma-sheet oxygen, plasmaspheric drainage plumes, and the plasma cloak". In: *Journal of Geophysical Research: Space Physics* 118.9, pp. 5695–5719. DOI: 10.1002/jgra.50527.

Bothmer, V. and R. Schwenn (1997). "The structure and origin of magnetic clouds in the solar wind". In: *Annales Geophysicae* 16.1, pp. 1–24. DOI: 10.1007/PL00021390.

Boudouridis, A., L. R. Lyons, E. Zesta, and J. M. Ruohoniemi (2007). "Dayside reconnection enhancement resulting from a solar wind dynamic pressure increase". In: *Journal of Geophysical Research: Space Physics* 112.A6. DOI: 10.1029/2006JA012141.

Boudouridis, A., L. R. Lyons, E. Zesta, J. M. Weygand, A. J. Ribeiro, and J. M. Ruohoniemi (2011). "Statistical study of the effect of solar wind dynamic pressure fronts on the dayside and nightside ionospheric convection". In: *Journal of Geophysical Research: Space Physics* 116.A10. DOI: 10.1029/2011JA016582.

Boudouridis, A., E. Zesta, L. R. Lyons, P. C. Anderson, and D. Lummerzheim (2005). "Enhanced solar wind geoeffectiveness after a sudden increase in dynamic pressure during southward IMF orientation". In: *Journal of Geophysical Research: Space Physics* 110.A5. DOI: 10.1029/2004JA010704.

Browett, S. D., R. C. Fear, A. Grocott, and S. E. Milan (2017). "Timescales for the penetration of IMF By into the Earth's magnetotail". In: *Journal of Geophysical Research: Space Physics* 122.1, pp. 579–593. DOI: 10.1002/2016JA023198.

Bruntz, R., R. E. Lopez, M. Wiltberger, and J. G. Lyon (2012). "Investigation of the viscous potential using an MHD simulation". In: *Journal of Geophysical Research: Space Physics* 117.A3. DOI: 10.1029/2011JA017022.

Burgess, D. and M. Scholer (2015). "Shocks". In: *Collisionless Shocks in Space Plasmas: Structure and Accelerated Particles*. Cambridge Atmospheric and Space Science Series. Cambridge University Press, pp. 1–26. DOI: 10.1017/CBO9781139044097.002.

Cao, X. and C. Paty (2017). "Diurnal and seasonal variability of Uranus's magnetosphere". In: *Journal of Geophysical Research: Space Physics* 122.6, pp. 6318–6331. DOI: 10.1002/2017JA024063.

Case, N. A., A. Grocott, S. Haaland, C. J. Martin, and T. Nagai (2018). "Response of Earth's Neutral Sheet to Reversals in the IMF By Component". In: *Journal of Geophysical Research: Space Physics* 123.10, pp. 8206–8218. DOI: 10.1029/2018JA025712.

Cassak, P. A. and S. A. Fuselier (2016). "Reconnection at Earth's Dayside Magnetopause". In: *Magnetic Reconnection: Concepts and Applications*. Ed. by W. Gonzalez and E. Parker. Vol. 427, p. 213. DOI: 10.1007/978-3-319-26432-5_6.

Chen, Y., G. Tóth, P. Cassak, X. Jia, T. I. Gombosi, J. A. Slavin, S. Markidis, I. B. Peng, V. K. Jordanova, and M. G. Henderson (2017). "Global Three-Dimensional Simulation of Earth's Dayside Reconnection Using a Two-Way Coupled Magnetohydrodynamics With Embedded Particle-in-Cell Model: Initial Results". In: *Journal of Geophysical Research: Space Physics* 122.10, pp. 10, 318–10, 335. DOI: 10.1002/2017JA024186.

Ciardi, A., S. V. Lebedev, A. Frank, E. G. Blackman, J. P. Chittenden, C. J. Jennings, D. J. Ampleford, S. N. Bland, S. C. Bott, J. Rapley, G. N. Hall, F. A. Suzuki-Vidal, A. Marocchino, T. Lery, and C. Stehle (2007). "The evolution of magnetic tower jets in the laboratory". In: *Physics of Plasmas* 14.5, p. 056501. DOI: 10.1063/1.2436479.

Cnossen, I. and A. D. Richmond (2012). "How changes in the tilt angle of the geomagnetic dipole affect the coupled magnetosphere-ionosphere-thermosphere system". In: *Journal of Geophysical Research: Space Physics* 117.10. DOI: 10.1029/2012JA018056.

Cnossen, I., A. D. Richmond, and M. Wiltberger (2012a). "The dependence of the coupled magnetosphere-ionosphere-thermosphere system on the Earth's magnetic dipole moment". In: *Journal of Geophysical Research: Space Physics* 117.5. DOI: 10.1029/2012JA017555.

Cnossen, I., M. Wiltberger, and J. E. Ouellette (2012b). "The effects of seasonal and diurnal variations in the Earth ' s magnetic dipole orientation on solar wind – magnetosphere-ionosphere coupling". In: *Journal of Geophysical Research: Space Physics* 117.A11, pp. 1–10. DOI: 10.1029/2012JA017825.

Connor, H. K., E. Zesta, D. M. Ober, and J. Raeder (2014). "The relation between transpolar potential and reconnection rates during sudden enhancement of solar wind dynamic pressure: OpenGGCM-CTIM results". In: *Journal of Geophysical Research: Space Physics* 119.5, pp. 3411–3429. DOI: 10.1002/2013JA019728.

Connor, H. K., E. Zesta, M. Fedrizzi, Y. Shi, J. Raeder, M. V. Codrescu, and T. J. Fuller-Rowell (2016). "Modeling the ionosphere-thermosphere response to a geomagnetic storm using physics-based magnetospheric energy input: OpenGGCM-CTIM results". In: *Journal of Space Weather and Space Climate* 6, A25. DOI: 10.1051/swsc/2016019.

Cowley, S. W. H. (2000). "Magnetosphere-Ionosphere Interactions: A Tutorial Review". In: *Magnetospheric Current Systems*. American Geophysical Union (AGU), pp. 91–106. DOI: 10.1029/GM118p0091.

Cowley, S. W. H. (1981). "Magnetospheric asymmetries associated with the y-component of the IMF". In: *Planetary and Space Science* 29.1, pp. 79–96. DOI: 10.1016/0032-0633(81)90141-0.

Cowley, S. W. H. (2013). "Response of Uranus' auroras to solar wind compressions at equinox". In: *Journal of Geophysical Research: Space Physics* 118.6, pp. 2897–2902. DOI: 10.1002/jgra.50323.

Cowley, S. W. H. and M. Lockwood (1992). "Excitation and decay of solar wind-driven flows in the magnetosphere-ionosphere system". In: *Annales Geophysicae* 10.1-2, pp. 103–115.

Coxon, J. C., S. E. Milan, J. A. Carter, L. B. Clausen, B. J. Anderson, and H. Korth (2016). "Seasonal and diurnal variations in AMPERE observations of the Birkeland currents compared to modeled results". In: *Journal of Geophysical Research A: Space Physics* 121.5, pp. 4027–4040. DOI: 10.1002/2015JA022050.

Coxon, J. C., R. M. Shore, M. P. Freeman, R. C. Fear, S. D. Browett, A. W. Smith, D. K. Whiter, and B. J. Anderson (2019). "Timescales of Birkeland Currents Driven by the IMF". In: *Geophysical Research Letters*, 2018GL081658. DOI: 10.1029/2018GL081658.

Crooker, N. U. (1979). "Dayside merging and cusp geometry". In: *Journal of Geophysical Research* 84.A3, p. 951. DOI: 10.1029/JA084iA03p00951.

Davies, E. E., C. Möstl, M. J. Owens, A. Weiss, T. Amerstorfer, J. Hinterreiter, M. Bauer, R. Bailey, and et al. (2021). "In situ multi-spacecraft and remote imaging observations of the first CME detected by Solar Orbiter and BepiColombo". In: *A&A*. DOI: 10.1051/0004-6361/202040113.

Davies, E. E., R. J. Forsyth, S. W. Good, and E. K. Kilpua (2020). "On the Radial and Longitudinal Variation of a Magnetic Cloud: ACE, Wind, ARTEMIS and Juno Observations". In: *Solar Physics* 295.11, pp. 1–25. DOI: 10.1007/s11207-020-01714-z.

DeJong, A. D., J. M. Bell, and A. Ridley (2018). "Comparison of the Ionosphere During an SMC Initiating Substorm and an Isolated Substorm". In: *Journal of Geophysical Research: Space Physics* 123.6, pp. 4939–4951. DOI: 10.1029/2017JA025055.

DeJong, A. D., A. J. Ridley, X. Cai, and C. R. Clauer (2009). "A statistical study of BRIs (SMCs), isolated substorms, and individual sawtooth injections". In: *Journal of Geophysical Research: Space Physics* 114.A8. DOI: 10.1029/2008JA013870.

Desai, R. T., M. P. Freeman, J. P. Eastwood, J. W. B. Eggington, M. O. Archer, Y. Y. Shprits, N. P. Meredith, F. A. Staples, H. Hietala, L. Mejnertsen, J. P. Chittenden, and

R. B. Horne (2021). "Fast-Forward Interplanetary Shock-driven Magnetopause Compressions in Gorgon Global-MHD Simulations". In: *Geophysical Research Letters*. In Review.

Dorelli, J. C. and A. Bhattacharjee (2009). "On the generation and topology of flux transfer events". In: *Journal of Geophysical Research: Space Physics* 114.A6. DOI: 10.1029/2008JA013410.

Dungey, J. W. (1961). "Interplanetary magnetic field and the auroral zones". In: *Physical Review Letters* 6.2, pp. 47–48. DOI: 10.1103/PhysRevLett.6.47.

Dunlop, M. W., Q. H. Zhang, Y. V. Bogdanova, M. Lockwood, Z. Pu, H. Hasegawa, J. Wang, M. G. Taylor, J. Berchem, B. Lavraud, J. Eastwood, M. Volwerk, C. Shen, J. K. Shi, D. Constantinescu, H. Frey, A. N. Fazakerley, D. Sibeck, P. Escoubet, J. A. Wild, and Z. X. Liu (2011a). "Extended magnetic reconnection across the dayside magnetopause". In: *Physical Review Letters* 107.2, pp. 1–6. DOI: 10.1103/PhysRevLett.107.025004.

Dunlop, M. W., Q. H. Zhang, Y. V. Bogdanova, K. J. Trattner, Z. Pu, H. Hasegawa, J. Berchem, M. G. T. Taylor, M. Volwerk, J. P. Eastwood, B. Lavraud, C. Shen, J. K. Shi, J. Wang, D. Constantinescu, A. N. Fazakerley, H. Frey, D. Sibeck, P. Escoubet, J. A. Wild, Z. X. Liu, and C. Carr (2011b). "Magnetopause reconnection across wide local time". In: *Annales Geophysicae* 29.9, pp. 1693–1697. DOI: 10.5194/angeo-29-1683-2011.

Eastwood, J. P., M. A. Hapgood, E. Biffis, D. Benedetti, M. M. Bisi, L. Green, R. D. Bentley, and C. Burnett (2018). "Quantifying the Economic Value of Space Weather Forecasting for Power Grids: An Exploratory Study". In: *Space Weather* 16.12, pp. 2052–2067. DOI: 10.1029/2018SW002003.

Eastwood, J. P., H. Hietala, G. Toth, T. D. Phan, and M. Fujimoto (2015). "What Controls the Structure and Dynamics of Earth's Magnetosphere?" In: *Space Science Reviews* 188.1-4, pp. 251–286. DOI: 10.1007/s11214-014-0050-x.

Eastwood, J. P., R. Nakamura, L. Turc, L. Mejnertsen, and M. Hesse (2017). "The Scientific Foundations of Forecasting Magnetospheric Space Weather". In: *Space Science Reviews* 212.3-4, pp. 1221–1252. DOI: 10.1007/s11214-017-0399-8.

Eastwood, J. P., T. D. Phan, M. Øieroset, M. A. Shay, K. Malakit, M. Swisdak, J. F. Drake, and A. Masters (2013). "Influence of asymmetries and guide fields on the magnetic reconnection diffusion region in collisionless space plasmas". In: *Plasma Physics and Controlled Fusion* 55.12. DOI: 10.1088/0741-3335/55/12/124001.

Eastwood, J. P. (2008). "The science of space weather". In: *Philosophical Transactions of the Royal Society A: Mathematical, Physical and Engineering Sciences* 366.1884, pp. 4489–4500. DOI: 10.1098/rsta.2008.0161.

Eggington, J. W. B., J. P. Eastwood, L. Mejnertsen, R. T. Desai, and J. P. Chittenden (2020). "Dipole Tilt Effect on Magnetopause Reconnection and the Steady-State Magnetosphere-Ionosphere System: Global MHD Simulations". In: *Journal of Geophysical Research: Space Physics* 125.7. e2019JA027510 10.1029/2019JA027510, e2019JA027510. DOI: 10.1029/2019JA027510.

Eggington, J. W. B., J. P. Eastwood, L. Mejnertsen, R. T. Desai, and J. P. Chittenden (2018). "Forging links in Earth's plasma environment". In: *Astronomy & Geophysics* 59.6, pp. 6.26–6.28. DOI: 10.1093/astrogeo/aty275.

Fear, R. C., S. E. Milan, A. N. Fazakerley, K.-H. Fornacon, C. M. Carr, and I. Dandouras (2009). "Simultaneous observations of flux transfer events by THEMIS, Cluster, Double Star, and SuperDARN: Acceleration of FTEs". In: *Journal of Geophysical Research: Space Physics* 114.A10. DOI: 10.1029/2009JA014310.

Fear, R. C., L. Trenchi, J. C. Coxon, and S. E. Milan (2017). "How Much Flux Does a Flux Transfer Event Transfer?" In: *Journal of Geophysical Research: Space Physics* 122.12, pp. 12310–12327. DOI: 10.1002/2017JA024730.

Freeman, M. P., N. C. Freeman, and C. J. Farrugia (1995). "A linear perturbation analysis of magnetopause motion in the Newton-Busemann limit". In: *Annales Geophysicae* 13.9, pp. 907–918. DOI: 10.1007/s00585-995-0907-0.

Fujita, S., T. Tanaka, T. Kikuchi, K. Fujimoto, K. Hosokawa, and M. Itonaga (2003a). "A numerical simulation of the geomagnetic sudden commencement: 1. Generation of the field-aligned current associated with the preliminary impulse". In: *Journal of Geophysical Research* 108.A12, p. 1416. DOI: 10.1029/2002JA009407.

Fujita, S., T. Tanaka, T. Kikuchi, K. Fujimoto, and M. Itonaga (2003b). "A numerical simulation of the geomagnetic sudden commencement: 2. Plasma processes in the main impulse". In: *Journal of Geophysical Research* 108.A12, p. 1417. DOI: 10.1029/2002JA009763.

Fuller-Rowell, T. J. and C. J. Schrijver (2009). "On the ionosphere and chromosphere". In: *Heliophysics: Plasma Physics of the Local Cosmos*. Ed. by C. J. Schrijver and G. L. Siscoe. Cambridge University Press, pp. 324–359. DOI: 10.1017/CBO9781107340657.013.

Fuselier, S. A., K. J. Trattner, S. M. Petrinec, K. R. Pritchard, J. L. Burch, P. A. Cassak, B. L. Giles, B. Lavraud, and R. J. Strangeway (2019). "Stationarity of the Reconnection X-Line at Earth's Magnetopause for Southward IMF". In: *Journal of Geophysical Research: Space Physics* 124.11, pp. 8524–8534. DOI: 10.1029/2019JA027143.

Ganushkina, N. Y., M. W. Liemohn, and S. Dubyagin (2018). "Current Systems in the Earth's Magnetosphere". In: *Reviews of Geophysics* 56.2, pp. 309–332. DOI: https://doi.org/10.1002/2017RG000590.

Glocer, A., J. Dorelli, G. Toth, C. M. Komar, and P. A. Cassak (2016). "Separator reconnection at the magnetopause for predominantly northward and southward IMF: Techniques and results". In: *Journal of Geophysical Research A: Space Physics* 121.1, pp. 140–156. DOI: 10.1002/2015JA021417.

Gonzalez, W. D. and F. S. Mozer (1974). "A quantitative model for the potential resulting from reconnection with an arbitrary interplanetary magnetic field". In: *Journal of Geophysical Research* 79.28, pp. 4186–4194. DOI: 10.1029/JA079i028p04186.

Good, S. W. and R. J. Forsyth (2016). "Interplanetary Coronal Mass Ejections Observed by MESSENGER and Venus Express". In: *Solar Physics* 291.1, pp. 239–263. DOI: 10.1007/s11207-015-0828-3.

Goodman, M. L. (1995). "A three-dimensional, iterative mapping procedure for the implementation of an ionosphere-magnetosphere anisotropic Ohm's law boundary condition in global magnetohydrodynamic simulations". In: *Annales Geophysicae* 13.8, pp. 843–853. DOI: 10.1007/s00585-995-0843-z.

Gordeev, E., V. Sergeev, I. Honkonen, M. Kuznetsova, L. Rastätter, M. Palmroth, P. Janhunen, G. Tóth, J. Lyon, and M. Wiltberger (2015). In: *Space Weather* 13.12, pp. 868–884. DOI: 10.1002/2015SW001307.

Gosling, J. T. (2010). "The structure and evolution of the three-dimensional solar wind". In: *Heliophysics: Evolving Solar Activity and the Climates of Space and Earth*. Ed. by C. J. Schrijver and G. L. Siscoe. Cambridge University Press, pp. 217–242. DOI: 10.1017/CBO9780511760358.009.

Green, J. L. and S. Boardsen (2006). "Duration and extent of the great auroral storm of 1859". In: *Advances in Space Research* 38.2. The Great Historical Geomagnetic Storm of 1859: A Modern Look, pp. 130–135. DOI: 10.1016/j.asr.2005.08.054.

Grießmeier, J.-M., A. Stadelmann, T. Penz, H. Lammer, F. Selsis, I. Ribas, E. F. Guinan, U. Motschmann, H. K. Biernat, and W. W. Weiss (2004). "The effect of tidal locking on the magnetospheric and atmospheric evolution of "Hot Jupiters"". In: *Astronomy & Astrophysics* 425.2, pp. 753–762. DOI: 10.1051/0004-6361:20035684.

Gubbins, D. (2008). "Earth science: Geomagnetic reversals". In: *Nature* 452.7184, pp. 165–167. DOI: 10.1038/452165a.

Guo, J., X. Feng, B. A. Emery, J. Zhang, C. Xiang, F. Shen, and W. Song (2011). "Energy transfer during intense geomagnetic storms driven by interplanetary coronal mass ejections and their sheath regions". In: *Journal of Geophysical Research: Space Physics* 116.A5. DOI: 10.1029/2011JA016490.

Gurnett, D. A. and A. Bhattacharjee (2005). *Introduction to Plasma Physics: With Space and Laboratory Applications*. Cambridge University Press. DOI: 10.1017/CBO9780511809125.

Haaland, S., B. Lybekk, L. Maes, K. Laundal, A. Pedersen, P. Tenfjord, A. Ohma, N. Østgaard, J. Reistad, and K. Snekvik (2017). "North-south asymmetries in cold plasma density in the magnetotail lobes: Cluster observations". In: *Journal of Geophysical Research: Space Physics* 122.1, pp. 136–149. DOI: 10.1002/2016JA023404.

Hadjidimos, A. (2000). In: *Journal of Computational and Applied Mathematics* 123.1-2, pp. 177–199. DOI: 10.1016/S0377-0427(00)00403-9.

Han, D.-S., H.-G. Yang, J. Liang, T. Iyemori, S. W. H. Cowley, and T. Araki (2010). "High-latitude reconnection effect observed at the dayside dip equator as a precursor of a sudden impulse". In: *Journal of Geophysical Research: Space Physics* 115.A8. DOI: 10.1029/2009JA014787.

Hansteen, V. H. (2009). In: *Heliophysics: Plasma Physics of the Local Cosmos*. Cambridge University Press, pp. 195–224. DOI: 10.1017/CBO9781107340657.

Hapgood, M. A. (1992). "Space physics coordinate transformations: A user guide". In: *Planetary and Space Science* 40.5, pp. 711–717. DOI: 10.1016/0032-0633(92)90012-D.

Hasegawa, H., N. Kitamura, Y. Saito, T. Nagai, I. Shinohara, S. Yokota, C. J. Pollock, B. L. Giles, J. C. Dorelli, D. J. Gershman, L. A. Avanov, S. Kreisler, W. R. Paterson,

M. O. Chandler, V. Coffey, J. L. Burch, R. B. Torbert, T. E. Moore, C. T. Russell, R. J. Strangeway, G. Le, M. Oka, T. D. Phan, B. Lavraud, S. Zenitani, and M. Hesse (2016). "Decay of mesoscale flux transfer events during quasi-continuous spatially extended reconnection at the magnetopause". In: *Geophysical Research Letters* 43.10, pp. 4755–4762. DOI: 10.1002/2016GL069225.

Haynes, A. L. and C. E. Parnell (2007). "A trilinear method for finding null points in a three-dimensional vector space". In: *Physics of Plasmas* 14.8. DOI: 10.1063/1.2756751.

Heelis, R. A. and A. Maute (2020). "Challenges to Understanding the Earth's Ionosphere and Thermosphere". In: *Journal of Geophysical Research: Space Physics* 125.7. DOI: 10.1029/2019JA027497.

Hesse, M. (1997). "On the mapping of ionospheric convection into the magnetosphere". In: *Journal of Geophysical Research A: Space Physics* 102.A5, pp. 9543–9551. DOI: 10.1029/96JA03999.

Hesse, M., T. G. Forbes, and J. Birn (2005). "On the Relation between Reconnected Magnetic Flux and Parallel Electric Fields in the Solar Corona". In: *The Astrophysical Journal* 631.2, pp. 1227–1238. DOI: 10.1086/432677.

Hesse, M., T. Neukirch, K. Schindler, M. Kuznetsova, and S. Zenitani (2011). "The diffusion region in collisionless magnetic reconnection". In: *Space Science Reviews*. Vol. 160. 1-4, pp. 3–23. DOI: 10.1007/s11214-010-9740-1.

Hoilijoki, S., V. M. Souza, B. M. Walsh, P. Janhunen, and M. Palmroth (2014). "Magnetopause reconnection and energy conversion as influenced by the dipole tilt and the IMF Bx". In: *Journal of Geophysical Research: Space Physics* 119.6, pp. 4484–4494. DOI: 10.1002/2013JA019693.

Honkonen, I., L. Rastätter, A. Grocott, A. Pulkkinen, M. Palmroth, J. Raeder, A. J. Ridley, and M. Wiltberger (2013). "On the performance of global magnetohydrodynamic models in the Earth's magnetosphere". In: *Space Weather* 11.5, pp. 313–326. DOI: 10.1002/swe.20055.

Hoppe, H., T. DeRose, T. Duchamp, J. McDonald, and W. Stuetzle (1992). "Surface Reconstruction from Unorganized Points". In: *SIGGRAPH Comput. Graph.* 26.2, pp. 71–78. DOI: 10.1145/142920.134011.

Hoshi, Y., H. Hasegawa, N. Kitamura, Y. Saito, and V. Angelopoulos (2018). "Seasonal and Solar Wind Control of the Reconnection Line Location on the Earth's Dayside Magnetopause". In: *Journal of Geophysical Research: Space Physics* 123.9, pp. 7498–7512. DOI: 10.1029/2018JA025305.

Hu, Y. Q., X. C. Guo, and C. Wang (2007). "On the ionospheric and reconnection potentials of the earth: Results from global MHD simulations". In: *Journal of Geophysical Research: Space Physics* 112.A7. DOI: 10.1029/2006JA012145.

Huang, Y., C. Y. Huang, Y.-J. Su, Y. Deng, and X. Fang (2014). "Ionization due to electron and proton precipitation during the August 2011 storm". In: *Journal of Geophysical Research: Space Physics* 119.4, pp. 3106–3116. DOI: 10.1002/2013JA019671.

Hubert, B., M. Palmroth, T. V. Laitinen, P. Janhunen, S. E. Milan, A. Grocott, S. W. H. Cowley, T. Pulkkinen, and J.-C. Gérard (2006). "Compression of the Earth's magnetotail by interplanetary shocks directly drives transient magnetic flux closure". In: *Geophysical Research Letters* 33.10. DOI: 10.1029/2006GL026008.

Hundhausen, A. J. (2019). "The Solar Wind". In: *Introduction to Space Physics*. Cambridge University Press, pp. 91–128. DOI: 10.1017/9781139878296.005.

Hwang, K.-J., D. G. Sibeck, B. L. Giles, C. J. Pollock, D. Gershman, L. Avanov, W. R. Paterson, J. C. Dorelli, R. E. Ergun, C. T. Russell, R. J. Strangeway, B. Mauk, I. J. Cohen, R. B. Torbert, and J. L. Burch (2016). "The substructure of a flux transfer event observed by the MMS spacecraft". In: *Geophysical Research Letters* 43.18, pp. 9434–9443. DOI: 10.1002/2016GL070934.

Janhunen, P., M. Palmroth, T. Laitinen, I. Honkonen, L. Juusola, G. Facskó, and T. I. Pulkkinen (2012). "The GUMICS-4 global MHD magnetosphere-ionosphere coupling simulation". In: *Journal of Atmospheric and Solar-Terrestrial Physics* 80, pp. 48–59. DOI: 10.1016/j.jastp.2012.03.006.

Jelínek, K., Z. Němeček, J. Šafránková, and J. Merka (2008). "Influence of the tilt angle on the bow shock shape and location". In: *Journal of Geophysical Research: Space Physics* 113.A5. DOI: 10.1029/2007JA012813.

Jennings, C. A. (2006). "Radiation transport effects in wire array Z pinches and magnetohydrodynamic modelling techniques". PhD thesis. Imperial College London.

Jensen, J. B., J. Raeder, K. Maynard, and W. D. Cramer (2017). "Particle Precipitation Effects on Convection and the Magnetic Reconnection Rate in Earth's Magnetosphere". In: *Journal of Geophysical Research: Space Physics* 122.11, pp. 11, 413–11, 427. DOI: 10.1002/2017JA024030.

Keller, K. A., M. Hesse, M. Kuznetsova, L. Rastätter, T. Moretto, T. I. Gombosi, and D. L. DeZeeuw (2002). "Global MHD modeling of the impact of a solar wind pressure change". In: *Journal of Geophysical Research* 107.A7, p. 1126. DOI: 10.1029/2001JA000060.

Kilpua, E. K. J., A. Balogh, R. von Steiger, and Y. D. Liu (2017). "Geoeffective Properties of Solar Transients and Stream Interaction Regions". In: *Space Science Reviews* 212.3, pp. 1271–1314. DOI: 10.1007/s11214-017-0411-3.

Kim, H., M. R. Lessard, S. L. Jones, K. A. Lynch, P. A. Fernandes, A. L. Aruliah, M. J. Engebretson, J. I. Moen, K. Oksavik, A. G. Yahnin, and T. K. Yeoman (2017). "Simultaneous observations of traveling convection vortices: Ionosphere-thermosphere coupling". In: *Journal of Geophysical Research: Space Physics* 122.5, pp. 4943–4959. DOI: 10.1002/2017JA023904.

King, A., J. Billingham, and S. Otto (2003). *Differential Equations: Linear, Nonlinear, Ordinary, Partial*. Cambridge University Press, p. 554. DOI: 10.1017/CBO9780511755293.

Kivelson, M. G. and C. T. Russell (1995). *Introduction to Space Physics*. Cambridge University Press, p. 568. DOI: 10.1063/1.2807586.

Komar, C. M., R. L. Fermo, and P. A. Cassak (2015). "Comparative analysis of dayside magnetic reconnection models in global magnetosphere simulations". In: *Journal of*

Geophysical Research: Space Physics 120, pp. 276–294. DOI: 10.1002/2014JA020587. Received.

Komar, C. M. and P. A. Cassak (2016). "The local dayside reconnection rate for oblique interplanetary magnetic fields". In: *Journal of Geophysical Research A: Space Physics* 121.6, pp. 5105–5120. DOI: 10.1002/2016JA022530.

Komar, C. M., P. A. Cassak, J. C. Dorelli, A. Glocer, and M. M. Kuznetsova (2013). "Tracing magnetic separators and their dependence on IMF clock angle in global magnetospheric simulations". In: *Journal of Geophysical Research: Space Physics* 118.8, pp. 4998–5007. DOI: 10.1002/jgra.50479.

Korte, M. and M. Mandea (2008). "Magnetic poles and dipole tilt variation over the past decades to millennia". In: *Earth, Planets and Space* 60.9, pp. 937–948. DOI: 10.1186/BF03352849.

Kubota, Y., R. Kataoka, M. Den, T. Tanaka, T. Nagatsuma, and S. Fujita (2015). "Global MHD simulation of magnetospheric response of preliminary impulse to large and sudden enhancement of the solar wind dynamic pressure". In: *Earth, Planets and Space* 67.1, p. 94. DOI: 10.1186/s40623-015-0270-7.

Laitinen, T. V., P. Janhunen, T. I. Pulkkinen, M. Palmroth, and H. E. Koskinen (2006). "On the characterization of magnetic reconnection in global MHD simulations". In: *Annales Geophysicae* 24.11, pp. 3059–3069. DOI: 10.5194/angeo-24-3059-2006.

Lilensten, J., P. L. Blelly, W. Kofman, and D. Alcaydé (1996). "Auroral ionospheric conductivities: a comparison between experiment and modeling, and theoretical $f_{10.7}$-dependent model for EISCAT and ESR". In: *Annales Geophysicae* 14.12, pp. 1297–1304. DOI: 10.1007/s00585-996-1297-7.

Liou, K., T. Sotirelis, and E. J. Mitchell (2018). "North-South Asymmetry in the Geographic Location of Auroral Substorms correlated with Ionospheric Effects". In: *Scientific Reports* 8.1, p. 17230. DOI: 10.1038/s41598-018-35091-2.

Liu, Z.-Q., J. Y. Lu, K. Kabin, Y. F. Yang, M. X. Zhao, and X. Cao (2012). "Dipole tilt control of the magnetopause for southward IMF from global magnetohydrodynamic simulations". In: *Journal of Geophysical Research: Space Physics* 117.A7. DOI: 10.1029/2011JA017441.

Livermore, P. W., C. C. Finlay, and M. Bayliff (2020). "Recent north magnetic pole acceleration towards Siberia caused by flux lobe elongation". In: *Nature Geoscience* 13.5, pp. 387–391. DOI: 10.1038/s41561-020-0570-9.

Longcope, D. W. (2005). "Topological methods for the analysis of solar magnetic fields". In: *Living Reviews in Solar Physics* 2.1, pp. 1–72. DOI: 10.12942/lrsp-2005-7.

Lotko, W. (2004). In: *Journal of Atmospheric and Solar-Terrestrial Physics* 66.15-16 SPEC. ISS. Pp. 1443–1456. DOI: 10.1016/j.jastp.2004.03.027.

Lu, J. Y., Z.-Q. Liu, K. Kabin, H. Jing, M. X. Zhao, and Y. Wang (2013). "The IMF dependence of the magnetopause from global MHD simulations". In: *Journal of Geophysical Research: Space Physics* 118.6, pp. 3113–3125. DOI: 10.1002/jgra.50324.

Lu, J. Y., Y. Zhou, X. Ma, M. Wang, K. Kabin, and H. Z. Yuan (2019a). "Earth's Bow Shock: A New Three-Dimensional Asymmetric Model With Dipole Tilt Effects". In: *Journal of Geophysical Research: Space Physics* 124.7, pp. 5396–5407. DOI: 10.1029/2018JA026144.

Lu, J., H. Zhang, M. Wang, C. Gu, and H. Guan (2019b). "Magnetosphere response to the IMF turning from north to south". In: *Earth and Planetary Physics* 3.1, pp. 8–16. DOI: 10.26464/epp2019002.

Lyon, J. G., J. A. Fedder, and C. M. Mobarry (2004). "The Lyon-Fedder-Mobarry (LFM) global MHD magnetospheric simulation code". In: *Journal of Atmospheric and Solar-Terrestrial Physics* 66.15-16, pp. 1333–1350. DOI: 10.1016/j.jastp.2004.03.020.

Lyons, L. R. and D. S. Evans (1984). "An association between discrete aurora and energetic particle boundaries". In: *Journal of Geophysical Research* 89.A4, p. 2395. DOI: 10.1029/JA089iA04p02395.

Lyons, L. (2000). "Geomagnetic disturbances: characteristics of, distinction between types, and relations to interplanetary conditions". In: *Journal of Atmospheric and Solar-Terrestrial Physics* 62.12, pp. 1087–1114. DOI: 10.1016/S1364-6826(00)00097-3.

Mailyan, B., C. Munteanu, and S. Haaland (2008). "What is the best method to calculate the solar wind propagation delay?" In: *Annales Geophysicae* 26.8, pp. 2383–2394. DOI: 10.5194/angeo-26-2383-2008.

Markidis, S., V. Olshevsky, G. Toth, Y. Chen, I. Peng, G. Lapenta, and T. Gombosi (2020). *Kinetic Modeling of Magnetospheres*.

Masters, A. (2015). "Magnetic reconnection at Neptune's magnetopause". In: *Journal of Geophysical Research: Space Physics* 120.1, pp. 479–493. DOI: 10.1002/2014JA020744.

Mejnertsen, L., J. P. Eastwood, J. P. Chittenden, and A. Masters (2016). "Global MHD simulations of Neptune's magnetosphere". In: *Journal of Geophysical Research: Space Physics* 121.8, pp. 7497–7513. DOI: 10.1002/2015JA022272.

Mejnertsen, L., J. P. Eastwood, H. Hietala, S. J. Schwartz, and J. P. Chittenden (2018). "Global MHD Simulations of the Earth's Bow Shock Shape and Motion Under Variable Solar Wind Conditions". In: *Journal of Geophysical Research: Space Physics*. DOI: 10.1002/2017JA024690.

Mejnertsen, L. (2018). "The Dynamics of the Outer Boundaries in Global Simulations of Planetary Magnetospheres". PhD thesis. Imperial College London, pp. 104–105. DOI: 10.25560/65696.

Menard, J., T. Brown, L. El-Guebaly, M. Boyer, J. Canik, B. Colling, R. Raman, Z. Wang, Y. Zhai, P. Buxton, B. Covele, C. D'Angelo, A. Davis, S. Gerhardt, M. Gryaznevich, M. Harb, T. Hender, S. Kaye, D. Kingham, M. Kotschenreuther, S. Mahajan, R. Maingi, E. Marriott, E. Meier, L. Mynsberge, C. Neumeyer, M. Ono, J.-K. Park, S. Sabbagh, V. Soukhanovskii, P. Valanju, and R. Woolley (2016). "Fusion nuclear science facilities and pilot plants based on the spherical tokamak". In: *Nuclear Fusion* 56.10, p. 106023. DOI: 10.1088/0029-5515/56/10/106023.

Merkin, V. G. and J. G. Lyon (2010). "Effects of the low-latitude ionospheric boundary condition on the global magnetosphere". In: *Journal of Geophysical Research: Space Physics* 115.10, pp. 1–15. DOI: 10.1029/2010JA015461.

Merkin, V. G., K. Papadopoulos, G. Milikh, A. S. Sharma, X. Shao, J. Lyon, and C. Goodrich (2003). "Effects of the solar wind electric field and ionospheric conductance on the cross polar cap potential: Results of global MHD modeling". In: *Geophysical Research Letters* 30.23. DOI: 10.1029/2003GL017903.

Milan, S. E. (2015). "Sun et Lumiere: Solar wind-magnetosphere coupling as deduced from ionospheric flows and polar auroras". In: *Astrophysics and Space Science Proceedings*. Vol. 41. Kluwer Academic Publishers, pp. 33–64. DOI: 10.1007/978-3-319-18359-6_2.

Milan, S. E., L. B. Clausen, J. C. Coxon, J. A. Carter, M. T. Walach, K. Laundal, N. Østgaard, P. Tenfjord, J. Reistad, K. Snekvik, H. Korth, and B. J. Anderson (2017). *Overview of Solar Wind–Magnetosphere–Ionosphere–Atmosphere Coupling and the Generation of Magnetospheric Currents*. DOI: 10.1007/s11214-017-0333-0.

Milan, S. E., S. W. H. Cowley, M. Lester, D. M. Wright, J. A. Slavin, M. Fillingim, C. W. Carlson, and H. J. Singer (2004). "Response of the magnetotail to changes in the open flux content of the magnetosphere". In: *Journal of Geophysical Research: Space Physics* 109.A4. DOI: 10.1029/2003JA010350.

Milan, S. E., J. S. Gosling, and B. Hubert (2012). "Relationship between interplanetary parameters and the magnetopause reconnection rate quantified from observations of the expanding polar cap". In: *Journal of Geophysical Research: Space Physics* 117.A3, n/a–n/a. DOI: 10.1029/2011JA017082.

Milan, S. E., M.-T. Walach, J. A. Carter, H. Sangha, and B. J. Anderson (2019). "Substorm Onset Latitude and the Steadiness of Magnetospheric Convection". In: *Journal of Geophysical Research: Space Physics* 124.3, pp. 1738–1752. DOI: 10.1029/2018JA025969.

Milan, S. E., J. A. Carter, H. Sangha, K. M. Laundal, N. Østgaard, P. Tenfjord, J. P. Reistad, K. Snekvik, J. C. Coxon, H. Korth, and B. J. Anderson (2018). "Timescales of Dayside and Nightside Field-Aligned Current Response to Changes in Solar Wind-Magnetosphere Coupling". In: *Journal of Geophysical Research: Space Physics* 123.9, pp. 7307–7319. DOI: 10.1029/2018JA025645.

Moen, J. and A. Brekke (1993). "The solar flux influence on quiet time conductances in the auroral ionosphere". In: *Geophysical Research Letters* 20.10, pp. 971–974. DOI: 10.1029/92GL02109.

Moore, L., T. Stallard, and M. Galand (2016). "Upper atmospheres of the giant planets". In: *Heliophysics: Active Stars, their Astrospheres, and Impacts on Planetary Environments*. Ed. by C. J. Schrijver, F. Bagenal, and J. J. Sojka. Cambridge University Press, pp. 175–200. DOI: 10.1017/CBO9781316106778.009.

Moriña, D., I. Serra, P. Puig, and Á. Corral (2019). "Probability estimation of a Carrington-like geomagnetic storm". In: *Scientific Reports* 9.1, pp. 1–9. DOI: 10.1038/s41598-019-38918-8.

Morley, S. K. and M. Lockwood (2006). "A numerical model of the ionospheric signatures of time-varying magnetic reconnection: III. Quasi-instantaneous convection responses in the Cowley-Lockwood paradigm". In: *Annales Geophysicae* 24.3, pp. 961–972. DOI: 10.5194/angeo-24-961-2006.

Motoba, T., K. Hosokawa, Y. Ogawa, N. Sato, A. Kadokura, S. C. Buchert, and H. Rème (2011). "In situ evidence for interplanetary magnetic field induced tail twisting associated with relative displacement of conjugate auroral features". In: *Journal of Geophysical Research: Space Physics* 116.A4. DOI: 10.1029/2010JA016206.

Mukhopadhyay, A., D. T. Welling, M. W. Liemohn, A. J. Ridley, S. Chakraborty, and B. J. Anderson (2020). "Conductance Model for Extreme Events: Impact of Auroral Conductance on Space Weather Forecasts". In: *Space Weather* 18.11, e2020SW002551. DOI: 10.1029/2020SW002551.

Murphy, K. R., C. E. J. Watt, I. R. Mann, I. Jonathan Rae, D. G. Sibeck, A. J. Boyd, C. F. Forsyth, D. L. Turner, S. G. Claudepierre, D. N. Baker, H. E. Spence, G. D. Reeves, J. B. Blake, and J. Fennell (2018). "The Global Statistical Response of the Outer Radiation Belt During Geomagnetic Storms". In: *Geophysical Research Letters* 45.9, pp. 3783–3792. DOI: 10.1002/2017GL076674.

Neugebauer, M. and C. W. Snyder (1962). "Solar Plasma Experiment". In: *Science* 138.3545, pp. 1095–1097. DOI: 10.1126/science.138.3545.1095-a.

Newell, P. T., T. Sotirelis, and S. Wing (2009). "Diffuse, monoenergetic, and broadband aurora: The global precipitation budget". In: *Journal of Geophysical Research: Space Physics* 114.A9. DOI: 10.1029/2009JA014326.

Nichols, J. D. and S. E. Milan (2016). In: *Monthly Notices of the Royal Astronomical Society* 461.3, pp. 2353–2366. DOI: 10.1093/mnras/stw1430.

Nishimura, Y., M. R. Lessard, Y. Katoh, Y. Miyoshi, E. Grono, N. Partamies, N. Sivadas, K. Hosokawa, M. Fukizawa, M. Samara, R. G. Michell, R. Kataoka, T. Sakanoi, D. K. Whiter, S. ichiro Oyama, Y. Ogawa, and S. Kurita (2020). *Diffuse and Pulsating Aurora*. DOI: 10.1007/s11214-019-0629-3.

Odstrcil, D. (2003). "Modeling 3-D solar wind structure". In: *Advances in Space Research* 32.4. Heliosphere at Solar Maximum, pp. 497–506. DOI: 10.1016/S0273-1177(03)00332-6.

Oliveira, D. M. and J. Raeder (2014). "Impact angle control of interplanetary shock geoeffectiveness". In: *Journal of Geophysical Research: Space Physics* 119.10, pp. 8188–8201. DOI: 10.1002/2014JA020275.

Ouellette, J. E., J. G. Lyon, O. J. Brambles, B. Zhang, and W. Lotko (2016). "The effects of plasmaspheric plumes on dayside reconnection". In: *Journal of Geophysical Research: Space Physics* 121.5, pp. 4111–4118. DOI: 10.1002/2016JA022597.

Owens, M. J. (2016). "DO THE LEGS OF MAGNETIC CLOUDS CONTAIN TWISTED FLUX-ROPE MAGNETIC FIELDS?" In: *The Astrophysical Journal* 818.2, p. 197. DOI: 10.3847/0004-637x/818/2/197.

Owens, M. J. and R. J. Forsyth (2013). "The heliospheric magnetic field". In: *Living Reviews in Solar Physics* 10.1, pp. 1–52. DOI: 10.12942/lrsp-2013-5.

Ozturk, D. S., S. Zou, J. A. Slavin, and A. J. Ridley (2019). "Response of the Geospace System to the Solar Wind Dynamic Pressure Decrease on 11 June 2017: Numerical Models and Observations". In: *Journal of Geophysical Research: Space Physics* 124.4, pp. 2613–2627. DOI: 10.1029/2018JA026315.

Palmroth, M., N. Partamies, J. Polvi, T. I. Pulkkinen, D. J. McComas, R. J. Barnes, P. Stauning, C. W. Smith, H. J. Singer, and R. Vainio (2007). "Solar wind–magnetosphere coupling efficiency for solar wind pressure impulses". In: *Geophysical Research Letters* 34.11. DOI: 10.1029/2006GL029059.

Palmroth, M., T. I. Pulkkinen, P. Janhunen, and C.-C. Wu (2003). "Stormtime energy transfer in global MHD simulation". In: *Journal of Geophysical Research* 108.A1, p. 1048. DOI: 10.1029/2002JA009446.

Palmroth, M., S. Hoilijoki, L. Juusola, T. I. Pulkkinen, H. Hietala, Y. Pfau-Kempf, U. Ganse, S. Von Alfthan, R. Vainio, and M. Hesse (2017). "Tail reconnection in the global magnetospheric context: Vlasiator first results". In: *Annales Geophysicae* 35.6, pp. 1269–1274. DOI: 10.5194/angeo-35-1269-2017.

Papitashvili, V. O., F. Christiansen, and T. Neubert (2002). "A new model of field-aligned currents derived from high-precision satellite magnetic field data". In: *Geophysical Research Letters* 29.14, pp. 28–1–28–4. DOI: 10.1029/2001GL014207.

Park, K. S., T. Ogino, and Y. H. Kim (2010). "Effects of the dipole tilt and northward and duskward IMF on dayside magnetic reconnection in a global MHD simulation". In: *Journal of Geophysical Research: Space Physics* 115.A2, n/a–n/a. DOI: 10.1029/2009JA014212.

Park, K. S., T. Ogino, and R. J. Walker (2006). "On the importance of antiparallel reconnection when the dipole tilt and IMF By are nonzero". In: *Journal of Geophysical Research: Space Physics* 111.A5. DOI: https://doi.org/10.1029/2004JA010972.

Parker, E. N. (1958). "Dynamics of the Interplanetary Gas and Magnetic Fields." In: 128, p. 664. DOI: 10.1086/146579.

Parnell, C. E., J. M. Smith, T. Neukirch, and E. R. Priest (1996). "The structure of three-dimensional magnetic neutral points". In: *Physics of Plasmas* 3.3, pp. 759–770. DOI: 10.1063/1.871810.

Paschmann, G., M. Øieroset, and T. Phan (2013). *In-situ observations of reconnection in space*. DOI: 10.1007/s11214-012-9957-2.

Peng, Z., C. Wang, and Y. Q. Hu (2010). "Role of IMF Bx in the solar wind-magnetosphere-ionosphere coupling". In: *Journal of Geophysical Research: Space Physics* 115.8, pp. 1–7. DOI: 10.1029/2010JA015454.

Petrukovich, A. A. (2011). "Origins of plasma sheet By". In: *Journal of Geophysical Research: Space Physics* 116.A7. DOI: 10.1029/2010JA016386.

Pettigrew, E. D., S. G. Shepherd, and J. M. Ruohoniemi (2010). "Climatological patterns of high-latitude convection in the Northern and Southern hemispheres: Dipole tilt dependencies and interhemispheric comparisons". In: *Journal of Geophysical Research: Space Physics* 115.A7. DOI: 10.1029/2009JA014956.

Pfau-Kempf, Y., M. Palmroth, A. Johlander, L. Turc, M. Alho, M. Battarbee, M. Dubart, M. Grandin, and U. Ganse (2020). "Hybrid-Vlasov modeling of three-dimensional dayside magnetopause reconnection". In: *Physics of Plasmas* 27.9, p. 092903. DOI: 10.1063/5.0020685.

Pitkänen, T., M. Hamrin, A. Kullen, R. Maggiolo, T. Karlsson, H. Nilsson, and P. Norqvist (2016). "Response of magnetotail twisting to variations in IMF By: A THEMIS case study 1–2 January 2009". In: *Geophysical Research Letters* 43.15, pp. 7822–7830. DOI: 10.1002/2016GL070068.

Pitkänen, T., A. Kullen, L. Cai, J.-S. Park, H. Vanhamäki, M. Hamrin, A. T. Aikio, G. S. Chong, A. De Spiegeleer, and Q. Shi (2021). "Asymmetry in the Earth's magnetotail neutral sheet rotation due to IMF B_y sign?" In: *Geoscience Letters* 8.1, p. 3. DOI: 10.1186/s40562-020-00171-7.

Pizzo, V. J. (1991). "The evolution of corotating stream fronts near the ecliptic plane in the inner solar system: 2. Three-dimensional tilted-dipole fronts". In: *Journal of Geophysical Research: Space Physics* 96.A4, pp. 5405–5420. DOI: 10.1029/91JA00155.

Powell, K. G., P. L. Roe, T. J. Linde, T. I. Gombosi, and D. L. De Zeeuw (1999). "A Solution-Adaptive Upwind Scheme for Ideal Magnetohydrodynamics". In: *Journal of Computational Physics* 154.2, pp. 284–309. DOI: 10.1006/jcph.1999.6299.

Raeder, J. (2006). "Flux Transfer Events: 1. generation mechanism for strong southward IMF". In: *Annales Geophysicae* 24.1, pp. 381–392. DOI: 10.5194/angeo-24-381-2006.

Raeder, J., J. Berchem, and M. Ashour-Abdalla (1998). "The Geospace Environment Modeling Grand Challenge: Results from a Global Geospace Circulation Model". In: *Journal of Geophysical Research: Space Physics* 103.A7, pp. 14787–14797. DOI: 10.1029/98ja00014.

Raeder, J., R. L. McPherron, L. A. Frank, S. Kokubun, G. Lu, T. Mukai, W. R. Paterson, J. B. Sigwarth, H. J. Singer, and J. A. Slavin (2001a). "Global simulation of the Geospace Environment Modeling substorm challenge event". In: *Journal of Geophysical Research: Space Physics* 106.A1, pp. 381–395. DOI: 10.1029/2000JA000605.

Raeder, J. (2003). "Global Magnetohydrodynamics – A Tutorial". In: *Space Plasma Simulation*. Vol. 615, pp. 212–246. DOI: 10.1007/3-540-36530-3.

Raeder, J., Y. Wang, and T. J. Fuller-Rowell (2001b). "Geomagnetic Storm Simulation with a Coupled Magnetosphere-Ionosphere-Thermosphere Model". In: *Space Weather*. American Geophysical Union (AGU), pp. 377–384. DOI: 10.1029/GM125p0377.

Richardson, J. D., J. W. Belcher, P. Garcia-Galindo, and L. F. Burlaga (2019). "Voyager 2 plasma observations of the heliopause and interstellar medium". In: *Nature Astronomy* 3.11, pp. 1019–1023. DOI: 10.1038/s41550-019-0929-2.

Richmond, A. D. and Y. Kamide (1988). "Mapping electrodynamic features of the high-latitude ionosphere from localized observations: Technique". In: *Journal of Geophysical Research* 93.A6, p. 5741. DOI: 10.1029/ja093ia06p05741.

Richter, A. K., K. C. Hsieh, A. H. Luttrell, E. Marsch, and R. Schwenn (1985). "Review of Interplanetary Shock Phenomena Near and within 1 AU". In: *Collisionless Shocks in the Heliosphere: Reviews of Current Research*. American Geophysical Union (AGU), pp. 33–50. DOI: 10.1029/GM035p0033.

Ridley, A. J. (2007). "Effects of seasonal changes in the ionospheric conductances on magnetospheric field-aligned currents". In: *Geophysical Research Letters* 34.5. DOI: 10.1029/2006GL028444.

Ridley, A. J., T. I. Gombosi, and D. L. Dezeeuw (2004). "Ionospheric control of the magnetosphere: conductance". In: *Annales Geophysicae* 22.2, pp. 567–584. DOI: 10.5194/angeo-22-567-2004.

Ridley, A. J., T. I. Gombosi, I. V. Sokolov, G. Tóth, and D. T. Welling (2010). "Numerical considerations in simulating the global magnetosphere". In: *Annales Geophysicae* 28.8, pp. 1589–1614. DOI: 10.5194/angeo-28-1589-2010.

Robinson, R. M., R. R. Vondrak, K. Miller, T. Dabbs, and D. Hardy (1987). "On calculating ionospheric conductances from the flux and energy of precipitating electrons". In: *Journal of Geophysical Research* 92.A3, p. 2565. DOI: 10.1029/ja092ia03p02565.

Rong, Z. J., A. T. Y. Lui, W. X. Wan, Y. Y. Yang, C. Shen, A. A. Petrukovich, Y. C. Zhang, T. L. Zhang, and Y. Wei (2015). "Time delay of interplanetary magnetic field penetration into Earth's magnetotail". In: *Journal of Geophysical Research: Space Physics* 120.5, pp. 3406–3414. DOI: 10.1002/2014JA020452.

Russell, C. T. (2000). "The solar wind interaction with the earth's magnetosphere: A tutorial". In: *IEEE Transactions on Plasma Science* 28.6, pp. 1818–1830. DOI: 10.1109/27.902211.

Russell, C. T. and M. K. Dougherty (2010). "Magnetic Fields of the Outer Planets". In: *Space Science Reviews* 152.1-4, pp. 251–269. DOI: 10.1007/s11214-009-9621-7.

Russell, C. T., J. T. Gosling, R. D. Zwickl, and E. J. Smith (1983). "Multiple spacecraft observations of interplanetary shocks: ISEE three-dimensional plasma measurements". In: *Journal of Geophysical Research: Space Physics* 88.A12, pp. 9941–9947. DOI: 10.1029/JA088iA12p09941.

Russell, C. T. and R. L. McPherron (1973). "Semiannual variation of geomagnetic activity". In: *Journal of Geophysical Research* 78.1, pp. 92–108. DOI: 10.1029/JA078i001p00092.

Russell, C. T., Y. L. Wang, and J. Raeder (2003). "Possible dipole tilt dependence of dayside magnetopause reconnection". In: *Geophysical Research Letters* 30.18. DOI: 10.1029/2003GL017725.

Samsonov, A. A., Z. Němeček, and J. Šafránková (2006). "Numerical MHD modeling of propagation of interplanetary shock through the magnetosheath". In: *Journal of Geophysical Research: Space Physics* 111.A8. DOI: 10.1029/2005JA011537.

Samsonov, A. A. and D. G. Sibeck (2013). "Large-scale flow vortices following a magnetospheric sudden impulse". In: *Journal of Geophysical Research: Space Physics* 118.6, pp. 3055–3064. DOI: 10.1002/jgra.50329.

Samsonov, A. A., D. G. Sibeck, and J. Imber (2007). "MHD simulation for the interaction of an interplanetary shock with the Earth's magnetosphere". In: *Journal of Geophysical Research: Space Physics* 112.A12. DOI: 10.1029/2007JA012627.

Samsonov, A. A., D. G. Sibeck, and Y. Yu (2010). "Transient changes in magnetospheric-ionospheric currents caused by the passage of an interplanetary shock: Northward interplanetary magnetic field case". In: *Journal of Geophysical Research: Space Physics* 115.A5. DOI: 10.1029/2009JA014751.

See, V., M. Jardine, A. A. Vidotto, P. Petit, S. C. Marsden, S. V. Jeffers, and J. D. Do Nascimento (2014). "The effects of stellar winds on the magnetospheres and potential habitability of exoplanets". In: *Astronomy and Astrophysics* 570, p. 99. DOI: 10.1051/0004-6361/201424323.

Shi, Y., D. M. Oliveira, D. J. Knipp, E. Zesta, T. Matsuo, and B. Anderson (2019). "Effects of Nearly Frontal and Highly Inclined Interplanetary Shocks on High-Latitude Field-Aligned Currents (FACs)". In: *Space Weather* 17.12, pp. 1659–1673. DOI: 10.1029/2019SW002367.

Shore, R. M., M. P. Freeman, J. C. Coxon, E. G. Thomas, J. W. Gjerloev, and N. Olsen (2019). "Spatial Variation in the Responses of the Surface External and Induced Magnetic Field to the Solar Wind". In: *Journal of Geophysical Research: Space Physics* 124.7, 2019JA026543. DOI: 10.1029/2019JA026543.

Slinker, S. P., J. A. Fedder, W. J. Hughes, and J. G. Lyon (1999). "Response of the ionosphere to a density pulse in the solar wind: Simulation of traveling convection vortices". In: *Geophysical Research Letters* 26.23, pp. 3549–3552. DOI: 10.1029/1999GL010688.

Smith, A. W., M. P. Freeman, I. J. Rae, and C. Forsyth (2019). "The Influence of Sudden Commencements on the Rate of Change of the Surface Horizontal Magnetic Field in the United Kingdom". In: *Space Weather* 17.11, pp. 1605–1617. DOI: 10.1029/2019SW002281.

Snekvik, K., N. Østgaard, P. Tenfjord, J. P. Reistad, K. M. Laundal, S. E. Milan, and S. E. Haaland (2017). "Dayside and nightside magnetic field responses at 780 km altitude to dayside reconnection". In: *Journal of Geophysical Research: Space Physics* 122.2, pp. 1670–1689. DOI: 10.1002/2016JA023177.

Solomon, S. C. (2010). "Terrestrial ionospheres". In: *Heliophysics: Evolving Solar Activity and the Climates of Space and Earth*. Ed. by C. J. Schrijver and G. L. Siscoe. Cambridge University Press, pp. 351–362. DOI: 10.1017/CBO9780511760358.014.

Sonnerup, B. U. Ö. (1974). "Magnetopause reconnection rate". In: *Journal of Geophysical Research* 79.10, pp. 1546–1549. DOI: 10.1029/ja079i010p01546.

Sorathia, K. A., V. G. Merkin, A. Y. Ukhorskiy, R. C. Allen, K. Nykyri, and S. Wing (2019). "Solar Wind Ion Entry Into the Magnetosphere During Northward IMF". In: *Journal of Geophysical Research: Space Physics* 124.7, pp. 5461–5481. DOI: 10.1029/2019JA026728.

Souza, V. M., W. D. Gonzalez, D. G. Sibeck, D. Koga, B. M. Walsh, and O. Mendes (2017). "Comparative study of three reconnection X line models at the Earth's dayside magnetopause using in situ observations". In: *Journal of Geophysical Research: Space Physics* 122.4, pp. 4228–4250. DOI: 10.1002/2016JA023790.

Tanaka, T. (1994). "Finite Volume TVD Scheme on an Unstructured Grid System for Three-Dimensional MHD Simulation of Inhomogeneous Systems Including Strong Background Potential Fields". In: *Journal of Computational Physics* 111.2, pp. 381–389. DOI: 10.1006/jcph.1994.1071.

Tayler, R. J. and J. G. Morgan (1981). "Thermonuclear Plasma Conditions in Stellar Interiors [and Discussion]". In: *Philosophical Transactions of the Royal Society of London. Series A, Mathematical and Physical Sciences* 300.1456, pp. 641–648.

Tenfjord, P., N. Østgaard, S. Haaland, K. Snekvik, K. M. Laundal, J. P. Reistad, R. Strangeway, S. E. Milan, M. Hesse, and A. Ohma (2018). "How the IMF By Induces a Local By Component During Northward IMF Bz and Characteristic Timescales". In: *Journal of Geophysical Research: Space Physics* 123.5, pp. 3333–3348. DOI: 10.1002/2018JA025186.

Tenfjord, P., N. Østgaard, K. Snekvik, K. M. Laundal, J. P. Reistad, S. Haaland, and S. E. Milan (2015). "How the IMF By induces a By component in the closed magnetosphere and how it leads to asymmetric currents and convection patterns in the two hemispheres". In: *Journal of Geophysical Research: Space Physics* 120.11, pp. 9368–9384. DOI: 10.1002/2015JA021579.

Tenfjord, P., N. Østgaard, R. Strangeway, S. Haaland, K. Snekvik, K. M. Laundal, J. P. Reistad, and S. E. Milan (2017). "Magnetospheric response and reconfiguration times following IMF By reversals". In: *Journal of Geophysical Research: Space Physics* 122.1, pp. 417–431. DOI: 10.1002/2016JA023018.

Thébault, E., C. C. Finlay, C. D. Beggan, P. Alken, J. Aubert, O. Barrois, F. Bertrand, T. Bondar, A. Boness, L. Brocco, E. Canet, A. Chambodut, A. Chulliat, P. Coïsson, F. Civet, A. Du, A. Fournier, I. Fratter, N. Gillet, B. Hamilton, M. Hamoudi, G. Hulot, T. Jager, M. Korte, W. Kuang, X. Lalanne, B. Langlais, J.-M. Léger, V. Lesur, F. J. Lowes, S. Macmillan, M. Mandea, C. Manoj, S. Maus, N. Olsen, V. Petrov, V. Ridley, M. Rother, T. J. Sabaka, D. Saturnino, R. Schachtschneider, O. Sirol, A. Tangborn, A. Thomson, L. Tøffner-Clausen, P. Vigneron, I. Wardinski, and T. Zvereva (2015). "International Geomagnetic Reference Field: the 12th generation". In: *Earth, Planets and Space* 67.1, p. 79. DOI: 10.1186/s40623-015-0228-9.

Tian, A. M., X. C. Shen, Q. Q. Shi, B. B. Tang, M. Nowada, Q. G. Zong, and S. Y. Fu (2016). "Dayside magnetospheric and ionospheric responses to solar wind pressure increase: Multispacecraft and ground observations". In: *Journal of Geophysical Research: Space Physics* 121.11, pp. 10, 813–10, 830. DOI: 10.1002/2016JA022459.

Toffoletto, F. R. and G. L. Siscoe (2009). "Solar-wind– magnetosphere coupling: an MHD perspective". In: *Heliophysics: Plasma Physics of the Local Cosmos*. Ed. by C. J. Schrijver and G. L. Siscoe. Cambridge University Press, pp. 295–323. DOI: 10.1017/CBO9781107-340657.012.

Torrilhon, M. (2003). "Non-uniform convergence of finite volume schemes for Riemann problems of ideal magnetohydrodynamics". In: *Journal of Computational Physics* 192.1, pp. 73–94. DOI: 10.1016/S0021-9991(03)00347-4.

Tóth, G., X. Jia, S. Markidis, I. B. Peng, Y. Chen, L. K. S. Daldorff, V. M. Tenishev, D. Borovikov, J. D. Haiducek, T. I. Gombosi, A. Glocer, and J. C. Dorelli (2016). "Extended magnetohydrodynamics with embedded particle-in-cell simulation of Ganymede's magnetosphere". In: *Journal of Geophysical Research: Space Physics* 121.2, pp. 1273–1293. DOI: 10.1002/2015JA021997.

Tóth, G., D. Kovács, K. C. Hansen, and T. I. Gombosi (2004). "Three-dimensional MHD simulations of the magnetosphere of Uranus". In: *Journal of Geophysical Research: Space Physics* 109.A11. DOI: 10.1029/2004JA010406.

Tóth, G., I. V. Sokolov, T. I. Gombosi, D. R. Chesney, C. R. Clauer, D. L. De Zeeuw, K. C. Hansen, K. J. Kane, W. B. Manchester, R. C. Oehmke, K. G. Powell, A. J. Ridley, I. I. Roussev, Q. F. Stout, O. Volberg, R. A. Wolf, S. Sazykin, A. Chan, B. Yu, and J. Kóta (2005). "Space Weather Modeling Framework: A new tool for the space science community". In: *Journal of Geophysical Research* 110.A12, A12226. DOI: 10.1029/2005JA011126.

Trattner, K. J., J. S. Mulcock, S. M. Petrinec, and S. A. Fuselier (2007). "Probing the boundary between antiparallel and component reconnection during southward interplanetary magnetic field conditions". In: *Journal of Geophysical Research: Space Physics* 112.8, pp. 1–16. DOI: 10.1029/2007JA012270.

Trattner, K. J., S. M. Petrinec, S. A. Fuselier, and T. D. Phan (2012). "The location of reconnection at the magnetopause: Testing the maximum magnetic shear model with THEMIS observations". In: *Journal of Geophysical Research: Space Physics* 117.A1. DOI: 10.1029/2011JA016959.

Treumann, R. A. and W. Baumjohann (1997). *Advanced Space Plasma Physics*. PUBLISHED BY IMPERIAL COLLEGE PRESS and DISTRIBUTED BY WORLD SCIENTIFIC PUBLISHING CO. DOI: 10.1142/p020.

Tsurutani, B. T. and G. S. Lakhina (2014). "An extreme coronal mass ejection and consequences for the magnetosphere and Earth". In: *Geophysical Research Letters* 41.2, pp. 287–292. DOI: 10.1002/2013GL058825.

Tsyganenko, N. A. (2002). In: *Journal of Geophysical Research: Space Physics* 107.A8. DOI: 10.1029/2001JA000219.

Uzdensky, D. A. (2003). "Petschek-like Reconnection with Current-driven Anomalous Resistivity and Its Application to Solar Flares". In: *The Astrophysical Journal* 587.1, pp. 450–457. DOI: 10.1086/368075.

Van Leer, B. (1977). "Towards the ultimate conservative difference scheme. IV. A new approach to numerical convection". In: *Journal of Computational Physics* 23.3, pp. 276–299. DOI: 10.1016/0021-9991(77)90095-X.

Vasyliunas, V. M. (2009). "Fundamentals of planetary magnetospheres". In: *Heliophysics: Plasma Physics of the Local Cosmos*. Ed. by C. J. Schrijver and G. L. Siscoe. Cambridge University Press, pp. 256–294. DOI: 10.1017/CBO9781107340657.011.

von Alfthan, S., D. Pokhotelov, Y. Kempf, S. Hoilijoki, I. Honkonen, A. Sandroos, and M. Palmroth (2014). "Vlasiator: First global hybrid-Vlasov simulations of Earth's foreshock and magnetosheath". In: *Journal of Atmospheric and Solar-Terrestrial Physics* 120, pp. 24–35. DOI: 10.1016/j.jastp.2014.08.012.

Walach, M.-T., A. Grocott, and S. E. Milan (2021). "Average Ionospheric Electric Field Morphologies During Geomagnetic Storm Phases". In: *Journal of Geophysical Research: Space Physics* 126.4. e2020JA028512 2020JA028512, e2020JA028512. DOI: https://doi.org/10.1029/2020JA028512.

Walach, M.-T. and S. E. Milan (2015). "Are steady magnetospheric convection events prolonged substorms?" In: *Journal of Geophysical Research: Space Physics* 120.3, pp. 1751–1758. DOI: 10.1002/2014JA020631.

Walach, M.-T., S. E. Milan, K. R. Murphy, J. A. Carter, B. A. Hubert, and A. Grocott (2017). "Comparative study of large-scale auroral signatures of substorms, steady magnetospheric convection events, and sawtooth events". In: *Journal of Geophysical Research: Space Physics* 122.6, pp. 6357–6373. DOI: 10.1002/2017JA023991.

Walker, R., R. Richard, T. Ogino, and M. Ashour-Abdalla (1999). "The response of the magnetotail to changes in the IMF orientation: The magnetotail's long memory". In: *Physics and Chemistry of the Earth, Part C: Solar, Terrestrial Planetary Science* 24.1. International Symposium on Solar-Terrestrial Coupling Processes, pp. 221–227. DOI: 10.1016/S1464-1917(98)00032-4.

Walsh, B. M., C. M. Komar, and Y. Pfau-Kempf (2017). "Spacecraft measurements constraining the spatial extent of a magnetopause reconnection X line". In: *Geophysical Research Letters* 44.7, pp. 3038–3046. DOI: 10.1002/2017GL073379.

Walt, S. van der, J. L. Schönberger, J. Nunez-Iglesias, F. Boulogne, J. D. Warner, N. Yager, E. Gouillart, and T. Yu (2014). "scikit-image: image processing in Python". In: *PeerJ* 2, e453. DOI: 10.7717/peerj.453.

Wang, C., J. P. Han, H. Li, Z. Peng, and J. D. Richardson (2014). "Solar wind-magnetosphere energy coupling function fitting: Results from a global MHD simulation". In: *Journal of Geophysical Research: Space Physics* 119.8, pp. 6199–6212. DOI: 10.1002/2014JA019834.

Wang, H., H. Lühr, and S. Y. Ma (2005). "Solar zenith angle and merging electric field control of field-aligned currents: A statistical study of the Southern Hemisphere". In: *Journal of Geophysical Research* 110.A3, A03306. DOI: 10.1029/2004JA010530.

Wang, Y., C. L. Shen, S. Wang, and P. Z. Ye (2003). "An empirical formula relating the geomagnetic storm's intensity to the interplanetary parameters: - and Δt". In: *Geophysical Research Letters* 30.20. DOI: 10.1029/2003GL017901.

Webb, D. F. and T. A. Howard (2012). "Coronal mass ejections: Observations". In: *Living Reviews in Solar Physics* 9.1, p. 3. DOI: 10.12942/lrsp-2012-3.

Welling, D. T. and A. J. Ridley (2010). "Validation of SWMF magnetic field and plasma". In: *Space Weather* 8.3. DOI: 10.1029/2009SW000494.

Wild, J. A., S. E. Milan, S. W. H. Cowley, M. W. Dunlop, C. J. Owen, J. M. Bosqued, M. G. G. T. Taylor, J. A. Davies, M. Lester, N. Sato, A. S. Yukimatu, A. N. Fazakerley, A. Balogh, and H. R. Eme (2003). *Coordinated interhemispheric SuperDARN radar observations of the ionospheric response to flux transfer events observed by the Cluster spacecraft at the high-latitude magnetopause*. Tech. rep., pp. 1807–1826.

Wilkins, M. L. (1980). "Use of artificial viscosity in multidimensional fluid dynamic calculations". In: *Journal of Computational Physics* 36.3, pp. 281–303. DOI: 10.1016/0021-9991(80)90161-8.

Wilson Iii, L. B., M. L. Stevens, J. C. Kasper, K. G. Klein, B. A. Maruca, S. D. Bale, T. A. Bowen, M. P. Pulupa, and C. S. Salem (2018). "The Statistical Properties of Solar Wind Temperature Parameters Near 1 au". In: *The Astrophysical Journal Supplement Series* 236.15pp, p. 41. DOI: 10.3847/1538-4365/aab71c.

Wiltberger, M., R. S. Weigel, W. Lotko, and J. A. Fedder (2009). "Modeling seasonal variations of auroral particle precipitation in a global-scale magnetosphere-ionosphere simulation". In: *J. Geophys. Res* 114.A1, p. 1204. DOI: 10.1029/2008JA013108.

Winslow, R. M., N. Lugaz, N. A. Schwadron, C. J. Farrugia, W. Yu, J. M. Raines, M. L. Mays, A. B. Galvin, and T. H. Zurbuchen (2016). "Longitudinal conjunction between MESSENGER and STEREO A: Development of ICME complexity through stream interactions". In: *Journal of Geophysical Research: Space Physics* 121.7, pp. 6092–6106. DOI: 10.1002/2015JA022307.

Wolf, R. A. (1975). In: *Space Science Reviews* 17.2-4, pp. 537–562.

Xiao, S., T. Zhang, Y. Ge, G. Wang, W. Baumjohann, and R. Nakamura (2016). "A statistical study on the shape and position of the magnetotail neutral sheet". In: *Annales Geophysicae* 34.2, pp. 303–311. DOI: 10.5194/angeo-34-303-2016.

Yee, K. (1966). "Numerical solution of initial boundary value problems involving maxwell's equations in isotropic media". In: *IEEE Transactions on Antennas and Propagation* 14.3, pp. 302–307. DOI: 10.1109/TAP.1966.1138693.

Yeh, T. (1976). "Day side reconnection between a dipolar geomagnetic field and a uniform interplanetary field". In: *Journal of Geophysical Research* 81.13, pp. 2140–2144. DOI: 10.1029/JA081i013p02140.

Yu, Y.-Q. and A. J. Ridley (2011). "Understanding the response of the ionosphere-magnetosphere system to sudden solar wind density increases". In: *Journal of Geophysical Research: Space Physics* 116.A4. DOI: 10.1029/2010JA015871.

Yu, Y. and A. J. Ridley (2009). "The response of the magnetosphere-ionosphere system to a sudden dynamic pressure enhancement under southward IMF conditions". In: *Annales Geophysicae* 27.12, pp. 4391–4407. DOI: 10.5194/angeo-27-4391-2009.

Zhang, S.-R., J. M. Holt, and M. McCready (2007). "High latitude convection based on long-term incoherent scatter radar observations in North America". In: *Journal of Atmospheric and Solar-Terrestrial Physics* 69.10-11, pp. 1273–1291. DOI: 10.1016/J.JASTP.2006.08.017.

Zhang, Y., L. J. Paxton, and H. Kil (2011). "Nightside polar rain aurora boundary gap and its applications for magnetotail reconnection". In: *Journal of Geophysical Research: Space Physics* 116.A11. DOI: 10.1029/2011JA016884.

Zhao, H. Y., X. C. Shen, B. B. Tang, A. M. Tian, Q. Q. Shi, J. M. Weygand, Z. H. Yao, Q.-G. Zong, S. Y. Fu, S. T. Yao, T. Xiao, and Z. Y. Pu (2016). "Magnetospheric vortices and their global effect after a solar wind dynamic pressure decrease". In: *Journal of Geophysical Research: Space Physics* 121.2, pp. 1071–1077. DOI: 10.1002/2015JA021646.

Zhu, C. B., H. Zhang, Y. S. Ge, Z. Y. Pu, W. L. Liu, W. X. Wan, L. B. Liu, Y. D. Chen, H. J. Le, and Y. F. Wang (2015). "Dipole tilt angle effect on magnetic reconnection locations on the magnetopause". In: *Journal of Geophysical Research: Space Physics* 120, pp. 5344–5354. DOI: 10.1002/2015JA020989.